Proceedings

of the Estonian Academy of Sciences

2026
75/1

ISSN 1736-6046 (print)
ISSN 1736-7530 (electronic)
Estonian Academy Publishers
www.eap.ee/proceedings

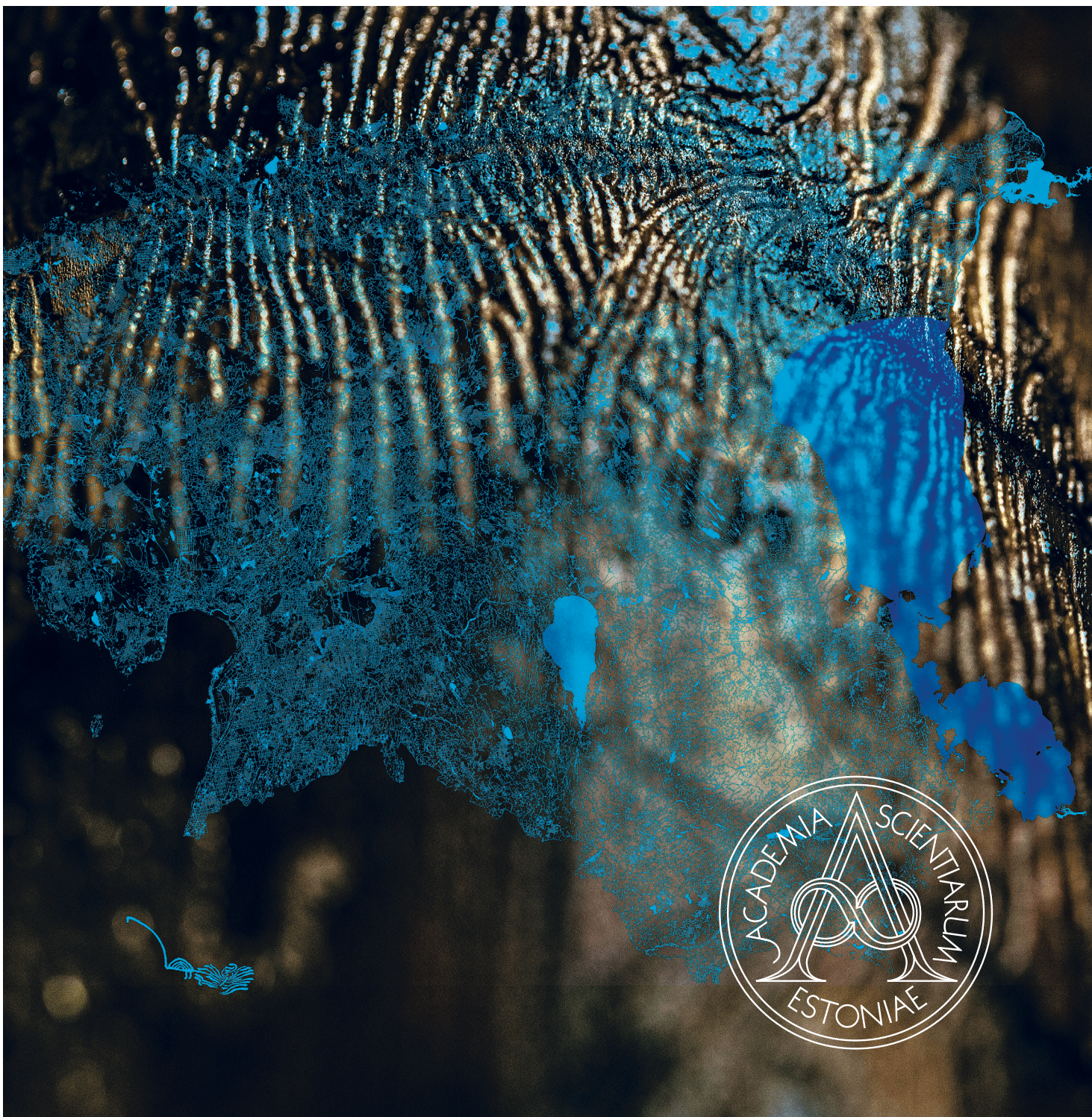

International open access scientific journal of the Estonian Academy of Sciences, published in collaboration with the Estonian Marine Institute at the University of Tartu, the Estonian University of Life Sciences, Tallinn University, and Tallinn University of Technology

Proceedings of the Estonian Academy of Sciences

Published since 1952

Proceedings of the Estonian Academy of Sciences is published quarterly

Abstracted/indexed in:
Science Citation Index Expanded™ (Web of Science), Journal Citation Reports/Science Edition, Cambridge Scientific Abstracts, Mathematical Reviews, Zentralblatt MATH, INSPEC, Scopus®, Chemical Abstracts, EBSCO, The Gale Group Inc., ProQuest LLC, Airiti Inc., DOAJ (Directory of Open Access Journals), Scilit, CNKI

Editorial Office:
Kohtu 6, 10130 Tallinn, Estonia
Email: hedi.tonso@eap.ee

Front cover:
Waterway Weaves 2 by Peeter Laurits, 2014. The artwork was given as a gift by President Toomas H. Ilves to President Barack Obama during his state visit to Estonia.

Printed by Alfapress, Reti tee 8, 75312 Peetri, Estonia

Proceedings of the Estonian Academy of Sciences
2026, **75**, 1, 1

https://doi.org/10.3176/proc.2026.1.03

www.eap.ee/proceedings
Estonian Academy Publishers

Available online 30 December 2025

EDITORIAL

Järv, J. 2026. *Proceedings of the Estonian Academy of Sciences*, Volume 75. *Proceedings of the Estonian Academy of Sciences*, **75**(1), 1. https://doi.org/10.3176/proc.2026.1.03

Proceedings of the Estonian Academy of Sciences, Volume 75

Publishing scientific journals has been an important and an honourable feature of academies of sciences throughout history. The first scientific journal *Philosophical Transactions* was established as early as 1665, a few years after the foundation of the Royal Society (the UK national academy of sciences). This journal was later transformed into the *Proceedings of the Royal Society* (A and B Series), and today the academy publishes several other scientific journals.

In keeping with this tradition, the Estonian Academy of Sciences also publishes scientific journals. Although the academy's publishing house was founded only in 1994, the first volume of the *Proceedings of the Estonian Academy of Sciences* was printed already in 1952.

Today, this multidisciplinary international journal publishes peer-reviewed research articles, review articles and short communications in the scientific fields covered by the Estonian Academy of Sciences. All publications have open access, and the publication of works supported by Estonian funding is free of charge. Articles are published electronically immediately after technical editing, which significantly shortens the production time. Even faster publication is possible through the 'fast track' process. However, this service is paid for by all authors.

All published papers are indexed in the main international databases (Web of Science, Scopus, DOAJ, EBSCO, ProQuest and others), ensuring the global dissemination of published results. Today, the backfiles of publications are available from the first volume of the journal (https://kirj.ee/archive). The electronic submission of manuscripts is available from 2021.

All these developments of the publication process are in line with the Estonian Academy Publishers' efforts to transform the *Proceedings of the Estonian Academy of Sciences* into a high quality modern and competitive scientific journal.

Jaak Järv
Editor-in-Chief

Proceedings of the Estonian Academy of Sciences
2026, **75**, 1, 2–14

https://doi.org/10.3176/proc.2026.1.01

www.eap.ee/proceedings
Estonian Academy Publishers

CONTROL THEORY

RESEARCH ARTICLE

Received 29 April 2025
Accepted 18 June 2025
Available online 15 December 2025

Keywords:
discrete-time systems, nonlinear systems, observer form, algebraic approach, vector fields, multi-input multi-output system

Corresponding author:
Tanel Mullari
tanel.mullari@taltech.ee

Citation:
Kaldmäe, A., Kaparin, V., Kotta, Ü., Mullari, T. and Tõnso, M. 2026. Classical observer form for discrete-time nonlinear system: MIMO case. *Proceedings of the Estonian Academy of Sciences*, **75**(1), 2–14.
https://doi.org/10.3176/proc.2026.1.01

Classical observer form for discrete-time nonlinear system: MIMO case

Arvo Kaldmäe[a], Vadim Kaparin[a], Ülle Kotta[a], Tanel Mullari[b] and Maris Tõnso[a]

[a] Department of Software Science, Tallinn University of Technology, Akadeemia tee 21/1, 12618 Tallinn, Estonia

[b] Department of Cybernetics, Tallinn University of Technology, Ehitajate tee 5, 19086 Tallinn, Estonia

ABSTRACT

The paper addresses the problem of transforming multi-input multi-output discrete-time nonlinear state equations into the classical observer form using state transformation. Necessary and sufficient geometric solvability conditions are given in terms of vector fields. The results obtained generalize the previous ones in several aspects. First, the results are also applicable to non-reversible systems. Second, they hold almost everywhere, not only around the equilibrium point of the system. The generalizations are possible due to the use of different mathematical tools. The proof of sufficiency also provides a method for finding the state transformation. The results are illustrated by two examples.

1. Introduction

A nonlinear state observer with linear error dynamics can be easily constructed for nonlinear state equations whenever they are in the observer form [5,14]. Therefore, the ability to transform the equations into such a form is very important. State equations in the observer form have a linear structure up to nonlinear injection terms that depend on measurable inputs and outputs. Since the class of systems that can be transformed into the classical observer form is quite restrictive, various generalizations are proposed in the literature. Some of them suggest extending the state equations by auxiliary dynamics, so that the extended system becomes transformable into the classical observer form [13,21]; others allow the injection terms to also depend on the past or future values of inputs and outputs [6–9,11,20], or imply input dependence of the linear part [3,12]. Different approaches also apply different mathematical frameworks with their own pros and cons. The majority of the results are derived for systems with a single output. However, their extension to a multi-input multi-output (MIMO) case is not straightforward and can be a challenge [2,4,10].

Starting from the classical observer form, this paper extends the single-output results from [15,16] to the MIMO case, thereby laying a foundation for further extension to generalized MIMO observer forms, similar to those from [18,19] for single-output systems. The main contribution of this paper is to establish necessary and sufficient conditions for state equivalence to the classical observer form. The conditions are formulated in terms of certain output-related vector fields and their backward shifts. Unlike the single-output case, in the multi-output counterpart these vector fields are, in general, not uniquely defined, which allows for freedom of choice but can complicate the verification of conditions. However, a similar issue is inherent also in earlier works [2,4]. The suggested approach is compared with the earlier results, and its applicability is demonstrated by several examples.

2. Preliminaries and problem statement

In this paper, we use the generic mathematical setting from [17]. Consider the discrete-time MIMO nonlinear control system

$$x^{\langle 1\rangle}(t) = \overline{\Phi}(x(t), u(t)), \quad y(t) = h(x(t)), \tag{1}$$

where $x^{\langle 1\rangle}(t) := x(t+1)$, $t \in \mathbb{Z}$, the state variable $x(t) \in \bar{X} \subseteq \mathbb{R}^n$, the control variable $u(t) \in U \subseteq \mathbb{R}^m$, the output variable $y \in Y \subseteq \mathbb{R}^p$, and the state transition map $\overline{\Phi} : \bar{X} \times U \to \bar{X}$ is supposed to be analytic. Both $\bar{X}$ and U are assumed to be open sets. We assume that the map $\overline{\Phi}$ can be extended to the map $\Phi = [\overline{\Phi}^{\mathrm{T}}, \chi^{\mathrm{T}}]^{\mathrm{T}} : (\bar{X} \times U) \to (\bar{X} \times \mathbb{R}^m)$ such that Φ has the global analytic inverse $\Phi^{-1} = [\Lambda^{\mathrm{T}}, \lambda^{\mathrm{T}}]^{\mathrm{T}} : \Phi(\bar{X} \times U) \to (\bar{X} \times U)$. Introduce the additional variable at time instant t, $z(t) \in \mathbb{R}^m$,

$$z(t) = \chi(x(t), u(t)). \tag{2}$$

The equations (1), (2) define the inversive difference field $\mathcal{K}$ of meromorphic functions in a finite number of variables from the set $C = \{x, u^{\langle k\rangle}, z^{\langle -l\rangle}, k \geq 0, l > 0\}$. Here, $u^{\langle k\rangle}$ denotes the k-th order forward shift of u and $z^{\langle -l\rangle}$ the l-th order backward shift of z. The first order forward shift of x is defined by (1) and the first order backward shifts of x and u by

$$x^{\langle -1\rangle} = \Lambda(x, z^{\langle -1\rangle}), \quad u^{\langle -1\rangle} = \lambda(x, z^{\langle -1\rangle}). \tag{3}$$

The higher order backward shifts of x and u can be found recursively. The forward and backward shifts of functions are defined by shifting the arguments of the functions and replacing the dependent variables $x^{\langle 1\rangle}$, $x^{\langle -1\rangle}$ and $u^{\langle -1\rangle}$ from (1) and (3).

Consider the infinite set of symbols $\mathrm{d}C = \{\mathrm{d}x, \mathrm{d}u^{\langle k\rangle}, \mathrm{d}z^{\langle -l\rangle}, k \geq 0, l \geq 1\}$ and let $\mathcal{E} := \mathrm{span}_{\mathcal{K}}\{\mathrm{d}C\}$ be the vector space spanned over $\mathcal{K}$ by the elements of $\mathrm{d}C$, called the 1-forms

$$\omega = \sum_{i=1}^{n} A_i \mathrm{d}x_i + \sum_{j=1}^{m} \sum_{k\geq 0} B_{jk} \mathrm{d}u_j^{\langle k\rangle} + \sum_{q=1}^{m} \sum_{l\geq 1} C_{ql} \mathrm{d}z_q^{\langle -l\rangle},$$

where only a finite number of coefficients differ from zero [1]. Define the space $\mathcal{E}^* = \mathrm{span}_{\mathcal{K}}\{\partial/\partial x, \partial/\partial u^{\langle k\rangle}, k \geq 0, \partial/\partial z^{\langle -l\rangle}, l \geq 1\}$, dual to $\mathcal{E}$, whose elements are the vector fields

$$\Gamma = \sum_{i=1}^{n} \gamma_i \frac{\partial}{\partial x_i} + \sum_{j=1}^{m} \sum_{k\geq 0} \overline{\gamma}_{jk} \frac{\partial}{\partial u_j^{\langle k\rangle}} + \sum_{q=1}^{m} \sum_{l\geq 1} \widetilde{\gamma}_{ql} \frac{\partial}{\partial z_q^{\langle -l\rangle}}.$$

Note that in computations the 1-form is typically interpreted as the row vector of its coefficients. Similarly, the vector field is interpreted as the column vector of its coefficients. Therefore, the scalar product of the 1-form and the vector field can be understood as a product of the row and column vectors. By duality between $\mathcal{E}$ and $\mathcal{E}^*$, the scalar products of 1-forms and vector fields satisfy the relations

$$\langle \mathrm{d}x_i, \Gamma\rangle = \gamma_i, \quad \langle \mathrm{d}u_j^{\langle k\rangle}, \Gamma\rangle = \overline{\gamma}_{jk}, \quad \langle \mathrm{d}z_q^{\langle -l\rangle}, \Gamma\rangle = \widetilde{\gamma}_{ql}.$$

Definition 1. [17] *For a vector field $\Gamma \in \mathrm{span}_{\mathcal{K}}\{\partial/\partial x\}$, its backward shift is the vector field*

$$\Gamma^{\langle -1\rangle} = \sum_{l=1}^{n} \left\langle \mathrm{d}\overline{\Phi}_l, \Gamma \right\rangle^{\langle -1\rangle} \frac{\partial}{\partial x_l} + \sum_{v=1}^{m} \langle \mathrm{d}\chi_v, \Gamma\rangle^{\langle -1\rangle} \frac{\partial}{\partial z_v^{\langle -1\rangle}}, \tag{4}$$

and the projection of $\Gamma^{\langle -1\rangle}$ is the vector field

$$\Gamma^{\langle -1\rangle\pi} = \sum_{l=1}^{n} \left\langle \mathrm{d}\overline{\Phi}_l, \Gamma \right\rangle^{\langle -1\rangle} \frac{\partial}{\partial x_l}. \tag{5}$$

Lemma 2. [15] *Let the vector fields $\Gamma_k = \sum_{i=1}^{n} \gamma_{ki}(x)\, \partial/\partial x_i$, $k = 1, \ldots, n$, be linearly independent. If the vector fields Γ_k commute, then generically one can define the state transformation $X_j = \Psi_j(x)$, $\Psi_j \in \mathcal{K}$, $j = 1, \ldots, n$, such that $\left\langle \mathrm{d}\Psi_j, \Gamma_k \right\rangle \equiv \delta_{jk}$, $j, k = 1, \ldots, n$, where δ_{jk} is the Kronecker delta.*

Throughout the paper, the following assumption is made.

Assumption 3. The system (1) is generically observable with the observability indices ρ_i, $i = 1, \dots, p$, if $\sum_{i=1}^{p} \rho_i = n$, and

$$\operatorname{rank}_{\mathcal{K}} \left(\left(\frac{\partial y_1}{\partial x} \right)^{\mathrm{T}} \dots \left(\frac{\partial y_1^{\langle \rho_1 - 1 \rangle}}{\partial x} \right)^{\mathrm{T}} \dots \left(\frac{\partial y_p}{\partial x} \right)^{\mathrm{T}} \dots \left(\frac{\partial y_p^{\langle \rho_p - 1 \rangle}}{\partial x} \right)^{\mathrm{T}} \right)^{\mathrm{T}} = n. \tag{6}$$

Without loss of generality, one can redefine the outputs to guarantee that $\rho_i \geq \rho_k$, if $i < k$.

Problem statement. The aim of this paper is to find, under Assumption 3, the coordinate transformation $X = \Psi(x)$, if it exists, such that in the new coordinates the system takes the observer form

$$\begin{aligned} X_{i,j}^{\langle 1 \rangle} &= X_{i,j+1} + \varphi_{i,j}(y_1, \dots, y_p, u_1, \dots, u_m), \quad i = 1, \dots, p, \quad j = 1, \dots, \rho_i - 1, \\ X_{i,\rho_i}^{\langle 1 \rangle} &= \varphi_{i,\rho_i}(y_1, \dots, y_p, u_1, \dots, u_m), \quad y_i = X_{i,1}. \end{aligned} \tag{7}$$

Proposition 4. *(Necessary condition) If the state equations* (1) *are transformable by the state transformation* $X = \Psi(x)$ *into the observer form* (7) *with the observability indices* $(\rho_1, \dots, \rho_p)$*, then*

$$\frac{\partial y_i^{\langle \rho_i \rangle}}{\partial y_k^{\langle j \rangle}} \equiv 0, \quad i = 1, \dots, p, \quad k = 1, \dots, i, \quad j = \rho_i, \dots, \rho_k - 1. \tag{8}$$

Proof. Compute from (7):

$$y_i^{\langle \rho_i \rangle} = \sum_{j=1}^{\rho_i} \varphi_{i,j}(y^{\langle \rho_i - j \rangle}, u^{\langle \rho_i - j \rangle}). \tag{9}$$

Because of (9), the expression of $y_i^{\langle \rho_i \rangle}$ does not depend on shifts of y higher than $\rho_i - 1$, meaning that (8) must be satisfied. □

3. Main result

Define the vector fields $\Xi_k \in \operatorname{span}_{\mathcal{K}}\{\partial/\partial x\}$, $k = 1, \dots, p$, in terms of which the main theorem will be presented, as the solutions of the set of equations

$$\left\langle \mathrm{d}y_i^{\langle j-1 \rangle}, \Xi_k \right\rangle \equiv \delta_{ik} \delta_{j\rho_k}, \quad i, k = 1, \dots, p, \quad j = 1, \dots, \min(\rho_i, \rho_k). \tag{10}$$

Note that for a fixed $k > 1$, when $\rho_k < \rho_1$, the number of equations in the system (10) that defines Ξ_k is less than the number of the coefficients of Ξ_k. This means that some coefficients of Ξ_k can be chosen freely. The vector fields are uniquely defined only if all observability indices are equal. The unknown functions (coefficients) in the vector fields Ξ_k can be found from the necessary and sufficient solvability conditions of Theorem 8 below. First note that because of the condition (ii), one has to search for coefficients as functions of the argument x only. Next, the condition (i) gives a number of equations to define the unknown functions. Of course, in general, there is certain freedom to choose these unknown functions, and then one may opt for the simplest choice. This approach is described in Section 5 with examples. The equations (10) extend those for the single-output case [16]. The extension is not obvious. The remarks below discuss the problems one faces in the other routes of extension.

Remark 5. Observe that, unlike [4], in the equations (10) that define the vector fields Ξ_k, $k = 1, \dots, p$, we require $j = 1, \dots, min(\rho_i, \rho_k)$. If one takes, as in [4], $j = 1, \dots, \rho_k$, then in the case where $i > k$ and $\rho_k > \rho_i$, the system of equations may become inconsistent. We will demonstrate this on a simple case of two outputs and the observability indices $(3, 2)$. In such a case there is no reason for the scalar product $\langle \mathrm{d}y_2^{\langle 2 \rangle}, \Xi_1 \rangle$ to be identically equal to zero. This is because $\mathrm{d}y_2^{\langle 2 \rangle}$ depends, in principle, linearly on $\mathrm{d}y_1$, $\mathrm{d}y_1^{\langle 1 \rangle}$, $\mathrm{d}y_1^{\langle 2 \rangle}$, $\mathrm{d}y_2$, and $\mathrm{d}y_2^{\langle 1 \rangle}$. Consequently, taking also into account the equations in (10), one has

$$\left\langle \mathrm{d}y_2^{\langle 2 \rangle}, \Xi_1 \right\rangle = a_1 \langle \mathrm{d}y_1, \Xi_1 \rangle + a_2 \left\langle \mathrm{d}y_1^{\langle 1 \rangle}, \Xi_1 \right\rangle + a_3 \left\langle \mathrm{d}y_1^{\langle 2 \rangle}, \Xi_1 \right\rangle + b_1 \langle \mathrm{d}y_2, \Xi_1 \rangle + b_2 \left\langle \mathrm{d}y_2^{\langle 1 \rangle}, \Xi_1 \right\rangle = a_3.$$

In the case where j is given as in (10), no contradictions arise, but the vector fields Ξ_1, $\Xi_1^{\langle -1\rangle\pi}$, $\Xi_1^{\langle -2\rangle\pi}$, Ξ_2, $\Xi_2^{\langle -1\rangle\pi}$ are not necessarily independent. The problem is removable if one additionally requires that $\langle \mathrm{d}y_2^{\langle 2\rangle}, \Xi_1\rangle \equiv 0$. Essentially this means that $\mathrm{d}y_2^{\langle 2\rangle}$ is not allowed to depend on $\mathrm{d}y_1^{\langle 2\rangle}$. In the general case, if $\rho_k > \rho_i$, one has to require that the equations in (10) additionally hold for $j = \rho_i + 1, \ldots, \rho_k$, which imposes restrictions on how $\mathrm{d}y_i^{\langle j-1\rangle}$ can depend on the other output shifts.

Remark 6. If in the equations (10) that define the vector fields Ξ_k, $k = 1, \ldots, p$, one takes $j = 1, \ldots, \rho_i$, then the vector fields Ξ_k are uniquely defined. However, if all observability indices are not equal, then the coefficients of all Ξ_k, $k = 1, \ldots, p$, are not the functions of x only. Consequently, the new states as the functions of old ones will not depend only on x either.

Compute the projections of the backward shifts of Ξ_k, $k = 1, \ldots, p$, up to the order $\rho_k - 1$ according to Definition 1.

Lemma 7. *Suppose that*

$$\left[\Xi_i, \Xi_k^{\langle -l\rangle\pi}\right] \equiv 0, \quad i, k = 1, \ldots, p, \quad l = 0, \ldots, \rho_k - 1 \tag{11}$$

and the coefficients of the vector fields $\Xi_k^{\langle -l\rangle\pi}$, $k = 1, \ldots, p$, $l = 0, \ldots, \rho_k - 1$, depend only on the variables x. Then the following holds:

$$\left[\Xi_i^{\langle -j\rangle\pi}, \Xi_k^{\langle -l\rangle\pi}\right] \equiv 0, \quad i, k = 1, \ldots, p, \quad j = 0, \ldots, \rho_i - 1, \quad l = 0, \ldots, \rho_k - 1. \tag{12}$$

Proof. Due to (11), the equality (12) is valid for $j = 0$. Suppose now that (12) holds for a certain index $q \in \{0, \ldots, \rho_i - 2\}$, i.e.

$$\left[\Xi_i^{\langle -q\rangle\pi}, \Xi_k^{\langle -\bar{l}\rangle\pi}\right] \equiv 0, \quad i, k = 1, \ldots, p, \quad \bar{l} = 0, \ldots, \rho_k - 2. \tag{13}$$

Show that the validity of (12) for $j = q + 1$ follows from (13). Shift both sides of (13) backward by one step, obtaining

$$\left[\left(\Xi_i^{\langle -q\rangle\pi}\right)^{\langle -1\rangle}, \left(\Xi_k^{\langle -\bar{l}\rangle\pi}\right)^{\langle -1\rangle}\right] \equiv 0.$$

Due to Definition 1,

$$\left(\Xi_i^{\langle -q\rangle\pi}\right)^{\langle -1\rangle} = \Xi_i^{\langle -q-1\rangle\pi} + \sum_{r=1}^{m} \mu_r \frac{\partial}{\partial z_r^{\langle -1\rangle}}, \quad \left(\Xi_k^{\langle -\bar{l}\rangle\pi}\right)^{\langle -1\rangle} = \Xi_k^{\langle -\bar{l}-1\rangle\pi} + \sum_{r=1}^{m} \bar{\mu}_r \frac{\partial}{\partial z_r^{\langle -1\rangle}}, \tag{14}$$

where

$$\mu_r = \left\langle \mathrm{d}\chi_r, \Xi_i^{\langle -q\rangle\pi} \right\rangle^{\langle -1\rangle}, \quad \bar{\mu}_r = \left\langle \mathrm{d}\chi_r, \Xi_i^{\langle -\bar{l}\rangle\pi} \right\rangle^{\langle -1\rangle}.$$

Taking into account (14), one can rewrite (13) as

$$\begin{aligned} &\left[\Xi_i^{\langle -q-1\rangle\pi}, \Xi_k^{\langle -\bar{l}-1\rangle\pi}\right] + \sum_{r=1}^{m} \left\langle \mathrm{d}\bar{\mu}_r, \Xi_i^{\langle -q-1\rangle\pi} \right\rangle \frac{\partial}{\partial z_r^{\langle -1\rangle}} - \sum_{r=1}^{m} \left\langle \mathrm{d}\mu_r, \Xi_k^{\langle -\bar{l}-1\rangle\pi} \right\rangle \frac{\partial}{\partial z_r^{\langle -1\rangle}} \\ &+ \sum_{r=1}^{m} \bar{\mu}_r \left[\frac{\partial}{\partial z_r^{\langle -1\rangle}}, \Xi_k^{\langle -\bar{l}-1\rangle\pi}\right] - \sum_{r=1}^{m} \mu_r \left[\frac{\partial}{\partial z_r^{\langle -1\rangle}}, \Xi_i^{\langle -q-1\rangle\pi}\right] + \sum_{r,s=1}^{m} \left[\mu_r \frac{\partial}{\partial z_r^{\langle -1\rangle}}, \bar{\mu}_s \frac{\partial}{\partial z_s^{\langle -1\rangle}}\right] \equiv 0. \end{aligned} \tag{15}$$

Because the first term on the left-hand side of (15) belongs to $\mathrm{span}_{\mathcal{K}}\{\partial/\partial x\}$, then it identically equals zero if the remaining terms either also identically equal zero, which is the case of the 4th and the 5th terms by the assumption of the lemma, or belong to $\mathrm{span}_{\mathcal{K}}\{\partial/\partial z^{\langle -1\rangle}\}$, which is the case of the 2nd, the 3rd and the 6th terms. Then

$$\left[\Xi_i^{\langle -q-1\rangle\pi}, \Xi_k^{\langle -\bar{l}-1\rangle\pi}\right] \equiv 0, \quad i, k = 1, \ldots, p, \quad \bar{l} = 0, \ldots, \rho_k - 2.$$

Denoting $l := \bar{l} + 1$, we see that (12) really holds in the case $j = q + 1$. □

In Theorem 8 below, we assume the system observability because the observability property as well as the observability indices are invariant under state transformation. Since the observer form is observable by definition, it makes no sense to address non-observable systems.

Theorem 8. *Under Assumption 3, the state equations* (1) *are transformable by a state transformation* $X = \Psi(x)$ *into the observer form* (7) *with the observability indices* $(\rho_1, \dots, \rho_p)$ *if and only if among the solutions of* (10) *there exist the vector fields* $\Xi_1, \dots, \Xi_p$ *that satisfy the following conditions:*

(i)
$$\left[\Xi_i, \Xi_k^{\langle -l\rangle\pi}\right] \equiv 0, \quad i,k = 1,\dots,p, \quad l = 0,\dots,\rho_k - 1,$$

(ii) *the coefficients of the vector fields* $\Xi_k^{\langle -l\rangle\pi}$, $k = 1,\dots,p$, $l = 0,\dots,\rho_k - 1$, *depend only on the variables* x,

(iii)
$$\left\langle \mathrm{d}y_i^{\langle j-1\rangle}, \Xi_k \right\rangle \equiv \delta_{ik}\delta_{j\rho_k}, \quad k = 1,\dots,p-1, \quad i = k+1,\dots,p, \quad j = \rho_i + 1,\dots,\rho_k.$$

Proof. Sufficiency. The sufficiency proof consists of two parts. (a) If (iii) holds, then the vector fields $\Xi_k^{\langle -l\rangle\pi}$, $k = 1,\dots,p$, $l = 0,\dots,\rho_k - 1$, are linearly independent. (b) If also (i) and (ii) are true, then one can define the new coordinates as the canonical parameters of n vector fields $\Xi_k^{\langle -l\rangle\pi}$, $k = 1,\dots,p$, $l = 0,\dots,\rho_k - 1$, in terms of which the state equations take the observer form (7).

(a) To prove the linear independence of $\Xi_k^{\langle -l\rangle\pi}$, $k = 1,\dots,p$, $l = 0,\dots,\rho_k - 1$, we prove first that the following holds:

$$\left\langle \mathrm{d}y_i^{\langle j-1\rangle}, \Xi_k^{\langle -l\rangle\pi} \right\rangle \equiv \delta_{ik}\delta_{j,\rho_k - l}, \quad i,k = 1,\dots,p, \quad l = 0,\dots,\rho_k - 1, \quad j = 1,\dots,\rho_k - l. \tag{16}$$

Since $\mathrm{d}y_i^{\langle j-1\rangle} \in \mathrm{span}_{\mathcal{K}}\{\mathrm{d}x, \mathrm{d}u, \dots, \mathrm{d}u^{\langle j-2\rangle}\}$, but $\Xi_k^{\langle -l\rangle\pi} \in \mathrm{span}_{\mathcal{K}}\{\partial/\partial x, \partial/\partial z^{\langle -1\rangle}, \dots, \partial/\partial z^{\langle -l\rangle}\}$, one can rewrite (16) as $\langle \mathrm{d}y_i^{\langle j-1\rangle}, \Xi_k^{\langle -l\rangle}\rangle \equiv \delta_{ik}\delta_{j,\rho_k - l}$. Shifting the latter forward l times and taking into account that $\delta_{j,\rho_k - l} = \delta_{j+l,\rho_k}$, one gets

$$\left\langle \mathrm{d}y_i^{\langle j+l-1\rangle}, \Xi_k \right\rangle \equiv \delta_{ik}\delta_{j+l,\rho_k}, \quad l = 0,\dots,\rho_k - 1, \quad j = 1,\dots,\rho_k - l.$$

Denoting $q := j + l$, then $q = 1,\dots,\rho_k$, and one finally obtains

$$\left\langle \mathrm{d}y_i^{\langle q-1\rangle}, \Xi_k \right\rangle \equiv \delta_{ik}\delta_{q\rho_k}, \quad i,k = 1,\dots,p, \quad q = 1,\dots,\rho_k, \tag{17}$$

the validity of which follows directly from (10), (iii) and system observability. Note that for (17) to hold, $\mathrm{d}y_i^{\langle j\rangle}$, $i = 1,\dots,p$, $j = 0,\dots,\rho_k - 1$ for each $k = 1,\dots,p$, should be linearly independent. If $i > k$, then $\rho_k \le \rho_i$, but this is not a problem since the condition (iii) has to be satisfied too. Therefore, for (17) to hold, one needs $\mathrm{d}y_i^{\langle j\rangle}$, $i = 1,\dots,p$, $j = 0,\dots,\rho_i - 1$, to be linearly independent, which is true under the observability assumption.

Now, using (16), prove that

$$\dim_{\mathcal{K}} \mathrm{span}_{\mathcal{K}}\{\Xi_k^{\langle -l\rangle\pi},\ k = 1,\dots,p,\ l = 0,\dots,\rho_k - 1\} = n. \tag{18}$$

For this purpose, we will prove that in the equality below all coefficients a_{kl} are identically equal to zero:

$$\sum_{k=1}^{p}\sum_{l=0}^{\rho_k - 1} a_{kl}\Xi_k^{\langle -l\rangle\pi} \equiv 0. \tag{19}$$

The proof is done step by step with ρ_1 steps, the step r showing that $a_{k,\rho_k - r} \equiv 0$ for the values of k for which $\rho_k \ge r$.

Step 1. Multiply both sides of (19) by $\mathrm{d}y_i$, $i = 1,\dots,p$:

$$\sum_{k=1}^{p}\sum_{l=0}^{\rho_k - 1} a_{kl}\left\langle \mathrm{d}y_i, \Xi_k^{\langle -l\rangle\pi} \right\rangle \equiv 0.$$

Due to (16), the latter takes the form

$$\sum_{k=1}^{p}\sum_{l=0}^{\rho_k - 1} a_{kl}\delta_{ik}\delta_{1,\rho_k - l} = a_{i,\rho_i - 1} \equiv 0$$

since $\delta_{1,\rho_k-l} = \delta_{l,\rho_k-1}$.

Step r. Assume that the steps up to $r-1$ are completed and $a_{i,\rho_i-r+1} = 0$ holds. One can rewrite (19) as

$$\sum_{k=1}^{p_{r-1}} \sum_{l=0}^{\rho_k-r} a_{kl} \Xi_k^{\langle -l\rangle \pi} \equiv 0, \tag{20}$$

where p_{r-1} is the number of outputs whose observability index is greater than $r-1$. Multiply both sides of (20) by $\mathrm{d}y_i^{\langle r-1\rangle}$, $i = 1, \ldots, p_{r-1}$:

$$\sum_{k=1}^{p_{r-1}} \sum_{l=0}^{\rho_k-r} a_{kl} \left\langle \mathrm{d}y_i^{\langle r-1\rangle}, \Xi_k^{\langle -l\rangle \pi} \right\rangle \equiv 0.$$

Due to (16), the latter takes the form

$$\sum_{k=1}^{p_{r-1}} \sum_{l=0}^{\rho_k-r} a_{kl} \delta_{ki} \delta_{r,\rho_k-l} = a_{i,\rho_i-r} \equiv 0.$$

(b) According to Lemma 7, the validity of (12) follows from (i) and (ii). Since the vector fields $\Xi_k^{\langle -l\rangle \pi}$ are linearly independent, one can apply Lemma 2 to define the new states $X_{i,j} = \Psi_{i,j}(x)$ as the canonical parameters of the vector fields in (18):

$$\left\langle \mathrm{d}\Psi_{i,j}, \Xi_k^{\langle -l\rangle \pi} \right\rangle \equiv \delta_{ik}\delta_{j,\rho_k-l}, \quad i,k = 1,\ldots,p, \quad j = 1,\ldots,\rho_i, \quad l = 0,\ldots,\rho_k-1. \tag{21}$$

Since the 1-forms $\mathrm{d}\Psi_{i,j}$ as the total differentials of the state transformation functions form a new basis for $\mathrm{span}_{\mathcal{K}}\{\mathrm{d}x\}$, it is clear that the 1-forms $\mathrm{d}\Psi_{i,j}^{\langle 1\rangle}$ can be written as the linear combinations

$$\mathrm{d}\Psi_{i,j}^{\langle 1\rangle} = \sum_{s=1}^{p} \sum_{q=1}^{\rho_s} \alpha_{isjq} \mathrm{d}\Psi_{s,q} + \sum_{v=1}^{m} \beta_{ijv} \mathrm{d}u_v, \quad i = 1,\ldots,p, \quad j = 1,\ldots,\rho_i. \tag{22}$$

Next, we will show that

$$\alpha_{isjq} = \delta_{is}\delta_{q,j+1}, \quad i,s = 1,\ldots,p, \quad j = 1,\ldots,\rho_i, \quad q = 2,\ldots,\rho_s. \tag{23}$$

Multiply both sides of (22) by the vector field $\Xi_k^{\langle -l\rangle \pi}$, $k = 1,\ldots,p$, $l = 0,\ldots,\rho_k-1$. Recall that $\Xi_k^{\langle -l\rangle \pi} \in \mathrm{span}_{\mathcal{K}}\{\partial/\partial x\}$; therefore, $\langle \mathrm{d}u_v, \Xi_k^{\langle -l\rangle \pi}\rangle \equiv 0$, $v = 1,\ldots,m$, and so

$$\left\langle \mathrm{d}\Psi_{i,j}^{\langle 1\rangle}, \Xi_k^{\langle -l\rangle \pi} \right\rangle = \sum_{s=1}^{p} \sum_{q=1}^{\rho_s} \alpha_{isjq} \left\langle \mathrm{d}\Psi_{s,q}, \Xi_k^{\langle -l\rangle \pi} \right\rangle. \tag{24}$$

Applying (21) to the scalar product on the right-hand side of (24), we get $\langle \mathrm{d}\Psi_{s,q}, \Xi_k^{\langle -l\rangle \pi}\rangle \equiv \delta_{sk}\delta_{q,\rho_k-l}$. Substituting this into (24), we get, by the definition of the Kronecker delta, $\langle \mathrm{d}\Psi_{i,j}^{\langle 1\rangle}, \Xi_k^{\langle -l\rangle \pi}\rangle = \langle \mathrm{d}\Psi_{i,j}^{\langle 1\rangle}, \Xi_k^{\langle -l\rangle}\rangle = \alpha_{ikj,\rho_k-l}$. The backward shift of this equality yields $\alpha_{ikj,\rho_k-l}^{\langle -1\rangle} = \langle \mathrm{d}\Psi_{i,j}, \Xi_k^{\langle -l-1\rangle}\rangle = \langle \mathrm{d}\Psi_{i,j}, \Xi_k^{\langle -l-1\rangle \pi}\rangle$, $l = 0,\ldots,\rho_k-2$. Due to (21), we obtain $\alpha_{ikj,\rho_k-l}^{\langle -1\rangle} \equiv \delta_{ik}\delta_{j,\rho_k-l-1}$. Denoting now $q := \rho_k - l$ for a fixed value of l, we get from the last equality $\alpha_{ikjq}^{\langle -1\rangle} \equiv \delta_{ik}\delta_{j,q-1}$, $j = 1,\ldots,\rho_i$ for $q = 2,\ldots,\rho_k$. Next, shift the obtained result forward and take into account that 1) the Kronecker delta is shift invariant and 2) $\delta_{j,q-1} = \delta_{q,j+1}$, to get $\alpha_{ikjq} = \delta_{ik}\delta_{q,j+1}$. That is, (23) holds.

According to (23), the equality (22) takes for $i = 1,\ldots,p$, $j = 1,\ldots,\rho_i - 1$ the form

$$\begin{aligned} \mathrm{d}\Psi_{i,j}^{\langle 1\rangle} &= \mathrm{d}\Psi_{i,j+1} + \sum_{s=1}^{p} \alpha_{isj1} \mathrm{d}\Psi_{s,1} + \sum_{v=1}^{m} \beta_{ijv} \mathrm{d}u_v, \\ \mathrm{d}\Psi_{i,\rho_i}^{\langle 1\rangle} &= \sum_{s=1}^{p} \alpha_{is\rho_i 1} \mathrm{d}\Psi_{s,1} + \sum_{v=1}^{m} \beta_{i\rho_i 1} \mathrm{d}u_v. \end{aligned} \tag{25}$$

We prove next that in the new coordinates

$$y_k = X_{k,1}, \quad k = 1,\ldots,p. \tag{26}$$

Taking $j = 1$ in (21), we see that for the validity of (26) the outputs must satisfy the conditions

$$\left\langle \mathrm{d}y_i, \Xi_k^{\langle -\rho_k+l\rangle\pi} \right\rangle \equiv \delta_{ik}\delta_{l1}, \quad i,k = 1,\dots,p, \quad l = 1,\dots,\rho_k. \tag{27}$$

We will prove that (27) is equivalent to (17). Since $\mathrm{d}y_i \in \mathrm{span}_{\mathcal{K}}\{\mathrm{d}x\}$, and by (4), $\Xi_k^{\langle -\rho_k+l\rangle} \in \mathrm{span}_{\mathcal{K}}\{\partial/\partial x, \partial/\partial z^{\langle -1\rangle}, \dots, \partial/\partial z^{\langle -\rho_k+l\rangle}\}$, in (27) the operator π may be omitted: $\langle \mathrm{d}y_i, \Xi_k^{\langle -\rho_k+l\rangle}\rangle \equiv \delta_{ik}\delta_{l1}$. Shifting both sides of the obtained equality $\rho_k - l$ times forward, while l is fixed, we get the equivalent equality $\langle \mathrm{d}y_i^{\langle \rho_k-l\rangle}, \Xi_k\rangle \equiv \delta_{ik}\delta_{l1}$. Denote $q := \rho_k - l + 1$, then $l = \rho_k - q + 1$. Because $l = 1,\dots,\rho_k$, then also $q = 1,\dots,\rho_k$, and the last equality takes the form

$$\left\langle \mathrm{d}y_i^{\langle q-1\rangle}, \Xi_k \right\rangle \equiv \delta_{ik}\delta_{\rho_k-q+1,1}, \quad i,k = 1,\dots,p, \quad q = 1,\dots,\rho_k.$$

Since $\delta_{\rho_k-q+1,1} \equiv \delta_{q\rho_k}$, we get (17). Consequently, (27) is valid and therefore (26) holds.

Because of (26), the equations (25) yield, after integration, the state equations in the form (7).

Necessity. Show first that the vector fields Ξ_k, defined by (10), are in the new coordinates the partial derivative operators

$$\Xi_k = \frac{\partial}{\partial X_{k,\rho_k}}, \quad k = 1,\dots,p. \tag{28}$$

To prove the validity of (28), one has to show that

$$\left\langle \mathrm{d}X_{i,j}, \Xi_k \right\rangle \equiv \delta_{ik}\delta_{j\rho_k}, \quad i,k = 1,\dots,p, \quad j = 1,\dots,\rho_i. \tag{29}$$

Express from (7) the new coordinates in terms of inputs, outputs and their forward shifts:

$$\begin{aligned} &X_{i,1} = y_i, \\ &X_{i,j} = y_i^{\langle j-1\rangle} - \varphi_{i,1}(y^{\langle j-2\rangle}, u^{\langle j-2\rangle}) - \dots - \varphi_{i,j-1}(y,u), \quad i = 1,\dots,p, \quad j = 2,\dots,\rho_i. \end{aligned} \tag{30}$$

Recall that by definition $\Xi_k \in \mathrm{span}_{\mathcal{K}}\{\partial/\partial X\}$ and compute for $i = 1,\dots,p$, $j = 2,\dots,\rho_i$,

$$\begin{aligned} \left\langle \mathrm{d}X_{i,1}, \Xi_k \right\rangle &= \langle \mathrm{d}y_i, \Xi_k \rangle, \\ \left\langle \mathrm{d}X_{i,j}, \Xi_k \right\rangle &= \left\langle \mathrm{d}y_i^{\langle j-1\rangle}, \Xi_k \right\rangle - \sum_{q=1}^{p} \frac{\partial \varphi_{i,1}(y^{\langle j-2\rangle}, u^{\langle j-2\rangle})}{\partial y_q^{\langle j-2\rangle}} \left\langle \mathrm{d}y_q^{\langle j-2\rangle}, \Xi_k \right\rangle - \dots \\ &\quad - \sum_{q=1}^{p} \frac{\partial \varphi_{i,j-1}(y,u)}{\partial y_q} \left\langle \mathrm{d}y_q, \Xi_k \right\rangle. \end{aligned} \tag{31}$$

Using the definition of the vector fields Ξ_k in (10), the validity of (29) follows from (31). Therefore, also (28) holds.

Next, prove that

$$\Xi_k^{\langle -l\rangle\pi} = \frac{\partial}{\partial X_{k,\rho_k-l}}, \quad k = 1,\dots,p, \quad l = 1,\dots,\rho_k - 1. \tag{32}$$

Compute first $\Xi_k^{\langle -1\rangle\pi}$, $k = 1,\dots,p$, using (5) and (29):

$$\Xi_k^{\langle -1\rangle\pi} = \sum_{i=1}^{p}\sum_{j=1}^{\rho_i} \left\langle \mathrm{d}X_{i,j}^{\langle 1\rangle}, \frac{\partial}{\partial X_{k,\rho_k}} \right\rangle^{\langle -1\rangle} \frac{\partial}{\partial X_{i,j}}.$$

Computing the total differentials of both sides of (7), one can easily see that $\langle \mathrm{d}X_{i,j}^{\langle 1\rangle}, \partial/\partial X_{k,\rho_k}\rangle \equiv \delta_{ik}\delta_{j+1,\rho_k}$. Since the Kronecker delta is shift invariant, we get (32) for $l = 1$. Suppose now that (32) holds for $r \in \{1,\dots,\rho_k - 2\}$ and prove that it holds for $r + 1$. Due to (5) and (32), one has

$$\Xi_k^{\langle -r-1\rangle\pi} = \sum_{i=1}^{p}\sum_{j=1}^{\rho_i} \left\langle \mathrm{d}X_{i,j}^{\langle 1\rangle}, \frac{\partial}{\partial X_{k,\rho_k-r}} \right\rangle^{\langle -1\rangle} \frac{\partial}{\partial X_{i,j}}.$$

As above, according to (7), we get $\langle \mathrm{d}X_{i,j}^{\langle 1\rangle}, \partial/\partial X_{k,\rho_k-r}\rangle \equiv \delta_{ik}\delta_{j+1,\rho_k+r}$ that will yield (32).

Since in the coordinates X the vector fields $\Xi_k^{\langle -l\rangle\pi}$, $k = 1, \dots, p$, $l = 0, \dots, \rho_k - 1$, are linearly independent partial derivative operators, the conditions (i) and (ii) hold for them.

Finally, show that also the condition (iii) is valid for (7). Note that if $i > k$, but $\rho_i = \rho_k$, then (iii) holds by (10). Next, consider the case $\rho_i < \rho_k$. Taking $j = \rho_i$, one gets from (30) $X_{i,\rho_i} = y_i^{\langle \rho_i - 1\rangle} - \varphi_{i,1}(y^{\langle \rho_i - 2\rangle}, u^{\langle \rho_i - 2\rangle}) - \dots - \varphi_{i,\rho_i - 1}(y, u)$. Shift the latter forward, substitute $X_{i,\rho_i}^{\langle 1\rangle}$ from (7) and shift the result again s steps forward, where $s = 0, \dots, \rho_k - \rho_i - 1$:

$$y_i^{\langle \rho_i + s\rangle} = \sum_{r=1}^{\rho_i} \varphi_{i,r}(y^{\langle \rho_i - r + s\rangle}, u^{\langle \rho_i - r + s\rangle}).$$

Denoting $j := \rho_i + s + 1$ yields

$$y_i^{\langle j-1\rangle} = \sum_{r=1}^{\rho_i} \varphi_{i,r}(y^{\langle j-r-1\rangle}, u^{\langle j-r-1\rangle}), \quad j = \rho_i + 1, \dots, \rho_k.$$

Recall that $\Xi_k \in \operatorname{span}_{\mathcal{K}}\{\partial/\partial X\}$ and compute

$$\left\langle \mathrm{d}y_i^{\langle j-1\rangle}, \Xi_k \right\rangle = \sum_{r=1}^{\rho_i} \sum_{q=1}^{p} \frac{\partial \varphi_{i,r}(y^{\langle j-r-1\rangle}, u^{\langle j-r-1\rangle})}{\partial y_q^{\langle j-r-1\rangle}} \left\langle \mathrm{d}y_q^{\langle j-r-1\rangle}, \Xi_k \right\rangle,$$
$$k = 1, \dots, p-1, \quad i = k+1, \dots, p, \quad j = \rho_i + 1, \dots, \rho_k.$$

Due to (10), all scalar products on the right-hand side identically equal zero since for all possible j and r values $j - r < \rho_k$. Consequently, (iii) holds. □

Remark 9. Note that the earlier result for the single-input single-output (SISO) case follows from Theorem 8 (see [16]).

4. Comparison with earlier result

The problem of transforming the state equations (1) into the form (7) by a state transformation has been studied before for MIMO discrete-time systems in [4]. First, compare the assumptions made in this paper with those from [4]. Note that in [4], the problem statement was slightly different, allowing the coefficients of $X_{i,j+1}$ in (7) to also depend on the input variable u. However, the paper [4] additionally gave a solution to the problem statement given in this paper as a special case.

Working point. The results of the paper [4] are valid locally around the equilibrium point $(x_0, u_0) = (0, 0)$. In this paper, however, a generic solution is given, meaning that the results are valid in an open and dense subset of the set $\bar{X} \times U$. Thus, the results of this paper are applicable to a larger domain than the solution in [4].

Assumptions. Both papers consider discrete-time control systems of the form (1) with $\overline{\Phi}$ analytic. However, the paper [4] assumes that $\overline{\Phi}$ is reversible in the neighbourhood of the point $(x_0, u_0) = (0, 0)$, while in this paper a less restrictive assumption is made, and a more general class of systems is studied. In this paper, it is assumed that the equations (1) are observable, whereas in [4], observability was given as part of the necessary and sufficient solvability conditions. The last difference is, of course, irrelevant.

Thus, in order to compare the results of this paper with those in [4], we make the following assumption.

Assumption 10. Assume that

- the equilibrium point $(x_0, u_0) = (0, 0)$ is the regular point of the observability matrix, meaning that the dimension of the observability space does not drop at this point (is not less than n);
- the state transition map $\overline{\Phi}$ is reversible in the neighbourhood of the point $(x_0, u_0) = (0, 0)$.

Solvability conditions. The solvability conditions in [4] are given in terms of two sets of vector fields: $r_{k,l}$, $k = 1, \dots, p$, $l = 1, \dots, \rho_k$, and $r_{k,l}(u)$, $k = 1, \dots, p$, $l = 2, \dots, \rho_k$. The vector fields

$r_{k,1}$ are defined from the set of equations below in the neighbourhood of the point $(x_0, u_0) = (0, 0)$ under the assumption that the state transition map $\overline{\Phi}_0$ is invertible in this neighbourhood:

$$\left\langle \mathrm{d}(h_i \circ \overline{\Phi}_0^{j-1}(x)), r_{k,1} \right\rangle = \delta_{i,k}\delta_{j,\rho_k},$$

where $\overline{\Phi}_0^0 = \mathrm{Id}$, $\overline{\Phi}_0^1(x) = \overline{\Phi}_0 = \overline{\Phi}(x, 0)$ and $\overline{\Phi}_0^{r+1}(x) = \overline{\Phi}_0(\overline{\Phi}_0^r(x))$ for $r > 1$. Then the vector fields $r_{k,l}$, $l = 2, \ldots, \rho_k$, are computed by transporting $r_{k,1}$ along $\overline{\Phi}_0(x)$ iteratively:

$$r_{k,l} = \mathrm{Ad}_{\overline{\Phi}_0} r_{k,l-1} := \left(\frac{\partial \overline{\Phi}_0}{\partial x} r_{k,l-1} \right)_{\overline{\Phi}_0^{-1}(x)}, \quad l > 1.$$

The vector fields $r_{k,l}(u)$, however, are found by transporting $r_{k,l-1}$ along $\overline{\Phi}(x, u)$:

$$r_{k,l}(u) = \mathrm{Ad}_{\overline{\Phi}} r_{k,l-1} := \left(\frac{\partial \overline{\Phi}}{\partial x} r_{k,l-1} \right)_{\overline{\Phi}^{-1}(x,u)}, \quad l > 1,$$

where $\overline{\Phi}^{-1}(x, u)$ is the inverse of $\overline{\Phi}(x, u)$ under the constant u, computed at the point (x, u).

Now, the solution in [4] is stated as follows.

Theorem 11. *Under Assumption 10, the state equations* (1) *are transformable by a state transformation* $X = \Psi(x)$ *into the observer form* (7) *in the neighbourhood of the point* $(x_0, u_0) = (0, 0)$ *with the observability indices* $(\rho_1, \ldots, \rho_p)$ *if and only if*

A1 $[r_{i,1}, r_{k,l}] = 0$ *for* $i, k = 1, \ldots, p$ *and* $l = 1, \ldots, \rho_k$*;*

A2 $r_{k,l}(u) = r_{k,l}$ *for* $k = 1, \ldots, p$ *and* $l = 2, \ldots, \rho_k$*;*

A3 $\operatorname{span} \mathcal{O}_i = \operatorname{span}\{\mathcal{O}_i \cap \mathcal{O}\}$*, where* $\mathcal{O} = \{\mathrm{d}y_j, \ldots, \mathrm{d}y_j^{\langle \rho_j - 1 \rangle}; j = 1, \ldots, p\}$ *and* $\mathcal{O}_i = \{\mathrm{d}y_j, \ldots, \mathrm{d}y_j^{\langle \rho_i - 1 \rangle}; j = 1, \ldots, p\} - \{\mathrm{d}y_i^{\langle \rho_i - 1 \rangle}\}$.

Note that the definition of $\mathcal{O}_i$ in [4] was incorrect, yielding that *A*3 is always satisfied, and the correct definition was given in the paper [2] by the same authors.

Recall that under Assumption 10, if z is chosen as $z = u$ and the conditions of Theorem 8 are satisfied, then under the reversibility assumption, one has that $r_{k,l} = \Xi_k^{\langle -l+1 \rangle}$, and so the condition *A*1 of Theorem 11 is satisfied. A detailed proof of the equality $r_{k,l} = \Xi_k^{\langle -l+1 \rangle}$ of the vector fields is given in [15] for the SISO case. The proof for the MIMO case is similar. Now, because of the equality $r_{k,l} = \Xi_k^{\langle -l+1 \rangle}$ and the fact that the $\mathrm{Ad}_{\overline{\Phi}}$ operator corresponds to the backward shift of a vector field, one has $r_{k,l}(u) = \mathrm{Ad}_{\overline{\Phi}} r_{k,l-1} = \mathrm{Ad}_{\overline{\Phi}} \Xi_k^{\langle -l+2 \rangle} = \Xi_k^{\langle -l+1 \rangle} = r_{k,l}$. Clearly, the condition *A*2 of Theorem 11 is satisfied. It remains to show that the condition (iii) of Theorem 8 yields that *A*3 is satisfied. First, note that the condition (iii) of Theorem 8 is equivalent to the condition (8). If the latter is satisfied, then $\mathrm{d}y_j^{\langle l \rangle} \in \operatorname{span} \mathcal{O}$ for all $j = 1, \ldots, p$ and $l \geq 0$. Thus, $\mathcal{O}_i \subseteq \mathcal{O}$ and the condition *A*3 is satisfied.

5. Examples

Example 1. Consider the state equations

$$\begin{aligned} &x_1^{\langle 1 \rangle} = x_3, \quad x_2^{\langle 1 \rangle} = x_1 (x_4 + 1), \quad x_3^{\langle 1 \rangle} = u + x_2 + x_5, \quad x_4^{\langle 1 \rangle} = \frac{u}{x_3}, \\ &x_5^{\langle 1 \rangle} = u x_2 - x_1 x_4 - x_1, \quad y_1 = x_1, \quad y_2 = x_2. \end{aligned} \tag{33}$$

The system (33) is not reversible but submersive and taking $z = x_1$ allows one to find the backward shifts

$$\begin{aligned} &x_1^{\langle -1 \rangle} = z^{\langle -1 \rangle}, \quad x_2^{\langle -1 \rangle} = \frac{x_2 + x_5}{x_1 x_4}, \quad x_3^{\langle -1 \rangle} = x_1, \\ &x_4^{\langle -1 \rangle} = \frac{x_2}{z^{\langle -1 \rangle}} - 1, \quad x_5^{\langle -1 \rangle} = x_3 - x_1 x_4 - \frac{x_2 + x_5}{x_1 x_4}, \quad u^{\langle -1 \rangle} = x_1 x_4. \end{aligned}$$

Computing $\mathrm{d}y_1 = \mathrm{d}x_1$, $\mathrm{d}y_1^{\langle 1\rangle} = \mathrm{d}x_3$, $\mathrm{d}y_1^{\langle 2\rangle} = \mathrm{d}x_2 + \mathrm{d}x_5 + \mathrm{d}u$, $\mathrm{d}y_2 = \mathrm{d}x_2$, $\mathrm{d}y_2^{\langle 1\rangle} = (x_4 + 1)\,\mathrm{d}x_1 + x_1\mathrm{d}x_4$ reveals that the rank of the observability matrix (6) is generically equal to $n = 5$; thus, the system is generically observable with the observability indices $\rho_1 = 3, \rho_2 = 2$.

Next, find the vector fields $\Xi_1 = \sum_{q=1}^{5} \xi_{1q}\partial/\partial x_q$ and $\Xi_2 = \sum_{q=1}^{5} \xi_{2q}\partial/\partial x_q$, where the functions ξ_{1q}, ξ_{2q} should be determined from (10). For $k = 1$, the set of equations (10) results in

$$\langle \mathrm{d}y_1, \Xi_1\rangle = 0, \quad \left\langle \mathrm{d}y_1^{\langle 1\rangle}, \Xi_1 \right\rangle = 0, \quad \left\langle \mathrm{d}y_1^{\langle 2\rangle}, \Xi_1 \right\rangle = 1, \quad \langle \mathrm{d}y_2, \Xi_1\rangle = 0, \quad \left\langle \mathrm{d}y_2^{\langle 1\rangle}, \Xi_1 \right\rangle = 0,$$

yielding the unique solution

$$\Xi_1 = \frac{\partial}{\partial x_5}.$$

However, for $k = 2$, the set of equations (10) results in four equations

$$\langle \mathrm{d}y_1, \Xi_2\rangle = 0, \quad \left\langle \mathrm{d}y_1^{\langle 1\rangle}, \Xi_2 \right\rangle = 0, \quad \langle \mathrm{d}y_2, \Xi_2\rangle = 0, \quad \left\langle \mathrm{d}y_2^{\langle 1\rangle}, \Xi_2 \right\rangle = 1,$$

while involving five unknown functions. Therefore, its solution Ξ_2 is not unique and depends on the unknown function ξ_{25}:

$$\Xi_2 = \frac{1}{x_1}\frac{\partial}{\partial x_4} + \xi_{25}\frac{\partial}{\partial x_5}.$$

The next task is to find $\xi_{25}(x)$ from the conditions (i)–(iii) of Theorem 8 that have to be satisfied. Consider, for instance,

$$[\Xi_1, \Xi_2] = \left(0,\ 0,\ 0,\ 0,\ \frac{\partial \xi_{25}}{\partial x_5}\right)^{\mathrm{T}}.$$

Equalizing the last coordinate of the above Lie bracket to zero gives a partial differential equation, whose solution is $\xi_{25} = C(x_1, x_2, x_3, x_4)$, with C being an arbitrary function of its arguments. For the sake of simplicity, we take $C \equiv 0$; thus, $\xi_{25} = \xi_{25}^{\langle -1\rangle} = 0$, leading to the updated vector field

$$\Xi_2 = \frac{1}{x_1}\frac{\partial}{\partial x_4}.$$

In order to check the condition (i), the following projections of the backward shifts of Ξ_1 and Ξ_2 are required:

$$\Xi_1^{\langle -1\rangle\pi} = \frac{\partial}{\partial x_3}, \quad \Xi_1^{\langle -2\rangle\pi} = \frac{\partial}{\partial x_1} - \frac{x_4}{x_1}\frac{\partial}{\partial x_4}, \quad \Xi_2^{\langle -1\rangle\pi} = \frac{\partial}{\partial x_2} - \frac{\partial}{\partial x_5}.$$

All Lie brackets in (i) equal zero; thus, the condition (i) is satisfied. The condition (ii) is also fulfilled since the coefficients of $\Xi_1, \Xi_1^{\langle -1\rangle\pi}, \Xi_1^{\langle -2\rangle\pi}, \Xi_2, \Xi_2^{\langle -1\rangle\pi}$ depend only on the variable x. The condition (iii) reduces to the requirement that $\left\langle \mathrm{d}y_2^{\langle 2\rangle}, \Xi_1 \right\rangle = 0$, which is valid since $\mathrm{d}y_2^{\langle 2\rangle} = \mathrm{d}x_3$.

Next, construct the state coordinates as the canonical parameters of the vector fields $\Xi_1, \Xi_1^{\langle -1\rangle\pi}$, $\Xi_1^{\langle -2\rangle\pi}, \Xi_2$ and $\Xi_2^{\langle -1\rangle\pi}$ by (21). Defining matrices

$$P := \begin{pmatrix} \mathrm{d}\Psi_{1,1} \\ \mathrm{d}\Psi_{1,2} \\ \mathrm{d}\Psi_{1,3} \\ \mathrm{d}\Psi_{2,1} \\ \mathrm{d}\Psi_{2,2} \end{pmatrix} \quad \text{and} \quad M := \begin{pmatrix} \Xi_1^{\langle -2\rangle\pi} & \Xi_1^{\langle -1\rangle\pi} & \Xi_1 & \Xi_2^{\langle -1\rangle\pi} & \Xi_2 \end{pmatrix} = \begin{pmatrix} 1 & 0 & 0 & 0 & 0 \\ 0 & 0 & 0 & 1 & 0 \\ 0 & 1 & 0 & 0 & 0 \\ -\frac{x_4}{x_1} & 0 & 0 & 0 & \frac{1}{x_1} \\ 0 & 0 & 1 & -1 & 0 \end{pmatrix}$$

allows one to write (21) as a matrix equation $PM = I_5$, with I_5 being the identity matrix. The matrix P can be found as the inverse of M,

$$P = M^{-1} = \begin{pmatrix} 1 & 0 & 0 & 0 & 0 \\ 0 & 0 & 1 & 0 & 0 \\ 0 & 1 & 0 & 0 & 1 \\ 0 & 1 & 0 & 0 & 0 \\ x_4 & 0 & 0 & x_1 & 0 \end{pmatrix},$$

the rows of which define the exact 1-forms (since the vector fields in M commute), the integration of which yields the new state coordinates $X_{1,1} = x_1$, $X_{1,2} = x_3$, $X_{1,3} = x_2 + x_5$, $X_{2,1} = x_2$, $X_{2,2} = x_1x_4$. In these coordinates, the state equations (33) take the observer form (7):

$$X_{1,1}^{\langle 1\rangle} = X_{1,2}, \quad X_{1,2}^{\langle 1\rangle} = u + X_{1,3}, \quad X_{1,3}^{\langle 1\rangle} = uy_2, \quad X_{2,1}^{\langle 1\rangle} = X_{2,2} + y_1, \quad X_{2,2}^{\langle 1\rangle} = u,$$
$$y_1 = X_{1,1}, \quad y_2 = X_{2,1}.$$

The purpose of the example below is to demonstrate that in the MIMO case, unlike the SISO case, the conditions (i) and (ii) of Theorem 8 are not sufficient to transform the state equations (1) into the observer form (7). The reason is that in the case where $\rho_k > \rho_i$ in (10), it is not enough to take $j = 1, \dots, \min(\rho_i, \rho_k)$; (10) must also hold for $j = \rho_i + 1, \dots, \rho_k$ to guarantee $y_i = X_{i,1}$, $i = 1, \dots, p$.

Example 2. Consider the state equations

$$x_1^{\langle 1\rangle} = x_1 + x_2, \quad x_2^{\langle 1\rangle} = x_1u + x_2, \quad x_3^{\langle 1\rangle} = x_3u^2 + x_2, \quad y_1 = x_1, \qquad y_2 = x_3 \tag{34}$$

that define the backward shifts

$$x_1^{\langle -1\rangle} = \frac{x_2 - x_1}{u^{\langle -1\rangle} - 1}, \quad x_2^{\langle -1\rangle} = \frac{x_1u^{\langle -1\rangle} - x_2}{u^{\langle -1\rangle} - 1}, \quad x_3^{\langle -1\rangle} = \frac{(x_3 - x_1)u^{\langle -1\rangle} - x_3 + x_2}{(u^{\langle -1\rangle} - 1)(u^{\langle -1\rangle})^2}.$$

Compute the total differentials $\mathrm{d}y_i^{\langle j-1\rangle}$, $i, j = 1, 2$, obtaining $\mathrm{d}y_1 = \mathrm{d}x_1$, $\mathrm{d}y_1^{\langle 1\rangle} = \mathrm{d}x_1 + \mathrm{d}x_2$, $\mathrm{d}y_2 = \mathrm{d}x_3$, $\mathrm{d}y_2^{\langle 1\rangle} = \mathrm{d}x_2 + u^2\mathrm{d}x_3 + 2x_3u\mathrm{d}u$. So, the system (34) is observable with the observability indices $\rho_1 = 2$, $\rho_2 = 1$.

Compute the vector fields Ξ_1 and Ξ_2 according to (10). First, find Ξ_1 from $\langle \mathrm{d}y_1, \Xi_1\rangle \equiv 0$, $\langle \mathrm{d}y_1^{\langle 1\rangle}, \Xi_1\rangle \equiv 1$, $\langle \mathrm{d}y_2, \Xi_1\rangle \equiv 0$, which yields

$$\Xi_1 = \frac{\partial}{\partial x_2}.$$

The equations to compute $\Xi_2 = \sum_{q=1}^{3} \xi_q \partial/\partial x_q$ now consist of two equations $\langle \mathrm{d}y_1, \Xi_2\rangle = \xi_1 = 0$, $\langle \mathrm{d}y_2, \Xi_2\rangle = \xi_3 = 1$, whereas the number of unknown functions is three, resulting in

$$\Xi_2 = \xi_2(x)\frac{\partial}{\partial x_2} + \frac{\partial}{\partial x_3},$$

where the unknown function ξ_2 is a function of the argument x only by the condition (ii) of Theorem 8. Compute also

$$\Xi_1^{\langle -1\rangle\pi} = \sum_{q=1}^{3} \left\langle \mathrm{d}x_q^{\langle -1\rangle}, \Xi_1 \right\rangle \frac{\partial}{\partial x_q} = \frac{\partial}{\partial x_1} + \frac{\partial}{\partial x_2} + \frac{\partial}{\partial x_3}.$$

Define ξ_2 so that the condition (i) is satisfied, meaning that all three vector fields commute:

$$[\Xi_1, \Xi_2] = \frac{\partial \xi_2}{\partial x_2}\frac{\partial}{\partial x_2} \equiv 0, \left[\Xi_1, \Xi_1^{\langle -1\rangle\pi}\right] \equiv 0, \left[\Xi_2, \Xi_1^{\langle -1\rangle\pi}\right] = -\left(\frac{\partial \xi_2}{\partial x_1} + \frac{\partial \xi_2}{\partial x_2} + \frac{\partial \xi_2}{\partial x_3}\right)\frac{\partial}{\partial x_2} \equiv 0. \tag{35}$$

From (35), it immediately follows that all Lie brackets identically equal zero only if ξ_2 is an arbitrary function of the argument $x_1 - x_3$. For simplicity, take $\xi_2 = 0$, which results in $\Xi_2 = \partial/\partial x_3$.

Define the new coordinates $X = \Psi(x)$ by (21) as the canonical parameters of $\Xi_1^{\langle -1\rangle\pi}$, Ξ_1 and Ξ_2: $X_{1,1} = x_1$, $X_{1,2} = x_2 - x_1$, $X_{2,1} = x_3 - x_1$. The inverse transformation is $x_1 = X_{1,1}$, $x_2 = X_{1,1} + X_{1,2}$, $x_3 = X_{1,1} + X_{2,1}$. In the new coordinates, the state equations read

$$X_{1,1}^{\langle 1\rangle} = X_{1,2} + 2y_1, \quad X_{1,2}^{\langle 1\rangle} = y_1(u - 1), \quad X_{2,1}^{\langle 1\rangle} = y_2u^2 - y_1. \tag{36}$$

The equations (36) are similar to the observer form (7), except that now $X_{2,1} \neq y_2$, but $X_{2,1} = y_2 - y_1$. The reason lies in the following. The validity of (iii) for $i = j = 2$ is not guaranteed since

$$\left\langle \mathrm{d}y_2^{\langle 1\rangle}, \Xi_1 \right\rangle = \left\langle \mathrm{d}x_2 + u^2\mathrm{d}x_3 + 2x_3u\mathrm{d}u, \frac{\partial}{\partial x_2} \right\rangle = 1 \not\equiv 0.$$

6. Conclusion

The paper studied the problem of transforming, by the state transformation, the multi-input multi-output discrete-time nonlinear state equations into the classical observer form. The necessary and sufficient solvability conditions were given that generalize those from [15,16] for the single-output case. The extension was not straightforward; quite the opposite, it was a challenging task in many extension steps. First, it was not obvious how to generalize (from the single-output case) the equations that define the vector fields Ξ_k, $k = 1, \ldots, p$, in terms of which the main theorem is formulated. Second, and more important, is the fact that, in general, the vector fields Ξ_k are not uniquely defined, unlike in the single-output case. The only exception is when all the observability indices are equal. Thus, even if a particular set of the vector fields Ξ_k (fixed solution) fails to satisfy the conditions of Theorem 8, there may still exist another solution that fulfils the conditions. The method to construct the required state transformation was also given. The obtained conditions address a larger class of systems than the earlier conditions. The comparison with the earlier results was also done. An interesting research perspective is to extend the results of this paper to the case where, instead of the state transformation, a parametrized state transformation that depends on a few known past input values, called the parameters, is used.

Data availability statement

All data are available in the article.

Acknowledgements

The work of A. Kaldmäe and M. Tõnso was supported by the Estonian Research Council grant PSG833. The work of V. Kaparin was supported by the Estonian Research Council grant PRG1463 and by the Estonian Centre of Excellence in Energy Efficiency (ENER) grant TK230, funded by the Estonian Ministry of Education and Research. The publication costs of this article were covered by the Estonian Academy of Sciences.

References

1. Aranda-Bricaire, E., Kotta, Ü. and Moog, C. H. Linearization of discrete-time systems. *SIAM J. Control Optim.*, 1996, **34**(6), 1999–2023. https://doi.org/10.1137/s0363012994267315
2. Califano, C., Monaco, S. and Normand-Cyrot, D. Canonical observer forms for multi-output systems up to coordinate and output transformations in discrete time. *Automatica*, 2009, **45**(11), 2483–2490. https://doi.org/10.1016/j.automatica.2009.07.003
3. Califano, C., Monaco, S. and Normand-Cyrot, D. On the observer design in discrete-time. *Syst. Control Lett.*, 2003, **49**(4), 255–265. https://doi.org/10.1016/S0167-6911(02)00344-4
4. Califano, C., Monaco, S. and Normand-Cyrot, D. On the observer design of multi output systems in discrete time. *IFAC Proc. Vol.*, 2005, **38**(1), 7–12. https://doi.org/10.3182/20050703-6-cz-1902.00655
5. Chung, S.-T. and Grizzle, J. W. Observer error linearization for sampled-data systems. In *Proceedings of the 28th IEEE Conference on Decision and Control, Tampa, FL, USA, 13–15 December 1989*. IEEE, 1989, 90–95. https://doi.org/10.1109/CDC.1989.70080
6. Huijberts, H. J. C. On existence of extended observers for nonlinear discrete-time systems. In *New Directions in Nonlinear Observer Design. Lecture Notes in Control and Information Sciences* (Nijmeijer, H. and Fossen, T. I., eds). Springer, London, 1999, **244**, 73–92. https://doi.org/10.1007/BFb0109922
7. Huijberts, H. J. C., Lilge, T. and Nijmeijer, H. Synchronization and observers for nonlinear discrete time systems. In *European Control Conference, Karlsruhe, Germany, 31 August–3 September 1999*. IEEE, 1999, 4643–4648. https://doi.org/10.23919/ECC.1999.7100068
8. Huijberts, H. J. C., Nijmeijer, H. and Pogromsky, A. Y. Discrete-time observers and synchronization. In *Controlling Chaos and Bifurcations in Engineering Systems* (Chen, G., ed.). CRC Press, Boca Raton, FL, 1999, 439–456.
9. Kaparin, V. and Kotta, Ü. Transformation of nonlinear discrete-time system into the extended observer form. *Int. J. Control*, 2018, **91**(4), 848–858. https://doi.org/10.1080/00207179.2017.1294264
10. Kaparin, V. and Kotta, Ü. Transformation of nonlinear MIMO discrete-time systems into the extended observer form. *Asian J. Control*, 2019, **21**(5), 2208–2217. https://doi.org/10.1002/asjc.1824
11. Kaparin, V., Kotta, Ü. and Mullari, T. Extended observer form: simple existence conditions. *Int. J. Control*, 2013, **86**(5), 794–803. https://doi.org/10.1080/00207179.2012.760048
12. Lee, H.-G. and Hong, J.-M. Algebraic conditions for state equivalence to a discrete-time nonlinear observer canonical form. *Syst. Control Lett.*, 2011, **60**(9), 756–762. https://doi.org/10.1016/j.sysconle.2011.06.001
13. Lee, H.-G. and Hong, J.-M. Discrete-time observer error linearizability via restricted dynamic systems. *IEEE Trans. Autom. Control*, 2012, **57**(6), 1543–1547. https://doi.org/10.1109/TAC.2011.2179874
14. Lee, W. and Nam, K. Observer design for autonomous discrete-time nonlinear systems. *Syst. Control Lett.*, 1991, **17**(1), 49–58. https://doi.org/10.1016/0167-6911(91)90098-Y
15. Mullari, T. and Kotta, Ü. Transformation of nonlinear discrete-time state equations into the observer form: extension to non-reversible case. *Proc. Estonian Acad. Sci.*, 2021, **70**(3), 235–247. https://doi.org/10.3176/proc.2021.3.03
16. Mullari, T. and Kotta, Ü. Transformation of nonlinear discrete-time state equations into the observer form: revision. *Proc. Estonian Acad. Sci.*, 2023, **72**(1), 1–5. https://doi.org/10.3176/proc.2023.1.01
17. Mullari, T., Kotta, Ü., Bartosiewicz, Z., Pawłuszewicz, E. and Moog, C. H. Forward and backward shifts of vector fields: towards the dual algebraic framework. *IEEE Trans. Autom. Control*,

2017, **62**(6), 3029–3033. https://doi.org/10.1109/tac.2016.2608718
18. Mullari, T., Kotta, Ü., Kaldmäe, A., Kaparin, V. and Simha, A. Extended observer form with vector fields. *Int. J. Control*, 2024, **97**(10), 2399–2412. https://doi.org/10.1080/00207179.2023.2274060
19. Mullari, T., Kotta, Ü., Kaldmäe, A., Kaparin, V., Tõnso, M. and Pawłuszewicz, E. Extended observer forms for discrete-time nonlinear systems. *IEEE Trans. Autom. Control*. Submitted for publication.
20. Simha, A., Kaparin, V., Mullari, T. and Kotta, Ü. Extended observer forms for submersive discrete-time systems. *IEEE Trans. Autom. Control*, 2024, **69**(4), 2684–2688. https://doi.org/10.1109/tac.2023.3336253
21. Zhang, J., Feng, G. and Xu, H. Observer design for nonlinear discrete-time systems: immersion and dynamic observer error linearization techniques. *Int. J. Robust Nonlinear Control*, 2010, **20**(5), 504–514. https://doi.org/10.1002/rnc.1443

Mitme sisendi ja väljundiga diskreetse mittelineaarse juhtimissüsteemi klassikaline vaatlejakuju

Arvo Kaldmäe, Vadim Kaparin, Ülle Kotta, Tanel Mullari ja Maris Tõnso

Artikkel käsitleb mitme sisendi ja väljundiga mittelineaarsete diskreetaja olekuvõrrandite olekuteisendusega viimist klassikalisele vaatlejakujule. Tarvilikud ja piisavad geomeetrilised lahenduvustingimused on esitatud vektorväljade kaudu. Leitud tulemused üldistavad varasemaid mitmes aspektis: esiteks on tulemused rakendatavad ka mittepööratavatele süsteemidele; teiseks kehtivad need peaaegu kõikjal, mitte ainult süsteemi tasakaalupunkti ümbruses. Üldistused on võimalikud tänu teistsuguse matemaatilise aparatuuri kasutamisele. Piisavuse tõestus annab ühtlasi meetodi olekuteisenduse leidmiseks. Tulemusi illustreeritakse kahe näite abil.

Proceedings of the Estonian Academy of Sciences
2026, **75**, 1, 15–33

https://doi.org/10.3176/proc.2026.1.02

www.eap.ee/proceedings
Estonian Academy Publishers

ESTONIAN LOCAL SHEEP WOOL PROPERTIES

RESEARCH ARTICLE

Received 6 June 2025
Accepted 1 August 2025
Available online 20 January 2026

Keywords:
Estonian sheep wool, wool fibre properties, wool yarn, wool knitwear, felted knitwear, textile

Corresponding author:
Liisa Torsus
torsus.liisa@gmail.com

Citation:
Torsus, L., Plamus, T., Kabun, K. and Kallavus, U. 2026. Revaluation of Estonian local sheep wool – impact of different wool types on textile material properties. *Proceedings of the Estonian Academy of Sciences*, **75**(1), 15–33. https://doi.org/10.3176/proc.2026.1.02

Revaluation of Estonian local sheep wool – impact of different wool types on textile material properties

Liisa Torsus[a], Tiia Plamus[a], Katrin Kabun[b] and Urve Kallavus[c]

[a] Department of Materials and Environmental Technology, Tallinn University of Technology, Ehitajate tee 5, 19086 Tallinn, Estonia

[b] Textile Design, Estonian Academy of Arts, Põhja pst 7, 10412 Tallinn, Estonia

[c] Department of Mechanical and Industrial Engineering, Tallinn University of Technology, Ehitajate tee 5, 19086 Tallinn, Estonia

ABSTRACT

The use of local sheep wool in Estonia – and consequently, sheep farming – has declined since the mid-20th century due to the increased availability of synthetic fibres and the import of finer, higher-quality wool. Nevertheless, it is possible to produce high-quality textiles from the more uneven local wool, indicating the need to revalue Estonian local wool and the textiles produced from it. There is limited research on Estonian local sheep wool (Estonian Darkhead, Estonian Whitehead, Kihnu Native sheep) fibre properties and no data on the combined effect of these fibre properties on textile material properties in various stages of textile production, such as yarn, knitted material, and knitted felted material. Therefore, specific fibre properties – including fibre length, linear density, diameter, cuticle scale height, and scale frequency – were analysed, and their combined effects on yarn, knitted material, and knitted felted material properties were evaluated. For comparison, wool from locally raised *Mérinos d'Arles* sheep was also analysed. The results showed that the fibres from the wool of Estonian breeds were more uneven, coarser, and longer, with higher linear density and lower cuticle scale frequency. However, yarns produced from these fibres demonstrated greater tensile properties. Material properties were influenced both by fibre and yarn properties.

1. Introduction

Sheep fleeces can be classified into three categories based on wool fibre types and their parameters [1,2]. These are archaic wool types with coarse overcoat wool hair, wool with transitional wool fibres, and fine wool. Hair sheep form a separate category [1]. Different wool types are used for different applications according to fibre properties. However, wool with less desirable properties – such as coarse and uneven fibres – is often left unused.

Estonian local wool is an undervalued bioresource, primarily due to its less desired properties. A significant portion of this wool is discarded, while at the same time, twice as much wool is imported for local textile production. The reason has been found to be the absence of a wool grading and purchasing system, as well as the absence of scouring facilities in Estonia [3–5]. To establish a functioning wool system, it is essential to understand the properties of local wool fibres and their effects on textile characteristics. However, in the case of Estonian sheep breeds' wool, research on fibre, yarn and textile properties, and their relationship is insufficient [6–9].

To enhance the use of Estonian wool and to develop a viable wool system, the influence of fibre properties on yarn and textile materials must be studied – the wool grading system should be based on fibre properties and possible applications of these fibres. Therefore, the aim of the study was to compare the properties of Estonian local sheep wool as fibres, yarns, knitted materials, and knitted felted materials, as well as to analyse how fibre properties affect textile properties. A possible application of felted knitwear was outerwear. Merino wool was additionally studied to compare Estonian breeds' wool to a desired and widely used wool in textile production. The following sub-sections provide an overview of sheep breeds and wool characteristics relevant to the study.

1.1. Sheep in Estonia

There are four Estonian sheep breeds: Estonian Native sheep (EML), with subgroups *Kihnu*, *Ruhnu*, *Hiiu*, *Saare*, and *Viru* [10,11]; Kihnu Native sheep (KML), an EML subgroup recognised as a separate breed; Estonian Darkhead sheep (ET); and Estonian

Fig. 1. Sheep in Estonia: Estonian Native sheep (KML breed) (a), imported sheep *Mérinos d'Arles* (b), Estonian Whitehead sheep (c), and Estonian Darkhead sheep (d). Photos by the authors.

Whitehead sheep (EV). The latter two were developed from EML sheep. In addition, many foreign breeds have been imported historically to meet the demand for fine wool [12,13]. Estonian sheep breeds are shown in Fig. 1.

EML sheep, native to Estonia [14,15], exhibit many aboriginal characteristics. Their wool is double-layered, consisting of an undercoat and overcoat and may also contain transitional wool fibres – coarser undercoat fibres with the properties of overcoat fibres. The undercoat contains fine, high-crimp fibres (10–40 µm), while the overcoat fibres are coarser and low-crimp (over 40 µm) [10]. EV and ET sheep were cultivated from EML sheep. Breeding began in 1926, and in 1958, both EV and ET were officially recognised as distinct breeds [16]. Both breeds produce transitional wool [1], and their wool has been characterised as having even quality and normal crimp [16].

1.2. Wool fibre properties

The properties of wool fibres are of great importance, as they influence the production of textile materials and the properties of the resulting yarns and textiles. Fibre properties vary among wool types and sheep breeds and are affected by breeding, living conditions, and nutrition [17]. Wool fibres typically range from 38 to 380 mm in length. A fibre length of 50–120 mm enables economical yarn manufacturing [18]. Fibre diameter is the primary parameter used for grading and pricing wool [19,20]. According to the micron system – the most technical classification – wool is categorised as fine (≤ 22.04 µm), medium or semi-fine (22.05–30.99 µm), coarse (31.00–36.19 µm), and very coarse (≥ 36.20 µm) [19]. Fibre fineness often determines the end use, as fibres with diameters over 30 µm may cause skin irritation and are therefore generally not used in apparel [20]. Crimp in wool fibres is associated with their mechanical properties [21]. The effect of crimp on fibre behaviour has been studied by Barach and Rainard [21], who have stated that the increase in crimp highly reduces the tensile strength of a fibre or yarn. Crimp also affects felting rate [22–24]. EML sheep wool is low-crimp, sometimes less than 1 cr/cm [12]. ET and EV wool have been characterised as having normal crimp [6], approximately 3–4 cr/cm [16]. Merino wool, in contrast, is high-crimp, usually exceeding 7 cr/cm [16,25]. The wool fibre cuticle consists of cuticle cells or scales with serrated edges. Scale frequency refers to the number of scales per 100 µm fibre length, often expressed as the number of scales per unit area or as an index in relation to the fibre diameter. Scale height indicates the height of the serrated scale edge above the underlying scale [26–29]. Both scale frequency and scale height influence felting tendency [26,27].

There has been little research on the fibre properties of local sheep breeds. While material properties have been assessed, fibre and yarn properties have not been widely studied, nor has their impact on material properties been thoroughly analysed. The relevant research is discussed below.

During the Soviet era, EV and ET wool were classified as crossbred wool of the 56 quality class (27.1–29.0 µm) [16]. A more detailed study of EV and ET wool was conducted in the 1990s by Kaie Zarens (now Ahlskog) [6]. Although the research focused on breeding, it provided comparative data. The average fibre diameter for EV wool was found to be 30.5 µm, while ET fibres were coarser, with an average diameter of 35.7 µm [6]. A more recent study was carried out at Pallas University of Applied Sciences (Tartu, Estonia) in 2019 [7]. In addition to examining the effects of sorting and processing, the study measured the fibre diameter of EML sheep wool. Fibre fineness was determined with an accuracy of ±5 µm. Ten fibres were measured from the sorted wool by wool type. The results showed that EML sheep wool fibre diameters ranged from 18 to 60 µm, with the average values as follows: lamb wool 37 µm, neck wool 31 µm, breech wool 32 µm, and coarse wool 52 µm [7]. The latest research on Estonian wool fibre parameters was conducted in a co-operation project between Estonia and Norway [8]. In this study, linear density was measured for KML, EV, and ET wool fibres, alongside yarn and material parameters. It should be noted that the testing environment did not comply with the standard atmosphere for conditioning and testing: the average temperature during testing was 26 ± 2 °C and the relative humidity was 44 ± 4% [8]. Linear density tests were conducted on unscoured wool samples taken from the sides and backs of sheep, as well as from slivers. The study determined the average linear density of unscoured wool as follows: EV – 16.21 dtex, ET – 13.31 dtex, and KML – 12.13 dtex. For wool fibres sampled from slivers, the average linear density was as follows: EV – 11.66 dtex, ET – 12.06 dtex, and KML – 11.15 dtex. The research also noted that linear density varied between herds [8].

1.3. Wool yarn properties

Three alternative yarn manufacturing systems are used to produce wool yarns industrially: the woollen (W), semi-worsted (SW), and worsted (WR) systems [18]. In Estonia, only the W and SW systems are currently in use. These systems differ in the number of processing stages, the machinery

used, the suitability for different wool types, and the properties of the resulting yarns [30]. The W system is the simplest, involving the fewest production stages, while the WR system is the most complex [18,30]. In W yarns, fibres are not aligned through a dedicated process, unlike in the SW and WR systems. Misalignment leads to protruding fibre ends in W yarns. Additionally, longer fibres can undergo reversals in direction, contributing less to yarn strength than in a fully extended position. Consequently, W yarns are generally weaker than SW and WR yarns, where fibres are aligned. WR yarns are stronger than SW yarns because short fibres are removed during combing [30]. W yarns tend to be coarser and exhibit greater diameter irregularities than SW and WR yarns [18]. Yarns are stronger when the fibres have been combed into a parallel arrangement [30]. Moreover, fibre strength affects yarn strength. Bouagga et al. [31], who studied the properties of Tunisian wool, found that fibre tensile strength, tenacity, and elongation are correlated with fibre diameter. According to their research, coarser fibres demonstrated greater strength.

In the Estonia–Norway co-operation project, the tensile strength of SW yarns made from ET, EV, and KML wool (with a thickness of 316 m/100 g) was tested. The testing environment differed from the standard atmosphere for conditioning and testing, with the average temperature being 26 ± 2 °C and the relative humidity 44 ± 4% during testing [8]. The average maximum force sustained was 2251.64 cN for ET, 2217.08 cN for EV, and 2584.47 cN for KML yarns. The average elongation values were 8.98% for ET, 8.27% for EV, and 10.18% for KML yarns. The study noted that both the maximum force sustained and elongation were similar for ET and EV yarns, while KML yarns extended more and withstood a higher maximum force [8].

1.4. Woollen knitted textile structure and its properties

In addition to fibre properties and the yarn production method, textile properties also depend on the material structure [32]. Fibre and yarn properties, along with the stitch density during knitting, affect fabric properties and felting properties [33].

Pilling is one of the most critical properties for knitted materials. Pilling formation rate is affected by physical fibre properties, including tenacity, elongation at break, fibre length, fibre cross-sectional shape, and linear density. Moreover, the process is affected by the number of fibre ends, yarn twist, and fabric structure. Generally, longer staple fibres lead to less pilling, as fewer fibre ends protrude from the fabric surface per unit area. Coarser fibres tend to pill less due to their greater stiffness. Furthermore, fibres with an irregular cross-section are less prone to pilling because of the difficulty in bringing fibres to the surface, resulting in greater friction due to the irregular cross-section [34].

Siiri Nool [9] has compared different wool yarns manufactured in Estonian wool mills for producing a knitted felted product. Natural white SW and W yarns made from local wool were used. The knitted materials were felted in a washing machine. Nool evaluated the felting tendency of different yarns by measuring the dimensional changes of the samples after felting. Five SW and four W yarns were tested. She observed that materials knitted and felted from native sheep SW yarns felt more. These samples lost approximately 35% in height and 20% in width after felting. Wool yarn samples shrank by 22% in height and 11% in width. The sample that felted the least was made from EV and Texel crossbreed sheep wool [9].

At the Textile Department of Pallas University of Applied Sciences, research was conducted on the effects of wool sorting and processing on the properties of yarns and fabrics, using EML wool as an example. It was found that SW yarn produced more pills than W yarn made from the same wool. However, the thickness of yarns varied. Additionally, in the case of knitted materials, yarns made from finer, high-crimp fibres exhibited better abrasion resistance [7].

As part of the Estonia–Norway project, both knitted and knitted felted materials were studied. The mass per unit area of the fabrics was measured, and felting shrinkage was calculated as follows: 17.6% for ET, 23.56% for EV, and 17.18% for KML. The air permeability of these materials was also tested, and the reduction in air permeability due to felting was found to be 39.5% for ET, 37.1% for EV, and 52.8% for KML [8]. Abrasion and pilling resistance were also evaluated. For the knitted and the knitted felted materials, the average abrasion resistance was as follows: ET – 80 000 and 41 133 rubs, EV – 78 333 and 70 000 rubs, and KML – 60 000 and 65 000 rubs [8], respectively. It was stated that the knitted felted fabrics had less pilling than the knitted fabrics [8,35].

1.5. Felting tendency of wool fibres, yarn, and textile

Felting is a unique property of various animal fibres, including sheep wool. The basic mechanism behind felting in wool is thought to be the directional frictional effect (DFE) [36]. In addition to DFE, several fibre properties influence the felting process [26,36–39]. Furthermore, felting is affected by external conditions, such as felting duration, medium parameters, and material properties and structure [37,38].

Unal and Atav [26] have noted that fibre properties such as fineness, length, cuticular height, and cuticle scale frequency affect felting tendency. The combination of properties determines the felting tendency of certain wool types. Generally, it is accepted that finer wool fibres felt more than coarser fibres [26,39]. This is due to the higher bending rigidity of coarser fibres. However, many researchers have found that fibre length has an even greater effect on felting [26,38,39]. Additionally, greater cuticle scale height and scale frequency tend to increase felting tendency [26,27]. Fibre crimp also has a significant impact on felting, particularly when felting is done using wool batts. Many researchers have found that lower crimp increases the felting rate [22–24].

Many authors have determined that yarn twist, density of the woven cloth, and tightness of the knit greatly affect shrinkage of wool fabrics. Bogaty et al. [40] have stated that yarns with a higher twist exhibit a lower shrinkage rate, while plying has no significant effect. Moreover, it was determined that the denser the knitted material the more shrink resistant it is [40]. The same applies to woven cloth [41]. Van der Vegt [38] further observed that yarns with lower twist require less mechanical action to start felting. This suggests that in-

creasing tension within a yarn or a yarn component (sliver or slubbing) reduces the rate of felting. Additionally, it has been found that SW yarns felt more readily than W yarns. This is because in SW and WR yarns, fibre crimp has largely been removed through gilling and combing. In contrast, W yarns retain more fibre crimp due to their bulkiness and the less aligned arrangement of fibres [37].

2. Materials and methods

2.1. Materials

In this study, wool fibres from three Estonian local sheep breeds were studied – Estonian Darkhead (ET), Estonian Whitehead (EV), Kihnu Native (KML) – and compared to those of a fourth breed, the locally grown *Mérinos d'Arles* (MRA). All abbreviations are listed in Table 1.

The aim was to give an overview of the properties of the selected wool types as fibres, yarns, and textiles, and to analyse how fibre properties affect textile properties. For testing, fibres per breed were obtained from a single herd. Therefore, the results do not give an overview of the average wool properties of each breed. Wool was collected from the following farms in Estonia: ET – Sireli farm, EV – Murese farm, KML – Õnnekivi farm, and MRA – Ala-Mähkli farm. All wool used in the experiments was white and scoured in Viljandi Vilma Wool Laboratory prior to testing. Approximately 10 kg of wool was collected from each farm. In all cases, the wool had not been sorted by quality. It was scoured to yield at least 5 kg of usable fibre for textile production. Wool was scoured in a semi-industrial washing machine Electrolux W5105S, using special wool scouring programmes. Scouring contained a rinsing and a washing cycle. The detergent 'Pro-fit Wool' by Cole & Wilson was used. ET, EV, and KML fibres were rinsed for 15 min in 60 °C water using 25 mL of detergent per 1 kg of wool. For MRA fibres with clean fibre bundle ends, the rinsing programme was the same, but 50 mL of detergent per 1 kg of wool was used. MRA wool with dirty fibre bundle ends was rinsed and soaked by hand three times for a total of 20 min in 40 °C water using 30 mL of detergent per 1 kg of wool. Washing was conducted at 60 °C for 75 min with 50 mL of detergent per 1 kg of wool.

A total of eight yarn types were produced. From each wool type (ET, EV, KML, MRA), two yarn types were spun – a W and a SW yarn. The photos are shown in Table 2. WR yarns were not produced, as no WR mills operate in Estonia. Yarn thickness was selected based on the most commonly produced size in Estonian wool mills: 8/2 yarn (com-

Table 1. Abbreviations for wool types, yarn production methods, and yarn types

Wool type by sheep breed	Abbreviation	Yarn production method	Abbreviation	Abbreviations for yarn types
Mérinos d'Arles sheep	MRA	semi-worsted	SW	SW_MRA
				SW_ET
Estonian Darkhead sheep	ET			SW_EV
				SW_KML
Estonian Whitehead sheep	EV	woollen	W	W_MRA
				W_ET
Kihnu Native sheep	KML			W_EV
				W_KML

Table 2. Produced yarns by wool type and yarn type; photos by digital microscope Dino-Lite, magnification 30x

Wool type → Yarn type ↓	ET	EV	KML	MRA
SW	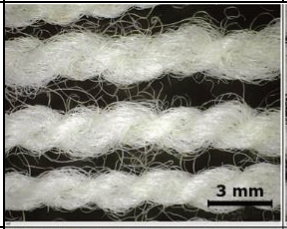	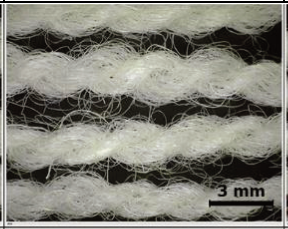		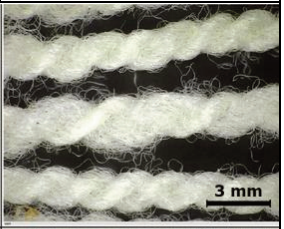
W	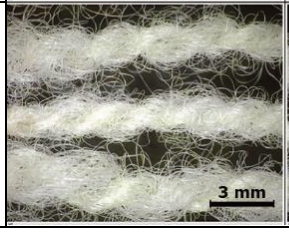	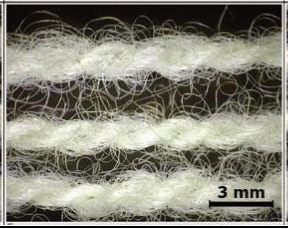	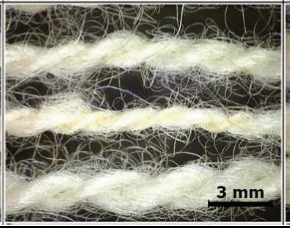	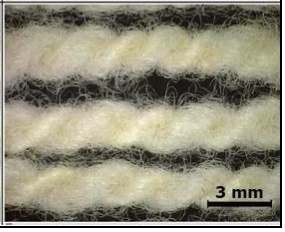

mercial value) was manufactured. Analysing the same wool types as different yarns aided in understanding which yarn and material properties were affected either by the fibre properties or by the yarn structure. W yarns were produced in Süvahavva wool mill (an old mule spinning machine park from 1890), and SW yarns were spun in Vilma wool laboratory (machine park by Ramella). All yarns were held in skeins prior to testing to avoid stretching.

Plain knit specimens from each yarn type were produced using a Nika KH-868 knitting machine, class 5. Yarn tension was adjusted to suit the yarn thickness; stitch tension was set to the lowest possible level for knitting each yarn type – '10'. The appropriate felting method was determined by reviewing various studies [9,42–44] and conducting preliminary experiments. The selected felting method, detailed in Table 3, was suitable for felting small specimens. The knitted materials made from W and SW yarns of each wool type were felted together in a domestic washing machine (Samsung WF0600NCW) using the same amount of detergent during each washing cycle (W yarns contained some carding oil even after the initial yarn scouring). Photos of the knitted and knitted felted materials are shown in Table 4.

2.2. Methods

The standard test methods used in this study are presented in Table 5.

All tests – except for fibre diameter, cuticle scale frequency, and scale height – were conducted in the standard atmosphere for conditioning and testing, at 20.0 ± 2.0 °C and 65.0 ± 4.0% relative humidity, in accordance with EVS-EN ISO 139:2005/A1:2011. Sampling followed EVS-EN 12751:2000. For fibre tests, a 50 g laboratory sample was taken from each wool type, from which a 1 mg test sample was obtained through mixing and halving.

Fibre properties were assessed to evaluate both the felting behaviour and the mechanical properties of the yarn and the material.

Fibre diameter was measured from 60 individual fibres per wool type. Fibres were cut to a suitable length, spread on a slide and examined under an optical microscope (Axioskop 2 by Zeiss).

Fibre length was measured from a total of 150 individual fibres per wool type. A single fibre was measured between forceps. The fibre was extended to remove crimp without stretching.

Table 3. Felting parameters

Felting parameters	First felting cycle	Second felting cycle
Temperature, °C	40	40
Time, min	65	65
Centrifuge, rev/min	1000	1000
Wool shampoo by Orto, mL per 100 g of material	15	0

Table 4. Photos of the knitted and knitted felted materials

Yarn type	Material type	Wool type: ET	EV	KML	MRA
SW	Knitted material	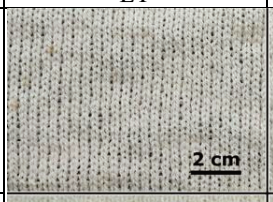	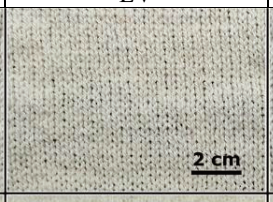	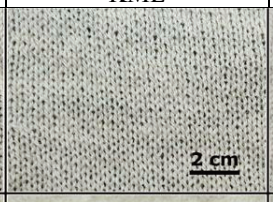	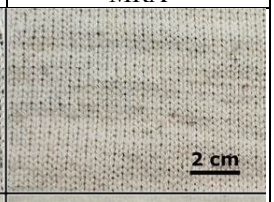
	Knitted felted material	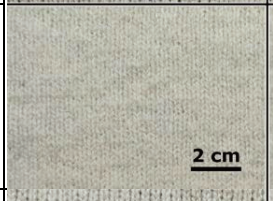	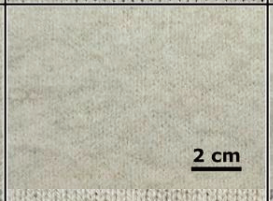	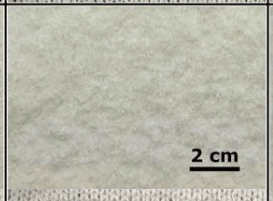	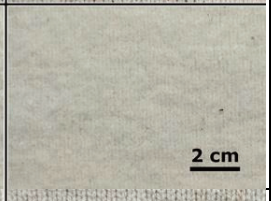
W	Knitted material	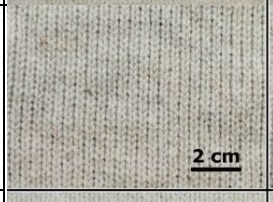	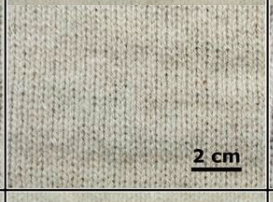	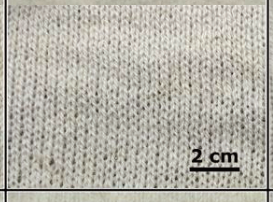	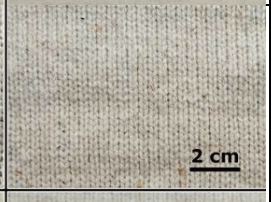
	Knitted felted material	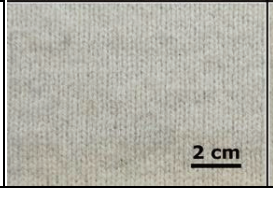	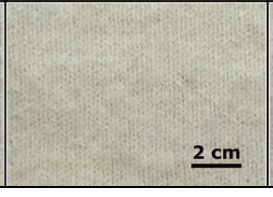	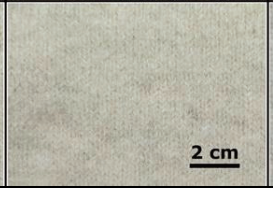	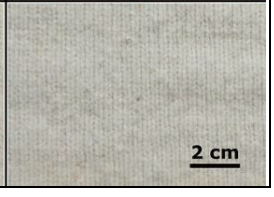

Table 5. Standard test methods

Textile material	Parameter	Standard test method
Fibre	Diameter	Microscopic observation
	Length	ASTM D5103-07(2018) – Standard test method for length and length distribution of manufactured staple fibers (single-fiber test) [45]
	Linear density	EVS-EN ISO 1973:2021 – Textile fibres – Determination of linear density – Gravimetric method and vibroscope method [46]
	Cuticle scale frequency	Microscopic observation
	Cuticle scale height	Microscopic observation
Yarn	Linear density	EVS-EN ISO 2060:2000 – Textiles – Yarn from packages – Determination of linear density (mass per unit length) by the skein method; options 1 and 4 [47]
	Twist	EVS-EN ISO 2061:2015 – Textiles – Determination of twist in yarns – Direct counting method [48]
	Tenacity and elongation	EVS-EN ISO 2062:2010 – Textiles – Yarns from packages – Determination of single-end breaking force and elongation at break using constant rate of extension (CRE) tester; method C [49]
	Yarn evenness	Testing: ASTM D2255-02 – Standard test method for grading spun yarns for appearance Grading: CSN 80 0704:1973 – Determination of thread appearance [50]
Knitted / knitted felted material	Mass per unit area	EVS-EN 12127:2000 – Textiles – Fabrics – Determination of mass per unit area using small samples [51]
	Air permeability	EVS-EN ISO 9237:2000 – Textiles – Determination of permeability of fabrics to air [52]
	Thickness	EVS-EN ISO 5084:2000 – Textiles – Determination of thickness of textiles and textile products [53]
	Pilling resistance	EVS-EN ISO 12945-2:2020 – Textiles – Determination of fabric propensity to surface pilling, fuzzing or matting – Part 2: Modified Martindale method [54,55]
	Abrasion resistance	EVS-EN ISO 12947-2:2016 – Textiles – Determination of the abrasion resistance of fabrics by the Martindale method – Part 2: Determination of specimen breakdown [56]

Fibre linear density was measured from 100 fibres per wool type. A single fibre was fixed to a vibroscope (Vibroskop by Lenzing) under a suitable tensioning force using tensioning force clips.

Fibre cuticle scale frequency and scale height were measured by scanning electron microscopy (SEM). Microscopic observation was based on established techniques used in previous studies [26–29]. Five fibres were analysed per wool type. Prior to imaging, the fibres were prepared by removing the crimp without stretching them. The specimens were coated with a gold-palladium layer using a Jeol Fine Coat Ion Sputter JFC-1100, with a coating time of 2 min 30 s. SEM imaging was performed using a Thermo Scientific Phenom XL scanning electron microscope at an accelerating voltage of 5 kV. Scale frequency was measured from one position on each fibre (Fig. 2a). For this, the number of scales per 100 µm fibre length was counted – fully visible scales were counted as 1.0, partially visible ones as 0.5. The fibre diameter at the measured position was also recorded. For comparison, the estimated number of scales per 10 000 µm² was calculated. Scale height was determined from two scales per fibre with a total of 10 measurements (Fig. 2b).

Yarn properties were assessed to characterise material performance and felting behaviour. W yarns contained carding oils and required washing prior to use, unlike SW yarns.

Yarn linear density was measured from 10 skeins per yarn type, skein length being 10.000 ± 0.0025 m. Each conditioned test skein was weighed using a Mettler AE 200 balance. The linear density Tt_c was then calculated using Eq. (1):

$$Tt_c = \frac{m_c \times 10^3}{L}, \tag{1}$$

where Tt_c is the linear density (tex), m_c is the mass of the conditioned test skein (g), and L is the length of the skein (m) [47].

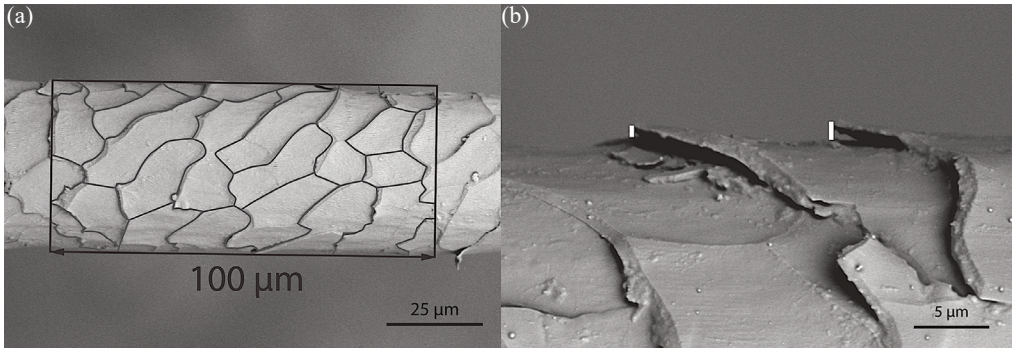

Fig. 2. SEM images: measuring the number of scales per 100 µm fibre length (a) and measuring scale height (b).

Yarn twist was determined from 10 specimens with a length of 60 cm from each yarn type. A specimen was fixed between the clamps of a twist counter, with a gauge length set to 500.0 ± 0.5 mm. The twist was removed and counted by turning a rotatable clamp. The average twist per test specimen t_x was calculated using Eq. (2):

$$t_x = \frac{1000\,x}{l}, \tag{2}$$

where t_x is the average twist (turns/m), l is the length of the test specimen before untwisting (mm), and x is the total number of turns observed in the test specimen [48].

Yarn tensile properties were tested on 10 specimens per yarn type. The gauge length of the tensile testing machine Instron 5866 was set to 500 ± 2 mm, and the length of the specimens was at least 100 mm longer. The specimen was clamped between the parallelly aligned test machine jaws with a pretension of 0.5 ± 0.1 cN/tex. Each specimen was extended until rupture. The extension rate of the moving clamp was set to 500 mm/min. A load cell with a maximum capacity of 500 N was used. Breaking force and elongation at break were recorded using the Instron Bluehill software. Breaking tenacity, expressed in centinewtons per tex, was calculated using Eq. (3):

$$B = \frac{F}{T}, \tag{3}$$

where B is the tenacity (cN/tex), F is the breaking force (cN), and T is the linear density (tex) [49].

Elongation at break, expressed as a percentage, was calculated using Eq. (4):

$$\varepsilon = \frac{\Delta l}{l_0} \times 100\%, \tag{4}$$

where ε is the elongation (%), Δl is the elongation at break (cm), and l_0 is the initial length of the specimen under pretension at the beginning of the test (cm) [49].

Yarn evenness was tested in accordance with the standards aimed for testing single spun cotton yarns but were deemed suitable for assessing wool yarns. Yarn boards (standard reference photos) were used for evaluation, graded from A (even yarn) to F (uneven yarn) [50]. For evaluation, the specimens were wrapped around a black surface in equally spaced turns. One specimen from each yarn type was assessed from both sides of the board in a VeriVide colour assessment cabinet under the artificial daylight D65. Bunches, covers, fuzz, neps, slubs, and thick and thin places were assessed. If the two sides of a specimen differed in appearance, the lower grade was assigned according to the standard.

Material properties – including stitch density, mass per unit area, air permeability, and thickness – were measured to assess felting behaviour. Pilling and abrasion resistance were also evaluated to assess material durability.

Mass per unit area was measured from five specimens per material. For each specimen, three length and three width measurements were recorded, and mean values were calculated. The area of each specimen was then determined from the mean values. Each specimen was weighed using a Mettler AE 200 balance. Mass per unit area M was calculated using Eq. (5):

$$M = \frac{m \times 1000}{A}, \tag{5}$$

where M is the mass per unit area (g/m^2), m is the mass of a test specimen (g), and A is the area of the same test specimen (cm^2) [51].

Air permeability was measured 20 times at different locations on each material using the FX 3340 MiniAir device, with a measuring range of 15–1500 l/m^2/s on a test area of 20 cm^2. A pressure drop of 100 Pa was applied. One side of each specimen was tested.

Thickness was measured from 10 different spots on each material. For testing, the specimen was placed undistorted on the reference plate of a Hans Schmidt & Co GmbH thickness gauge DD-50-T. The presser-foot, applying a pressure of 1 ± 0.01 kPa, was lowered onto the specimen, and the gauge length reading was recorded after 30 ± 5 s.

Pilling resistance was tested on three specimens per material on James Heal 5-position Martindale abrasion testing machine. The test specimen holder, guide spindle, and holder ring had a mass of 155 ± 1 g. The assessment of pilling and fuzzing was performed visually after a defined number of pilling rubs (125, 500, 1000, 2000, 5000, and 7000) and graded from '5' (no change) to '1' (greatest change) [54,55]. Visual assessments were conducted under the artificial daylight D65 in the VeriVide colour assessment cabinet.

Abrasion resistance was tested on three specimens per material on James Heal 5-position Martindale abrasion testing machine. The abrasion load parameters were set according to the apparel fabrics (9 kPa). Foam backings were not used. The test was conducted until 36 000 rub cycles were completed (a premium requirement for outerwear coat fabrics [57]). Visual assessments were done under the artificial daylight D56 in the VeriVide colour assessment cabinet after every 1000 rubs (up to 6000), 2000 rubs (from 6001 to 20 000), and 5000 rubs (from 20 001).

Felting tendency was evaluated by examining the influence of fibre properties on yarn characteristics and by comparing the properties of knitted and knitted felted materials.

3. Results and discussion

3.1. Fibres

3.1.1. Fibre diameter

The average fibre diameters of ET, EV, KML, and MRA wool are presented in Fig. 3. Fibre diameter distributions of ET, EV, KML, and MRA wool are shown in Figs 4–7. MRA wool exhibited the most uniform fibre diameter distribution across the wool batch, indicating consistency both between animals and within individual fleeces. In contrast, the other wool types showed broader distributions with multiple diameter range groups. On average, ET and EV fibres were very coarse, measuring 42.0 ± 8.8 µm and 41.6 ± 8.4 µm, respectively. KML fibres

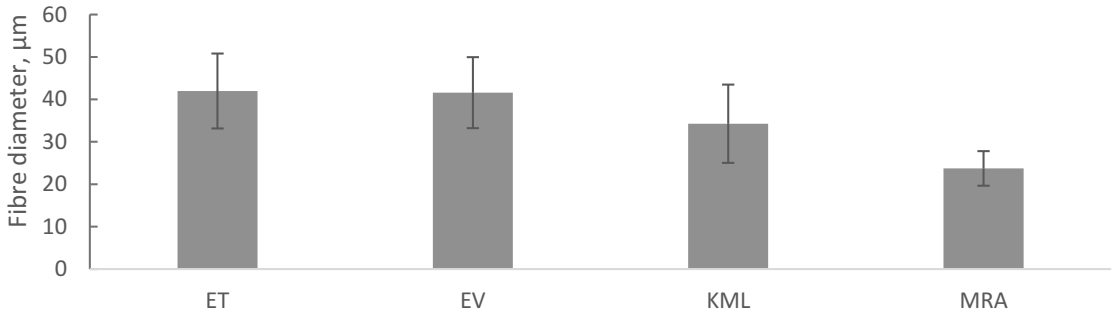

Fig. 3. Average fibre diameter.

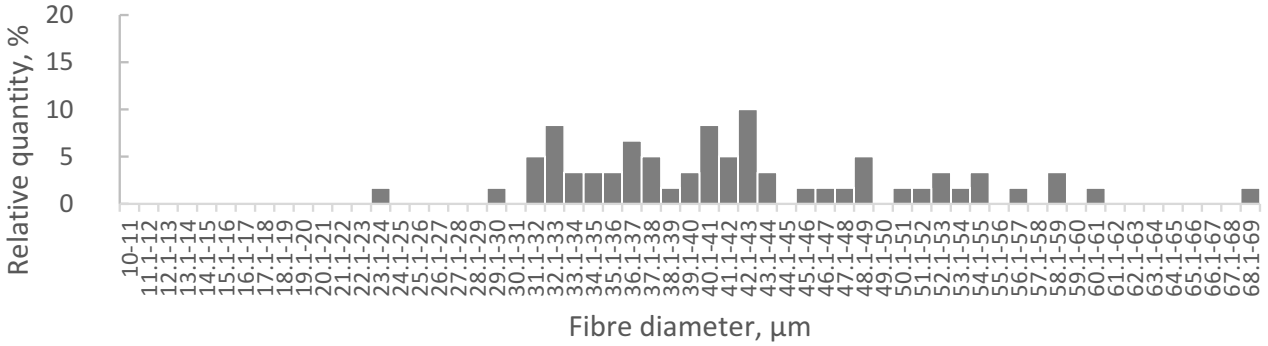

Fig. 4. Fibre diameter distribution of Estonian Darkhead (ET) sheep wool.

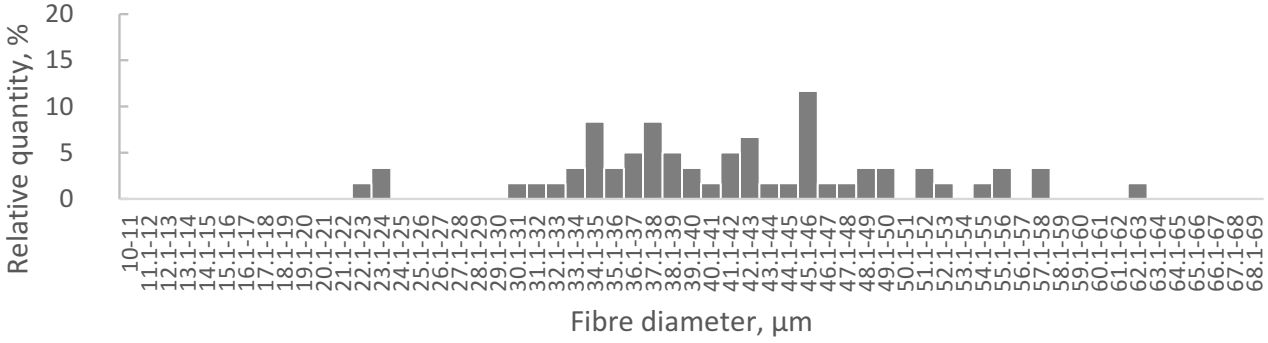

Fig. 5. Fibre diameter distribution of Estonian Whitehead (EV) sheep wool.

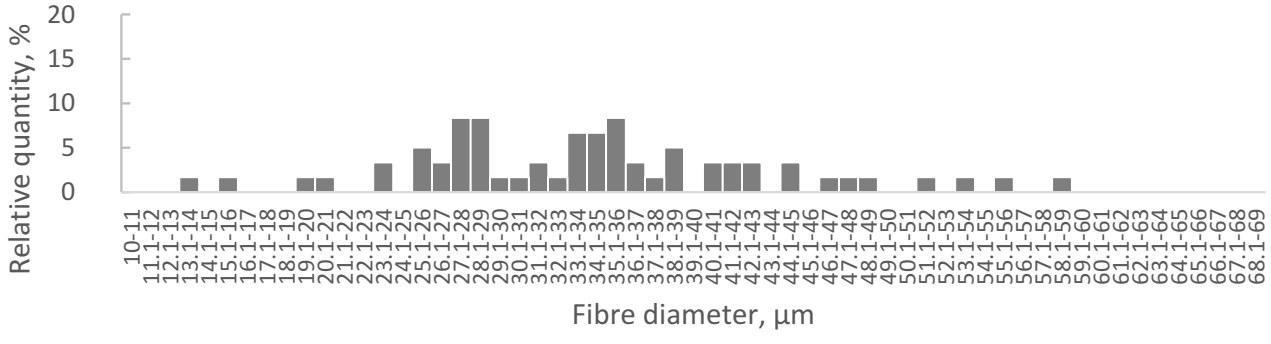

Fig. 6. Fibre diameter distribution of Kihnu Native (KML) sheep wool.

were coarse, with an average diameter of 34.3 ± 9.2 µm. MRA fibres were semi-fine, 23.7 ± 4.1 µm (according to the Soviet time system – fine, < 25.0 µm [16]). Optical microscopy revealed that 16.7% of the measured EV fibres were medullated, which affected the fibre linear density measurements by reducing fibre mass. The high linear density of KML fibres may be attributed to morphological differences, although these were not examined in this study.

The average fibre fineness of ET and EV wool, compared to the results from previous research, was coarser. Respectively, ET and EV average fibre fineness was 13.0 and 12.6 µm coarser compared to the measurements from 1980 [16], and

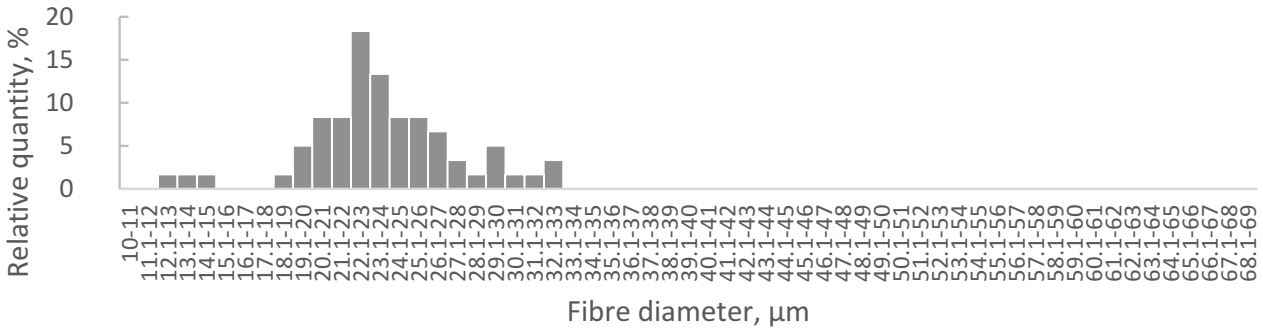

Fig. 7. Fibre diameter distribution of *Mérinos d'Arles* (MRA) sheep wool.

6.3 and 11.1 µm coarser compared to the measurements from the 1990s [6]. The fineness of the KML wool measured in this study was broadly consistent with the results from Pallas University of Applied Sciences [7].

3.1.2. Fibre length

The average fibre lengths of ET, EV, KML, and MRA wool are presented in Fig. 8. Fibre length distributions are shown in Figs 9–12. EV and MRA wool exhibited a single prominent peak in their distributions, indicating a relatively uniform fibre length within and between fleeces. The broader distribution observed in EV wool may be attributed to ongoing breeding efforts. In contrast, the fibre length distributions of ET and KML wool displayed multiple peaks, suggesting greater variability within the wool batches. EV wool contained the longest fibres, with an average length of 136 ± 34 mm. The average length of the other fibres was: KML 124 ± 41 mm, ET 121 ± 31 mm, and MRA 102 ± 23 mm. MRA wool was the most uniform. EV and ET wool was not as even, likely due to ongoing breeding – animals with varying wool quality exist within the same herd.

A 1980 study reported the average fibre length of both ET and EV wool as 106 mm [16]. The average fibre lengths measured in the current study were 15 mm and 30 mm longer, respectively. No previous data were available for KML wool.

3.1.3. Linear density of wool fibres

The average fibre linear density of ET, EV, KML, and MRA wool is presented in Fig. 13. Among all the samples, MRA wool exhibited the most uniform linear density. EV fibres were the most uniform among the Estonian breeds, though their distribution was still broader than that of MRA. Similarly to the fibre length results, ET and KML wool fibres showed broader distributions with multiple linear density groups, which once again was probably due to the variety of fibres in the wool batch. Linear density measurements indicated that, on average, KML wool fibres were the coarsest, 19.1 ± 7.4 dtex, followed by ET, 18.7 ± 4.8 dtex, and EV,

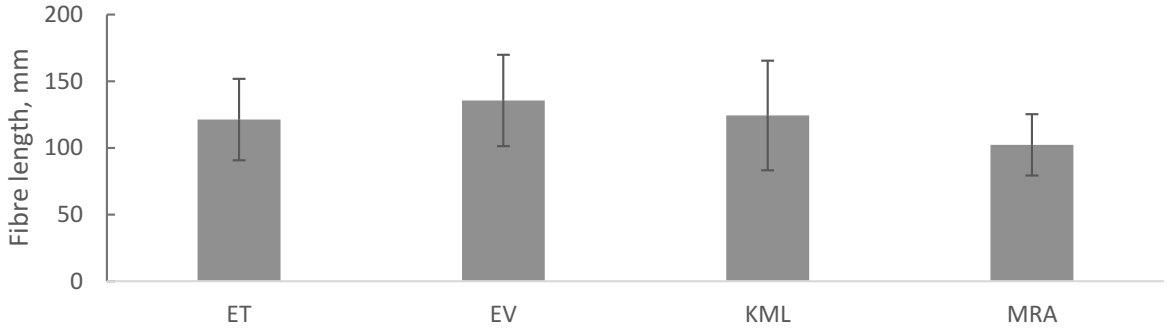

Fig. 8. Average fibre length.

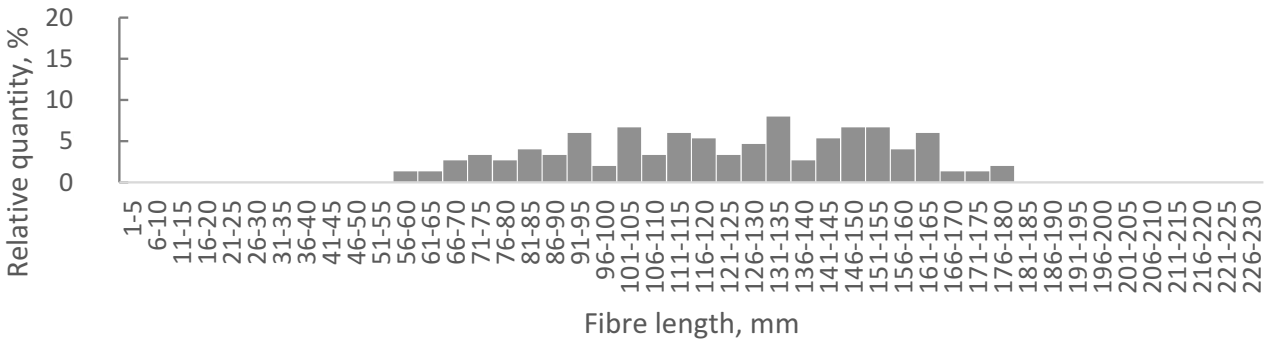

Fig. 9. Fibre length distribution of Estonian Darkhead (ET) sheep wool.

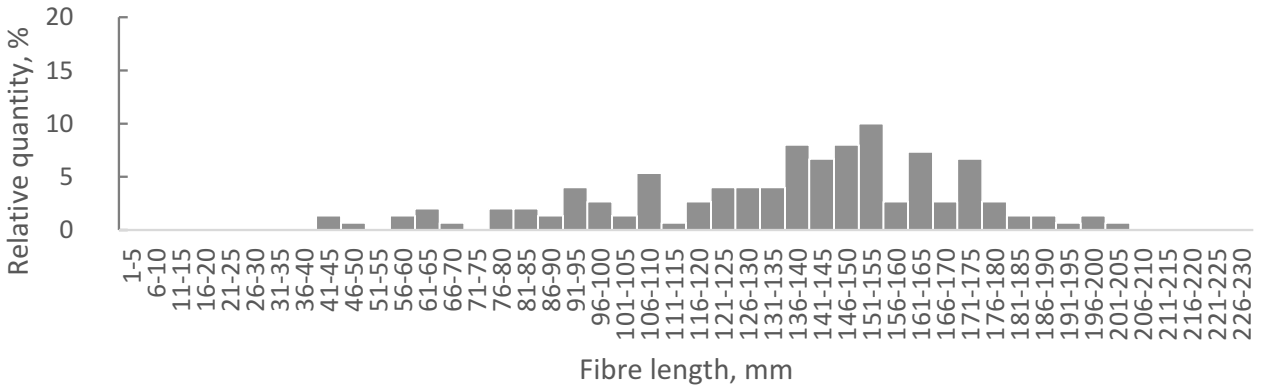

Fig. 10. Fibre length distribution of Estonian Whitehead (EV) sheep wool.

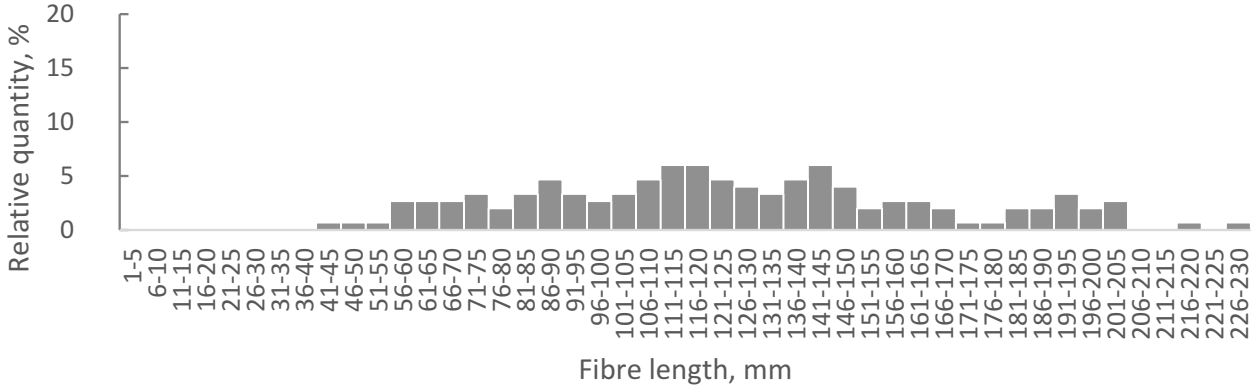

Fig. 11. Fibre length distribution of Kihnu Native (KML) sheep wool.

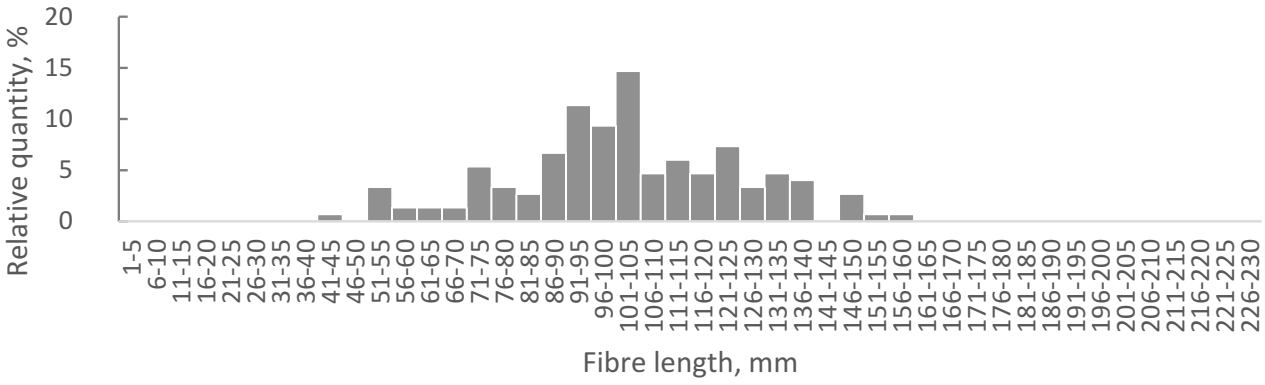

Fig. 12. Fibre length distribution of *Mérinos d'Arles* (MRA) sheep wool.

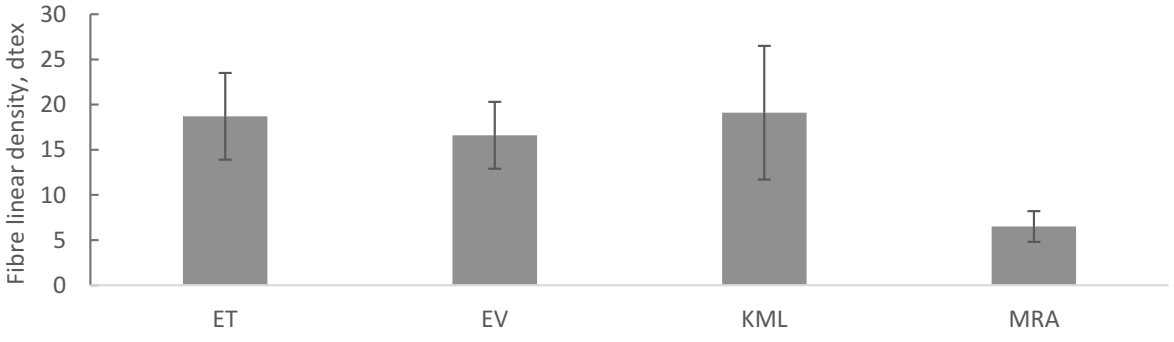

Fig. 13. Average fibre linear density.

16.6 ± 3.7 dtex. The linear density of MRA wool fibres was the lowest and therefore indicated the finest fibres, 6.5 ± 1.7 dtex.

The average linear density values obtained in this study were higher than those reported in the Estonia–Norway co-operation project, which measured unscoured wool [8]. However, the conditioning and testing conditions in that project differed from the standard atmosphere. The average linear density of the ET, EV, and KML wool measured in the current study was 5.39, 0.39, and 6.97 dtex higher, respectively. These differences may result from variations in herds, sampling methods, or testing environments.

3.1.4. Fibre cuticle scale frequency and cuticle scale height

The average fibre cuticle scale frequency and cuticle scale height are summarised in Table 6. These parameters have not previously been measured on Estonian wool. Representative SEM images are presented in Fig. 14. The results indicated that finer fibres generally exhibited a higher scale frequency than coarser ones – with the exception of EV wool. This observation contrasts with the findings of Raja et al. [27], who reported no significant difference between coarse and semi-fine fibres. The estimated average number of scales per 10 000 μm^2 ranged from 37.9 ± 7.0 to 46.4 ± 12.9. The average scale height was greater in finer wool types – again with the exception of EV wool. EV fibres exhibited highly serrated scale edges, distinguishing them from the other wool types. The average cuticular scale height ranged from 0.63 ± 0.18 to 0.88 ± 0.41 μm.

3.2. Yarns

3.2.1. Yarn linear density

The average yarn linear density is summarised in Fig. 15. For SW yarns, the linear density ranged from 346 ± 10 tex to 424 ± 16 tex, and for W yarns, from 460 ± 54 tex to 478 ± 28 tex. W yarns exhibited higher linear density values compared to SW yarns – a difference attributed to the variation in produc-

Table 6. Cuticle scale frequency and scale height

Wool type	Average number of scales per 100 μm fibre length	SD	Average estimated number of scales per 10 000 μm^2	SD	Average scale height, μm	SD, μm
ET	18.0	2.9	37.9	7.0	0.63	0.18
EV	18.1	5.5	39.4	7.9	0.88	0.41
KML	17.2	3.8	39.6	9.5	0.71	0.32
MRA	9.8	2.2	46.4	12.9	0.75	0.18

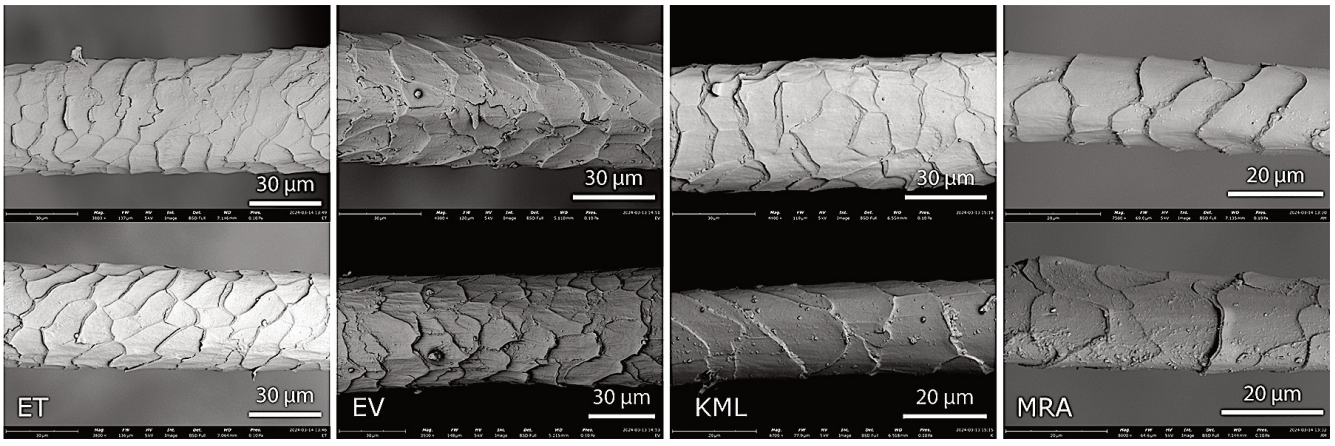

Fig. 14. SEM images of examples of wool fibres.

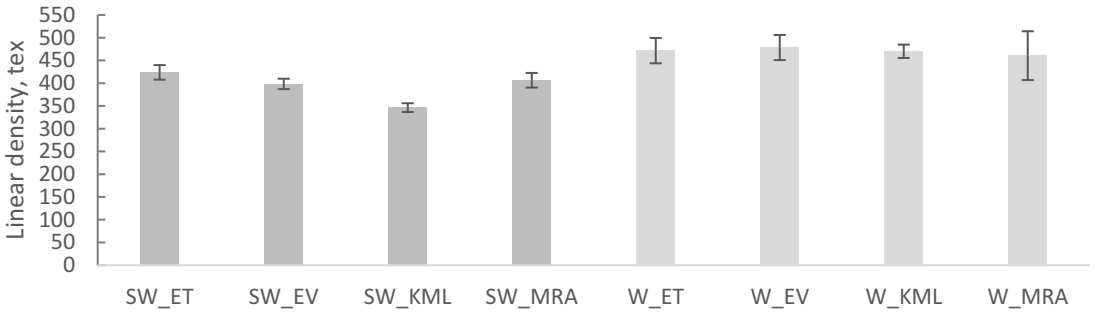

Fig. 15. Linear density of yarns.

tion methods. SW yarns differed between each other; in W yarns differences or irregularities occurred within the yarns themselves.

SW yarns varied due to the following reasons: during pin drafting of the slivers drafting times varied, drafting rate had to be regulated constantly, and sliver breakage occurred occasionally, influencing the consistency of sliver thickness. Consequently, yarn thickness had to be adjusted and compared visually during spinning, causing differences between yarns. In W yarns, unevenness mainly occurred due to outdated machinery. The average linear density of W yarns was more similar since the weight of the wool batch (which was similar for all yarns) largely determined yarn thickness. Among all yarns, the SW_KML yarn had the lowest linear density (346 ± 10 tex), while the W_EV yarn had the highest (478 ± 28 tex). In the following figures, a darker shade of grey indicates SW yarns and lighter shade W yarns.

3.2.2. Yarn twist

All the produced yarns exhibited a twist direction of Z (right-hand) in one-ply and S (left-hand) in plied form. The mean twist of different yarn types is presented in Fig. 16. The average yarn twist ranged from 146.5 ± 5.2 to 178.0 ± 10.7 turns/m for SW yarns and 163.8 ± 11.3 to 179.8 ± 11.6 turns/m for W yarns. Variability among SW yarns occurred between different yarn types, whereas in W yarns, irregularities were observed within individual yarns. When comparing the yarns by wool type, the average twist was similar between the two production methods, with W yarns exhibiting slightly higher twist values. The yarn with the lowest twist was SW_KML (146.5 ± 5.2 turns/m), while the highest twist was observed in W_MRA (179.8 ± 11.6 turns/m).

3.2.3. Yarn tensile properties

The average breaking tenacity of yarns (Fig. 17) ranged from 4.6 ± 0.2 to 6.4 ± 0.7 cN/tex in SW and 2.3 ± 0.3 to 4.2 ± 0.2 cN/tex in W yarns. Tenacity was higher in SW yarns, since parallelly aligned fibres are harder to pull out of a yarn. For both SW and W yarns, the tenacity values followed the same order by wool type, suggesting correlation with fibre properties. No correlation was found between wool fibre diameter and yarn tenacity, contrary to findings by Bouagga et al. [31]. The absence of correlation may be attributed to the high variance in fibre diameter.

Yarn tenacity was influenced by fibre length and crimp (visual assessment). Yarns produced from KML fibres exhibited the highest average tenacity within both production categories (SW_KML 6.4 ± 0.7 cN/tex and W_KML 4.2 ± 0.2 cN/tex). KML fibres were the second longest and contained few medullated fibres. In contrast, MRA yarns showed the lowest tenacity values (SW_MRA 4.6 ± 0.2 cN/tex and W_MRA 2.3 ± 0.3 cN/tex). Additionally, MRA average fibre length was the shortest. Moreover, fibre crimp influenced tenacity. KML fibres had the lowest and MRA fibres the highest crimp. Decrease in length and increase in fibre crimp reduced the strength of a yarn. The same was stated by Barach and Rainard [21].

Elongation at break of the different yarn types (Fig. 18) did not follow a clear pattern. The average elongation at break ranged from 23 ± 3% to 31 ± 5% in SW and from 24 ± 3% to 27 ± 3% in W yarns. Nevertheless, the order by wool type was consistent in both production methods: yarns made from KML fibres had the highest elongation at break (SW_KML 31 ± 5% and W_KML 27 ± 2%), followed by MRA, EV, and finally ET yarns. The reason, once again, could have been

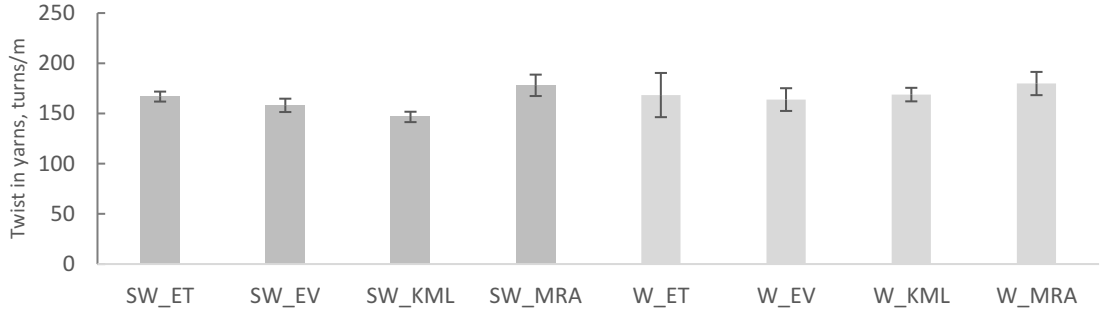

Fig. 16. Twist in yarns.

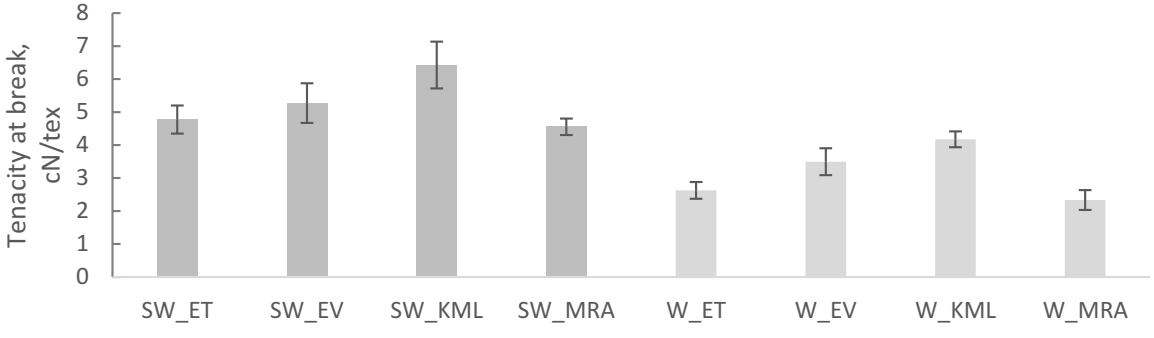

Fig. 17. Yarn breaking tenacity.

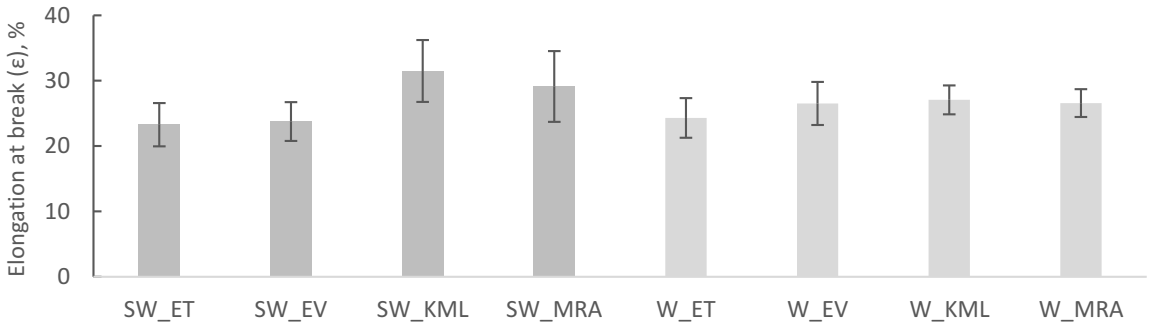

Fig. 18. Elongation at break of yarns.

fibre morphology. To make further conclusions regarding elongation and tenacity, broken specimen ends and morphological properties of fibres should be assessed. In both yarn production categories, KML yarns demonstrated the highest values of both tenacity and elongation at break.

Yarn tensile properties (maximum force and elongation) have previously been studied in the Estonia–Norway cooperation project [8]. Compared to the current research, the order of data by fibre type for average elongation at break was similar – native sheep yarn was the strongest and exhibited the greatest elongation. ET and EV results were similar to one another, yet the yarns were not as strong and elongated less. However, the results themselves differed – in the current study, maximum force was recorded to be lower and elongation much higher. This discrepancy is likely due to differences in testing and conditioning environments. The Estonia–Norway project employed higher temperature and lower humidity levels compared to the standard atmosphere. When humidity is higher (as in the standard atmosphere), then the strength of wool decreases and elongation increases.

3.2.4. Evenness of yarns – grading yarns for appearance

Grades for yarn evenness are summarised in Table 7. Overall, W yarns were more uneven, primarily due to the production process – in W yarns, fibres were not aligned along the yarn axis through a dedicated alignment process, which can lead to fibre reversals and, consequently, irregularities in the yarn structure. In SW yarns, fibres were aligned by a separate gilling process, thereby reducing irregularities inside yarns. Among the SW yarns, the one produced from MRA fibres was the most uneven, likely due to difficulties encountered during processing.

3.3. Fabrics

3.3.1. Mass per unit area of knitted and knitted felted materials

As a result of felting, the material becomes thicker and denser, leading to an increase in mass per unit area. Consequently, the area of the specimen decreases during felting. Dimensional change of the specimens is presented in Figs 19 and 20. Due to the felting process, the properties of knitted felted materials differ from knitted materials. Therefore, they can be used to assess felting shrinkage. Felting shrinkage is further discussed in Subsection 3.3.6.

The results of mass per unit area are presented in Fig. 21. The average mass per unit area ranged from 400 ± 14 to 600 ± 41 g/m^2 in the knitted and 555 to 1186 g/m^2 in the knitted felted materials. As SW yarns had a lower linear

Table 7. Yarn evenness graded from two sides of a yarn board, from A (even) to F (uneven)

Side No.	Grade by yarn type							
	SW_ET	SW_EV	SW_KML	SW_MRA	W_ET	W_EV	W_KML	W_MRA
1	B	C	C	E	D	D	C	D
2	C	D	B	D	D	D	C	D
Overall grade	C	D	C	E	D	D	C	D

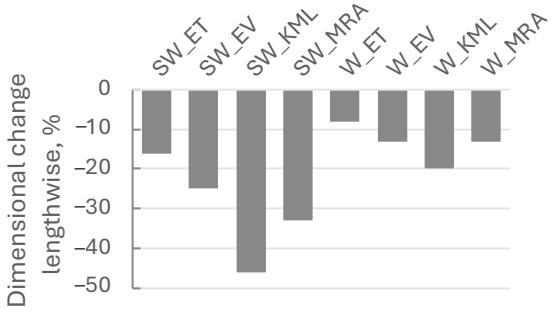

Fig. 19. Dimensional change of the knitted and knitted felted materials after felting, lengthwise (a single large specimen was felted).

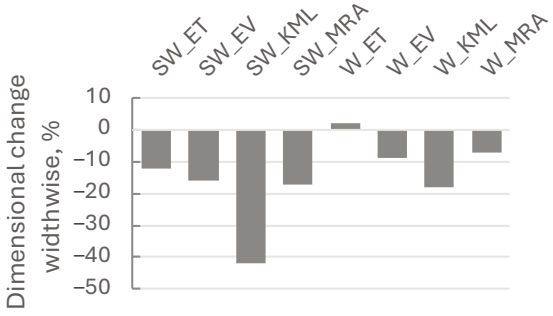

Fig. 20. Dimensional change of the knitted and knitted felted materials after felting, widthwise (a single large specimen was felted).

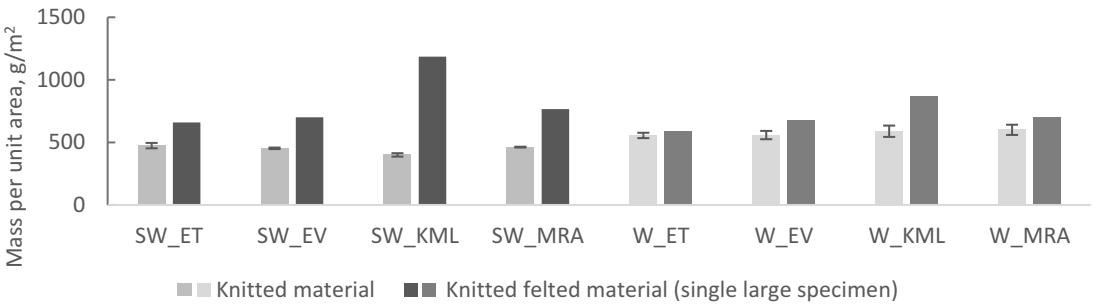

Fig. 21. Mass per unit area results of the knitted and knitted felted materials. In the case of the knitted felted materials, a single specimen was felted and therefore the standard deviation cannot be shown.

density, the knitted fabrics produced from these yarns were lighter. The knitted materials made from W yarns were heavier. Additionally, the evenness of yarns influenced the uniformity of the knitted material. In all the cases, mass per unit area increased after felting. The knitted felted materials made from SW yarns exhibited higher mass per unit area compared to those made from W yarns of the same wool type. The knitted felted materials produced from KML fibres had the highest mass per unit area – 1186 g/m^2 for SW_KML and 863 g/m^2 for W_KML. The knitted felted materials produced from ET fibres had the lowest mass per unit area – 659 g/m^2 for SW_ET and 589 g/m^2 for W_ET. Change in mass per unit area and dimensional change due to felting are further discussed in Subsection 3.3.6.

3.3.2. Air permeability of knitted and knitted felted materials

The results of air permeability of both the knitted and the knitted felted materials are presented in Fig. 22. The average air permeability ranged from 612 ± 88 to >1500 l/m^2/s in the knitted and from 294 ± 13 to 979 ± 67 l/m^2/s in the knitted felted materials. As all the yarns were knitted using the same stitch dial density to enable comparison after felting and fulling, air permeability in the knitted state was primarily influenced by yarn thickness and the evenness of the yarns. The materials produced from thinner yarns exhibited higher air permeability. The knitted materials made from SW_K and SW_EV yarns exceeded the measuring range of the device 15–1500 l/m^2/s.

Air permeability was also measured to characterise the felting properties of the fibres and yarns. In all the cases, felting reduced air permeability. A greater decrease in air permeability occurred when the specimens' mass per unit area had increased more (specimen had felted more). The lowest air permeability values were recorded for the knitted felted materials made from MRA fibres: 294 ± 13 l/m^2/s for knitted felted material produced from SW_MRA yarn and 368 ± 26 l/m^2/s for that produced from W_MRA yarn. This was likely due to the finer fibre diameter, which resulted in smaller voids and thus reduced air flow. Change in air permeability due to felting is further discussed in Subsection 3.3.6.

3.3.3. Thickness of knitted and knitted felted materials

Thickness of the knitted materials is summarised in Fig. 23. The average thickness ranged from 2.85 ± 0.07 mm to 4.46 ± 0.12 mm in the knitted and from 5.28 ± 0.23 to 8.18 ± 0.11 mm in the knitted felted materials. Yarn linear density influenced the thickness of the knitted materials. In the knitted felted materials, thickness was primarily affected by felting shrinkage. Increase in thickness during felting was greater in the materials made from SW yarns. Among the knitted felted samples, those made from KML yarns were the thickest – 8.18 ± 0.11 mm for SW_KML and 6.72 ± 0.16 mm for W_KML. The knitted felted materials produced from ET fibres were the thinnest – 5.31 ± 0.07 mm for SW_ET and 5.57 ± 0.07 mm for W_ET. Change in thickness is further discussed in Subsection 3.3.6.

3.3.4. Pilling resistance of knitted and knitted felted materials

The average results for the propensity to pilling of the knitted and knitted felted materials are presented in Table 8. All materials met the premium requirements specified for knitted materials in *Ecodesign criteria for consumer textiles*, 2021 edition [57] – grade 3–4 after 2000 pilling rubs and grade 2–3 after 7000 pilling rubs.

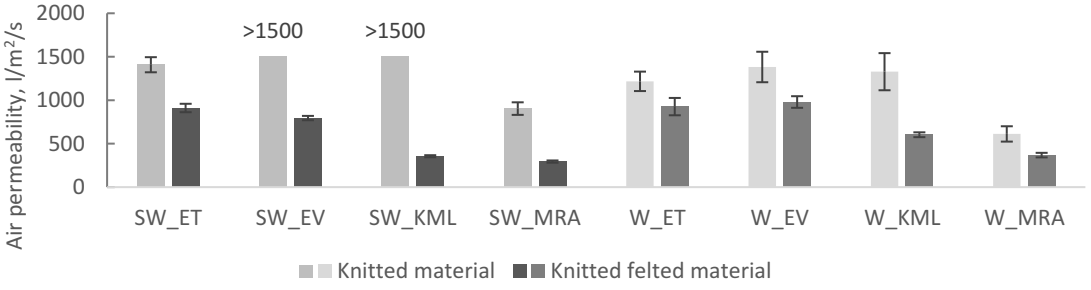

Fig. 22. Air permeability results of the knitted and knitted felted materials.

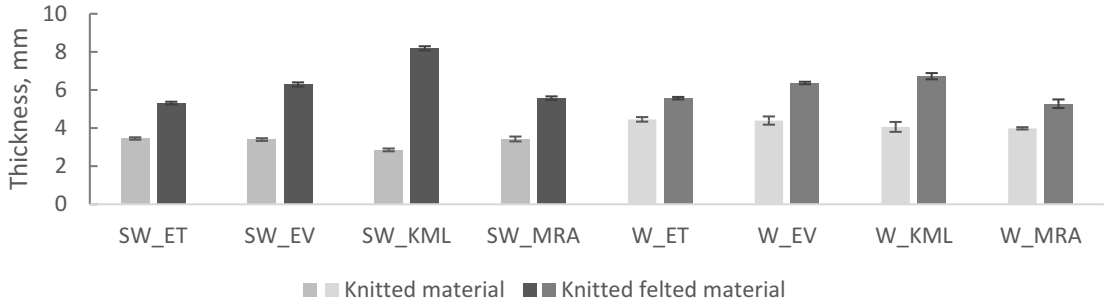

Fig 23. Thickness results of the knitted and knitted felted materials.

Table 8. Knitted and knitted felted material average pilling results, graded from 5 (no change) to 1 (severe change)

No. of pilling rubs	Knitted material average pilling results								Knitted felted material average pilling results							
	Grades by yarn type								Grades by yarn type							
	SW_ ET	SW_ EV	SW_ KML	SW_ MRA	W_ ET	W_ EV	W_ KML	W_ MRA	SW_ ET	SW_ EV	SW_ KML	SW_ MRA	W_ ET	W_ EV	W_ KML	W_ MRA
125	5	5	5	5	5	5	5	5	5	5	5	4	5	5	5	4
500	5	5	5	4	5	5	5	5	5	5	5	3	5	5	5	4
1000	5	5	4	4	5	5	5	4	4	5	5	3	5	5	5	3
2000	5	4	4	4	5	5	5	4	4	4	4	3	5	5	4	3
5000	4	4	3	3	4	5	5	4	3	4	4	3	4	5	4	3
7000	4	4	3	3	4	4	4	4	3	4	4	3	4	4	4	3

W yarns demonstrated better pilling resistance. This may be attributed to their higher linear density, which contributed to a denser structure in the knitted materials. Among W yarns, which were more similar in the average linear density and twist, the yarns containing longer fibres had higher pilling resistance (W_EV, W_KML). These yarns (fibres) also had higher tenacity. The yarns made of finer fibres produced most pills (MRA yarns). Moreover, soft-twist yarns (SW_KML) or the yarns containing un-spun regions (SW_MRA, W_MRA) exhibited lower pilling resistance compared to the yarns with higher twist. In these yarns, fibres were not tightly bound within the yarn structure, which favoured pilling.

During the felting process, lanolin and residual oils from the yarn production were washed off. This resulted in a hairier fabric surface, which overall favoured pilling slightly more. An exception was observed with the SW yarn produced from KML fibres – in this case, felting compensated for the yarn's softer twist, leading to a felted material with improved pilling resistance.

3.3.5. Abrasion resistance of knitted and knitted felted materials

All the knitted and knitted felted materials exhibited abrasion resistance of ≥ 36 000 rubs without reaching the endpoint, thereby meeting the premium requirement specified for coat and jacket materials in *Ecodesign criteria for consumer textiles* [57]. During abrasion resistance testing, pilling developed on the specimens. The life of the pills appeared to be influenced by yarn and fibre tenacity, as the order by pill life corresponded to tenacity values. In the knitted material tests, the specimens made from MRA and ET yarns exhibited shorter pill lifespans – these yarns also had lower tenacity values. Conversely, the materials produced from EV and KML fibres showed longer pill lifespans – these yarns additionally had higher tenacity results.

Pilling was present longer on SW yarns compared to W yarns. This can be explained by the more parallel alignment of fibres in SW yarns, which are therefore harder to pull out of the yarn. As a result, the phase where open fibre ends are pulled out of the yarn lasts longer, which lengthens the pilling phase and also the life cycle of the material. On the knitted materials made from SW_EV, SW_KML, and W_KML yarns, pills remained visible for 36 000 rubs. On the knitted felted materials, pilling was present longer compared to the knitted ones, and the pills were larger. Few pills were present at 36 000 rubs on all materials. However, in all the cases, the fibres protruding from the fuzzy felted surfaces were eventually abraded away.

3.3.6. Felting shrinkage of knitted and knitted felted materials

Materials knitted from W yarns might have felted less due to fibre crimp present in the bulkier W yarns. Additionally, SW yarns likely felted more as a result of their slightly lower twist, lower linear density of yarns, and a less dense material structure (especially SW_KML), all of which have been associated with increased shrinkage, as noted by Bogaty et al. [40]. In W_MRA yarn, the dense structure might have prevented high felting. Furthermore, the results suggested that felting was influenced by fibre properties, as the felting order by wool types was the same or similar across both production methods. KML fibres demonstrated the greatest felting tendency, followed by MRA and EV fibres, with ET fibres exhibiting the lowest tendency to felt.

Felting tendency was affected by fibre property combinations specific to each wool type. KML fibres displayed the lowest crimp, were among the longest by average fibre length, contained the longest fibre group, and by fineness were in between the researched wool types – in reality classified as coarse. These properties, except for coarseness,

have been found to enhance felting, including greater fibre length [26,38,39] and lower crimp [22–24]. Fine fibres have been stated to felt more [26,39]. Moreover, KML fibres exhibited the second highest fibre scale frequency, and their scale height was moderate, similar to that of MRA wool. Both scale height and cuticle scale frequency have generally been reported to increase felting tendency [26,27].

It is highly probable that the combination of high fibre length, low crimp, and high cuticle scale frequency compensated for fibre coarseness in the case of KML fibres. In contrast, MRA fibres likely exhibited lower felting tendency due to their shorter fibre length and higher crimp, both of which are known to reduce felting. The low crimp and long length of KML fibres may have outweighed the felting potential typically associated with finer fibres. Among the other wool types, EV fibres exhibited a greater felting tendency than ET fibres, with ET fibres felting the least. While EV and ET fibres were similar in terms of diameter (both being very coarse) and crimp (normal), EV fibres were longer on average and had the highest cuticle scale height and greater scale frequency than ET fibres. Both the cuticle scale frequency and height of ET fibres were overall the lowest. These findings further support the conclusion that fibre length, cuticle scale frequency, and cuticle scale height positively influence felting behaviour. Results from all the experiments are presented in Table 9 and Fig. 24.

Within the SW yarn category, the knitted material produced from ET yarn felted the least, whereas the one made from KML fibres felted the most. Therefore, area shrinkage ranged from –27% to –69%, change in mass per unit area from +34% to +206%, change in air permeability from –35% to –76%, and thickness from +54% to +187%. The same pattern was present in the case of W yarns: the knitted material made from ET yarn felted the least and the one made from KML yarn the most, area shrinkage ranged from –6% to –35%, change in mass per unit area from +4% to +43%, change in air permeability from –24% to –55%, and thickness ranged from +25% to +66%.

The felting shrinkage results obtained in the current study were similar to the ones obtained by Siiri Nool [9]. It was observed that materials made from EML SW yarns felt the most. Additionally, the order of felting shrinkage by wool type in the case of ET and EV wool was consistent with the findings from the Estonia–Norway co-operation project [8]. The materials produced from ET wool felted the least and the ones from EV wool slightly more. The felting shrinkage

Table 9. Felting shrinkage and change in properties of the material after felting

Yarn type	Dimensional change – change in area, %	Change in mass per unit area, %	Change in air permeability, %	Change in thickness, %
SW_ET	–27	+34	–35*	+54
SW_EV	–37	+52	–47*	+85
SW_KML	–69	+206	–76*	+187
SW_MRA	–45	+73	–67	+62
W_ET	–6	+4	–24	+25
W_EV	–21	+19	–29*	+45
W_KML	–35	+43	–55*	+66
W_MRA	–18	+14	–40	+32

* Assessment accuracy was limited because air permeability exceeded the device's measuring range in a number of samples, resulting in changes greater than the reported values

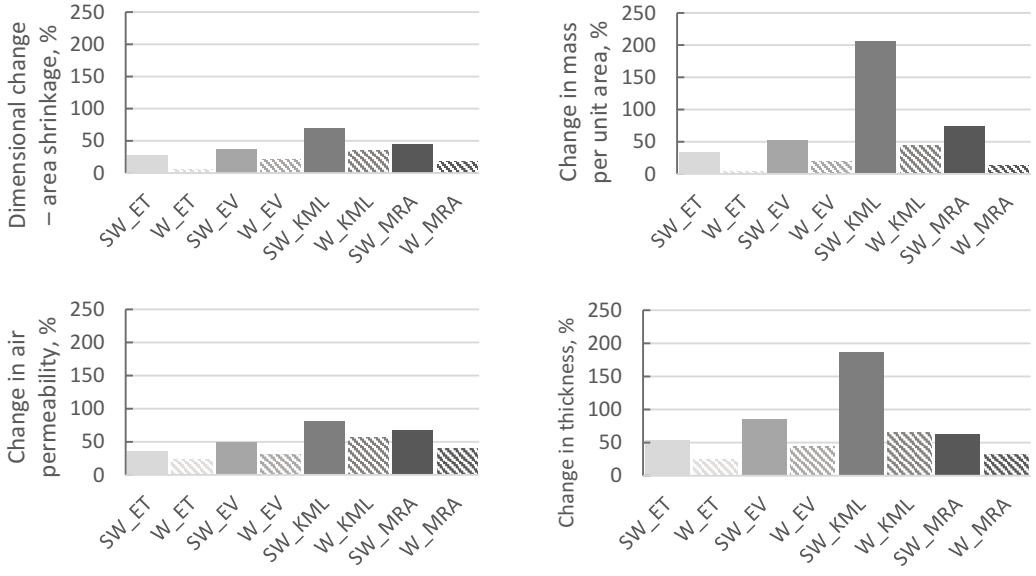

Fig. 24. Characterisation of felting, comparison between SW and W yarns. SW yarns are indicated with a fully coloured column, W yarns with a striped column.

of KML wool was reported to be lower than the one observed in the current study.

4. Conclusions

The studied wool fibres of Estonian breeds were found to be less even compared to the local MRA wool. MRA wool was of better quality. EV wool fibres were the most even from the studied Estonian breeds' wool. Compared to the local MRA wool, Estonian breeds' wool was found to be coarser, longer, and with higher linear density and lower cuticle scale frequency, while cuticle scale height varied. The main difference between Estonian breeds' and Merino wool was fibre fineness (MRA wool was 23.7 ± 4.1 µm on average and Estonian wool on average over 10 µm coarser).

Fibre properties were found to influence yarn performance. SW yarns were stronger compared to W yarns. Yarn tenacity was most affected by fibre length and crimp (visual assessment). The highest tenacity was observed in yarns made from long, low crimp fibres. KML yarns achieved the highest tenacity within both production categories (SW_KML 6.4 ± 0.7 cN/tex and W_KML 4.2 ± 0.2 cN/tex), and KML fibres had the lowest crimp and were among the longest (124 ± 41 mm). On the other hand, MRA yarns exhibited the lowest tenacity (SW_MRA 4.6 ± 0.2 cN/tex and W_MRA 2.3 ± 0.3 cN/tex), and MRA fibres had the highest crimp and were the shortest (102 ± 23 mm).

Material performance and felting were influenced by both fibre and yarn properties. In the pilling resistance test, all the knitted and knitted felted materials met the premium requirements set in the Ecodesign criteria – grade 3–4 after 2000 pilling rubs and grade 2–3 after 7000 pilling rubs. Pilling resistance of the knitted materials was predominantly influenced by linear density of yarn, twist in yarns, and fibre length and diameter. W yarns' pilling resistance was higher due to the higher linear density of the yarns, which produced a slightly denser fabric structure. Yarns made of longer and coarser fibres produced fewer pills. The knitted felted materials generally favoured pilling more – residual carding oils and lanolin were washed off during felting, which made the surface of the material hairy and therefore more prone to pilling.

In abrasion resistance tests, all the materials withstood the premium requirements set in the Ecodesign criteria, which is ≥ 36 000 rubs. The life of pills was associated with yarn and fibre tenacity. On materials made from yarns (fibres) with lower tenacity, life of pills was shorter. Moreover, pilling was present longer on SW than W yarns – fibres in SW yarns are more parallelly aligned and are harder to pull out of the yarn. This lengthens the life cycle of the material. Pilling was present longer on the knitted felted materials compared to the knitted materials, and the pills were larger.

Felting was influenced by fibre and yarn properties, and slightly by material structural differences. Yarn production technology influenced felting – SW yarns generally felted more than W yarns. W yarns might have felted less due to the presence of fibre crimp of bulkier W yarns. Additionally, slightly lower twist, lower linear density of yarns, and less dense structure of the material (especially SW_KML) could have enhanced the felting of SW yarns. Felting was affected by fibre properties – the order by wool types between the two production technologies in many cases was the same or similar. KML fibres had the greatest felting tendency, followed by MRA and EV fibres. ET fibres' felting tendency was the lowest. Fibre properties that enhanced felting were lower crimp, longer fibre length, finer diameter, higher cuticle scale frequency, and higher cuticle scale height.

The findings of the study are essential for

1) establishing a working wool grading system, which is based on the influence of fibre properties on textile material behaviour during use, and
2) finding suitable application for Estonian breeds' wool.

Author contributions

Liisa Torsus: conceptualisation, methodology, validation, research, resources, data curation, writing – original draft preparation, visualisation; **Tiia Plamus**: conceptualisation, methodology, validation, data curation, writing – review and editing, supervision; **Katrin Kabun**: conceptualisation, validation, writing – review and editing, supervision; **Urve Kallavus**: data curation – SEM, writing – review and editing.

Data availability statement

Data are contained within the article.

Acknowledgements

We would like to thank Astri Kaljus and Reet Pettai, who aided with yarn production in Vilma wool laboratory and Süvahavva wool mill, and Laura Kuningas, a specialist at Tallinn University of Technology, who aided with consulting on different test methods. The publication costs of this article were partially covered by the Estonian Academy of Sciences.

References

1. Kabun, K. *Archaically High-Tech: Knowledge-Based Use of Sheep Wool*. The Estonian Academy of Arts Department of Textile Design, Tallinn, 2022.
2. Finch, K. *Lecture 2: Wool*. 1977.
3. Eesti Lambakasvatajate Selts, Villa töörühm (Estonian Sheep Breeders Association, Wool Working Group). *Villa ja villatööstuse arengukava 2016–2036 (Development plan for wool and the wool industry 2016–2036)*. 2015.
4. Matsin, A., Tali, K., Kabun, K. and Kool, L. Ülevaade Eesti villamajandusest 2022 (Estonian wool industry: the current state). *Studia Vernacula*, 2022, **14**, 206–223.
5. Dillon, P. Sheep, woolcraft and regenerative land-use. Presented at the *International Wool Conference, Viljandi, Estonia, 17–18 November 2022.*
6. Zarens, K. *The wool quality of Estonian sheep and phenotypical correlation between wool characteristics*. Master's thesis. Estonian Agricultural University, Tartu, 1997.
7. Västrik, V. and Kool, L. Villa sorteerimise ja töötlemise mõju lõnga ja kangaste omadustele Muhu saarel kasvanud maalammaste näitel (Effect of the sorting and processing of wool on the properties of yarn and fabric, on the example of the Estonian Native Sheep grown on Muhu Island). *Studia Vernacula*, 2019, **10**, 122–145. https:// doi.org/10.12697/sv.2019.10.122-145

8. Matsin, A., Beilmann, M., Blomli, M. E., Kaljus, A., Lehis, L., Espelien, I. S. et al. *From wool to fabric. Estonian and Norwegian sheep's wool as a textile material. Production, properties and possibilities of use on the example of the wool of six sheep breeds.* https://sisu.ut.ee/wp-content/uploads/sites/591/wool_to_fabric_a4_12.pdf (accessed 2023-09-22).
9. Nool, S. *Villa töötlemise võimalused Eesti villavabrikutes. Eesti päritolu lambavillast lõnga testimine ja kasutamine silmuskoelise toote loomisel (Possibilities of processing local wool in Estonian wool factories. Testing and using Estonian woollen yarn for creating a knitted product).* Bachelor's thesis. Pallas University of Applied Sciences, Tartu, 2019.
10. Ärmpalu-Idvand, A. Kihnu maalammas on elus ja hea tervise juures (The Kihnu native sheep is alive and well). *Eesti Loodus*, **10**, 2009.
11. Saarma, U. Eesti ja Euroopa põlislammaste lugu kahe teadusuuringu valguses (The story of Estonian and European native sheep in the light of two scientific studies). *Eesti Loodus*, **10**, 2009.
12. Nõmmera, E. and Jaama, K. *Lambavill: villa omadused, sordid ja -kaubandus (Sheep Wool: Properties, Varieties, and Wool Trade)*. Agronoom, Tallinn, 1943.
13. Eesti vill ja eesti lambad (Estonian wool and Estonian sheep). *Eesti Sõna*, **188**, 1943.
14. Kihnu Native Sheep Breeders Society. *Kihnu maalamba aretussäilitusprogramm. Tõuraamatupidamine. Jõudluskontrolli läbiviimise ja geneetilise hindamise kord (Breeding and conservation programme for the Kihnu native sheep. Studbook management. Procedures for performance testing and genetic evaluation)*. 2020.
15. Rannamäe, E. Kolm tuhat aastat lambaid Eestis: zooarheoloogiline leiuaines ja emaliinide geneetiline mitmekesisus (Three thousand years of sheep in Estonia: zooarchaeological evidence and the genetic diversity of maternal lineages). *Õpetatud Eesti Seltsi aastaraamat 2016 (Yearbook of the Learned Estonian Society 2016)*. 2017.
16. Hõim, H. and Jaama, K. *Eriloomakasvatus (Special Animal Husbandry)*. Valgus, Tallinn, 1988.
17. Ahlskog, K. Evaluation and quality of wool. Presented at the *International Wool Conference, Viljandi, Estonia, 17–18 November 2022*.
18. Hatch, K. L. *Textile Science*. West Publishing Company, Minneapolis, 1993.
19. American Wool. *Wool grades and the sheep that grow the wool*. https://www.scribd.com/document/793715035/Wool-Grades-and-the-Sheep-that-Grow-the-Wool-Scan-1 (accessed 2024-01-23).
20. Holman, B. W. B. and Malau-Aduli, A. E. O. A review of sheep wool quality traits. *Annual Research & Review in Biology*, 2012, **2**(1), 1–14. https://journalarrb.com/index.php/ARRB/article/view/1260
21. Barach, J. L. and Rainard, L. W. Effect of crimp on fiber behavior: part II: addition of crimp to wool fibers and its effect on fiber properties. *Textile Research Journal*, 1950, **20**(5), 308–316. https://doi.org/10.1177/004051755002000506
22. Veldsman, D. P. and Kritzinger, C. C. 93 – studies on the felting properties of South African Merino wools. *Journal of the Textile Institute Transactions*, 1960, **51**(12), T1257–T1270. https://doi.org/10.1080/19447026008662561
23. Fraser, R. D. B. and Pressley, T. A. Felting investigations: part I: potential substitutes for rabbit fur in hat felts. *Textile Research Journal*, 1958, **28**(6), 478–485. https://doi.org/10.1177/004051755802800607
24. Crewther, W. G. and Dowling, L. M. Felting investigations: part II: relationship between wool fiber crimp and rate of felting. *Textile Research Journal*, 1961, **31**(1), 14–18. https://doi.org/10.1177/004051756103100102
25. Boncamper, I. *Tekstiilkiud: käsiraamat (Textile Fibres: A Handbook)*. Eesti Rõiva- ja Tekstiililiit, Tallinn, 2000.
26. Unal, P. G. and Atav, R. Determination of the relationship between fiber characteristics and felting tendency of luxury fibers from various origins. *Textile Research Journal*, 2018, **88**(6), 636–643. https://doi.org/10.1177/0040517516685282
27. Raja, A. S. M., Shakyawar, D. B., Kumar, A., Pareek, P. K. and Temani, P. Feltability of coarse wool and its application as technical felt. *Indian Journal of Fibre & Textile Research*, 2013, **38**, 395–399.
28. Yu, H., Hurren, C., Liu, X. and Wang, X. Understanding the difference in softness of Australian Soft Rolling Skin wool and conventional Merino wool. *Textile Research Journal*, 2022, **92**(17–18), 3130–3141. https://doi.org/10.1177/00405175211050524
29. Paul, S., Hewitt, A., Rana, S. and Goswami, P. Development of novel parameters for characterising scale morphology of wool fibre and its correlation with dye diffusion coefficient of acid dye. *Scientific Reports*, 2023, **13**(1), 18444. https://doi.org/10.1038/s41598-023-45689-w
30. Cottle, D. and Wood, E. *Overview of early stage wool processing*. https://www.scribd.com/document/490658701/WOOL-482-582-12-T-01 (accessed 2024-02-16).
31. Bouagga, T., Harizi, T., Sakli, F. and Zoccola, M. Correlation between the mechanical behavior and chemical, physical and thermal characteristics of wool: a study on Tunisian wool. *Journal of Natural Fibres*, 2020, **17**(1) 28–40. https://doi.org/10.1080/15440478.2018.1461727
32. Clark, M. (ed.) *Handbook of Textile and Industrial Dyeing: Principles, Processes and Types of Dyes*. Woodhead Publishing, Cambridge, 2011.
33. Hayavadana, J. (ed.) *Woven Fabric Structure Design and Product Planning*. Woodhead Publishing, New Delhi, 2015. https://doi.org/10.1201/b18876
34. Ukponmwan, J. O., Mukhopadhyay, A. and Chatterjee, K. N. *Pilling*. The Textile Institute, Manchester, 1998.
35. Matsin, A. Estonian and Norwegian local sheep wool – research and study materials for textile students in higher education. Presented at the *International Wool Conference, Viljandi, Estonia, 17–18 November 2022.*
36. Simpson, W. S. and Crawshaw, G. H. (eds) *Wool: Science and Technology*. The Textile Institute, Boca Raton, 2002.
37. Kenyon, P. R. *The assessment of natural variation in felting and shrinkage in wool from two flocks.* Master's thesis. Massey University, Palmerston North, 1997.
38. Van der Vegt, A. K. *A study on the mechanism of wool felting*. PhD thesis. Delft University of Technology, Delft, 1955.
39. Liu, X. and Wang, X. A comparative study on the felting propensity of animal fibers. *Textile Research Journal*, 2007, **77**(12), 957–963. https://doi.org/10.1177/0040517507083517
40. Bogaty, H., Weiner, L. I., Sookne, A. M. and Harrist, M. Effect of construction on the laundering shrinkage of knitted woolens. *Textile Research Journal*, 1951, **21**(2), 102–109. https://doi.org/10.1177/004051755102100207
41. Johnson, A. Influence of fiber length on the milling shrinkage of wool cloths. *Textile Research Journal*, 1953, **23**(12), 937. https://doi.org/10.1177/004051755302301211
42. Boutrop, J. *Fulling/felting resists*. https://share.google/WunpJBqJAc0qdIblE (accessed 2024-02-08).
43. Speakman, J. B., Stott, E. and Chang, H. 27 – a contribution to the theory of milling – part 2. *Journal of the Textile Institute Transactions*, 1933, **24**(7), T273–T292. https://doi.org/10.1080/19447023308661595
44. Feldtman, H. D. and McPhee, J. R. The effect of temperature on the felting of shrink-resistant wool. *Textile Research Journal*, 1964, **34**(3), 199–206. https://doi.org/10.1177/004051756403400303
45. ASTM D5103-07(2018). *Standard test method for length and length distribution of manufactured staple fibers (single-fiber test)*.
46. EVS-EN ISO 1973:2021. *Textile fibres – Determination of linear density – Gravimetric method and vibroscope method.*

47. EVS-EN ISO 2060:2000. *Textiles – Yarn from packages – Determination of linear density (mass per unit length) by the skein method.*
48. EVS-EN ISO 2061:2015. *Textiles – Determination of twist in yarns – Direct counting method.*
49. Viikna, A. *Kiuteadus (Fibre Science)*. Tallinna Tehnikaülikooli Kirjastus, Tallinn, 2005.
50. CSN 80 0704:1973. *Determination of yarn appearance*.
51. EVS-EN 12127:2000. *Textiles – Fabrics – Determination of mass per unit area using small samples*.
52. EVS-EN ISO 9237:2000. *Textiles – Determination of permeability of fabrics to air*.
53. EVS-EN ISO 5084:2000. *Textiles – Determination of thickness of textiles and textile products*.
54. EVS-EN ISO 12945-2:2020. *Textiles – Determination of fabric propensity to surface pilling, fuzzing or matting – Part 2: Modified Martindale method*.
55. EVS-EN ISO 12945-4:2020. *Textiles – Determination of fabric propensity to surface pilling, fuzzing or matting – Part 4: Assessment of pilling, fuzzing or matting by visual analysis*.
56. EVS-EN ISO 12947-2:2016. *Textiles – Determination of the abrasion resistance of fabrics by the Martindale method – Part 2: Determination of specimen breakdown.*
57. Ovam. *Ecodesign criteria for consumer textiles*. 2021. https://circulareconomy.europa.eu/platform/sites/default/files/ecodesign_criteria_for_consumer_textiles.pdf (accessed 2023-10-02).

Eesti kohaliku lambavilla taasväärtustamine – erinevate villatüüpide mõju tekstiilmaterjali omadustele

Liisa Torsus, Tiia Plamus, Katrin Kabun ja Urve Kallavus

Eesti lambatõugude vill leiab väheldast kasutust. See on väärindamata bioressurss, mis vajab taasväärtustamist. Kohaliku villa kasutuse suurendamiseks on peetud vajalikuks villa käitlemise ja hindamise süsteemi loomist ning villapesula asutamist. Sellise süsteemi loomiseks on vaja teada villakiu omaduste mõju tekstiilmaterjali omadustele. Varasemad kohalikud uuringud on olnud ebapiisavad just kiu omaduste ning silmuskootud materjali ja vanutatud silmuskootud materjali vaheliste seoste uurimisel. Käesolevas artiklis võrreldakse Eesti kohaliku lambavilla kiu, lõnga ja tekstiilmaterjali omadusi ning analüüsitakse kiu omaduste mõju tekstiilmaterjalile. Võrdluse loomiseks kaasati ka kohalik meriinovill, mis on tekstiilitööstuses laialdaselt kasutusel olev villatüüp. Uuringus hinnati villakiu omaduste mõju lõnga, silmuskootud materjali ja vanutatud silmuskootud materjali omadustele. Katsete tulemused võimaldavad leida kohalikule villale erinevaid kasutusvaldkondi ning anda soovitusi villa hindamissüsteemi väljatöötamiseks.

Tulemused näitasid, et Eesti lambatõugude vill on kohaliku meriinovillaga võrreldes pikem, kuid ebaühtlasema pikkusega, jämedam, kohati säsikanaliga ning väiksema soomuste sagedusega ja üldjuhul madalama soomuste kõrgusega. Eesti lambatõugude villast kedratud lõngad osutusid seevastu tugevamaks. Tugevaimates lõngades kasutatud kiud olid pikemad, laugema säbarusega ja vähese säsivillkarvade sisaldusega. Poolkammlõngad olid tugevamad. Pikkade ja jämedate kiudude kasutus ja lõnga suurem keerdumus vähendasid materjali kalduvust topiliseks muutuda. Vanutatud materjalid muutusid topiliseks kergemini kui silmuskootud materjalid, kuid talusid hõõrdumist paremini, kui neis oli kasutatud tugevamaid lõngu.

Viltumisomadusi mõjutasid kiu omadused – laugem säbarus, pikem kiud, väiksem diameeter ning suurem soomuste sagedus ja kõrgus soodustasid viltumist. Villakiu pikkus mõjutas viltumist rohkem kui peenus. Poolkammlõngadest valmistatud materjalid vanusid rohkem. Kiu omaduste erinevused mõjutasid lõnga ja tekstiilmaterjali omadusi ning kvaliteeti, mistõttu on vaja luua villa hindamissüsteem, mis arvestab nii kiu omadusi kui ka villatüüpe. Maalamba vill erines Eesti tumeda- ja valgepealise tõu villast, mis sarnanevad mitme omaduse poolest ja sobivad seetõttu ka segamiseks. Hindamissüsteem peaks arvestama nii villakiu pikkust kui ka läbimõõtu: kiu pikkus mõjutab otseselt tekstiilmaterjali tugevust, peenus aga villase rõiva kandmismugavust. Medullatsioon vähendas villa tugevust. Eesti lambatõugude villa ebaühtlus ei avaldanud lõnga ega materjali omadustele negatiivset mõju võrreldes kohaliku ühtlasema meriinovillaga.

Proceedings of the Estonian Academy of Sciences
2026, **75**, 1, 34–46

https://doi.org/10.3176/proc.2026.1.04

www.eap.ee/proceedings
Estonian Academy Publishers

CONTROL THEORY, MULTI-AGENT SYSTEMS

RESEARCH ARTICLE

Received 21 April 2025
Accepted 26 August 2025
Available online 26 January 2026

Keywords:
multi-agent system, reset event-triggered control, nonlinear dynamics, state error, consensus

Corresponding author:
Xingjian Fu
fxj@bistu.edu.cn

Citation:
Cheng, Y. and Fu, X. 2026. Distributed consensus for second-order multi-agent systems based on reset event-triggered mechanism. *Proceedings of the Estonian Academy of Sciences*, **75**(1), 34–46. https://doi.org/10.3176/proc.2026.1.04

Distributed consensus for second-order multi-agent systems based on reset event-triggered mechanism

Yi Cheng and Xingjian Fu

School of Automation, Beijing Information Science and Technology University, Beijing 100192, China

ABSTRACT

This paper investigates the consensus problem of disturbed second-order nonlinear multi-agent systems (MASs) under directed topology. A reset event-triggered control (RETC) is proposed that combines the reset mechanism with dynamic event-triggered control (ETC) strategies. The introduction of RETC overcomes the limitation of the traditional ETC that frequently triggers when approaching the consensus position. The external dynamic variables in the trigger conditions can be adjusted according to the predefined reset conditions. When the local state deviation reaches the preset threshold, the dynamic variable is reset to the initial value, greatly reducing the frequency of event triggering, and the strategies are fully distributed. The parameters and reset threshold depend only on the local state of the agents, without global information. The paper applies the Lyapunov stability theory to conduct a rigorous theoretical analysis of control strategies and verifies its effectiveness in improving transient consensus and reducing communication burden through simulations.

1. Introduction

As a prominent research focus in the field of control, the cooperative control of multi-agent systems (MASs) has shown significant potential in diverse applications, including consensus control [19,27], distributed optimization [1,11], and cluster collaboration [7]. This method refers to the approach where multiple agents with perception, communication, and mobility capabilities achieve the desired objectives collectively through local information exchange in a distributed environment. As the basis of collaborative control, the consensus problem has received extensive attention [18,20,22]. The core of cooperative control lies in establishing the relationship between individual agent behaviors and the overall group objective, with consensus providing the theoretical foundation for realizing this relationship [22].

The main task of the consensus problem of the MAS is to design the controller so that all the agents in the system tend to the same state [8,14]. Based on the graph theory, the convergence properties of linear systems with connected topology were proved by [14]. By analyzing delay effects in discrete-time multi-intelligent systems, a new mathematical tool was proposed by [8] to define consistency boundaries. In order to solve the influence of external disturbance, more complex system models were considered in [17] and [13], and the control method was further extended. The problem of non-matching disturbance was discussed in [24]. Yet, most existing approaches assume that the agents can continuously communicate with each other. However, in practical application scenarios, MASs often cannot fulfill this condition.

To reduce the consumption of communication resources under the premise of system stability, an event-triggered mechanism has been introduced into the consensus control of multi-agents [4,12]. Different from the traditional periodic triggering, this approach adopts a state-driven communication strategy in which communication links are activated and control protocols are updated only when specific triggering conditions are satisfied. This mechanism enables a dynamic trade-off between control accuracy and communication load.

According to the type of trigger function, event-triggered mechanisms are generally classified into static and dynamic categories. To address errors arising from system uncertainties, Deng et al. [4] investigated the tracking problem of nonlinear MASs and developed an adaptive controller for all subsystems based on a specially designed observer. However, with the growing complexity of practical applications, the limitations of static thresholds have become increasingly evident. For example, an excessively high threshold may delay system convergence, whereas an overly low threshold can lead to redundant communications [12].

Subsequently, a dynamic event-triggered algorithm was proposed by introducing dynamic variables [9,10]. The dynamic event-triggered mechanism makes the threshold of the event-triggered function change adaptively with the measurement error, which effectively avoids the situation that the trigger threshold is invariable under the static event-triggered mechanism. In recent years, the dynamic event-triggered mechanism has become a key technique for meeting the requirements of saving communication resources and flexible design. In [9], dynamic threshold parameters were introduced into the queuing control problem of a MAS, and an optimal balance was achieved between the communication efficiency of the system and the desired queuing performance. However, the research focused on the idealized formation task and did not address the impact of system dynamic complexity on the robustness of the triggering mechanism.

To address these challenges, Ge et al. [10] applied a dynamic event-triggered mechanism to the complex energy system of islanded microgrids. For multi-unmanned boat systems with limited communication, Ding et al. [6] designed a distributed control protocol based on adaptive algorithms and slip film control. The problem of time delay in a second-order MAS was improved in [15]. However, most of the studies assumed that external disturbances were negligible and did not account for adaptability under persistent perturbations. This limitation was solved in [21]. For MASs with external disturbances, Ruan et al. adopted a dynamic threshold event-triggered method in the channels from sensor to observer and from control protocol to actuator, thereby effectively avoiding excessive updates of the control protocol. Eventually, the system stated index could converge to a bounded range.

Dynamic event-triggered mechanisms have proven effective, but a key limitation remains: while they perform well when the system is far from equilibrium, frequent triggering still occurs near consensus due to the time-decaying nature of dynamic variables. To ensure stability, conservative parameter settings were adopted in [3], yet this approach failed to eliminate the Zeno phenomenon within a prescribed time. Subsequently, a new time-varying function was used to solve this problem [2]. Further, Liu et al. [16] extended the study to second-order MASs to realize the pre-determined time utility consensus and verified the validity of the results by using the example of self-driving cars on the internet. However, most existing work has concentrated on asymptotic consensus, with limited attention to transient performance. Therefore, the problem of improving the transient performance of the system while ensuring consensus has received widespread attention.

In order to address these challenges, this paper proposes a reset-based event-triggered mechanism, providing a novel perspective for improving the transient performance of the system [5,23,25,26]. The advantage of this method is that when the system state satisfies the preset conditions, the dynamic process is reconstructed by the strategy of finite amplitude state reset. The dependence of traditional continuous control on the monotonicity of the Lyapunov function is overcome, and the convergence process is accelerated. For this reason, the reset control is innovatively introduced into the dynamic variable update process: when the system state enters the ε neighborhood, the state reset of the auxiliary variable $\eta_i(t)$ with limited amplitude is performed, rather than the continuous variable decay strategy in the traditional event trigger.

The main contributions of this article are as follows:

1. A novel hybrid reset event-triggered mechanism is proposed that overcomes the dependence of the traditional dynamic event-triggered mechanism on the monotonicity of the Lyapunov function through the ε neighborhood partitioning and the finite amplitude reset operation, and has the potential to improve the transient consensus performance of MASs.

2. Event-triggered mechanisms that rely on global parameters are required by [21]. A completely distributed control law is proposed in this paper. Triggering parameters are based only on local neighboring state errors, which significantly enhances the adaptability of the algorithm to dynamic topologies.

3. Existing studies [9,10] mostly use a single control mechanism, making it difficult to balance communication efficiency and anti-jamming capability. This paper achieves consensus while eliminating the Zeno phenomenon through the coupled design of perturbation compensation and reset-triggering conditions.

In summary, this paper innovatively combines reset control and event-triggered mechanisms in the consensus control of MASs, and proposes a solution that effectively improves the performance of transient consensus and provides a new perspective for system analysis and design.

2. Problem formulation and preliminaries

The information interaction between agents can be described by the topology graph $\mathcal{G} = (\mathcal{V}, \mathcal{E}, \mathcal{A})$. For a topology graph composed of N agents, $\mathcal{V} = \{v_1, v_2, \ldots, v_n\}$ represents the set of nodes, and $\mathcal{E} = \{(v_i, v_j) \mid v_i \in \mathcal{V}, v_j \in \mathcal{V}, i \neq j\}$ denotes the set of edges. A directed edge $(v_i, v_j) \in \mathcal{E}$ indicates that agent i can receive information from agent j. At this point, v_j is called the neighboring agent of v_i. The weight adjacency matrix $\mathcal{A} = [a_{ij}] \in \mathbf{R}^{N\times N}$; if $(v_i, v_j) \in \mathcal{E}$, then $a_{ij} > 0$, otherwise $a_{ij} = 0$. The degree matrix $D = \mathrm{diag}\{d_1, \cdots, d_i, \cdots, d_M\}$ is defined, where $d_i = \sum_{j=1, j\neq i}^{M} a_{ij}$. The corresponding Laplacian matrix $\mathcal{L} = [l_{ij}] \in \mathbf{R}^{N\times N}$ of the graph $\mathcal{G}$ is defined as $\mathcal{L} = D - A$. The leader–follower adjacency matrix in a second-order MAS is $B = \mathrm{diag}\{b_1, b_2, \ldots, b_n\}$. When the follower is connected to the leader, $b_i = 1$, otherwise $b_i = 0$. When there exists a directed path between any two nodes that reaches connectivity, it is called a strongly connected graph $\mathcal{G}$.

This paper investigates second-order nonlinear MASs, where the dynamics of the leader and the follower i are described as follows:

$$\begin{cases} \dot{x}_0(t) = v_0(t) \\ \dot{v}_0(t) = f\,(t, x_0(t), v_0(t)) \end{cases}, \tag{1}$$

$$\begin{cases} \dot{x}_i(t) = v_i(t) \\ \dot{v}_i(t) = u_i(t) + d_i(t) + f\,(t, x_i(t), v_i(t)) \end{cases}, i = 1, 2, \cdots, n, \tag{2}$$

where $x_0(t) \in R^m$, $v_0(t) \in R^m$ are respectively expressed as the state and speed of the leader at the moment t; $x_i(t) \in R^m$, $v_i(t) \in R^m$, and $u_i(t) \in R^m$ are the state, speed, and control inputs of the follower i, respectively; $f(t, x_0(t), v_0(t))$ and $f\,(t, x_i(t), v_i(t))$ denote the unknown nonlinear continuous functions of the leader and the follower i, respectively; $d_i(t)$ denotes the unknown perturbations of the follower and satisfies $\|d(t)\| \leq D$, $d(t) = \left[d_1^{\mathrm{T}}(t), d_2^{\mathrm{T}}(t), \cdots, d_N^{\mathrm{T}}(t)\right]^{\mathrm{T}}$, where D is a positive constant.

The main lemmas and assumptions employed in the proof are summarized as follows:

Assumption 1. At least one follower can obtain the navigator's information; that is, the navigator–follower adjacency matrix $B \neq 0$.

Assumption 2. For a nonlinear continuous function $f(\cdot)$ in a second-order nonlinear MAS, which satisfies the Lipschitz condition, $\forall x, y, v, z \in \mathbb{R}$, there exist two positive constants p and q such that the following inequality holds:

$$|f(t, x, v) - f(t, y, z)| \leq p|x - y| + q|v - z|. \tag{3}$$

Lemma 1. [15] (Young's inequality) *Let* $p > 1$, $\frac{1}{p} + \frac{1}{q} = 1$. *Then, for any* $\sigma_1\sigma_2 > 0$, $\sigma_1\sigma_2 \leq \frac{\sigma_1^p}{p} + \frac{\sigma_2^q}{q}$.

Lemma 2. [2] (Sliding-mode interference compensation inequality) *Set constant* $D > 0$ *such that the jamming signal* $d(t)$ *satisfies the boundedness condition* $d(t) \leq D$, *where* D *is the upper bounds of known interference. For any time-varying signal* $\sigma(t) = \bar{x}^T(t) + \bar{v}^T(t)$, *the following inequality holds:*

$$\sigma(t)\,(d(t) - D\mathrm{sgn}(\sigma(t))) \leq 0. \tag{4}$$

Lemma 3. [25] *Let* $\mathcal{H} \in R^{n\times n}$ *be a symmetric positive definite matrix, and eigenvalues satisfy* $0 < \lambda_{\min}(\mathcal{H}) \leq \lambda_{\max}(\mathcal{H})$. *For any vector* $x \in R^n$, *the following inequality holds:*

$$\lambda_{\min}(\mathcal{H})\|x\|^2 \le x^{\mathrm{T}}\mathcal{H}x \le \lambda_{\max}(\mathcal{H})\|x\|^2, \tag{5}$$

where $\|x\|^2 = x^T x$, $\lambda_{\min}(\mathcal{H})$, *and* $\lambda_{\max}(\mathcal{H})$ *are the minimum and maximum eigenvalues of* $\mathcal{H}$, *respectively.*

Lemma 4. [26] *For* $\forall x, y \in R$ *and* $\alpha > 0$, *the following properties hold true:*

$$|xy| \le \frac{\alpha}{2}x^2 + \frac{1}{2\alpha}y^2. \tag{6}$$

Lemma 5. [23] *Consider the system described by Eqs* (1) *and* (2). *The MAS can achieve leading–following consensus if and only if the initial state of any agent satisfies the following conditions:*

$$\begin{aligned} &\lim_{t\to\infty}\|x_i(t) - x_0(t)\| = 0, i = 1, 2, \cdots, n, \\ &\lim_{t\to\infty}\|v_i(t) - v_0(t)\| = 0, i = 1, 2, \cdots, n. \end{aligned} \tag{7}$$

3. Main result

This paper investigates the consensus problem of second-order MASs under a reset event-triggered strategy. To facilitate the design of the event-triggering condition, the state measurement error is defined as follows (which also follows the idea in [12]):

$$\Delta_i(t) = \sum_{j\in\mathcal{N}_i} a_{ij}(x_i(t) - x_j(t) + v_i(t) - v_j(t)) + b_i\frac{1}{\alpha}(x_i(t) - x_0(t) + v_i(t) - v_0(t))^{\alpha}. \tag{8}$$

Define the triggering error of agent i as:

$$e_i(t) = \Delta_i(t_k) - \Delta_i(t). \tag{9}$$

The consensus error of agent i is:

$$\begin{aligned} \bar{x}_i(t) &= x_i(t) - x_0(t), \\ \bar{v}_i(t) &= v_i(t) - v_0(t). \end{aligned} \tag{10}$$

The control law for agent i is designed as follows:

$$\begin{aligned} u_i(t) = &- k\sum_{j\in\mathcal{N}_i} a_{ij}(x_i(t_k^i) - x_j(t_k^i) + v_i(t_k^i) - v_j(t_k^i)) \\ &+ b_i\frac{1}{\alpha}\left(x_i(t_k^i) - x_0(t_k^i) + v_i(t_k^i) - v_0(t_k^i)\right)^{\alpha} - D\mathrm{sgn}\left(\bar{x}^{\mathrm{T}}(t) + \bar{v}^{\mathrm{T}}(t)\right), \end{aligned} \tag{11}$$

where $k > 0$ is the control gain to be designed, $D\mathrm{sgn}\left(\bar{x}^{\mathrm{T}}(t) + \bar{v}^{\mathrm{T}}(t)\right)$ is the disturbance compensation term, t_k^i is the triggering time of the k-th event of agent i, and the trigger time sequence is $\left\{t_0^i, t_1^i, \ldots, t_k^i, \ldots\right\}$.

Define the trigger conditions for the reset event of agent i:

$$\|e_i(t)\|^2 > \left[\frac{2\alpha}{k}\lambda_{\min}k(L + B\otimes I_m) - \frac{2\alpha\omega}{k} - \alpha\left(2\alpha + 1\right)\right]\Omega(t) - 2\alpha(C_1C_2)^2 + \eta_i(t), \tag{12}$$

where $\Omega(t) = \sum_{i=1}^{n}\left(\|\bar{x}_i(t)\|^2 + \|\bar{v}_i(t)\|^2\right)$, $0 < \alpha < 1$, and $\eta_i(t)$ is a dynamic adjustment function, designed as:

$$\eta_i(\mathrm{t}) = \begin{cases} \eta_i(0), \Omega(t) < \varepsilon \\ \eta_i(0)e^{-\alpha(t-t_k)}, \Omega(t) \ge \varepsilon \end{cases}, \tag{13}$$

where $\beta > 0, \eta_i = 0, \varepsilon$ is an adjustable parameter that determines when the variable $\eta_i(t)$ will be reset to its initial value, and t_k is the most recent trigger moment. Combined with the error definition, the system equation can be rewritten as:

$$\begin{cases} \dot{\bar{x}}_i(t) = \bar{v}_i(t), \\ \dot{\bar{v}}_i(t) = -ke_i(t) - k\left[\sum_{j\in\mathcal{N}_i} a_{ij}(\bar{x}_i(t) - \bar{x}_j(t) + \bar{v}_i(t) - \bar{v}_j(t)) + b_i\frac{1}{\alpha}(\bar{x}_i(t) + \bar{v}_i(t))^{\alpha}\right] \\ +f\left(t, x_i(t), v_i(t)\right) - f\left(t, x_0(t), v_0(t)\right) + d_i(t) - D\mathrm{sgn}(\bar{x}^{\mathrm{T}}(t) + \bar{v}^{\mathrm{T}}(t)). \end{cases} \tag{14}$$

Using the Kronecker inner product, Eq. (14) can be further rewritten as:

$$\begin{aligned}
\dot{\bar{x}}_i(t) =& \bar{v}(t),\\
\dot{\bar{v}}_i(t) =& -ke(t) - k\left[(L\otimes I_m)(\bar{x}(t)+\bar{v}(t)) + \frac{1}{\alpha}(B\otimes I_m)(\bar{x}_i(t)+\bar{v}_i(t))^{\alpha}\right]\\
&+ F(t,x_i(t),v_i(t)) - F(t,x_0(t),v_0(t)) + d_i(t) - D\mathrm{sgn}(\bar{x}^{\mathrm{T}}(t)+\bar{v}^{\mathrm{T}}(t)),
\end{aligned} \tag{15}$$

where

$$\begin{aligned}
\bar{x}(t) &= (\bar{x}_1^{\mathrm{T}}(t), \bar{x}_2^{\mathrm{T}}(t), \cdots, \bar{x}_n^{\mathrm{T}}(t))^{\mathrm{T}},\\
\bar{v}(t) &= (\bar{v}_1^{\mathrm{T}}(t), \bar{v}_2^{\mathrm{T}}(t), \cdots, \bar{v}_n^{\mathrm{T}}(t))^{\mathrm{T}},\\
e(t) &= (e_1^{\mathrm{T}}(t), e_2^{\mathrm{T}}(t), \cdots, e_n^{\mathrm{T}}(t))^{\mathrm{T}},\\
F(t,x_i(t),v_i(t)) &= (f(t,x_1(t),v_1(t)), f(t,x_2(t),v_2(t)), \cdots, f(t,x_n(t),v_n(t)))^{\mathrm{T}}.
\end{aligned}$$

Theorem 1. *Under Assumptions 1 and 2, consider the MAS described by Eqs* (1) *and* (2). *If the parameter* α *satisfies the conditions, then:*

$$0 < \alpha < \frac{\lambda_{\min}(k(L+B)\otimes I_m) - \omega}{k} - \frac{1}{2}. \tag{16}$$

Under the consensus protocol (7) and the reset event-triggered mechanism (10) and (11), the MAS can achieve leader–following consensus.

Proof. Choose the Lyapunov function

$$V(t) = \frac{1}{2}\varepsilon^{\mathrm{T}}(t)P\varepsilon(t), \tag{17}$$

where $\varepsilon(t) = \begin{bmatrix}\bar{x}^{\mathrm{T}}(t) & \bar{v}^{\mathrm{T}}(t)\end{bmatrix}^{\mathrm{T}}$, $P = \begin{bmatrix}2k(L\otimes I_m) & I_n\otimes I_m\\ I_n\otimes I_m & I_n\otimes I_m\end{bmatrix}$.

The derivation of Eq. (17) yields:

$$\begin{aligned}
&\dot{V}(t) = \dot{V}(t) = \varepsilon^{\mathrm{T}}(t)P\dot{\varepsilon}(t)\\
&= \begin{bmatrix}\bar{x}^{\mathrm{T}}(t) & \bar{v}^{\mathrm{T}}(t)\end{bmatrix}\begin{bmatrix}2k(L\otimes I_m + B\otimes I_m) & I_n\otimes I_m\\ I_n\otimes I_m & I_n\otimes I_m\end{bmatrix}\\
&\begin{bmatrix}\bar{v}(t)\\ -ke(t) - k\left[(L\otimes I_m)(\bar{x}(t)+\bar{v}(t)) + \frac{1}{\alpha}(B\otimes I_m)(\bar{x}(t)+\bar{v}(t))^{\alpha}\right]\\ +F(t,x_i(t),v_i(t)) - F(t,x_0(t),v_0(t)) + d_i(t) - D\mathrm{sgn}(\bar{x}(t)+\bar{v}(t))\end{bmatrix}\\
&= \bar{v}^{\mathrm{T}}(t)\bar{v}(t) + 2k\bar{x}^{\mathrm{T}}(t)(L\otimes I_m + B\otimes I_m)\bar{v}(t)\\
&- k\left(\bar{x}^{\mathrm{T}}(t)+\bar{v}^{\mathrm{T}}(t)\right)e(t) - k\left(\bar{x}^{\mathrm{T}}(t)+\bar{v}^{\mathrm{T}}(t)\right)(L\otimes I_m)(\bar{x}(t)+\bar{v}(t))\\
&- \frac{k}{\alpha}\left(\bar{x}^{\mathrm{T}}(t)+\bar{v}^{\mathrm{T}}(t)\right)(B\otimes I_m)(\bar{x}(t)+\bar{v}(t))^{\alpha}\\
&+ \left(\bar{x}^{\mathrm{T}}(t)+\bar{v}^{\mathrm{T}}(t)\right)(F(t,x_i(t),v_i(t)) - F(t,x_0(t),v_0(t)))\\
&+ \left(\bar{x}^{\mathrm{T}}(t)+\bar{v}^{\mathrm{T}}(t)\right)\left(d(t) - D\mathrm{sgn}(\bar{x}^{\mathrm{T}}(t)+\bar{v}^{\mathrm{T}}(t)\right).
\end{aligned} \tag{18}$$

According to Lemma 1, expand the nonlinear terms:

$$\begin{aligned}
&- k\left(\bar{x}^{\mathrm{T}}(t)+\bar{v}^{\mathrm{T}}(t)\right)(L\otimes I_m)(\bar{x}(t)+\bar{v}(t))\\
&- \frac{k}{\alpha}\left(\bar{x}^{\mathrm{T}}(t)+\bar{v}^{\mathrm{T}}(t)\right)(B\otimes I_m)(\bar{x}(t)+\bar{v}(t))^{\alpha}\\
&\le -k\left(\bar{x}^{\mathrm{T}}(t)+\bar{v}^{\mathrm{T}}(t)\right)(L\otimes I_m)(\bar{x}(t)+\bar{v}(t))\\
&- \frac{k}{\alpha}\left(\bar{x}^{\mathrm{T}}(t)+\bar{v}^{\mathrm{T}}(t)\right)(B\otimes I_m)\,\alpha(\bar{x}(t)+\bar{v}(t)) + [1-\alpha]_{m\times 1}\\
&= -k\left(\bar{x}^{\mathrm{T}}(t)+\bar{v}^{\mathrm{T}}(t)\right)(L\otimes I_m + B\otimes I_m)(\bar{x}(t)+\bar{v}(t))\\
&- k\left(\bar{x}^{\mathrm{T}}(t)+\bar{v}^{\mathrm{T}}(t)\right)(B\otimes I_m)\left[\frac{1-\alpha}{\alpha}\right]_{m\times 1}.
\end{aligned} \tag{19}$$

Combine the results with similar terms in Eq. (18) and process $-k\left(\bar{x}^{\mathrm{T}}(t)+\bar{v}^{\mathrm{T}}(t)\right)(B\otimes I_m)\left[\frac{1-\alpha}{\alpha}\right]_{m\times 1}$:

$$\begin{aligned}
&2k\bar{x}^{\mathrm{T}}(t)\left(L\otimes I_m+B\otimes I_m\right)\bar{v}(t)+\bar{v}^{\mathrm{T}}(t)\bar{v}(t)\\
&-k\left(\bar{x}^{\mathrm{T}}(t)+\bar{v}^{\mathrm{T}}(t)\right)\left(L\otimes I_m+B\otimes I_m\right)\left(\bar{x}(t)+\bar{v}(t)\right)\\
&=2k\bar{x}^{\mathrm{T}}(t)\left(L\otimes I_m+B\otimes I_m\right)\bar{v}(t)\\
&-k\bar{x}^{\mathrm{T}}(t)\left(L\otimes I_m+B\otimes I_m\right)\bar{v}(t)-k\bar{v}^{\mathrm{T}}(t)\left(L\otimes I_m+B\otimes I_m\right)\bar{x}(t)\\
&-k\bar{x}^{\mathrm{T}}(t)\left(L\otimes I_m+B\otimes I_m\right)\bar{x}(t)-k\bar{v}^{\mathrm{T}}(t)\left(L\otimes I_m+B\otimes I_m\right)\bar{v}(t)+\bar{v}^{\mathrm{T}}(t)\bar{v}(t)\\
&=\bar{v}^{\mathrm{T}}(t)\bar{v}(t)-k\bar{x}^{\mathrm{T}}(t)\left(L\otimes I_m+B\otimes I_m\right)\bar{x}(t)-k\bar{v}^{\mathrm{T}}(t)\left(L\otimes I_m+B\otimes I_m\right)\bar{v}(t)
\end{aligned}\tag{20}$$

$$-k\left(\bar{x}^{\mathrm{T}}(t)+\bar{v}^{\mathrm{T}}(t)\right)(B\otimes I_m)\left[\frac{1-\alpha}{\alpha}\right]_{m\times 1}\leq k\left(\|\bar{x}_i(t)\|^2+\|\bar{v}_i(t)\|^2\right)\|B\otimes I_m\|\left\|\frac{1-\alpha}{\alpha}\right\|,\tag{21}$$

where $0<\alpha<1$, $C_1=\left\|\frac{1-\alpha}{\alpha}\right\|, C_2=\|B\otimes I_m\|$. Using the variation $ab\leq\frac{a^2}{2\epsilon}+\frac{\epsilon b^2}{2}(\epsilon>0)$ of Lemma 1 and taking $\epsilon=\frac{1}{k}$, we get:

$$\begin{aligned}
&k\left(\|\bar{x}_i(t)\|+\|\bar{v}_i(t)\|\right)C_1C_2\leq\frac{1}{2\epsilon}\sum_{i=1}^{n}\left(\|\bar{x}_i(t)\|^2+\|\bar{v}_i(t)\|^2\right)+\epsilon(kC_1C_2)^2\\
&\leq\frac{k}{2}\sum_{i=1}^{n}\left(\|\bar{x}_i(t)\|^2+\|\bar{v}_i(t)\|^2\right)+k(C_1C_2)^2.
\end{aligned}\tag{22}$$

Handling $\bar{v}^{\mathrm{T}}(t)\bar{v}(t)-k\bar{x}^{\mathrm{T}}(t)\left(L\otimes I_m+B\otimes I_m\right)\bar{x}(t)-k\bar{v}^{\mathrm{T}}(t)\left(L\otimes I_m+B\otimes I_m\right)\bar{v}(t)$ and according to Lemma 3, we get:

$$\begin{aligned}
&-\bar{x}^{\mathrm{T}}\left(L+B\right)\otimes I_m\bar{x}\leq 0,\quad -\bar{v}^{\mathrm{T}}\left(L+B\right)\otimes I_m\bar{v}\leq 0.\\
&-k\bar{x}^{\mathrm{T}}\left(L+B\right)\otimes I_m\bar{x}\leq 0,\quad -k\bar{v}^{\mathrm{T}}\left(L+B\right)\otimes I_m\bar{v}\leq 0.
\end{aligned}\tag{23}$$

According to the properties of the eigenvalues of a diagonal matrix, we have

$$\begin{aligned}
&\bar{v}^{\mathrm{T}}(t)\bar{v}(t)-k\bar{x}^{\mathrm{T}}(t)\left(L\otimes I_m\right)\left(\bar{x}(t)\right)-k\bar{v}^{\mathrm{T}}(t)\left(L\otimes I_m\right)\left(\bar{v}(t)\right)\\
&\leq\sum_{i=1}^{n}\|\bar{v}_i(t)\|^2-\lambda_{\min}\left(k\left(L+B\right)\otimes I_m\right)\sum_{i=1}^{n}\left(\|\bar{x}_i(t)\|^2+\|\bar{v}_i(t)\|^2\right)\leq 0,
\end{aligned}\tag{24}$$

where $\lambda_{\min}(L)$ denotes the smallest non-zero eigenvalue of L.

Based on Assumption 2 and the basic inequality $2xy\leq x^2+y^2$, we obtain:

$$\begin{aligned}
&\left(\bar{x}(t)+\bar{v}(t)\right)\left(F\left(t,x_i(t),v_i(t)\right)-F\left(t,x_0(t),v_0(t)\right)\right)\\
&\leq\sum_{i=1}^{n}\left|\bar{x}_i(t)+\bar{v}_i(t)\right|\left[p\left|x_i(t)-x_0(t)\right|+q\left|v_i(t)-v_0(t)\right|\right]\\
&\leq\sum_{i=1}^{n}\left|\bar{x}_i(t)+\bar{v}_i(t)\right|\left[p\left|\bar{x}_i(t)\right|+q\left|\bar{v}_i(t)\right|\right]\\
&=\sum_{i=1}^{n}\left[p\|\bar{x}_i(t)\|^2+(p+q)\bar{x}_i(t)\bar{v}_i(t)+q\|\bar{v}_i(t)\|^2\right]\\
&\leq\frac{3p+q}{2}\sum_{i=1}^{n}\|\bar{x}_i(t)\|^2+\frac{p+3q}{2}\sum_{i=1}^{n}\|\bar{v}_i(t)\|^2\\
&=\omega_1\sum_{i=1}^{n}\|\bar{x}_i(t)\|^2+\omega_2\sum_{i=1}^{n}\|\bar{v}_i(t)\|^2,
\end{aligned}\tag{25}$$

where $\omega_1=\frac{3p+q}{2}, \omega_2=\frac{p+3q}{2}$.

Remark 1. Many engineering systems operate within bounded-rate domains, such as robot swarms and unmanned aerial vehicle (UAV) formations constrained by actuator and sensor limits, as well as sensor networks whose state variables (e.g., temperature, voltage) evolve at restricted rates, leading naturally to locally Lipschitz dynamics. As noted in [15], the framework extends to local or piecewise Lipschitz continuity and broader input-to-state stability (ISS)-type conditions.

According to Lemma 2, we have $(\bar{x}(t) + \bar{v}(t))\,(d(t) - D\mathrm{sgn}\,(\bar{x}(t) + \bar{v}(t))) \leq 0$.

To handle the error term $-k\left(\bar{x}^{\mathrm{T}}(t) + \bar{v}^{\mathrm{T}}(t)\right)e(t)$, Lemma 4 $|xy| \leq \frac{\alpha}{2}x^2 + \frac{1}{2\alpha}y^2$ is applied, yielding:

$$\begin{aligned}
&-k\sum_{i=1}^{n}\left[\left(\bar{x}_i^{\mathrm{T}}(t) + \bar{v}_i^{\mathrm{T}}(t)\right)e_i(t)\right] \\
&\leq \frac{\alpha k}{2}\sum_{i=1}^{n}\left(\|\bar{x}_i(t)\|^2 + 2\,\|\bar{x}_i(t)\|\,\|\bar{v}_i(t)\| + \|\bar{v}_i(t)\|^2\right) + \frac{k}{2\alpha}\sum_{i=1}^{n}\|e_i(t)\|^2 \\
&\leq ak\sum_{i=1}^{n}\left(\|\bar{x}_i(t)\|^2 + \|\bar{v}_i(t)\|^2\right) + \frac{k}{2\alpha}\sum_{i=1}^{n}\|e_i(t)\|^2.
\end{aligned} \tag{26}$$

Therefore,

$$\begin{aligned}
\dot{V}(t) \leq{}& \sum_{i=1}^{n}\|\bar{v}_i(t)\|^2 - \lambda_{\min}\left(k(L+B)\otimes I_m\right)\sum_{i=1}^{n}\left(\|\bar{x}_i(t)\|^2 + \|\bar{v}_i(t)\|^2\right) \\
&+ \frac{k}{2}\sum_{i=1}^{n}\left(\|\bar{x}_i(t)\|^2 + \|\bar{v}_i(t)\|^2\right) + k(C_1C_2)^2 \\
&+ \omega_1\sum_{i=1}^{n}\|\bar{x}_i(t)\|^2 + \omega_2\sum_{i=1}^{n}\|\bar{v}_i(t)\|^2 \\
&+ ak\sum_{i=1}^{n}\left(\|\bar{x}_i(t)\|^2 + \|\bar{v}_i(t)\|^2\right) + \frac{k}{2\alpha}\sum_{i=1}^{n}\|e_i(t)\|^2 \\
&+ \left(\bar{x}^{\mathrm{T}}(t) + \bar{v}^{\mathrm{T}}(t)\right)\left[d(t) - D\mathrm{sgn}(\bar{x}^{\mathrm{T}}(t) + \bar{v}^{\mathrm{T}}(t))\right] \\
\leq{}& \left[\alpha k + \omega - \lambda_{\min}\left(k(L+B)\otimes I_m\right) + \frac{k}{2}\right]\sum_{i=1}^{n}\left(\|\bar{x}_i(t)\|^2 + \|\bar{v}_i(t)\|^2\right) \\
&+ k(C_1C_2)^2 + \frac{k}{2\alpha}\sum_{i=1}^{n}\|e_i(t)\|^2,
\end{aligned} \tag{27}$$

where $\omega = \max\{\omega_1, \omega_2 + 1\}$.

When the parameters satisfy

$$\begin{aligned}
&\alpha k + \omega - \lambda_{\min}\left(k(L+B)\otimes I_m\right) + \frac{k}{2} < 0 \\
&\sum_{i=1}^{n}\|e_i(t)\|^2 \leq \left[\frac{2\alpha}{k}\lambda_{\min}(k(L + B\otimes I_m) - \frac{2\alpha\omega}{k} - \alpha\,(2\alpha+1)\right] \\
&\sum_{i=1}^{n}\left(\|\bar{x}_i(t)\|^2 + \|\bar{v}_i(t)\|^2\right) - 2\alpha(C_1C_2)^2,
\end{aligned} \tag{28}$$

then

$$\begin{aligned}
&\dot{V}(t) \leq \frac{k}{2\alpha}\|e_i(t)\|^2 - \left[\lambda_{\min}(k(L + B\otimes I_m) - \omega - \alpha k - \frac{k}{2}\right] \\
&\sum_{i=1}^{n}\left(\|\bar{x}_i(t)\|^2 + \|\bar{v}_i(t)\|^2\right) + k(C_1C_2)^2 \leq 0.
\end{aligned} \tag{29}$$

□

The proof of the Zeno phenomenon is provided in the following.

Theorem 2. *Consider the MAS described by Eqs* (1) *and* (2). *If the reset event-triggered condition* (13) *and the condition of Theorem 1 are satisfied, the Zeno phenomenon can be avoided. In this case, there exists a positive minimum trigger interval* $\Delta t_{\min}$ *so that the interval between the two consecutive trigger moments for any agent* r *satisfies* $t_{k+1}^r - t_k^r \geq \Delta t_{min} > 0$. *The minimum trigger interval* $\Delta t_{\min}$ *is:*

$$\Delta t_{\min} = \tau_r = \sqrt{\frac{\Upsilon_1 - \Upsilon_2 + \eta_{\max}}{\gamma^2}}, \tag{30}$$

where $\Upsilon_1 = \left[\frac{2a}{k}\lambda_{\min}\left(k\left(L+B\right)\otimes I_m\right) - \frac{2a\omega}{k} - \alpha\left(2\alpha+1\right)\right]\Omega_{\max}$, $\Upsilon_2 = 2\alpha(C_1C_2)^2$.

Proof. Assume that the rate of change of the state error is bounded: $\|\dot{\Delta}_i(t)\| \leq \gamma\ (\gamma > 0)$. Integrate the state error and obtain

$$\|e_i(t)\| = \|\Delta_i(t_k) - \Delta_i(t)\| \leq \gamma(t - t_k^i). \tag{31}$$

When the reset event-triggered condition is satisfied, the above equation can be rewritten as follows:

$$\begin{aligned}\gamma^2(t-t_k^i)^2 > &\left[\frac{2a}{k}\lambda_{\min}\left(k\left(L+B\right)\otimes I_m\right) - \frac{2a\omega}{k} - \alpha\left(2\alpha+1\right)\right]\Omega(t)\\ &- 2\alpha(C_1C_2)^2 + \eta_i(t).\end{aligned} \tag{32}$$

According to Theorem 1, the above equation satisfies the system consensus condition, $\Omega(t)$ is bounded, there is $\Omega_{\max} > 0$ such that $\Omega(t) \leq \Omega_{\max}$, and when $\Omega(t) \geq \epsilon$, $\eta_i(t) = e^{-\alpha t} \leq \eta_{\max} = \eta_i(0)$.

Accordingly, there exists at least a minimum event-trigger τ_r for agent r to satisfy

$$\gamma^2{\tau_r}^2 > \left[\frac{2a}{k}\lambda_{\min}\left(k\left(L+B\right)\otimes I_m\right) - \frac{2a\omega}{k} - \alpha\left(2\alpha+1\right)\right]\Omega_{\max} - 2\alpha(C_1C_2)^2 + \eta_{\max}. \tag{33}$$

The minimum trigger interval satisfies

$$\Delta t_r^k > \sqrt{\frac{\Upsilon_1 - \Upsilon_2 + \eta_{\max}}{\gamma^2}} \triangleq \tau_r > 0. \tag{34}$$

The time interval between any two triggering instants satisfies $\Delta t_r^k > \Delta t_{min} > 0$. Therefore, the minimum event-trigger interval is strictly greater than zero, and no Zeno phenomenon occurs.

Remark 2. Unlike traditional dynamic event-triggered mechanisms, which typically require a trade-off between reducing triggering frequency and preserving system-dynamic performance, the proposed reset-based triggering strategy can dynamically adjust the triggering conditions while effectively reducing the number of communications. More importantly, the proposed method achieves a lower triggering frequency without compromising convergence performance, and the Zeno behavior is also effectively avoided.

4. Simulation

This section validates the effectiveness of the proposed reset event-triggered consensus algorithm through simulation experiments. A MAS with one leader and four followers is considered. The system dynamics of the leader and the follower are described by Eqs (1) and (2), respectively, and the communication topology is shown in Fig. 1.

The nonlinearity function and the external disturbance of agent i are $(2v_i(t)) + 0.01x_i(t)$ and $d_i(t) = 0.1\cos x_i(t)$, respectively. From the communications topology of Fig. 1, the Laplacian matrix L, the leader–follower matrix B, and the adjacency matrix A are:

$$L = \begin{bmatrix} 1 & -1 & 0 & 0 \\ -1 & 1 & 0 & 0 \\ 0 & 0 & 1 & -1 \\ 0 & 0 & -1 & 1 \end{bmatrix},\quad B = \begin{bmatrix} 1 & 0 & 0 & 0 \\ 0 & 0 & 0 & 0 \\ 0 & 0 & 1 & 0 \\ 0 & 0 & 0 & 0 \end{bmatrix},\quad A = \begin{bmatrix} 0 & 1 & 0 & 0 \\ 1 & 0 & 0 & 0 \\ 0 & 0 & 0 & 1 \\ 0 & 0 & 1 & 0 \end{bmatrix}.$$

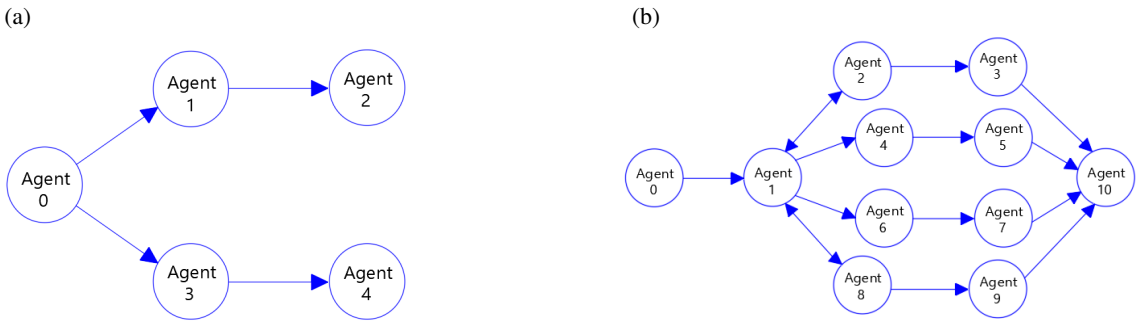

Fig. 1. System communication topology: 5-agent communication topology (a) and 11-agent communication topology (b).

The initial position and speed of the leader agent are set to $x_0(0) = 6$, $v_0(0) = 3$, and $v_0(0) = 3$, respectively. The initial position and speed of the leader agent are set to $x(0) = [-6 \quad 1 \quad 0.5 \quad -3.5]$ and $v(0) = [-5.1 \quad -1 \quad 3.2 \quad 4.5]$. According to the condition (26), choose $\varepsilon = 0.1$, $k = 1$. It can be derived from the Laplacian matrix that $\lambda_{\min}\left(k(L+B) \otimes I_m\right) \approx 0.382$. According to Eq. (14), $0 < \alpha < 1.6$. Therefore, we set $\alpha = 1$. The experimental results are shown in Figs 2–6. Figure 2a shows the system state convergence curves, and Fig. 2b presents the control inputs and triggering moments for $\eta_i(0) = 0$. Under the action of the controller (7), the speed and position of the agent gradually converge to a uniform state. Figure 2b shows the corresponding triggering moments, where agents 1–4 triggered 1053, 918, 753, and 1588 times, respectively.

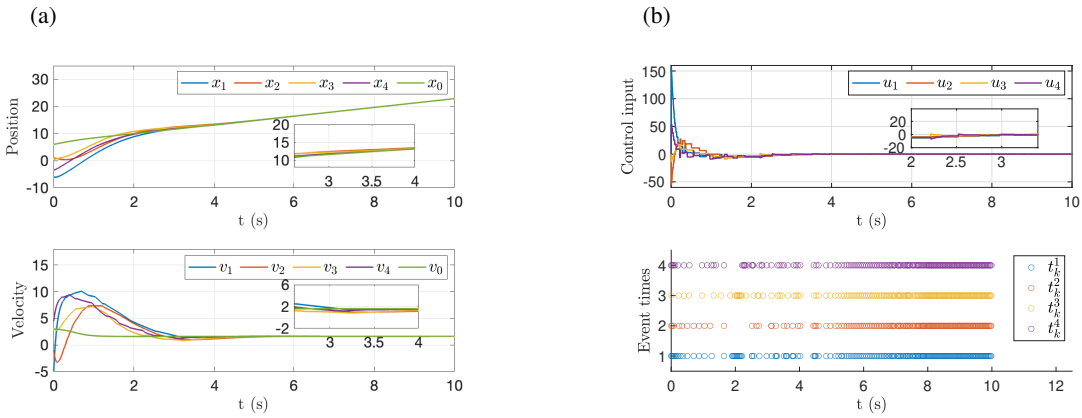

Fig. 2. Performance of 5 agents under static event-triggered control (SETC): system state convergence curves (a), control inputs $u_i(t)$ and triggering moments t_k (b).

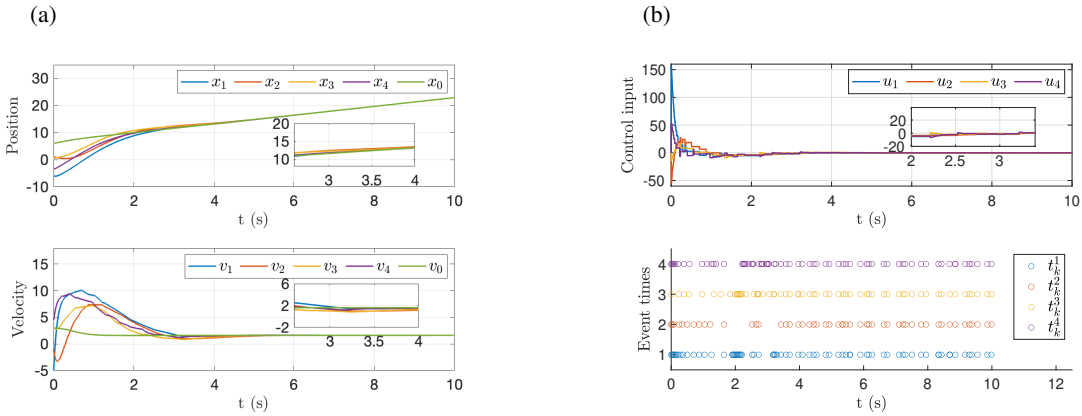

Fig. 3. Performance of 5 agents under reset event-triggered control (RETC): system state convergence curves (a), control inputs $u_i(t)$ and triggering moments t_k (b).

Let $\eta_i(0) = 0.01$, while keeping all other control parameters unchanged. The experimental results are presented in Fig. 3a,b. It can be observed that the number of triggering events is significantly reduced without compromising the original control performance. Specifically, agents 1–4 triggered 438, 180, 279, and 508 times, respectively.

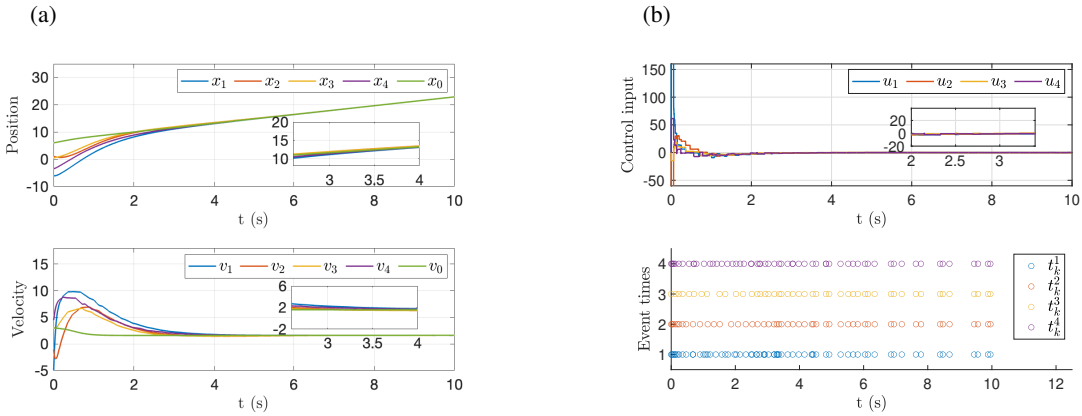

Fig. 4. Performance of 5 agents under RETC: system state convergence curves (a), control inputs $u_i(t)$ and triggering moments t_k (b).

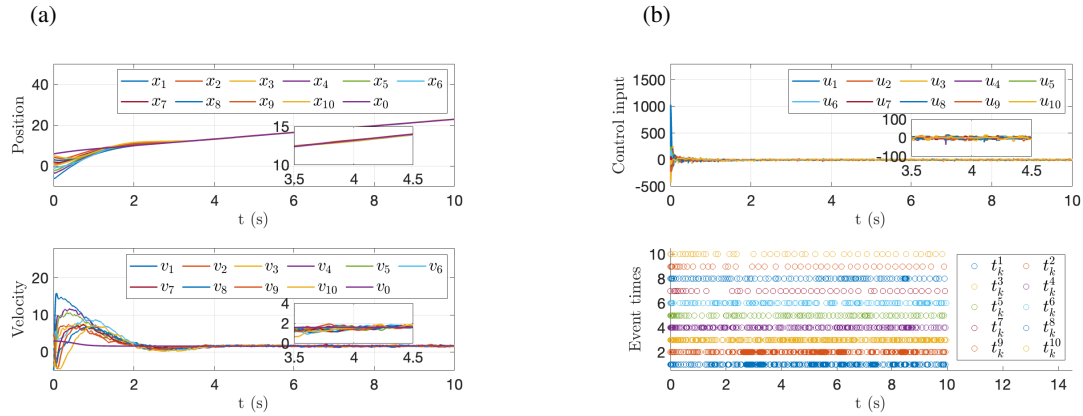

Fig. 5. Performance of 11 agents under SETC: system state convergence curves (a), control inputs $u_i(t)$ and triggering moments t_k (b).

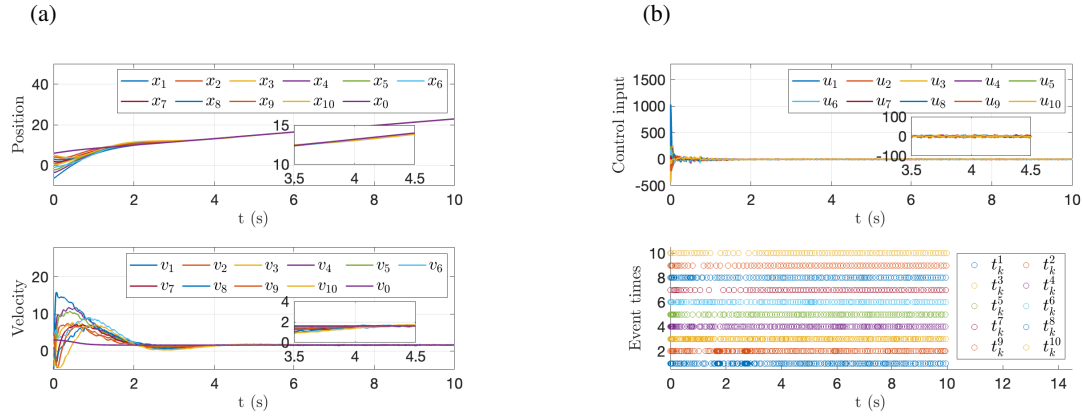

Fig. 6. Performance of 11 agents under RETC: system state convergence curves (a), control inputs $u_i(t)$ and triggering moments t_k (b).

Table 1 compares the distinction in the number of triggers between the proposed method and the general method in detail. Specifically, RETC represents the method proposed in this paper, while SETC denotes the conventional triggering approach without dynamic reset strategies. Figure 4b shows that the proposed method has a significant effect on reducing the number of triggers after the system state converges. When $\eta_i(0) = 0$, agents 1–4 trigger 670, 788, 546, and 1272 times, respectively, during 5–10 s. When $\eta_i(0) = 0.01$, the numbers are 207, 68, 80, and 244, respectively.

Table 1. Comparison of the number of triggers between RETC and SETC for 5 agents. Only follower agents are counted; the leader does not trigger events

Agent	1	2	3	4	Total
RETC	438	180	279	508	1405
SETC	1053	918	753	1588	4312

Table 2. Comparison of the number of triggers between RETC and SETC for 11 agents. Only follower agents are counted; the leader does not trigger events

Agent	1	2	3	4	5	6	7	8	9	10	Total
RETC	358	341	398	227	125	162	85	157	94	85	2032
SETC	1266	1219	959	525	146	318	43	186	48	45	4755

By using the reset event-triggering strategy proposed in this paper, the number of triggering decreases by 19.6% in the period of 0–5 s, 82.2% in the period of 5–10 s, and 67.4% in the whole period.

The issue of frequent triggering of event-triggering laws in the later stage of system convergence has been resolved. The occupation of communication resources has been greatly reduced. This is very important in large-scale clusters and complex environments.

After that, take $\alpha = 11/7$. The experimental results are shown in Fig. 4. With the increase of α, the convergence speed of the system is accelerated. At the same time, it can be seen from the triggering moments that the agents' triggering moments are asynchronous. The effectiveness of the distributed event-triggered mechanism has been verified.

Similarly, the simulation for the 11-agent topology is conducted under both SETC and RETC. The results presented in Figs 5 and 6 show that the proposed reset event-triggered mechanism significantly reduces the number of triggers, effectively minimizing communication overhead. The detailed comparison for 11 agents is provided in Table 2.

5. Conclusion

The consensus problem of second-order nonlinear multi-agent systems (MASs) under directed topology is investigated based on a reset event-triggered mechanism. A hybrid control strategy combining dynamic event triggering and reset control is introduced, where the event-triggering conditions and the initial values of external dynamic variables are constructed from the state information of each agent and its neighbors at the triggering instants. By tuning the interaction strength parameters of the system, it is determined when the dynamic variables should be reset to their initial values, thereby effectively reducing the triggering frequency as the system approaches consensus. The asymptotic stability of the closed-loop system and the exclusion of the Zeno behavior are rigorously established using the Lyapunov stability theory. Numerical simulations under external disturbances are conducted, with comparisons to the event-triggered methods in [5] and [6]. The results confirm the effectiveness of the proposed reset event-triggered mechanism and demonstrate its superiority in reducing communication burden.

Data availability statement

Data sharing is not applicable to this article as no new data were created or analyzed in this study.

Acknowledgments

This work was supported by the National Natural Science Foundation of China under grant No. 62103057. The publication costs of this article were partially covered by the Estonian Academy of Sciences.

References

1. Amirkhani, A. and Barshooi, A. H. Consensus in multi-agent systems: a review. *Artificial Intelligence Review*, 2022, **55**(5), 3897–3935. https://doi.org/10.1007/s10462-021-10097-x
2. Chen, X., Sun, Q., Yu, H. and Hao, F. Predefined-time practical consensus for multi-agent systems via event-triggered control. *Journal of the Franklin Institute*, 2023, **360**(3), 2116–2132. https://doi.org/10.1016/j.jfranklin.2023.01.001
3. Chen, X., Yu, H. and Hao, F. Prescribed-time event-triggered bipartite consensus of multiagent systems. *IEEE Transactions on Cybernetics*, 2022, **52**(4), 2589–2598. https://doi.org/10.1109/TCYB.2020.3004572

4. Deng, C., Wen, C., Huang, J., Zhang, X.-M. and Zou, Y. Distributed observer-based cooperative control approach for uncertain nonlinear MASs under event-triggered communication. *IEEE Transactions on Automatic Control*, 2022, **67**(5), 2669–2676. https://doi.org/10.1109/TAC.2021.3090739
5. Ding, L., Han, Q.-L., Ge, X. and Zhang, X.-M. An overview of recent advances in event-triggered consensus of multiagent systems. *IEEE Transactions on Cybernetics*, 2018, **48**(4), 1110–1123. https://doi.org/10.1109/TCYB.2017.2771560
6. Ding, L., Han, Q.-L. and Zhang, X.-M. Distributed secondary control for active power sharing and frequency regulation in islanded microgrids using an event-triggered communication mechanism. *IEEE Transactions on Industrial Informatics*, 2019, **15**(7), 3910–3922. https://doi.org/10.1109/TII.2018.2884494
7. El Moufid, M., Nadir, Y., Benhadou, S. and Medromi, H. An architecture of an interactive multimodal urban mobility system. *International Journal for Simulation and Multidisciplinary Design Optimization*, 2019, **10**, A13. https://doi.org/10.1051/smdo/2019015
8. Fu, J., Wen, G., Yu, W. and Ding, Z. Finite-time consensus for second-order multi-agent systems with input saturation. *IEEE Transactions on Circuits and Systems II: Express Briefs*, 2017, **65**(11), 1758–1762. https://doi.org/10.1109/TCSII.2017.2759193
9. Ge, X. and Han, Q.-L. Distributed formation control of networked multi-agent systems using a dynamic event-triggered communication mechanism. *IEEE Transactions on Industrial Electronics*, 2017, **64**(10), 8118–8127. https://doi.org/10.1109/TIE.2017.2701778
10. Ge, X., Han, Q.-L., Zhang, X.-M. and Ding, D. Dynamic event-triggered control and estimation: a survey. *International Journal of Automation and Computing*, 2021, **18**(6), 857–886. https://doi.org/10.1007/s11633-021-1306-z
11. Griparic, K., Polic, M., Krizmancic, M. and Bogdan, S. Consensus-based distributed connectivity control in multi-agent systems. *IEEE Transactions on Network Science and Engineering*, 2022, **9**(3), 1264–1281. https://doi.org/10.1109/TNSE.2021.3139045
12. Hu, L., Wang, D. and Qiao, J. Static/dynamic event-triggered learning control for constrained nonlinear systems. *Nonlinear Dynamics*, 2024, **112**(16), 14159–14174. https://doi.org/10.1007/s11071-024-09778-3
13. Iqbal, M., Kolios, P. and Polycarpou, M. M. Finite-and fixed-time consensus protocols for multi-agent systems with time-varying topologies. *IEEE Control Systems Letters*, 2022, **6**, 1568–1573. https://doi.org/10.1109/LCSYS.2021.3124938
14. Li, X., Liu, J.-C. and Li, X.-G. Consensus of first-order discrete-time multi-agent systems with time delays. *Journal of the Franklin Institute*, 2019, **356**(10), 5315–5331. https://doi.org/10.1016/j.jfranklin.2018.11.052
15. Liang, W., Niu, X., Lan, Y. and Fang, W. Event-triggered consensus of second-order time-delayed nonlinear multi-agent systems. *Journal of Systems Science and Mathematical Sciences*, 2024, **44**(07), 1841–1852 (in Chinese). https://doi.org/10.12341/jssms23448
16. Liu, J., Shi, J., Wu, Y., Wang, X., Sun, J. and Sun, C. Event-based predefined-time second-order practical consensus with application to connected automated vehicles. *IEEE Transactions on Intelligent Vehicles*, 2023, **8**(11), 4524–4535. https://doi.org/10.1109/TIV.2023.3306802
17. Liu, T., Sheng, A., Qi, G. and Li, Y. Leader-following consensus of singular nonlinear multi-agent systems with unknown external disturbances. In *40th Chinese Control Conference (CCC), Shanghai, China, 26–28 July 2021*. IEEE, 2021, 5217–5221. https://doi.org/10.23919/CCC52363.2021.9550732
18. Lizzio, F. F., Capello, E. and Guglieri, G. A review of consensus-based multi-agent UAV implementations. *Journal of Intelligent Robotic Systems*, 2022, **106**(2), 43. https://doi.org/10.1007/s10846-022-01743-9
19. Mahela, O. P., Khosravy, M., Gupta, N., Khan, B., Alhelou, H. H. and Mahla, R. Comprehensive overview of multi-agent systems for controlling smart grids. *CSEE Journal of Power and Energy Systems*, 2020, **8**(1), 115–131.
20. Qin, J., Ma, Q., Shi, Y. and Wang, L. Recent advances in consensus of multi-agent systems: a brief survey. *IEEE Transactions on Industrial Electronics*, 2017, **64**(6), 4972–4983. https://doi.org/10.1109/TIE.2016.2636810
21. Ruan, X., Feng, J., Xu, C. and Wang, J. Observer-based dynamic event-triggered strategies for leader-following consensus of multi-agent systems with disturbances. *IEEE Transactions on Network Science and Engineering*, 2020, **7**(4), 3148–3158. https://doi.org/10.1109/TNSE.2020.3017493
22. Vecliuc, D.-D. Brief survey on collaborative and non-collaborative behaviors in multi-agent systems. *Bulletin of the Polytechnic Institute of Iași, Electrical Engineering, Power Engineering, Electronics Section*, 2023, **69**(4), 31–43. https://doi.org/10.2478/bipie-2023-0020
23. Wang, L. and Dong, J. Reset event-triggered adaptive fuzzy consensus for nonlinear fractional-order multiagent systems with actuator faults. *IEEE Transactions on Cybernetics*, 2023, **53**(3), 1868–1879. https://doi.org/10.1109/TCYB.2022.3163528
24. Xiao-Tong, S., Ge, G. and Peng-Fei, Z. Fixed-time consensus tracking of multi-agent systems under unmatched disturbances. *Acta Automatica Sinica*, 2020, **12**(9), 1–9 (in Chinese). https://doi.org/10.16383/j.aas.c190339
25. Zhao, G., Hua, C. and Guan, X. Reset control for consensus of multiagent systems with event-triggered communication. *IEEE Transactions on Cybernetics*, 2021, **51**(11), 5387–5396. https://doi.org/10.1109/TCYB.2019.2956491
26. Zhao, G., Hua, C. and Guan, X. Reset observer-based Zeno-free dynamic event-triggered control approach to consensus of multiagent systems with disturbances. *IEEE Transactions on Cybernetics*, 2022, **52**(4), 2329–2339. https://doi.org/10.1109/TCYB.2020.3003330
27. Zhu, Z., Du, Q., Wang, Z. and Li, G. A survey of multi-agent cross domain cooperative perception. *Electronics*, 2022, **11**(7), 1091. https://doi.org/10.3390/electronics11071091

Jaotatud konsensus teist järku multiagent-süsteemide jaoks lähtestusega sündmuspõhise mehhanismi baasil

Yi Cheng ja Xingjian Fu

Uuritud on teist järku mittelineaarsete multiagent-süsteemide konsensusprobleemi suunatud topoloogia korral, tuginedes lähtestusega sündmuspõhisele mehhanismile. Kasutusele on võetud hübriidne juhtimisstrateegia, mis ühendab dünaamilise sündmuspõhise käivitamise ja lähtestusjuhtimise. Sündmuste käivitamise tingimused ja väliste dünaamiliste muutujate algväärtused konstrueeritakse iga agendi ja tema naabrite seisunditeabe põhjal käivitamishetkedel. Süsteemi interaktsioonitugevuse parameetrite konfigureerimisega määratakse kindlaks, millal dünaamilised muutujad tuleks lähtestada algväärtustega, vähendades seeläbi käivitamissagedust süsteemi konsensuse poole liikumisel. Ljapunovi stabiilsusteooria abil on rangelt tõestatud suletud ahelaga süsteemi asümptootiline stabiilsus ning Zeno-käitumise välistamine. Läbi on viidud numbrilised simulatsioonid väliste häiringute korral ning tulemusi on võrreldud töödes [5] ja [6] esitatud sündmuspõhiste meetoditega. Tulemused kinnitavad pakutud lähtestusega sündmuspõhise mehhanismi tõhusust ja näitavad selle eeliseid kommunikatsioonikoormuse vähendamisel.

Proceedings of the Estonian Academy of Sciences
2026, **75**, 1, 47–55

https://doi.org/10.3176/proc.2026.1.05

www.eap.ee/proceedings
Estonian Academy Publishers

BLACKCURRANT GENOTYPES, FATTY ACID PROFILE

RESEARCH ARTICLE

Received 19 May 2025
Accepted 9 September 2025
Available online 2 February 2026

Keywords:
blackcurrant, berry weight, seed composition, essential fatty acids

Corresponding author:
Ave Kikas
ave.kikas@emu.ee

Citation:
Sarv, V., Rätsep, R., Malbe, M., Kaldmäe, H., Kuusik, S., Raudsepp, P. et al. 2026. Evaluation of seed content and fatty acid profile in blackcurrant (*Ribes nigrum* L.) genotypes. *Proceedings of the Estonian Academy of Sciences*, **75**(1), 47–55. https://doi.org/10.3176/proc.2026.1.05

Evaluation of seed content and fatty acid profile in blackcurrant (*Ribes nigrum* L.) genotypes

Viive Sarv[a], Reelika Rätsep[a,b], Marge Malbe[a], Hedi Kaldmäe[a], Sirje Kuusik[b], Piret Raudsepp[b], Asta-Virve Libek[a] and Ave Kikas[a]

[a] Polli Horticultural Research Centre, Chair of Horticulture, Institute of Agricultural and Environmental Sciences, Estonian University of Life Sciences, Uus 2, 69108 Polli, Estonia

[b] Institute of Veterinary Medicine and Animal Sciences, Estonian University of Life Sciences, F. R. Kreutzwaldi 62, 51006 Tartu, Estonia

ABSTRACT

Twenty-two blackcurrant genotypes, 'Karri', 'Almo', 'Ats', 'Elo', 'Varmas', 'Mairi', 'Asker', 'Pilėnai', 'Vyčiai', 'Ben Alder', 'Ben Nevis', 'Ben Lomond', 'Ben Sarek', 'Intercontinental', 'Titania', 'Öjebyn', 'Ļentjai', 'Pamyati Vavilova', 'Zagadka', 10B, 1-96-16, and 2-96-51, were evaluated in two subsequent years. The aim of the research was to compare berry weight, seed content in the berries, and fatty acid profile in the seeds. The composition of fatty acids was identified and quantified using gas chromatography.

Blackcurrant berry weight varied between 1.0 and 1.7 g, depending on the genotype, being the highest in genotypes 'Mairi', 'Karri', 'Intercontinental', and 'Ļentjai'. Seed content in berries ranged from 2.2% to 4.6% and was the highest in 'Karri' and 'Elo'. Oil content correlated positively with the proportion of seeds per fresh weight of berries. Therefore, the highest seed content correlated with the highest oil content per fresh weight of berries in 'Karri' and 'Elo', 1.2% and 1.3%, respectively. On average over two years, the total oil content in the seeds ranged from 24.4% to 31.2%, showing the highest levels in 'Ben Nevis', 'Pamyati Vavilova', and 'Asker'. The most abundant fatty acid identified in blackcurrant seeds was linoleic acid, ranging from 40.1% to 48.6%, followed by α-linolenic acid, from 11.7% to 16.5%, oleic acid, from 10.3% to 16.4%, and γ-linolenic acid, from 10.9% to 15.6%.

Introduction

A European Commission document (2023) titled 'Upgrading the EU's policy toolbox for nutrition leadership' highlights the necessity of utilizing renewable resources (Dekeyser and Rampa 2023). Plant-based biomass, such as berry pomace, represents renewable resources of biological origin. This biomass, rich in bioactive substances, is produced in substantial quantities during juice production. Berry seed oils constitute a noteworthy group of plant oils with favourable nutritional characteristics, including a beneficial fatty acid (FA) profile, oxidative stability, and positive health effects. These oils are suitable for human consumption and, as such, may have potential applications in the food industry (Sławińska et al. 2023). Furthermore, previous studies have demonstrated that the composition of fruit pomace seed oil remains stable even after long-term frozen storage, making pomace a valuable raw material for oil extraction (Radocaj et al. 2014). Plant-derived FAs are of considerable dietary and cosmetic significance due to their high content of polyunsaturated FAs (PUFAs) as well as saturated and monounsaturated FAs (MUFAs). These FAs exhibit variation in the cis–trans isomerism, chain length, and the position of the first double bond. Nutritionally, FAs can be categorized into essential and non-essential types. While humans and animals lack the enzymatic capacity to synthesize essential FAs (EFAs) such as linoleic acid (LA; C18:2 n-6), α-linolenic acid (ALA; C18:3 n-3), and γ-linolenic acid (GLA; C18:3) from oleic acid (OA; C18:1 n-9) due to the absence of required desaturases, higher plants are capable of synthesizing LA, ALA, and GLA. Given their crucial role in human health, EFAs must be obtained through diet. EFAs are essential for cellular growth and brain function (Chauhan et al. 2023) and have therapeutic effects in preventing and managing diseases such as arthritis, cardio-

vascular and inflammatory diseases, cancer, and hyperlipidemia (Kuhnt et al. 2012; Omachi et al. 2024).

Omega-3 (n-3) and omega-6 (n-6) FAs serve as precursors for eicosanoids, lipid-based signalling molecules vital for innate immune responses (Sheppe and Edelmann 2021). The optimal ratio of n-6 to n-3 FAs (ranging from 2.5:1 to 4:1) is important in human nutrition. However, contemporary diets often contain an excess of n-6 FAs and a deficiency in n-3 FAs, disrupting this balance. In European countries, the n-6 to n-3 ratio is approximately 20:1, while in the United States, it reaches as high as 30:1. Therefore, it is essential to ensure a sufficient intake of n-3 FAs, while limiting the consumption of oils rich in n-6 FAs (Michalak and Kiełtyka-Dadasiewicz 2018).

Several studies have demonstrated that oils derived from fruit seeds play a significant role in health promotion by slowing the aging process and reducing stress (Beattie et al. 2005; Pieszka et al. 2013; Michalak and Kiełtyka-Dadasiewicz 2018). However, the mean intake of fruits and berries in Nordic and Baltic countries is between 100 and 200 grams per day (Rosell and Fadnes 2024), which is below the recommended level for sufficient consumption. For instance, in Estonia, the recommended daily intake of fruits and berries is at least 240 grams, as outlined by the National Institute of Health Development (Tervise Arengu Instituut 2025).

Additionally, fruit seed oils could be incorporated into cosmetic formulations due to their beneficial effects on the skin. For example, the sea buckthorn seed oil has shown the ability to improve skin hydration, protect against transdermal water loss, facilitate the transport of other oil components through the skin, and allow them to reach different layers of the epidermis. Furthermore, its radical-scavenging activity helps to protect the skin from oxidative damage and slow the aging process, thus making it a common ingredient in anti-wrinkle and anti-aging cosmetic products (Sławińska et al. 2023). Hendawy et al. (2021) found that the consumption of raspberry seed oil, which has an optimal n-6 to n-3 FA ratio (2–3:1), improved hepatic enzyme activities, reduced glucose levels, and mitigated insulin resistance by improving inflammatory and oxidative stress markers. Similarly, Pieszka et al. (2015a, 2015b) reported low n-6/n-3 ratios in chokeberry and blackcurrant seed oils, 1.45 and 2.61, respectively, and Konopka et al. (2023) claimed the recommended n-6/n-3 FA ratio (below 4–5:1) for seed oils of blackberry, blackcurrant, blueberry, raspberry, and strawberry. In addition, the inclusion of strawberry seed oil in the diet normalized lipid metabolism and affected metabolite formation in the distal intestine of Wistar rats (Hendawy et al. 2021). Interestingly, the evaluation of 16 rowanberry genotypes showed considerable variation in the n-6/n-3 ratio within *Sorbus aucuparia*, ranging from 6.70 to 25.19 (Sarv et al. 2024). Šavikin et al. (2013) reported that various *Ribes* species are recognized as potential sources of high-value FAs, particularly ALA, GLA (18:3 n-6), and stearidonic acid (SDA).

Blackcurrant (*Ribes nigrum* L.) is one of the most appreciated berry crops for fresh consumption and processing after strawberry cultivated in Estonia. Blackcurrant has also high importance in many other countries, such as Scotland, Sweden, Lithuania, Latvia, and Russia, as a number of valuable cultivars have been bred in these countries. Fruit weight and nutritional value of the blackcurrant fruit depend primarily on the genotype but also on the temperatures during fruit ripening (Kahu et al. 2009; Kaldmäe et al. 2013; Kikas et al. 2017). The value of blackcurrant fruits, buds, and leaves has been demonstrated (Tabart et al. 2006), but the trend of using fruit seeds has increased. More precise data on their nutritional composition would allow for a better understanding of their role in diet as well as their potential health benefits. This, in turn, could have a significant impact on environmental sustainability by reducing waste and promoting resource efficiency. During juice production, a huge amount of valuable residues remain, including seeds, which contain approximately 20% oil that is rich in PUFAs (Wójciak et al. 2022) and tocopherols (Šavikin et al. 2013; Pieszka et al. 2015a; Pieszka et al. 2015b; Basegmez et al. 2017). In addition to GLA (18:3 n-6), blackcurrant oil contains significant amounts of other nutritionally important FAs, such as ALA and SDA (18:4 n-3) (Yang et al. 2011; Šavikin et al. 2013). Furthermore, the oil has a beneficial n-6/n-3 ratio of 3–4:1 (Wójciak et al. 2022). The study of Gustinelli et al. (2018) showed that the seed oil of blackcurrant possessed stronger antioxidant activity as well as a higher content of vitamin E and carotenoids than the seed oils of cloudberry and bilberry. Although several studies have reported data on the FA composition of blackcurrants, significant variability exists, influenced by the climatic conditions and place of growth but particularly by the parents of the berries in the pedigree due to their genetic predisposition (Goffman and Galletti 2001; Ruiz del Castillo et al. 2002; Šavikin et al. 2013; Flores and Ruiz del Castillo 2016). For instance, the content of GLA in blackcurrant seed oils has varied from 11% to 24%, depending on the cultivar (Ruiz del Castillo and Dobson 2002; Jurgoński et al. 2018). The earlier study of Šavikin (2013) revealed that cluster analysis based on the seed oil FA profiles could be a good method for distinguishing the origin of blackcurrant genotypes. Detailed data on the chemical composition of blackcurrant genotypes would allow for a better understanding of their role in nutrition as well as their potential health benefits. Therefore, the aim of our study was to compare the seed content and FA composition of 22 blackcurrant genotypes cultivated in Estonia.

Materials and methods

Plant material for experiments

The research was carried out at the Polli Horticultural Research Centre (58° 7′ N, 25° 32′ E) of the Estonian University of Life Sciences. The soil type in the trial area was a sandy loam, containing 1.6% humus, and the preceding crop was cereal (rye and barley). The genotypes ‘Karri’, ‘Almo’, ‘Ats’, ‘Elo’, ‘Varmas’, ‘Mairi’, ‘Asker’, ‘Pilėnai’, ‘Vyčiai’, ‘Ben Alder’, ‘Ben Nevis’, ‘Ben Lomond’, ‘Ben Sarek’,

'Intercontinental', 'Titania', 'Öjebyn', 'Ļentjai', 'Pamyati Vavilova', 'Zagadka', 10B, 1-96-16, and 2-96-51 were chosen for evaluation. Berry samples (500 g) of the 22 genotypes were hand-picked in the middle of the harvest season in two consecutive years from a test plot established six to seven years earlier. The lineage of the genotypes selected for the study is shown in the pedigree Table 1. The genotypes included in the study originated from six countries: Estonia (10 genotypes), Scotland (4), Sweden (3), Russia (2), Belarus (1), and Lithuania (2).

The average berry weight was determined by weighing 20 fruits per sample. The seeds were separated from 100 g of berries by sieving and, thereafter, the seed percentage in fruit was calculated.

Seed oil extraction

The seed oil content was analysed using AOAC Method 948.22. The oil was extracted from the sample using petroleum ether as a solvent in a Soxhlet apparatus for 12 hours. After extraction, the residues were dried in an oven at 105 °C until they reached a constant weight. The oil content was expressed as a percentage of the dry weight, either per seed or per fruit.

Determination of fatty acids

For determining the FA composition, berries were crushed in water (1:1), and seeds were separated from pulp by washing and sieving. FAs of seeds were extracted and methylated by a one-step procedure using toluene as a solvent (Sukhija and Palmquist 1988). Methyl heptadecanoate (C17:0) was used as an internal standard. FA methyl esters were quantified by gas chromatography using an Agilent 6890A gas chromatograph (Agilent Technologies Inc., USA) equipped with an autosampler, under the following conditions: a 100 m × 0.25 mm CP7420 capillary column with a 0.25 µm film thickness. Helium was used as the carrier gas. The initial oven temperature was 70 °C, which was held for 1 min, and then it was increased to 100 °C at a rate of 5 °C/min and held for 2 min. The oven temperature was increased to 165 °C at a rate of 10 °C/min and held for 55 min. Then the oven temperature was increased to 180 °C at a rate of 2 °C/min and held for 20 min. Further, it was increased to 225 °C at a rate of 5 °C/min and held for 20 min. Finally, the oven temperature was increased to 240 °C at a rate of 5 °C/min and held for 5 min. The injector and detector were at 250 °C. A constant carrier gas pressure was 23 psi. The identification of common FAs was accomplished by comparing sample

Table 1. Pedigree of 22 blackcurrant genotypes

Genotype	Pedigree	Country
10B	Öjebyn × Kantata 50	Estonia
1-96-16	Elo × Öjebyn	Estonia
2-96-51	Pamyati Vavilova × Ļentjai	Estonia
Almo	Kantata 50 × Öjebyn	Estonia
Asker	Pamyati Vavilova × Öjebyn	Estonia
Ats	Öjebyn × Varmas	Estonia
Ben Alder	Ben More × Ben Lomond	Scotland
Ben Lomond	(Brödtorp × Janslunda) × (Consort × Magnus)	Scotland
Ben Nevis	(Brödtorp × Janslunda) × (Consort × Magnus)	Scotland
Ben Sarek	Seedling (Goliath × Öjebyn) free pollination	Scotland
Elo	Öjebyn × Kantata 50	Estonia
Intercontinental	Ri74020-11 × Titania	Sweden
Karri	Mulgi must × Kantata 50	Estonia
Ļentjai	Brödtorp × Minaj Shmyriov	Russia
Mairi	Öjebyn × Kantata 50	Estonia
Pamyati Vavilova	Paulinka × Belorusskaya Sladkaya	Belarus
Pilėnai	Minaj Shmyriov × Öjebyn	Lithuania
Zagadka	Niina × Sopernik	Russia
Titania	Altaiskaya dessertnaya × (Consort × Kajaanin Musta)	Sweden
Varmas	Albos × Uus must	Estonia
Vyčiai	Minaj Shmyriov free pollination	Lithuania
Öjebyn	unknown	Sweden

peak retention times with FA methyl ester standard mixtures (Supelco 37 Component FAME Mix, Nu-Chek Prep GLC 603, 408, using Agilent Technologies ChemStation software). Results for all FAs were expressed as g/100 g of the total FA or g/100 g sample.

Statistical analysis

Statistical analysis was performed using Statistica 13.0 (StatSoft Inc., USA). Correlation analysis was used in order to determine relationships among analysed and measured traits in the 22 blackcurrant genotypes ($p < 0.05$, $N = 22$). A single-linkage Euclidean distance cluster analysis (Sibson 1973) was performed for individual FAs (percentage of the total FAs in seeds) of the 22 blackcurrant genotypes. Average fruit weight (g), seeds per fruit (%), and FAs per fruit and in seeds (%) in tables are presented as mean ± standard deviation.

Results and discussion

Blackcurrant berry weight and seed content

In the current study, the variations in berry weight and seed content were observed across different blackcurrant (*Ribes nigrum* L.) genotypes. The berry weight varied between 1.0 and 1.7 g, being the highest in the genotype 'Mairi' (1.7 g), followed by the similar weight of 'Karri' (1.6 g), 'Intercontinental' (1.6 g), and 'Ļentjai' (1.6 g) (Table 2). These values were consistent with earlier experiments (Libek and Kikas 2002; Kaldmäe et al. 2013; Kikas et al. 2017), where similar fruit weight results were obtained for the same genotypes, 'Mairi', 'Karri', 'Intercontinental', and 'Ļentjai', ranging from 1.3–1.6 g, 1.4–1.8 g, 1.5–1.8 g, and 1.7 g, respectively, in different studies.

In this study, the seed content in the fruit of the 22 genotypes ranged from 2.2% to 4.6%, being the highest in the genotypes 'Karri' and 'Elo', 4.6 % and 4.5 %, respectively (Table 2). The highest seed content in 'Karri' and 'Elo' corresponded to their highest oil concentration per fruit, 1.2 % and 1.3 %, respectively (Table 2). It should be mentioned that the cultivars 'Mairi', 'Karri', and 'Elo' have the genotype 'Kantata 50' in their pedigree (Table 1), which may contribute to similarities in fruit quality among them. In addition to the genotypes 'Karri' and 'Elo', the local breeding line 1-96-16, whose parents include 'Elo', had a high seed content (> 4.0%), while oil concentration per fruit was the third highest (1.1%) (Table 2). Interestingly, in the previous study of Šavikin et al. (2013), conducted in Serbia, the seed contents of 'Ben Lomond', 'Ben Nevis', 'Titania', and 'Öjebyn', as well as the respective oil contents in the seeds, were lower than in our trials.

On average over two years, the total oil content in the seeds of the 22 genotypes ranged from 24.4% to 31.2%, showing the highest levels in 'Ben Nevis', 'Pamyati Vavilova', and 'Asker' with 31.2%, 31.2%, and 31.1%, respectively.

Table 2. Average fruit weight, seeds per fruit, and fatty acid content per fruit and in seeds of 22 blackcurrant genotypes (Polli, Estonia)

Cultivar	Fruit weight (g)	Seeds per fruit (%)	Oil content per fruit (%)	Oil content in seeds (%)
10B	$1.4 \pm 0.28^{a–f}$	$3.1 \pm 0.27^{f–i}$	$0.9 \pm 0.02^{e–h}$	$27.4 \pm 2.83^{d–g}$
1-96-16	1.1 ± 0.07^{gh}	4.1 ± 0.01^{bc}	1.1 ± 0.18^{bc}	$26.7 \pm 4.36^{e–h}$
2-96-51	$1.2 \pm 0.07^{e–h}$	2.5 ± 0.04^{jk}	$0.7 \pm 0.01^{g–j}$	30.3 ± 1.03^{abc}
Almo	$1.2 \pm 0.00^{d–h}$	$3.2 \pm 0.19^{e–h}$	$0.9 \pm 0.18^{d–g}$	$28.7 \pm 3.86^{a–e}$
Asker	$1.2 \pm 0.07^{e–h}$	3.2 ± 0.08^{efg}	1.0 ± 0.06^{cde}	31.1 ± 2.53^{a}
Ats	$1.5 \pm 0.14^{a–d}$	2.2 ± 0.38^{k}	0.6 ± 0.11^{jk}	$27.6 \pm 0.11^{b–g}$
Ben Alder	1.0 ± 0.07^{h}	$3.1 \pm 0.20^{f–i}$	$0.8 \pm 0.00^{f–i}$	25.6 ± 1.43^{fgh}
Ben Lomond	$1.3 \pm 0.28^{b–g}$	4.0 ± 0.56^{cd}	1.1 ± 0.04^{bc}	$28.3 \pm 2.83^{b–f}$
Ben Nevis	$1.3 \pm 0.28^{b–g}$	3.7 ± 0.20^{cde}	1.1 ± 0.05^{ab}	31.2 ± 3.09^{a}
Ben Sarek	$1.5 \pm 0.07^{a–e}$	$2.9 \pm 0.55^{g–j}$	$0.7 \pm 0.06^{h–k}$	25.2 ± 2.71^{h}
Elo	$1.3 \pm 0.07^{c–h}$	4.5 ± 0.73^{ab}	1.2 ± 0.01^{ab}	$27.6 \pm 4.23^{c–g}$
Intercontinental	1.6 ± 0.07^{abc}	2.2 ± 0.76^{k}	0.6 ± 0.13^{k}	$26.6 \pm 3.12^{e–h}$
Karri	1.6 ± 0.14^{ab}	4.6 ± 0.46^{a}	1.3 ± 0.09^{a}	$28.4 \pm 4.70^{a–e}$
Ļentjai	1.6 ± 0.21^{abc}	$2.9 \pm 0.36^{g–j}$	$0.9 \pm 0.03^{e–h}$	$29.8 \pm 2.55^{a–d}$
Mairi	1.7 ± 0.35^{a}	2.6 ± 0.14^{jk}	$0.8 \pm 0.12^{g–j}$	$30.0 \pm 2.97^{a–d}$
Pamyati Vavilova	1.1 ± 0.14^{fgh}	$3.1 \pm 0.07^{f–i}$	$1.0 \pm 0.04^{c–f}$	31.2 ± 1.99^{a}
Pilėnai	$1.3 \pm 0.00^{b–g}$	$2.7 \pm 0.23^{h–k}$	$0.8 \pm 0.06^{f–i}$	30.4 ± 0.52^{ab}
Zagadka	$1.2 \pm 0.00^{d–h}$	3.6 ± 0.17^{def}	$0.9 \pm 0.04^{e–h}$	24.4 ± 2.29^{h}
Titania	$1.3 \pm 0.21^{c–h}$	2.6 ± 0.11^{ijk}	$0.7 \pm 0.03^{h–k}$	$27.6 \pm 2.24^{c–g}$
Varmas	$1.4 \pm 0.07^{a–g}$	2.3 ± 0.23^{k}	0.7 ± 0.07^{ijk}	$28.7 \pm 0.19^{a–e}$
Vyčiai	$1.5 \pm 0.14^{a–d}$	3.2 ± 0.35^{fgh}	$0.9 \pm 0.03^{d–g}$	$28.9 \pm 2.29^{a–e}$
Öjebyn	1.1 ± 0.07^{gh}	4.0 ± 0.29^{bcd}	1.1 ± 0.09^{bcd}	$27.0 \pm 4.07^{e–h}$

Different letters in columns mark significant differences at $p \leq 0.05$

The genotype 'Mairi', in addition to the largest fruit weight, had quite a high concentration of oil in the seeds (30.0 %). However, the proportion of seeds in the fruit of 'Mairi' was relatively small compared to the corresponding value of the other genotypes studied.

The genotypes 'Mairi', 2-96-51, 'Pilėnai', 'Asker', 'Ben Nevis', and 'Pamyati Vavilova' possessed the oil content of > 30% in seeds, with the values of 30.0%, 30.3%, 30.4%, 31.1%, 31.2%, and 31.2%, respectively. The content of the seeds tended to be higher in fruits with a smaller weight (e.g. 'Asker', 'Ben Lomond', 'Ben Nevis', 'Pamyati Vavilova', and 'Pilėnai'), but this was not the case for every tested genotype. The variation in seed content is noteworthy as seed proportion can influence textural qualities and processing possibilities of the fruits as well as be related to the content of bioactive components in seeds.

Fatty acid content in blackcurrant seeds

In terms of FA composition, the most predominant FAs identified in blackcurrant seeds were LA, ranging from 40.1% to 48.6%, followed by ALA, from 11.7% to 16.5%, OA, from 10.3% to 16.4%, and GLA, from 10.9% to 15.6% (Table 3). The content of SDA ranged from 2.2% to 3.6%. The content of SDA was high in 'Ben Alder' (3.2%) and 'Pamyati Vavilova' (3.6%). The genotype 'Karri' possessed the highest LA content (48.1% of the total FAs), but the other identified FAs in this cultivar remained below the calculated average of the 22 tested genotypes. Three cultivars, 'Ben Sarek', 'Ļentjai', and 'Pamyati Vavilova', had contents of five FAs that were higher than the average of the tested genotypes. The results regarding the major FAs in the blackcurrant seeds correspond to the findings of other researchers (Ruiz del Castillo et al. 2002; Šavikin et al. 2013; Flores and Ruiz del Castillo 2016). Ruiz del Castillo et al. (2002) found the contents of FAs in the following order: LA (42.3%–53.3%) > GLA (11.6%–24.6%) > ALA (10.0%–19.2%) > OA (6.6%–11.9%) > PA (palmitic acid) (5.6%–7.3%) > SDA (2.4%–4.3%) from the total FAs on average over 36 different genotypes. In their study, LA was found to be the major component, at a level of up to 50% of the total FAs.

Correlation analysis

A strong positive correlation (r = 0.95) was found between the oil content in fruits and the proportion of seeds per fresh weight of berries (Table 4). The content of oil in fruits depends more on the proportion of seeds in the fruits than on the fruit weight/size. Some genotypes can have large fruits and small seeds or vice versa. High correlation is showing that the cultivars with higher seed to pulp ratio have greater oil concentration that can influence their nutritional value and suitability for oil extraction.

Table 5 shows the content of nutritionally important FAs in blackcurrant seeds. The n-6/n-3 ratio of all the examined currant varieties was below 4, which falls within the recommended range of 1:1 to 5:1 for maintaining a healthy balance. A balanced n-6/n-3 ratio is crucial for optimal physiological

Table 3. Average percentage of nutritionally significant FAs of the total FAs in the seeds of 22 blackcurrant genotypes (Polli, Estonia)

Genotype	LA C18:2 n-6	ALA C18:3 n-3	OA C18:1 c-9	GLA C18:3 n-6	PA C16:0	SA C18:4 n-3
10B	46.4 ± 0.71^{cde}	14.0 ± 1.73$^{b–f}$	13.8 ± 0.24$^{c–g}$	12.3 ± 0.77$^{f–i}$	6.4 ± 0.33$^{b–g}$	2.4 ± 0.05^{ijk}
1-96-16	45.0 ± 0.65^{efg}	13.9 ± 1.74$^{b–f}$	16.4 ± 0.01^{a}	11.2 ± 1.04^{hi}	6.3 ± 0.21$^{c–h}$	2.3 ± 0.09^{jkl}
2-96-51	43.3 ± 1.80^{hi}	14.7 ± 1.58$^{a–d}$	12.7 ± 1.77$^{f–i}$	14.1 ± 2.22$^{a–f}$	6.3 ± 0.14$^{c–h}$	2.9 ± 0.09^{c}
Almo	45.3 ± 0.33$^{d–g}$	12.9 ± 0.85$^{d–h}$	14.9 ± 0.75$^{a–e}$	13.4 ± 0.33$^{b–g}$	6.0 ± 0.51^{ghi}	2.6 ± 0.17$^{e–i}$
Asker	45.0 ± 1.33^{efg}	12.3 ± 1.27^{fgh}	15.0 ± 0.51$^{a–d}$	13.6 ± 1.09$^{b–g}$	6.3 ± 0.30$^{d–h}$	2.4 ± 0.02^{ijk}
Ats	45.6 ± 0.36$^{d–g}$	11.9 ± 1.64^{gh}	12.9 ± 0.16$^{f–i}$	14.9 ± 2.23^{ab}	6.6 ± 0.56$^{a–e}$	2.5 ± 0.19^{hij}
Ben Alder	44.3 ± 0.54^{gh}	16.5 ± 1.91^{a}	10.3 ± 1.1^{j}	13.9 ± 2.41$^{a–f}$	6.7 ± 0.25$^{a–d}$	3.2 ± 0.30^{b}
Ben Lomond	44.4 ± 2.32^{gh}	15.5 ± 3.06^{ab}	11.8 ± 0.95^{ij}	12.6 ± 3.06$^{e–i}$	6.8 ± 0.83^{ab}	2.7 ± 0.27$^{c–h}$
Ben Nevis	46.6 ± 1.03^{bcd}	15.5 ± 2.17^{ab}	11.9 ± 0.32^{hij}	10.9 ± 1.89^{i}	6.5 ± 0.69$^{a–f}$	2.5 ± 0.25$^{f–i}$
Ben Sarek	45.4 ± 0.03$^{d–g}$	14.2 ± 2.45$^{b–e}$	11.3 ± 0.29^{ij}	14.5 ± 2.72$^{a–d}$	6.5 ± 0.34$^{a–e}$	2.8 ± 0.30$^{c–g}$
Elo	45.6 ± 1.64$^{d–g}$	12.9 ± 1.68$^{d–h}$	15.7 ± 0.03^{ab}	12.0 ± 1.56^{ghi}	6.2 ± 0.74$^{e–h}$	2.2 ± 0.11^{l}
Intercontinental	42.4 ± 0.16^{i}	13.7 ± 2.91$^{c–f}$	15.0 ± 1.70$^{a–d}$	13.5 ± 2.71$^{b–g}$	6.3 ± 0.51$^{c–h}$	2.8 ± 0.13^{cd}
Karri	48.1 ± 0.15^{a}	13.5 ± 0.66$^{c–g}$	13.1 ± 0.43$^{e–i}$	12.3 ± 1.12$^{f–i}$	6.0 ± 0.35$^{f–i}$	2.2 ± 0.22^{kl}
Ļentjai	45.3 ± 1.27$^{d–g}$	14.4 ± 2.41$^{b–e}$	11.8 ± 1.03^{ij}	13.8 ± 2.25$^{a–g}$	6.9 ± 0.24^{a}	2.7 ± 0.02$^{c–h}$
Mairi	44.3 ± 0.09^{gh}	12.7 ± 1.12$^{e–h}$	15.1 ± 0.46$^{a–d}$	14.3 ± 0.69$^{a–e}$	5.6 ± 0.15^{i}	2.6 ± 0.02$^{d–i}$
Pamyati Vavilova	40.1 ± 0.98^{j}	15.1 ± 1.92^{abc}	13.7 ± 0.16$^{d–g}$	15.5 ± 1.38^{a}	6.4 ± 0.38$^{b–g}$	3.6 ± 0.01^{a}
Pilėnai	44.8 ± 1.99^{fg}	14.0 ± 1.70$^{b–f}$	14.3 ± 2.62$^{b–f}$	12.7 ± 1.99$^{d–i}$	6.6 ± 0.02$^{a–e}$	2.5 ± 0.16^{hij}
Zagadka	43.1 ± 0.80^{hi}	15.6 ± 2.20^{ab}	12.0 ± 0.17$^{g–j}$	14.6 ± 1.53^{abc}	6.9 ± 0.25^{a}	2.8 ± 0.11^{cde}
Titania	45.9 ± 1.16$^{c–f}$	13.3 ± 1.20$^{d–h}$	14.2 ± 0.98$^{b–f}$	12.5 ± 1.02$^{e–i}$	6.8 ± 0.20^{abc}	2.5 ± 0.05$^{g–j}$
Varmas	42.7 ± 0.36^{i}	11.7 ± 1.22^{h}	15.5 ± 0.04^{abc}	15.6 ± 0.91^{a}	6.2 ± 0.02$^{e–h}$	2.8 ± 0.10$^{c–f}$
Vyčiai	47.9 ± 0.85^{ab}	14.6 ± 1.33^{bcd}	10.5 ± 0.64^{j}	13.0±0.96$^{c–h}$	6.5 ± 0.21$^{a–f}$	2.6 ± 0.13$^{e–i}$
Öjebyn	47.1 ± 1.20^{abc}	14.0 ± 0.78$^{b–f}$	14.4 ± 0.58$^{b–f}$	11.5 ± 0.38^{hi}	5.9 ± 0.40^{hi}	2.2 ± 0.09^{kl}

Different letters in columns mark significant differences at $p \leq 0.05$

Table 4. Correlation coefficients among the analysed and measured traits in 22 blackcurrant genotypes (Polli, Estonia)

Variable	Mean	SD	Fruit weight (g)	Seeds per fruit (%)	Oil content per fruit (%)	Oil content in seeds (%)
Fruit weight (g)	1.3	0.2	1.00	–0.26	–0.22	0.11
Seeds per fruit (%)	3.2	0.7	–0.26	1.00	0.95*	–0.14
Oil content per fruit (%)	0.9	0.2	–0.22	0.95	1.00	0.17
Oil content in seeds (%)	28.3	2.0	0.11	–0.14	0.17	1.00

* Correlation is significant at $p < 0.05$

Table 5. The amount of saturated (SFA), polyunsaturated (PUFA), and monounsaturated (MUFA) FAs in the seeds of 22 blackcurrant genotypes (Polli, Estonia)

Genotype	SFA (%)	MUFA (%)	PUFA (%)	n-6	n-3	n-6/n-3	18n-6/18n-3
10B	8.2	15.7	75.4	59.0	16.4	3.6	0.9
1-96-16	8.5	18.2	72.6	56.4	16.2	3.5	0.8
2-96-51	8.7	14.7	75.3	57.7	17.6	3.3	1.0
Almo	8.1	16.8	74.4	58.9	15.5	3.8	1.0
Asker	8.4	17.0	73.6	58.9	14.7	4.0	1.1
Ats	8.8	14.8	75.2	60.7	14.5	4.2	1.3
Ben Alder	8.8	12.1	78.1	58.5	19.6	3.0	0.9
Ben Lomond	9.5	13.8	75.5	57.3	18.2	3.2	0.8
Ben Nevis	9.0	13.8	75.8	57.8	18.0	3.2	0.7
Ben Sarek	8.9	13.2	77.2	60.2	17.0	3.6	1.1
Elo	8.1	17.7	72.8	57.7	15.1	3.9	0.9
Intercontinental	8.8	16.9	72.7	56.2	16.5	3.5	1.0
Karri	8.1	15.0	76.4	60.7	15.7	3.9	0.9
Ļentjai	9.0	13.6	76.5	59.4	17.2	3.5	1.0
Mairi	8.1	17.0	74.2	58.9	15.3	3.9	1.1
Pamyati Vavilova	8.8	15.7	74.5	55.8	18.7	3.0	1.0
Pilėnai	8.6	16.3	74.3	57.8	16.5	3.5	0.9
Zagadka	9.1	13.8	76.4	58.0	18.4	3.2	1.0
Titania	8.8	16.1	74.4	58.6	15.8	3.7	1.0
Varmas	8.7	17.5	73.0	58.5	14.5	4.1	1.3
Vyčiai	8.1	12.5	78.5	61.3	17.2	3.6	0.9
Öjebyn	8.0	16.3	75.0	58.8	16.2	3.6	0.8

processes. Western diets are known to contain excessive amounts of n-6 FAs, which have been linked to pro-inflammatory effects. A favourable n-6/n-3 ratio suggests that an increased consumption of foods rich in blackcurrant seeds could help to reduce inflammatory responses, including those associated with cardiovascular diseases and metabolic disorders. Developing novel food products from juice production pomace could provide a concentrated source of n-3 FAs, potentially increasing n-3 intake and having a benefit for human health.

Cluster analysis linked close together the genotypes according to the parents in the pedigree (Fig. 1). The shortest linkage (distance ≤1.9) and a common shoulder of a cluster was between the genotypes that had ‘Öjebyn’ or ‘Kantata 50’ or both in their pedigree: 10B, ‘Titania’, ‘Pilėnai’, ‘Öjebyn’, ‘Almo’, ‘Asker’, ‘Mairi’, 1-96-16, and ‘Elo’. According to the previous study of Šavikin et al. (2013), cluster analysis based on the seed oil FA profiles is a convenient method for distinguishing the origin of blackcurrant seeds. In their study, all *Ribes nigrum* L. genotypes were categorized in one cluster at a low linkage distance. However, in the current study, the genotype ‘Pamyati Vavilova’ was distinguished from the other genotypes due to its lowest concentration of LA and highest concentrations of GLA and SA. These differences are influenced by the pedigree of the only genotype studied, originating from Belarus, which has no common parents with the other genotypes.

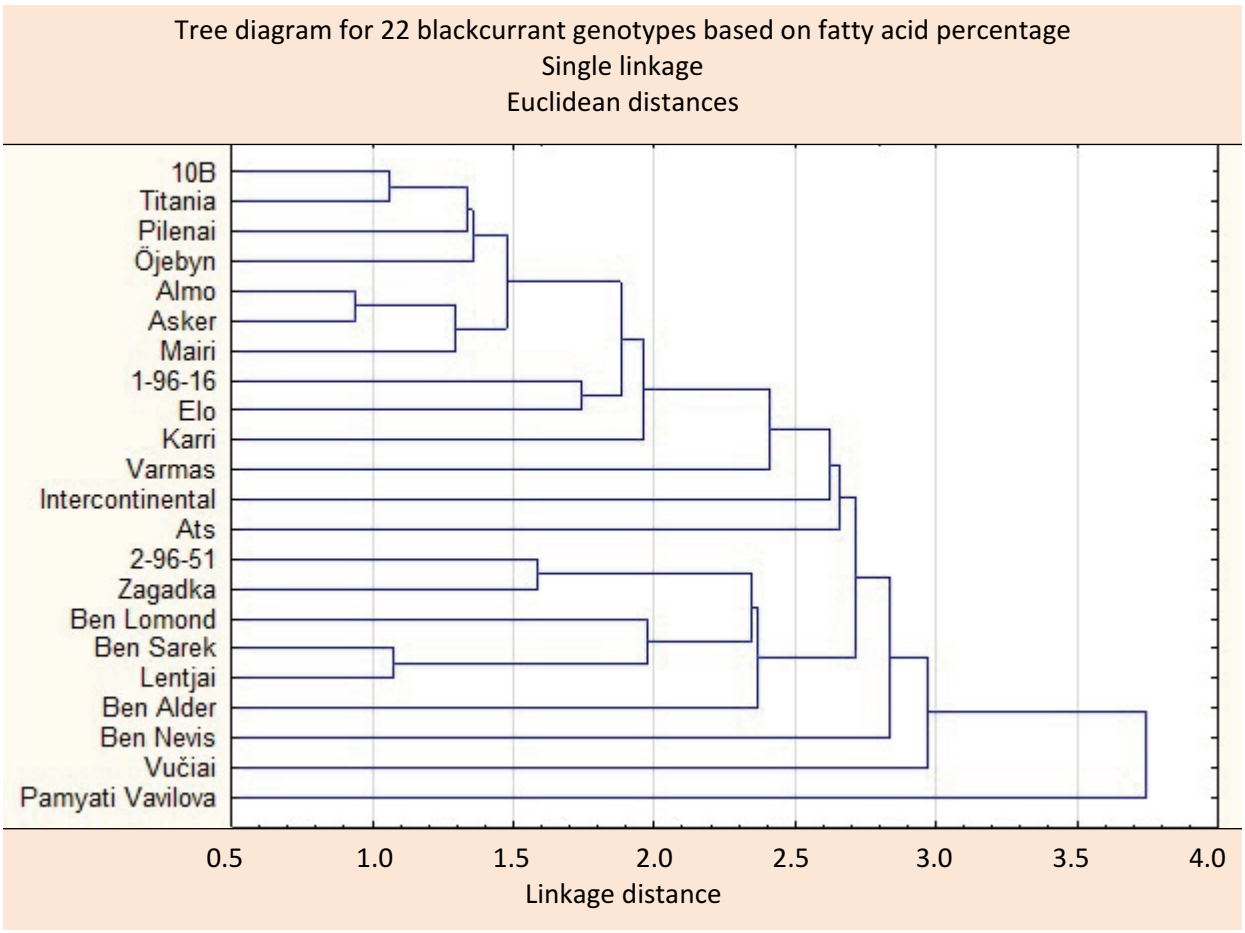

Fig. 1. A diagram based on the Euclidean distances between 22 blackcurrant genotypes evaluated according to the percentage of individual FAs from total FAs in the seeds of *Ribes nigrum* L.

Conclusions

Based on the current work, it can be concluded that the seed content of the studied blackcurrants varied by genotype by 2.2%–4.6%, being the highest in the genotypes 'Karri' and 'Elo'. The highest seed content in these genotypes was in correlation with their highest oil concentration per fruit. It was demonstrated that the oil content in berries depended more on the proportion of seeds in the berries than on the weight/size of the berries. Seed content is an important factor in cultivar selection and breeding programmes. Understanding the genetic basis for the variation of seed content can help to develop blackcurrant varieties oriented to specific market demands.

Based on the percentage of individual FAs from the total FAs in the blackcurrant seeds, the cluster analysis linked close together the genotypes that had 'Öjebyn' or 'Kantata 50' or both in the pedigree. Three cultivars, 'Ben Sarek', 'Ļentjai', and 'Pamyati Vavilova', had five FAs higher than the average of the tested genotypes. Blackcurrant seeds are a valuable source of unsaturated FAs, mainly α-linolenic acid, oleic acid, and γ-linolenic acid. A balanced ratio of n-6/n-3 FAs (< 4) makes blackcurrant seeds valuable from a nutritional point of view. Cluster analysis based on the seed oil FA profiles is a convenient method for distinguishing the origin of seeds.

More information about the composition of blackcurrant (*Ribes nigrum* L.) berries can provide additional opportunities for the utilization of juice production by-products to develop novel foods and cosmetic products or in animal nutrition. This, in turn, can have a significant impact on environmental sustainability by reducing food production waste and promoting resource usage efficiency.

Data availability statement

All research data are contained within the article and can be shared upon request from the authors.

Acknowledgements

This research was financially supported by the Estonian Science Foundation (research grants No. 6801 and 7703), the Ministry of Education and Research of Estonia (target financing project No. 1092711s06), the European Regional Development Fund (project EU50282), and the European Regional Development Fund (ERDF) project 'Knowledge-based health and natural products to create higher added value in the horticulture and food sector' (SFOS No. 2021–2027.5.02.23-0095). Additional support was provided by the Estonian Ministry of Regional Affairs and Agriculture through the 'National plant breeding programme 2020–2030' and the programme 'Collection, conservation and utilization of plant genetic resources for food and agriculture 2021–2027'. The publication costs of this article were covered by the Estonian Academy of Sciences.

References

Basegmez, H. I. O., Povilaitis, D., Kitrytė, V., Kraujalienė, V., Šulniūtė, V., Alasalvar, C. et al. 2017. Biorefining of blackcurrant pomace into high value functional ingredients using supercritical CO_2, pressurized liquid and enzyme assisted extractions. *The Journal of Supercritical Fluids*, **124**, 10–19. https://doi.org/10.1016/j.supflu.2017.01.003

Beattie, J., Crozier, A. and Duthie, G. G. 2005. Potential health benefits of berries. *Current Nutrition & Food Science*, **1**(1), 71–86. https://doi.org/10.2174/1573401052953294

Chauhan, A. S., Patel, A. K., Nimker, V., Singhania, R. R., Chen, C.-W., Patel, A. K. et al. 2024. Biorefining of essential polyunsaturated fatty acids from microbial sources: current updates and prospects. *Systems Microbiology and Biomanufacturing*, **4**, 425–447. https://doi.org/10.1007/s43393-023-00207-x

Dekeyser, K. and Rampa, F. 2023. *Upgrading the EU's policy toolbox for nutrition leadership*. https://ecdpm.org/work/upgrading-eus-policy-toolbox-nutrition-leadership (accessed 2025-02-19).

Flores, G. and Ruiz del Castillo, M. L. 2016. Enhancement of nutritionally significant constituents of black currant seeds by chemical elicitor application. *Food Chemistry*, **194**, 1260–1265. https://doi.org/10.1016/j.foodchem.2015.09.006

Goffman, F. D. and Galletti, S. 2001. Gamma-linolenic acid and tocopherol contents in the seed oil of 47 accessions from several *Ribes* species. *Journal of Agricultural and Food Chemistry*, **49**(1), 349–354. https://doi.org/10.1021/jf0006729

Gustinelli, G., Eliasson, L., Svelander, C., Andlid, T., Lundin, L., Ahrné, L. et al. 2018. Supercritical fluid extraction of berry seeds: chemical composition and antioxidant activity. *Journal of Food Quality*, **2018**(1), 046074. https://doi.org/10.1155/2018/6046074

Hendawy, O., Gomaa, H. A. M., Hussein, S., Alzarea, S. I., Qasim, S., Abdel Rahman, F. E.-Z. S. et al. 2021. Cold-pressed raspberry seeds oil ameliorates high-fat diet triggered non-alcoholic fatty liver disease. *Saudi Pharmaceutical Journal*, **29**(11), 1303–1313. https://doi.org/10.1016/j.jsps.2021.09.014

Jurgoński, A., Koza, J., Chu, D.-T. and Opyd, P. M. 2018. Berry seed oils as potential cardioprotective food supplements. *Nutrire*, **43**, 26. https://doi.org/10.1186/s41110-018-0086-x

Kahu, K., Jänes, H., Luik, A. and Klaas, L. 2009. Yield and fruit quality of organically cultivated blackcurrant cultivars. *Acta Agriculturae Scandinavica Section B – Soil & Plant Science*, **59**(1), 63–69. https://doi.org/10.1080/09064710701865139

Kaldmäe, H., Kikas, A., Arus, L. and Libek, A.-V. 2013. Genotype and microclimate conditions influence ripening pattern and quality of blackcurrant (*Ribes nigrum* L.) fruit. *Zemdirbyste-Agriculture*, **100**(2), 167–174. https://doi.org/10.13080/z-a.2013.100.021

Kikas, A., Kahu, K., Arus, L., Kaldmäe, H., Rätsep, R. and Libek, A.-V. 2017. Qualitative properties of the fruits of blackcurrant *Ribes nigrum* L. genotypes in conventional and organic cultivation. *Proceedings of the Latvian Academy of Sciences, Section B. Natural, Exact, and Applied Sciences*, **71**(3), 190–197. https://doi.org/10.1515/prolas-2017-0032

Konopka, I., Tańska, M., Dąbrowski, G., Ogrodowska, D. and Czaplicki, S. 2023. Edible oils from selected unconventional sources – a comprehensive review of fatty acid composition and phytochemicals content. *Applied Sciences*, **13**(23), 12829. https://doi.org/10.3390/app132312829

Kuhnt, K., Degen, C., Jaudszus, A. and Jahreis, G. 2012. Searching for health beneficial *n*-3 and *n*-6 fatty acids in plant seeds. *European Journal of Lipid Science and Technology*, **114**(2), 153–160. https://doi.org/10.1002/ejlt.201100008

Libek, A. and Kikas, A. 2002. Evaluation of blackcurrant cultivars in Estonia. *Acta Horticulturae*, **585**, 209–213. https://doi.org/10.17660/ActaHortic.2002.585.33

Michalak, M. and Kiełtyka-Dadasiewicz, A. 2018. Oils from fruit seeds and their dietetic and cosmetic significance. *Herba Polonica*, **64**(4), 63–70.

Omachi, D. O., Aryee, A. N. A. and Onuh, J. O. 2024. Functional lipids and cardiovascular disease reduction: a concise review. *Nutrients*, **16**(15), 2453. https://doi.org/10.3390/nu16152453

Pieszka, M., Tombarkiewicz, B., Roman, A., Migdal, W. and Niedziolka, J. 2013. Effect of bioactive substances found in rapeseed, raspberry and strawberry seed oils on blood lipid profile and selected parameters of oxidative status in rats. *Environmental Toxicology and Pharmacology*, **36**(3), 1055–1062. https://doi.org/10.1016/j.etap.2013.09.007

Pieszka, M., Migdał, W., Gąsior, R., Rudzińska, M., Bederska-Łojewska, D., Pieszka, M. et al. 2015a. Native oils from apple, blackcurrant, raspberry, and strawberry seeds as a source of polyenoic fatty acids, tocochromanols, and phytosterols: a health implication. *Journal of Chemistry*, **2015**, 59541. https://doi.org/10.1155/2015/659541

Pieszka, M., Gogol, P., Pietras, M. and Pieszka, M. 2015b. Valuable components of dried pomaces of chokeberry, black currant, strawberry, apple and carrot as a source of natural antioxidants and nutraceuticals in the animal diet. *Annals of Animal Science*, **15**(2), 475–491. https://doi.org/10.2478/aoas-2014-0072

Radočaj, O., Vujasinovic, V., Dimic, E. and Basic, Z. 2014. Blackberry (*Rubus fruticosus* L.) and raspberry (*Rubus idaeus* L.) seed oils extracted from dried press pomace after longterm frozen storage of berries can be used as functional food ingredients. *European Journal of Lipid Science and Technology*, **116**(8), 1015–1024. https://doi.org/10.1002/ejlt.201400014

Rosell, M. and Fadnes, L. T. 2024. Vegetables, fruits, and berries – a scoping review for Nordic Nutrition Recommendations 2023. *Food & Nutrition Research*, **68**. https://doi.org/10.29219/fnr.v68.10455

Ruiz del Castillo, M. L. and Dobson, G. 2002. Varietal differences in terpene composition of blackcurrant (*Ribes nigrum* L) berries by solid phase microextraction/gas chromatography. *Journal of the Science of Food and Agriculture*, **82**(13), 1510–1515. https://doi.org/10.1002/jsfa.1210

Ruiz del Castillo, M. L., Dobson, G., Brennan, R. and Gordon, S. 2002. Genotypic variation in fatty acid content of blackcurrant seeds. *Journal of Agricultural and Food Chemistry*, **50**(2), 332–335. https://doi.org/10.1021/jf010899j

Sarv, V., Hussain, S., Rätsep, R. and Kikas, A. 2024. The proximate composition, mineral and pectin content and fatty acid profile of the pomace fraction of 16 rowanberry cultivars. *Plants*, **13**(12), 1615. https://doi.org/10.3390/plants13121615

Šavikin, K. P., Dordevic, B. S., Ristic, M. S., Krivokuca-Dokic, D., Pljevljakušic, D. S. and Vulic, T. 2013. Variation in the fatty-acid content in seeds of various black, red, and white currant varieties. *Chemistry and Biodiversity*, **10**(1), 157–165. https://doi.org/10.1002/cbdv.201200223

Sheppe, A. E. F. and Edelmann, M. J. 2021. Roles of eicosanoids in regulating inflammation and neutrophil migration as an innate host response to bacterial infections. *Infection and Immunity*, **89**. https://doi.org/10.1128/iai.00095-21

Sibson, R. 1973. SLINK: an optimally efficient algorithm for the single-link cluster method. *The Computer Journal*, **16**(1), 30–34. https://doi.org/10.1093/comjnl/16.1.30

Sławińska, N., Prochoń, K. and Olas, B. 2023. A review on berry seeds – a special emphasis on their chemical content and health-promoting properties. *Nutrients*, **15**(6), 1422. https://doi.org/10.3390/nu15061422

Sukhija, P. S. and Palmquist, D. L. 1988. Rapid method for determination of total fatty acid content and composition of feedstuffs and feces. *Journal of Agricultural and Food Chemistry*, **36**(6), 1202–1206. https://doi.org/10.1021/jf00084a019

Tabart, J., Kevers, C., Pincemail, J., Defraigne, J.-O. and Dommes, J. 2006. Antioxidant capacity of black currant varies with organ, season, and cultivar. *Journal of Agricultural and Food Chemistry*, **54**(17), 6271–6276. https://doi.org/10.1021/jf061112y

Tervise Arengu Instituut. 2025. *Eesti riiklikud toitumise, liikumise ja uneaja soovitused. Tabelraamat (Estonian national recommendations for nutrition, exercise, and sleep. Table book)*. https://www.tai.ee/et/valjaanded/eesti-riiklikud-toitumise-liikumise-ja-uneaja-soovitused-tabelraamat (accessed 2025-02-14).

Wójciak, M., Mazurek, B., Tyśkiewicz, K., Kondracka, M., Wójcicka, G., Blicharski, T. et al. 2022. Blackcurrant (*Ribes nigrum* L.) seeds – a valuable byproduct for further processing. *Molecules*, **27**(24), 8679. https://doi.org/10.3390/molecules27248679

Yang, B., Ahotupa, M., Määttä, P. and Kallio, H. 2011. Composition and antioxidative activities of supercritical CO_2-extracted oils from seeds and soft parts of northern berries. *Food Research International*, **44**(7), 2009–2017. https://doi.org/10.1016/j.foodres.2011.02.025

Musta sõstra (*Ribes nigrum* L.) genotüüpide seemnete sisalduse ja rasvhapete profiili hindamine

Viive Sarv, Reelika Rätsep, Marge Malbe, Hedi Kaldmäe, Sirje Kuusik, Piret Raudsepp, Asta-Virve Libek ja Ave Kikas

Kahel järjestikusel aastal uuriti kokku 22 musta sõstra genotüüpi: 'Karri', 'Almo', 'Ats', 'Elo', 'Varmas', 'Mairi', 'Asker', 'Pilėnai', 'Vyčiai', 'Ben Alder', 'Ben Nevis', 'Ben Lomond', 'Ben Sarek', 'Intercontinental', 'Titania', 'Öjebyn', 'Ļentjai', 'Pamyati Vavilova', 'Zagadka', 10B, 1-96-16 ja 2-96-51. Uurimistöö eesmärk oli võrrelda marjade massi, seemnete sisaldust marjades ning seemnetes sisalduvate rasvhapete profiili. Rasvhapete koostist määrati ja kvantifitseeriti gaasikromatograafiga.

Musta sõstra marjade mass varieerus genotüübist sõltuvalt 1,0–1,7 g vahemikus, olles suurim genotüüpide 'Mairi', 'Karri', 'Intercontinental' ja 'Ļentjai' korral. Seemnete sisaldus marjades jäi 2,2%–4,6% vahemikku, olles suurim genotüüpide 'Karri' ja 'Elo' puhul. Õlisisaldus korreleerus positiivselt seemnete sisaldusega marjade märgkaalu kohta, olles suurim genotüüpide 'Karri' ja 'Elo' korral – vastavalt 1,2% ja 1,3%. Kahe aasta keskmine õlisisaldus seemnetes varieerus 24,4%–31,2% vahemikus, olles suurim genotüüpide 'Ben Nevis', 'Pamyati Vavilova' ja 'Asker' puhul. Rasvhapetest leidus musta sõstra seemnetes kõige rohkem linoolhapet (LA, 40,1%–48,6%), millele järgnesid α-linoleenhape (ALA, 11,7%–16,5%), oleiinhape (OA, 10,3%–16,4%) ja γ-linoleenhape (GLA, 10,9%–15,6%).

Proceedings of the Estonian Academy of Sciences
2026, **75**, 1, 56–74

https://doi.org/10.3176/proc.2026.1.06

www.eap.ee/proceedings
Estonian Academy Publishers

SPACE-AIR-GROUND NETWORK, WIRELESS COMMUNICATION, COMPUTING OFFLOADING

RESEARCH ARTICLE

Received 19 September 2025
Accepted 10 December 2025
Available online 20 February 2026

Keywords:
Internet of Things, wireless communication, space-air-ground integrated network, computing offloading, resource allocation

Corresponding author:
Guoqiang Zheng
lyzhenggq@126.com

Citation:
Li, Z., Zheng, G., Han, Z., Xia, P., Ma, H. and Ji, B. 2026. Joint task offloading and resource allocation for remote IoT in space-air-ground networks architecture. *Proceedings of the Estonian Academy of Sciences*, **75**(1), 56–74. https://doi.org/10.3176/proc.2026.1.06

Joint task offloading and resource allocation for remote IoT in space-air-ground networks architecture

Zhenhua Li, Guoqiang Zheng, Zhe Han, Pingjie Xia, Huahong Ma and Baofeng Ji

College of Information Engineering, Henan University of Science and Technology, Luoyang 471023, China

ABSTRACT

In remote areas with insufficient ground infrastructure, user devices (UDs) are constrained by limited computing resources, which poses substantial challenges to achieving low-latency and energy-efficient data processing. To address these issues, this paper proposes a dual-layer heterogeneous network architecture that makes full use of unmanned aerial vehicle (UAV) and low Earth orbit (LEO) computing resources. Considering the high mobility of LEO satellites, the characteristics of channel variations, and the queuing delay of user task offloading, the optimization objective is modeled as a mixed-integer nonlinear programming problem, aiming to minimize the weighted sum of delay and energy consumption (i.e., the total system cost). A low-complexity alternating optimization algorithm is proposed. The original problem is decomposed into three subproblems: bandwidth allocation, central processing unit (CPU) frequency allocation, and task scheduling optimization, which are solved using convex optimization, the Lagrange multiplier method, and the alternating direction method of multipliers (ADMM), respectively. Finally, the Pareto method is used to seek the best trade-off among the optimization objectives. The simulation results indicate that the average total system cost of the alternating optimization for task offloading and resource allocation (AOTORA) decreases by 25.8%, 11.63%, 12.48%, and 6.84% compared with random optimization, equal bandwidth allocation, the offloading LEO satellite algorithm, and distributionally robust optimization, respectively.

1. Introduction

With the rapid advancement of mobile communication and network technology, user devices (UDs) face growing demands for low latency, high energy efficiency, and enhanced experience, requiring sufficient computational capacity for efficient task processing [31]. New standards and technologies for next-generation mobile systems that include Internet of Things (IoT), cloud computing, and edge computing [13,14,25,29] are being proposed and implemented, while cloud computing is highly dependent on the network, and centralized management tends to lead to competition for users' resources, which in turn triggers service disruptions or higher response latency. The Cloudlet concept [30] proposes the concept of first edge computing, which means offloading computation and storage to the periphery of the network (e.g., edge nodes) adjacent to UDs in order to provide computation resources and storage to nearby UDs [23].

However, due to the limitation of network capacity and coverage, the traditional terrestrial edge computing system cannot meet the computing needs of Internet of Remote Things (IoRT) users in remote areas such as oceans and mountains [19]. Fortunately, space-air-ground integrated networks (SAGIN) constitute a vital part of future communication systems, offering seamless coverage and adaptability to diverse services. SAGIN utilizes a heterogeneous architecture and consists of three network segments: satellite, airborne, and ground segments [6]. For the airborne part, unmanned aerial vehicles (UAVs) serve as an effective auxiliary device, offering flexible deployment, broad coverage, and low cost [38]. For the satellite part, the low Earth orbit

(LEO) satellite networks provide extensive coverage and extend connectivity to remote regions such as oceans and mountains, enabling reliable long-term communications for ground users. In addition, the network architecture exhibits significant complexity. The link quality and coverage of aerial networks vary dynamically, resulting in fluctuations in server availability and communication latency. Moreover, distinct network segments within SAGIN possess heterogeneous link qualities and capacity constraints, making the design of efficient computational offloading strategies a critical challenge [8,28].

In the study of ground- or UAV-assisted computation offloading and resource allocation, Li et al. [16] aimed to minimize the overall system cost and proposed a method that combines partial offloading with collaborative mobile edge computing (MEC). They transformed the problem into a multi-objective optimization problem and solved it using a two-tier alternating optimization framework. Su et al. [34] proposed a collaborative optimization framework that jointly considers task offloading and UAV trajectory design to minimize the energy consumption of UDs. Shen et al. [32] presented a novel UAV-based computation offloading scheme aimed at minimizing both the mean task completion latency and energy consumption in vehicular networks. Qi et al. [27] introduced a dual collaborative computation offloading strategy leveraging multiple UAVs in a MEC framework, aiming to optimize user scheduling of UAV paths to improve the system's energy efficiency. Zhong et al. [44] proposed a dual UAV-supported edge computing system aimed at minimizing the total user latency by optimizing UAV trajectories, computational resource allocation, and UAV function switching. Although Li et al. [16] optimized the computing costs for ground terminal devices, the scalability is poor, and the deployment locations of edge servers are fixed with a limited coverage radius. In addition, research work in [16,27,32,44] mainly focuses on single-layer network architectures, which have limitations in both space and resources: first, it ignores the collaborative architecture between UAVs and LEO satellites; second, drones are constrained by hardware resources, and their limited onboard computing capabilities make efficient trajectory planning in complex environments such as oceans and mountains challenging.

Therefore, we explore the distribution of computational tasks and resource management in the integrated dual-layer system of UAVs and LEO satellites. Chen et al. [4] introduced a space-centric approach for offloading computational tasks, considering the limited coverage time and limited resources of LEO satellites for maintaining service continuity, minimizing the overall execution cost by optimizing the offloading decision and power control. Li et al. [15] investigated low-energy UAVs and LEO satellites-assisted mobile edge computing in SAGIN, aiming to optimize the long-term energy performance of UAV machines and LEO satellites by jointly optimizing task scheduling, UAV trajectories, and bandwidth allocation. Zhang et al. [22] and Liu et al. [41] studied the task offloading mechanism under the SAGIN architecture, but with different focuses. The former considered the dynamics of the device in a comprehensive manner, while the latter focused on power-constrained IoT device scenarios. Li et al. [17] proposed a new space-air-ground-sea multi-layer computing offloading architecture, using high-altitude platform stations as relay nodes and optimizing task offloading and resource allocation through multi-agent proximal policy optimization (MAPPO) to minimize multi-objective issues such as latency, energy consumption, and operational costs. Most of the existing studies employ intelligent algorithms such as deep reinforcement learning (DRL), multi-agent stochastic learning (MASL), or MAPPO to address the optimization problem. However, the scenarios considered in this work involve complex environments, such as mountainous regions. Since DRL relies on deep neural networks, it is difficult to deploy on resource-constrained platforms such as UAVs. Moreover, training such models may take from several days to months, which fails to meet the real-time requirements of UDs.

In comparison, alternating optimization, as an efficient low-complexity algorithm, provides a more concrete and feasible solution approach for resource-constrained dynamic environments. He et al. [10] explored the data offloading problem in SAGIN and proposed an approximation strategy to optimize task scheduling and power control, balancing energy consumption and completion time. Mao et al. [24] presented a joint space-air cloud-edge computing structure aiming to minimize the maximum computational latency between IoT devices through the joint optimization of correlation control, transmission power, task allocation, and bandwidth distribution. Sriharsha et al. [33] proposed a combination of terrestrial fixed MEC and UAV relaying to minimize the total energy consumption of the user equipment by optimizing UAV trajectory and connection scheduling. Mei et al. [26] proposed a space-air-ground cooperative network using non-orthogonal multiple

access (NOMA) technology, employing a block coordinate descent method to decompose the original problem into multiple interrelated coupled subproblems, jointly optimizing power control and computation frequency allocation, as well as task offloading strategies, aiming to minimize system energy consumption. Existing works optimize the energy consumption or latency of UDs, but ignore the limited computing power or coverage time of LEO satellites [10,24,26,33].

In addition, in complex dynamic scenarios, Xie et al. [39] proposed an enhanced snow ablation optimization algorithm (ESAO), which significantly enhances convergence speed and global search capability by introducing an adaptive T-distribution, Cauchy mutation, and leader boundary control strategy. Liu et al. [20] demonstrated how to combine hybrid neural network models with metaheuristic optimization strategies to effectively address nonlinear system prediction tasks. Liu et al. [21] further emphasized the importance of implementing customized evolutionary optimization in complex energy management systems. ESAO in Xie et al. [39] and alternating optimization belong to different optimization paradigms, but ESAO needs to gradually converge to a satisfactory solution through hundreds or even thousands of iterations, at the cost of higher computational complexity. This study focuses on the optimized allocation of static resources, providing a fundamental solution for resource management in space-air-ground integrated networks. However, real-world network environments are highly dynamic, and the next challenge this research faces is inherently related to the existing outstanding work. First, in terms of temporal dynamics, the task of randomly arriving problems is similar to the oil temperature prediction problem addressed by Liu et al. [20], with the core issue being how to accurately characterize a dynamically changing process. Second, in terms of the nature of the problem, this study, similarly to another work by Liu et al. [21], falls under the category of multi-objective optimization under constrained resources, laying a foundation for later leveraging of their advanced hybrid optimization algorithm frameworks (such as DE-HHO) to address more complex dynamic scheduling scenarios in this problem.

Based on the above research, to address communication and computing needs in remote areas and emergency scenarios, this paper constructs an space-air-ground network in which a drone swarm carrying edge servers collaborates with LEO satellites. In this network architecture, drones provide temporary and rapid computing services, while satellites ensure broader communication coverage. However, the high mobility of satellites results in limited coverage time and periodically varying channels, posing challenges for heterogeneous network resource management. Therefore, we propose a joint optimization problem to minimize the total computation cost for ground users (weighted sum of computation delay and energy consumption) by jointly optimizing bandwidth allocation, computing resource allocation, and task offloading scheduling, under the constraints of maximum workload and communication resources. The main contributions are summarized as follows:

1. A dual-layer heterogeneous network system that fully utilizes UAV and LEO computing resources is proposed. Considering the high mobility of LEO, channel variation characteristics, and user task offloading queuing delay, the optimization objective is modeled as a mixed-integer nonlinear programming problem, aiming to minimize the weighted sum of latency and energy consumption.

2. To address this issue, we propose a low-complexity alternating optimization algorithm. The original problem is decomposed into three subproblems: bandwidth allocation, central processing unit (CPU) frequency allocation, and task scheduling optimization. Convex optimization, the Lagrange multiplier method, and the alternating direction method of multipliers (ADMM) are used to solve them, respectively, and finally, the Pareto approach is applied to seek the best trade-off among the optimization objectives.

3. Simulation results demonstrate the convergence and superiority of the proposed alternating optimization for task offloading and resource allocation (AOTORA) algorithm. Compared with other benchmark schemes (random optimization, equal bandwidth allocation, full satellite offloading, and distributed robust optimization), the average total computational cost per user is reduced by 25.8%, 11.63%, 12.48%, and 6.48%, respectively.

The remainder of this paper is organized as follows: Section 2 presents the system models, Section 3 presents the formulation and analysis of the problem, Section 4 develops the AOTORA algorithm to solve the problem, Section 5 provides an analysis of the simulation results, Section 6 summarizes the research findings, discusses limitations, and outlines future research directions.

2. System model and problem description

2.1. Network model

This paper considers a dual-layer space-air-ground internet of the IoRT network, and the specific system model is illustrated in Fig. 1a. The space-based network is composed of L LEO satellites equipped with edge servers, one of which is selected to establish a communication link with the ground, and the set of LEO satellites is denoted by $l \in \mathcal{L} = \{1, 2, \ldots, l, \ldots, L\}$. LEO satellite communication links are updated periodically over time. The air-based network consists of N UAVs equipped with edge servers, which are fixed in position and hover in the air, and the set is represented by $n \in \mathcal{N} = \{1, 2, \ldots, n, \ldots, N\}$. Both satellites and drones can provide computing services to ground-based devices. The terrestrial network consists of M UDs, and the set is represented by $m \in \mathcal{M} = \{1, 2, \ldots, m, \ldots, M\}$.

Depending on the UDs, the computational tasks take different computational approaches, which can be offloaded to the LEO satellites or forwarded to the UAVs for processing by the ground users via wireless links. Assuming that each UD has only one computational task $J_m = \{D_m, \lambda_m\}$, where D_m denotes the task data size of the UD and λ_m denotes the CPU frequency cycle needed to process a single bit of data. Since tasks cannot be split, UDs must choose between UAVs and LEO satellites as offloading targets [36]. In addition, considering the variable channel environment among the UDs and the LEO satellites, UDs need to select the appropriate LEO satellites for mission computation. Table 1 provides an overview of the main symbols of the system.

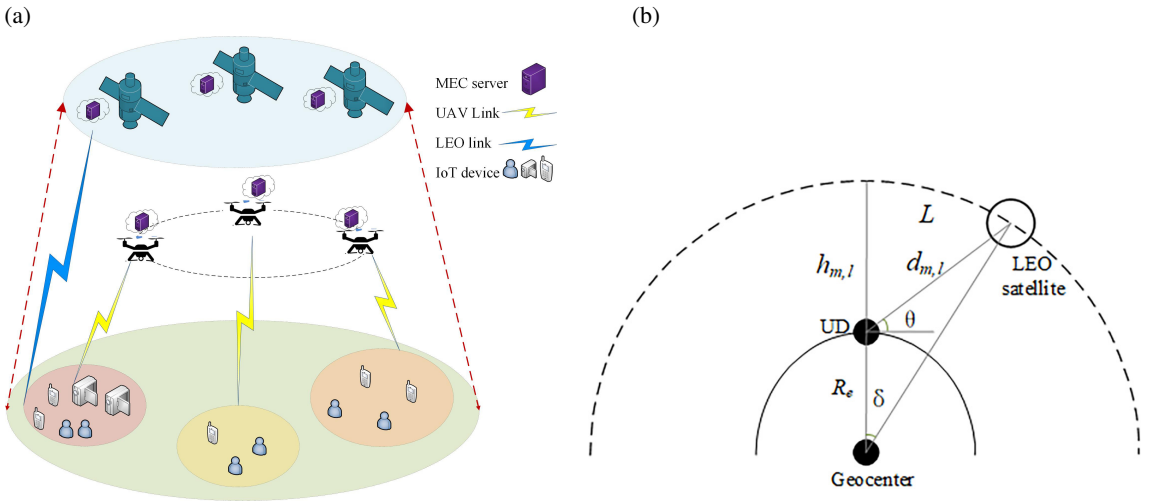

Fig. 1. System network model: UD network model (a) and the position relationship between UD and LEO satellite (b).

2.2. Coverage model

The high maneuverability of LEO satellites results in dynamic variations in their coverage areas, which makes it challenging to maintain continuous and stable communication links. Therefore, the satellite coverage model must account for these dynamic changes. According to [36], communication and computation can only occur when specific geometric relationships are met (see Fig. 1b). LEO satellites operate in predetermined orbits, $h_{m,l}$ represents the distance from the UDs to the LEO satellite orbit, R_e denotes the Earth's radius, and $d_{m,l}$ is the distance between the UDs and the LEO satellite. θ represents the elevation angle of the UDs, and the solving formula is

$$\theta = \arccos\left(\frac{R_e + h_{m,l}}{d_{m,l}} \cdot \sin\delta\right). \tag{1}$$

The geocentric angle δ from the Earth's center covering the LEO satellite's range is calculated as

$$\delta = \arccos\left(\frac{R_e}{R_e + h_{m,l}} \cdot \cos\theta\right) - \theta. \tag{2}$$

Table 1. System variables

Notation	Definition
$M/N/L$	Number of UDs/UAVs/LEO satellite
$J_m = \{D_m, \lambda_m\}$	UD m task data size and CPU required for computation
$d_{m,l}$	Distance between UD m and LEO satellite l
$h_{m,l}$	Distance between UD m and satellite orbit
H_m^n / H_m^l	Channel gains from UD m to UAV n and to satellite l
$R_{m,n} / R_{m,l}$	Distance between UD m and satellite orbit
B^n / B^l	Bandwidth of UAV n and satellite l
$\beta_{m,n}$	Bandwidth coefficient of UAV n allocated to UD m
$f_{m,n} / f_{m,l}$	Computational resources from UAV n and satellite l to UD m
$F_n^{\max} / F_l^{\max}$	Maximum computational resources of UAV n and satellite l
$p_{m,n} / p_{m,l}$	Uplink transmit power of UD m
p^n / p^l	Launch power of UAV n and satellite l
$t_{m,n}^{\text{up}} / t_{m,n}^{\text{com}} / t_{m,n}^{\text{wait}}$	Transmission, computation, and wait time between task D_m and UAV n
$E_{m,n}^{\text{up}} / E_{m,n}^{\text{com}}$	Transmission and computation energy consumption between task J_m and UAV n
$t_{m,l}^{\text{up}} / t_{m,l}^{\text{com}} / t_{m,l}^{\text{delay}} / t_{m,l}^{\text{wait}}$	Transmission, computation, propagation, and wait time between task J_m and satellite l
$E_{m,l}^{\text{up}} / E_{m,l}^{\text{com}}$	Transmission and computation energy consumption between task J_m and satellite l
$t_{m,n} / t_{m,l}$	Computation time of task J_m on UAV n or satellite l
$E_{m,n} / E_{m,l}$	Computation energy consumption of task J_m on UAV n or satellite l
$a_{m,n} / a_{m,l}$	Offloading decisions from UD m to UAV n and satellite l
T_m / E_m	Total computation delay and total energy consumption of all tasks
γ	Lagrange multiplier vector
ρ	Penalty parameter
$\bar{\omega}$	Weight factor
σ^2	Noise power
$T_{\max} / T_{\min}$	Maximum and minimum total delay required for all tasks
$E_{\max} / E_{\min}$	Maximum and minimum total energy consumption for all tasks

Therefore, the maximum communication time between the UD and LEO satellite is

$$T_c = \frac{L}{v_s}, \tag{3}$$

where v_s represents the satellite's velocity, and L represents the arc length of the communication time between the UD and LEO satellite, which can be calculated by

$$L = 2 \cdot \left(R_e + h_{m,l}\right) \cdot \delta. \tag{4}$$

The satellite orbit altitude $h_{m,l}$ and the Earth's radius R_e are system constants. The orbital velocity of a satellite is v_s, determined by the orbital altitude, and the satellite is in the same orbit, which is also a constant for near-circular orbits. Most importantly, the geocentric angle δ proved to be a self-consistent and definite mathematical solution through Eq. (2). Once the satellite and user position are determined, the coverage angle δ is a fixed value, resulting in the communication arc length L and the final time T also being fixed. An update cycle is set, and after each cycle, the system will re-compare the channel conditions of each satellite and determine the optimum. We choose satellite coverage time constraints, periodically updated channels, and fixed-interval mission data volume randomness as modeling starting points, which aim to focus on solving the core complexity of NP-hard resource allocation.

2.3. Communication model

Given that the size of computational results is significantly smaller than that of input data, the downlink transmission rate is much higher than the uplink rate. This paper focuses solely on uplink transmission latency and energy consumption, while neglecting the downlink latency and energy overhead from satellites and UAVs to UDs. Both the ground devices' and the UAVs' positions are fixed, the location of UD m is represented as $W_m = (x_m, y_m, 0)$, the UAV hovers at an altitude of h with the coordinates $W_n = (x_n, y_n, h)$, and the channel gain between UD m and UAV n is denoted as

$$H_m^n = \frac{\gamma_0}{\left[\sqrt{(x_m - x_n)^2 + (y_m - y_n)^2 + h^2}\right]^\kappa}, \tag{5}$$

where γ_0 is the channel power gain at a reference distance of 1 m and κ is the path loss exponent for the UD–UAV link.

When a ground-based IoT UD selects a LEO satellite for task offloading, the satellite begins to perform in-orbit computations for the upcoming task. All LEO satellites operate at the same orbital altitude $h_{m,l}$, and the UD m and LEO satellite l channels are modeled by

$$H_m^l = \frac{G\lambda}{4\pi d_{m,l}(t)} \cdot h_{\text{shadow}} \cdot h_{\text{multipath}}, \tag{6}$$

where G indicates the antenna gain, λ denotes the signal wavelength, $d_{m,l}(t)$ denotes the distance between UD m and LEO satellite l in the same cycle, and h_{shadow} and $h_{\text{multipath}}$ denote the shadow fading and multipath effects, respectively.

UD m transmits upward through the wireless channel. When UD m connects to UAV n or LEO satellite l, the uplink transmission rates are respectively expressed as

$$R_{m,n} = \beta_{m,n} B^n \log_2\left(1 + \frac{H_m^n p_{m,n}}{\sum\limits_{i \neq m} H_i^n p_{i,n} + \sigma^2}\right), \tag{7}$$

$$R_{m,l} = B^l \log_2\left(1 + \frac{p_{m,l} H_m^l}{\sigma^2}\right), \tag{8}$$

where $\beta_{m,n}$ represents the bandwidth allocation coefficient assigned by UAV n to UD m, and B^m, B^l denote the available channel bandwidths for UAV n and LEO satellite l, respectively. The terms $p_{m,n}$, $p_{m,l}$ correspond to the transmission powers between UD m and UAV n, as well as between UD m and LEO satellite l. $\sum\limits_{i \neq m} H_i^n p_{i,n}$ denotes the total interference caused by other terrestrial UDs transmitting data from UD m to UAV n based on the same channel, and σ^2 signifies the background noise inherent in communications between ground UDs and other devices.

2.4. Computation model

For UDs, two computational offloading schemes are available. The binary variables $a_{m,n}$ and $b_{m,l}$ are defined as the offloading decision variables for ground UDs, where $a_{m,n} = 1$ signifies that UD m is allocated to UAV n, otherwise $a_{m,n} = 0$. Similarly, $b_{m,l} = 1$ indicates that UD m is allocated to satellite l, otherwise $b_{m,l} = 0$. Determine the optimal UDs' offloading selection by minimizing the UDs' total computational cost.

(1) UAV computing: Within the UAV computing framework, the computational task J_m is transferred to UAV n for execution. The computational power (CPU cycles/s) allocated by UAV n to UD m is denoted as $f_{m,n}$, which may vary across different UD m. The maximum computational power of UAV n is denoted as $F_n^{\max}$. The processing latency of the computational task J_m by UAV is denoted as

$$t_{m,n}^{\text{up}} = \frac{D_m}{R_{m,n}}, \tag{9}$$

$$t_{m,n}^{\text{com}} = \frac{\lambda_m}{f_{m,n}}, \tag{10}$$

where $t_{m,n}^{\text{up}}$ and $t_{m,n}^{\text{com}}$ represent the transmission latency and computational latency of user task J_m to UAV n, respectively.

Additionally, if the UAV resources are currently occupied, the waiting delay for the next unloading task is $t_{m,n}^{\text{wait}}$. The total execution time for task J_m from UD m to UAV n is

$$t_{m,n}^{\text{com}} = t_{m,n}^{\text{up}} + t_{m,n}^{\text{com}} + t_{m,n}^{\text{wait}}. \tag{11}$$

The energy consumption of task J_m computed from UAV is denoted as

$$E_{m,n}^{\text{up}} = p^m t_{m,n}^{\text{up}}, \tag{12}$$

$$E_{m,n}^{\text{com}} = p^n \cdot \frac{\lambda_m}{f_{m,n}}, \tag{13}$$

$$E_{m,n} = E_{m,n}^{\text{up}} + E_{m,n}^{\text{com}}, \tag{14}$$

where p^m and p^n are the transmit powers of UD m and UAV n. $E_{m,n}^{\text{up}}$, $E_{m,n}^{\text{com}}$, and $E_{m,n}$ denote the corresponding transmission energy consumption, computational energy, and total energy consumption of task J_m on UAV n.

(2) LEO satellite computing: Within the satellite computing framework, the computational task J_m is transferred to satellite l for execution. The computational power (CPU cycles/s) allocated by satellite l to UD m is denoted as $f_{m,l}$, which can be different for different UD m. The maximum computational power of satellite l is denoted as $F_l^{\max}$. However, the communication process between UDs and the satellite is subject to propagation latency. The execution latency of the computational task J_m by satellite l is denoted as

$$t_{m,l}^{\text{up}} = \frac{D_m}{R_{m,l}}, \tag{15}$$

$$t_{m,l}^{\text{delay}} = \frac{d_{m,l}}{c}, \tag{16}$$

$$t_{m,l}^{\text{com}} = \frac{\lambda_m}{f_{m,l}}, \tag{17}$$

where $d_{m,l}$ is the distance between UD m and satellite l, c is the speed of light, and $t_{m,l}^{\text{up}}$, $t_{m,l}^{\text{delay}}$, and $t_{m,l}^{\text{com}}$ represent the transmission latency, propagation latency, and computational latency, respectively.

Additionally, if the LEO satellite resources are currently occupied, the waiting delay for the next unloading task is $t_{m,l}^{\text{wait}}$. The total execution time for task J_m from UD m to LEO l is

$$t_{m,l} = t_{m,l}^{\text{up}} + t_{m,l}^{\text{delay}} + t_{m,l}^{\text{com}} + t_{m,l}^{\text{wait}}. \tag{18}$$

The energy consumption of task J_m computed from satellite l is denoted as

$$E_{m,l}^{\text{up}} = p^m t_{m,l}^{\text{up}}, \tag{19}$$

$$E_{m,l}^{\text{com}} = p^l \cdot \frac{\lambda_m}{f_{m,l}}, \tag{20}$$

$$E_{m,l} = E_{m,l}^{\text{up}} + E_{m,l}^{\text{com}}, \tag{21}$$

where p^l is the transmit power of LEO satellite l. $E_{m,l}^{\text{up}}$, $E_{m,l}^{\text{com}}$, and $E_{m,l}$ denote the corresponding transmission energy consumption, computational energy consumption, and total energy consumption of task J_m on satellite l.

3. Problem description

Based on the computational models above, the total delay and total energy consumption required for system computing tasks are expressed as follows:

$$T_m = \sum_{m \in \mathcal{M}} a_{m,n} t_{m,n} + b_{m,l} t_{m,l}, \tag{22}$$

$$E_m = \sum_{m \in \mathcal{M}} a_{m,n} E_{m,n} + b_{m,l} E_{m,l}. \tag{23}$$

We studied the joint optimization problem of bandwidth allocation, computational resource allocation, and user scheduling, aiming to minimize total system cost, which is formulated as

$$\begin{aligned}
\text{P: } & \min_{a,b,\beta,f} \sum_{m\in\mathcal{M}} \{\bar{\omega}T_m + (1-\bar{\omega})E_m\} \\
& \text{s.t. C1: } \{a_{m,n}, b_{m,l}\} \in \{0,1\}, \forall m, n, \\
& \quad \text{C2: } \sum_{n\in\mathcal{N}} a_{m,n} + \sum_{l\in\mathcal{L}} b_{m,l} = 1, \forall m, \\
& \quad \text{C3: } 0 \le f_{m,n} \le F_n^{\max}, \sum_{m\in\mathcal{M}} f_{m,n} \le F_n^{\max}, \\
& \quad \text{C4: } 0 \le f_{m,l} \le F_l^{\max}, \sum_{m\in\mathcal{M}} f_{m,l} \le F_l^{\max}, \\
& \quad \text{C5: } 0 \le \beta_{m,n} \le 1, \forall m, n, \\
& \quad \text{C6: } \sum_{m\in\mathcal{M}} \beta_{m,n} \le 1, \forall n, \\
& \quad \text{C7: } b_{m,l} t_{m,l} \le T_c.
\end{aligned} \tag{24}$$

We set the objective optimization problem P (i.e., the total system cost) as Cost, where $\bar{\omega}$ is the weighting factor, $\bar{\omega} = (0, 1]$. Constraint C1 denotes that the offloading decision for each UD is a binary variable, constraint C2 indicates that only one offloading method can be selected per UD, constraints C3 and C4 stipulate that the computational resources allocated to the UDs do not exceed the inherent limitations of the UAVs or satellites, C5 and C6 ensure that the total bandwidth allocated by the UAV to the UD does not exceed its available bandwidth, and constraint C7 ensures that the UD task offloading time to the satellite is within its coverage time.

Since the optimization objectives T and E have different magnitudes and units, the two conflicting objectives are normalized, which can provide a complete Pareto optimal solution for our problem [12]. We introduce a weighting factor $\bar{\omega}$ to balance the objective functions:

$$\begin{aligned}
\text{P0: } & \min_{a,b,\beta,f} \sum_{m\in\mathcal{M}} \left\{ \bar{\omega} \frac{T_m - T_{\min}}{T_{\max} - T_{\min}} + (1-\bar{\omega}) \frac{E_m - E_{\min}}{E_{\max} - E_{\min}} \right\} \\
& \text{s.t. C1–C8.}
\end{aligned} \tag{25}$$

Here, $T_{\max}$ and $T_{\min}$ represent the maximum and minimum values of the total system computation delay, respectively, while $E_{\max}$ and $E_{\min}$ represent the maximum and minimum values of the total system computation delay for the reformulated problem P0. We can obtain the following formula:

$$\begin{aligned}
\text{P0: } & \min_{a,b,\beta,f} \sum_{m\in\mathcal{M}} \{\bar{\omega}AT_m + (1-\bar{\omega})BE_m\} \\
& \text{s.t. C1–C8.}
\end{aligned} \tag{26}$$

The solution value of problem P0 is denoted by Q, where $V = \bar{\omega}\frac{T_{\min}}{T_{\max}-T_{\min}} + (1-\bar{\omega})\frac{E_{\min}}{E_{\max}-E_{\min}}$, $A = \frac{1}{T_{\max}-T_{\min}}$, $B = \frac{1}{E_{\max}-E_{\min}}$ are constants and $\bar{\omega}$ is the weighting factor $\bar{\omega} = (0, 1]$.

The numerical value of the optimization objective depends on the transfer rate of the user task, computational resource allocation, and user offload scheduling. Owing to their closer proximity to UDs compared with satellites, UAVs can serve multiple users simultaneously. Furthermore, efficient bandwidth allocation can further reduce transmission costs. Moreover, given the limited computational resources of UAVs and satellites, efficient resource allocation for UDs is essential to minimize computational costs. Finally, to realize space-air-ground integrated networking, user terminals must dynamically integrate UAVs and satellites by jointly scheduling their complementary resources, thereby minimizing the total cost for all users. However, optimizing offload scheduling is complex due to its binary nature, affecting both bandwidth and resource allocation, with these variables being interdependent. The non-convexity of the optimization objective P and constraints C1 and C2 makes direct solving difficult. In this paper, we decompose the optimization problem and provide solutions for the subproblems discussed in Section 4.

4. Proposed solution

Based on the above analysis, the optimization objective is a mixed-integer nonlinear programming (MINLP) problem, which is difficult to solve directly. We decompose it into three subproblems: bandwidth allocation, computational resource allocation, and task offload scheduling, and solve them by convex optimization, the Lagrange multiplier method, and ADMM algorithms, respectively. Finally, an AOTORA algorithm is proposed jointly for the three subproblems to minimize the total user computational cost.

4.1. Bandwidth allocation optimization

Given the parameters a and b, the bandwidth and computational resources optimization problem is not coupled; therefore, this paper is divided into two subsections, 4.1 and 4.2, to explain the solution process. Subsection 4.1 focuses on optimizing the bandwidth allocation problem. Through the observation and analysis, we find that P1 is an LP problem, where the meaning of $\beta_{m,n}$ is a portion of the bandwidth between UDs and UAVs. The optimization problem can be expressed as

$$\begin{aligned}
\text{P1:}\quad & \min_{\beta} \varphi \\
\text{s.t.}\ & \sum_{m\in\mathcal{M}} \bar{\omega}\left(\frac{D_m}{\beta_{m,n}B^n\log_2(1+\chi)}\right) + (1-\bar{\omega})\left(p^m\cdot\frac{D_m}{\beta_{m,n}B^n\log_2(1+\chi)}\right) \le \varphi \\
& 0 \le \beta_{m,n} \le 1, \forall m, n, \\
& \sum_{m\in\mathcal{M}} \beta_{m,n} \le 1, \forall n,
\end{aligned} \tag{27}$$

where $\mathcal{X} = \frac{H_m^n p_{m,n}}{\sum_{m\neq i} H_i^n p_{i,n}+\sigma^2}$. By taking the second derivative of the optimization variable $\beta_{m,n}$ in P1, we can obtain $\frac{\partial^2(\varphi)}{\partial(\beta_{m,n})^2} > 0$, so P1 is a convex function, which is addressed using the convex optimization algorithm tool, the CVX toolkit [9], to obtain β^*.

4.2. Optimization of computing resource allocation

Given the parameters a, b and the bandwidth allocation β, the optimization problem with respect to the computational resource f can be formulated as

$$\begin{aligned}
\text{P2.1:}\ & \min_{f_{m,n}} \sum_{m\in\mathcal{M}} \left[\bar{\omega}\left(\frac{\lambda_m}{f_{m,n}}\right) + (1-\bar{\omega})\left(p^n\cdot\frac{\lambda_m}{f_{m,n}}\right)\right] \\
& \text{s.t.}\ 0 \le f_{m,n} \le F_n^{\max} \\
& \sum_{m\in\mathcal{M}} f_{m,n} \le F_n^{\max}.
\end{aligned} \tag{28}$$

$$\begin{aligned}
\text{P2.2:}\ & \min_{f_{m,l}} \sum_{m\in\mathcal{M}} \left[\bar{\omega}\left(\frac{\lambda_m}{f_{m,l}}\right) + (1-\bar{\omega})\left(p^l\cdot\frac{\lambda_m}{f_{m,l}}\right)\right] \\
& \text{s.t.}\ 0 \le f_{m,l} \le F_l^{\max} \\
& \sum_{m\in\mathcal{M}} f_{m,l} \le F_l^{\max}.
\end{aligned} \tag{29}$$

We set the objective function of Eq. (28) as φ_1, and we obtain

$$\begin{aligned}
& \frac{\partial(\varphi_1)}{\partial(f_{m,n})} = -\bar{\omega}\frac{\lambda_m}{f_{m,n}} - (1-\bar{\omega})\frac{p^m\cdot\lambda_m}{f_{m,n}} < 0, \\
& \frac{\partial^2(\varphi_1)}{\partial(f_{m,n})^2} > 0, \\
& \frac{\partial^2(\varphi_1)}{\partial(f_{m,n})\partial(f_{m',n})} = 0, \\
& 0 \le m \le M,\ m \ne m'.
\end{aligned} \tag{30}$$

We observe that the objective function φ_1 of problem P2.1 is positive definite and can be addressed using the Lagrange multiplier method (similarly for P2.2). The Lagrange functions are expressed as

$$L_1(f_{m,n}, \mu) = \sum_{m\in\mathcal{M}} \left[\bar{\omega}\left(\frac{\lambda_m}{f_{m,n}}\right) + (1-\bar{\omega})\left(p^n \cdot \frac{\lambda_m}{f_{m,n}}\right)\right] + \mu\left(\sum_{m\in M} f_{m,n} - F_n^{\max}\right), \tag{31}$$

$$L_2(f_{m,l}, \nu) = \sum_{m\in\mathcal{M}} \left[\bar{\omega}\left(\frac{\lambda_m}{f_{m,l}}\right) + (1-\bar{\omega})\left(p^l \cdot \frac{\lambda_m}{f_{m,l}}\right)\right] + \nu\left(\sum_{m\in M} f_{m,l} - F_l^{\max}\right), \tag{32}$$

where μ and ν are both non-negative, and the Karush–Kuhn–Tucker (KKT) conditions for Eq. (31) are formulated as

$$\frac{\partial L(f_{m,n}, \mu)}{\partial f_{m,n}} = -\left[\bar{\omega}\frac{\lambda_m}{(f_{m,n})^2} + (1-\bar{\omega})\frac{p^n \cdot \lambda_m}{(f_{m,n})^2}\right] + \mu = 0, \tag{33}$$

$$\frac{\partial L(f_{m,n}, \mu)}{\partial \mu} = \sum_{m\in\mathcal{M}} f_{m,n} - F_n^{\max} = 0, \tag{34}$$

$$\mu\left(\sum_{m\in\mathcal{M}} f_{m,n} - F_n^{\max}\right) = 0. \tag{35}$$

From the above equations, we obtain

$$\sqrt{\mu} = \sum_{m\in\mathcal{M}} \frac{\sqrt{\bar{\omega}\cdot\lambda_m + (1-\bar{\omega})\cdot\lambda_m\cdot p^n}}{F_n^{\max}}. \tag{36}$$

Therefore, the optimal solution ${f_{m,n}}^*$ can be expressed as

$${f_{m,n}}^* = \frac{\lambda_m(\bar{\omega} + (1-\bar{\omega})\cdot p^n)}{\sum_{m\in\mathcal{M}}\sqrt{\lambda_m(\bar{\omega} + (1-\bar{\omega})\cdot p^n)}} \cdot F_n^{\max}. \tag{37}$$

Similarly, according to the KKT conditions of Eq. (32), the optimal solution ${f_{m,l}}^*$ can be expressed as

$${f_{m,l}}^* = \frac{\lambda_m(\bar{\omega} + (1-\bar{\omega})\cdot p^l)}{\sum_{m\in M}\sqrt{\lambda_m(\bar{\omega} + (1-\bar{\omega})\cdot p^l)}} \cdot F_l^{\max}. \tag{38}$$

4.3. User scheduling optimization

Given β and f found in subsections 4.1 and 4.2 above, the optimization problem for the offloading decisions a and b is described as

$$\begin{aligned} &\text{P3: } \min_{a,b} \sum_{m\in\mathcal{M}} \left\{\bar{\omega}T_m + (1-\bar{\omega})E_m\right\} \\ &\text{s.t. C1–C8.} \end{aligned} \tag{39}$$

Since a and b are binary variables, integer programming algorithms such as genetic algorithms have slower search speeds and require more training time, while the computation load of the cutting plane method is large, which increases the complexity of problem solving to some extent [2,11,42]. Taking these factors into account, this paper introduces a distributed computation offloading algorithm based on ADMM to solve the problem. However, this algorithm needs to evaluate the feasible region of each variable, introducing linear relaxation and transforming the original problem P3 into a convex optimization problem. The feasible regions of the optimization variables a and b, $\wedge_a$ and $\wedge_b$, are defined as follows:

$$\wedge = \begin{Bmatrix} \wedge_a \\ \wedge_b \end{Bmatrix} \left| \begin{array}{l} \sum_{m\in\mathcal{M}} a_{m,n} f_{m,n} \le F_n^{\max}, 0 \le a_{m,n} \le 1, \forall m, n. \\ \sum_{m\in\mathcal{M}} b_{m,l} f_{m,l} \le F_l^{\max}, 0 \le b_{m,l} \le 1, \forall m, l. \\ b_{m,l} t_{m,l} \le T_c, \forall m, l. \end{array} \right\}. \tag{40}$$

The original question P3 can be rewritten as

$$\begin{aligned} \text{P3}'\text{:} \min_{a,b} & \sum_{m\in\mathcal{M}} \left\{ \bar{\omega} T_m + (1-\bar{\omega}) E_m \right\} \\ \text{s.t.} \quad & \text{Eq. (45), C2, C8.} \end{aligned} \tag{41}$$

The augmented Lagrange function is as follows:

$$\begin{aligned} L_\rho(a,b) = \text{P3}'(a_{m,n}, b_{m,l}) + \gamma^T \left(\sum_{n\in\mathcal{N}} a_{m,n} + \sum_{l\in\mathcal{L}} b_{m,l} - \mathbf{1} \right) \\ + \frac{\rho}{2} \left(\sum_{n\in\mathcal{N}} a_{m,n} + \sum_{l\in\mathcal{L}} b_{m,l} - \mathbf{1} \right)^2, \end{aligned} \tag{42}$$

where γ is the Lagrange multiplier vector, ρ is the penalty parameter, and $\mathbf{1}$ is the M-dimensional vector. This objective function and constraints are convex; a, b, and γ are updated in sequential order as

$$\begin{aligned} a^{(i+1)} = \arg\min_a \Bigg[\text{P3}' \left(a_{m,n}, {b_{m,l}}^{(i)} \right) + (\gamma^{(i)})^T \left(\sum_{n\in\mathcal{N}} a_{m,n} + \sum_{l\in\mathcal{L}} {b_{m,l}}^{(i)} - \mathbf{1} \right) \\ + \frac{\rho}{2} \left(\sum_{n\in\mathcal{N}} a_{m,n} + \sum_{l\in\mathcal{L}} {b_{m,l}}^{(i)} - \mathbf{1} \right)^2 \Bigg], \end{aligned} \tag{43}$$

$$\begin{aligned} b^{(i+1)} = \arg\min_b \Bigg[\text{P3}' \left({a_{m,n}}^{(i+1)}, b_{m,l} \right) + (\gamma^{(i)})^T \left(\sum_{n\in\mathcal{N}} {a_{m,n}}^{(i+1)} + \sum_{l\in\mathcal{L}} b_{m,l} - \mathbf{1} \right) \\ + \frac{\rho}{2} \left(\sum_{n\in\mathcal{N}} {a_{m,n}}^{(i+1)} + \sum_{l\in\mathcal{L}} b_{m,l} - \mathbf{1} \right)^2 \Bigg], \end{aligned} \tag{44}$$

$$\begin{aligned} \gamma^{(i+1)} = \arg\min_\gamma \Bigg[\text{P3}' \left({a_{m,n}}^{(i+1)}, {b_{m,l}}^{(i+1)} \right) + (\gamma)^T \left(\sum_{n\in\mathcal{N}} {a_{m,n}}^{(i+1)} + \sum_{l\in\mathcal{L}} {b_{m,l}}^{(i+1)} - \mathbf{1} \right) \\ + \frac{\rho}{2} \left(\sum_{n\in\mathcal{N}} {a_{m,n}}^{(i+1)} + \sum_{l\in\mathcal{L}} {b_{m,l}}^{(i+1)} - \mathbf{1} \right)^2 \Bigg]. \end{aligned} \tag{45}$$

The termination condition, defined by $\left\| a^{(i+1)} - a^{(i)} \right\| \le \varepsilon_{d2}$, $\left\| b^{(i+1)} - b^{(i)} \right\| \le \varepsilon_{d1}$, is satisfied when the algorithm stops or reaches the limit of iterations I. In this section, the original problem is solved by transforming the discrete variables into continuous variables so that the nonlinear problem P3 is turned into a linear problem and an explanation is given. Now, the continuous variable is reduced to a binary variable taking values a and b. The specific recovery method is as follows:

$$a^* = \begin{cases} 1, & \text{if } a_{m,n} = \max\{a_{m,n}, b_{m,l}\}, \forall m, n, l \\ 0, & \text{otherwise} \end{cases}. \tag{46}$$

We denote the binary variable as $\wedge^* = \{a^*, b^*\}$. The method for solving P3 is detailed in Algorithm 1.

Algorithm 1. ADMM for solving P3.

Input: $M, N, \varepsilon_{d2}, \varepsilon_{d1}$.
Initialize: $a^{(0)}, b^{(0)}, f^{(0)} = \left\{f_{m,n}{}^{(0)}, f_{m,l}{}^{(0)}\right\}, \beta^{(0)}, i = 0$.
Repeat:
    update the global variable $a^{(i+1)}$ according to Eq. (43),
    update the global variable $b^{(i+1)}$ according to Eq. (44),
    update the global variable $\gamma^{(i+1)}$ according to $a^{(i+1)}$, $b^{(i+1)}$, and Eq. (45).
$i = i + 1$
until $||a^{(i+1)} - a^{(i)}||_2 \leq \varepsilon_{d2}$, $||b^{(i+1)} - b^{(i)}||_2 \leq \varepsilon_{d1}$.
Output the optimized solutions a^* and b^*.

4.4. Overall algorithm convergence and complexity analysis

The algorithm iteratively solves three subproblems, refining the solution at each step. By introducing relaxation and approximation, the iterative updates converge to near-optimal results. Algorithm 2 outlines the iterative process for solving the overall optimization problem P. In each iteration, when we fix two of the variable blocks, the remaining single subproblem is usually convex or can be transformed into a convex problem. This means that solving each subproblem strictly reduces the total system cost. Since there is a lower bound on the total cost determined by system constraints, the cost sequence generated by the algorithm is monotonically decreasing and bounded below, which guarantees that the algorithm will converge to a stable point. Similar alternating schemes have also been shown to converge efficiently in existing literature [24,36]. Algorithm 2 outlines the iterative process for solving the overall optimization problem P. A more detailed convergence proof is as follows:

First, in the r-th iteration, for a given $\{\wedge^r = \{a^r, b^r\}\}$, we obtain

$$Q\left(\beta^{(r)}, f^{(r)}, \Lambda^{(r)}\right) \geq Q\left(\beta^{(r+1)}, f^{(r)}, \Lambda^{(r)}\right). \tag{47}$$

Second, for a given $\{\beta^{(r)}, \wedge^r = \{a^r, b^r\}\}$, by obtaining the optimal computing CPU frequency through Eqs (37) and (38), we get

$$Q\left(\beta^{(r+1)}, f^{(r)}, \Lambda^{(r)}\right) \geq Q\left(\beta^{(r+1)}, f^{(r+1)}, \Lambda^{(r)}\right). \tag{48}$$

Third, in the ADMM-based Algorithm 1, the objective value L of problem P3 decreases monotonically with the iteration index i:

$$L_\rho\left(a^{(i)}, b^{(i)}\right) \geq L_\rho\left(a^{(i+1)}, b^{(i+1)}\right), \tag{49}$$

$$L_\rho\left(a^{(i+1)}, b^{(i)}\right) \geq L_\rho\left(a^{(i+1)}, b^{(i+1)}\right), \tag{50}$$

$$L_\rho\left(a^{(i)}, b^{(i+1)}\right) \geq L_\rho\left(a^{(i+1)}, b^{(i+1)}\right). \tag{51}$$

Algorithm 2. AOTORA for solving P.

Input: $\varepsilon, r = 0, \beta^{(0)}, f^{(0)} = \left\{f_{m,n}{}^{(0)}, f_{m,l}{}^{(0)},\right\}, \wedge^{(0)} = \left\{a^{(0)}, b^{(0)}\right\}$.
Repeat:
    solve for $\beta^{(r+1)}$via the CVX toolbox with given $a^{(r)}$ and $b^{(r)}$,
    solve for $f^{(r+1)}$ via the Lagrange multiplier method with given $a^{(r)}$ and $b^{(r)}$,
    solve for $\wedge^{(r+1)}$ by Algorithm 1.
$r = r + 1$
until $|Q^{(r+1)}(\beta, f, \wedge) - Q^{(r+1)}(\beta, f, \wedge)|_2 \leq \varepsilon$.
Binary variables a and b recovery.
Output the optimized solutions $\beta^{(r+1)^*}$,$f^{(r+1)^*}$, $\wedge^{(r+1)^*}$.

Therefore, for a given $\{\beta^{(r+1)}, f^{(r+1)} = \{f_{m,n}{}^{(r+1)}, f_{m,l}{}^{(r+1)}\}\}$, it has the following relationship:

$$Q\left(\beta^{(r+1)}, f^{(r+1)}, \Lambda^{(r)}\right) \geq Q\left(\beta^{(r+1)}, f^{(r+1)}, \Lambda^{(r+1)}\right). \tag{52}$$

Based on the above analysis, we can conclude that

$$Q\left(\beta^{(r)}, f^{(r)}, \Lambda^{(r)}\right) \geq Q\left(\beta^{(r+1)}, f^{(r+1)}, \Lambda^{(r+1)}\right). \tag{53}$$

The convergence of Algorithm 2 is guaranteed by the following two points: on the one hand, its objective function value E decreases monotonically with the number of iterations r; on the other hand, the algorithm always keeps the solution within the feasible domain that satisfies all IoT device constraints. Therefore, it can be proven that Algorithm 2 has convergence properties.

Next, we evaluate the complexity of the AOTORA algorithm. We use the CVX toolbox to solve problem P1, and its computational complexity is $O(MN)$. We solve problem P2 using the KKT conditions obtained through the Lagrange multiplier method, with the complexity denoted as $O(2M + N + 1)$. In problem P3, the optimization involves $3M$ variables and $3M(N + 1)$ constraints, and its complexity is $O(3M(3M(N + 1)))$. In summary, the full complexity per iteration of the AOTORA algorithm is $O(MN+2M+N+1+3M(3M(N+1)))$, and the overall algorithm complexity is $R \cdot O(MN + 2M + N + 1 + 3M(3M(N + 1))) = R \cdot O(M^2)$, where R represents the final iteration count of Algorithm 2.

Finally, the alternating optimization (AO) framework adopted in this paper is theoretically based on the block coordinate descent method [1]. The core idea of this principle is to approximate the optimal solution of the original problem by decomposing a complex joint optimization problem into several easier-to-solve subproblems and sequentially optimizing individual blocks of variables while keeping the others fixed. Compared with ESAO algorithm of Xie et al. [39], AO achieves directional development through systematic variable rotation, whereas ESAO relies on random mutations for global exploration. The two algorithms are thus suitable for problems with a clear structure and a black-box complexity, respectively. This study is further inspired by Liu et al.'s [20,21] predict-then-optimize hybrid architecture. In the future, combining the AO framework with time-series prediction models is planned to enable a shift from passive response to proactive planning, promoting the evolution of air-space-ground network optimization toward anticipatory decision-making.

5. Performance evaluation

5.1. Simulation setup

We examine the performance of the alternating iteration algorithm with guaranteed convergence by setting up an experimental environment, proving the effectiveness and convergence of the proposed AOTORA algorithm through simulation, and comparing it with other benchmark algorithms in different environments to evaluate its performance. The other primary parameters involved in the experiments are shown in Table 2 [3,7,16,18,37].

Table 2. System parameters

Parameter	Value	Parameter	Value
M	30	B^n	40 MHz
N	9	B^l	5 GHz
h	50 m	$F_n^{\max}$	3 Gcycles/s
κ	2	$F_l^{\max}$	8 Gcycles/s
D_m	[3,6] MB	p^m	1 W
λ_m	[100,300] Mcycle	p^n	5 W
γ_0	–60	p^l	10 W
θ	25 C°	$h_{m,l}$	700 km

In this paper, MATLAB is employed for simulation. Three LEO satellites are flying an area of 1000 m × 1000 m at an altitude of 700 km with the orbit altitude of $h_{m,l}$ = 700 km. The distance between UD m and LEO satellite l is $d_{m,l}$. M UDs and N UAVs are randomly placed in the predetermined region. Assuming that UAVs are hovering at a set altitude h, the channel power gain γ_0 at a reference distance of 1 m is set to –60 dB, the path loss exponent for the UD–UAV link is $\kappa = 2$, each UD transmits with a power of 1 W, whereas the UAV and the satellite transmit with powers of 5 W and 10 W, respectively. The noise power is 10^{-13} W. The task size and computational cycle requirements for each UD are randomly set within a fixed interval.

5.2. Simulation results and performance analysis

The article compares the algorithm proposed in this paper with four benchmark algorithms, including random optimization (RO) [5], centralized offloading scheme (COS) [5], equal bandwidth allocation (EBA) [43], offloading low-earth-orbit satellite (OLS) [40], and distributionally robust optimization (DRO) [35]. RO means that the ground user randomly offloads self-generated tasks to the UAV or satellite with equal probability. In the COS scheme, the ground-based cloud data center serves as the central coordinator of the inputs, and the interior point method is used to solve the optimization problem. EBA means that all users perform computational offloading with the UAV, providing equal bandwidth communication services. OLS means that all UDs will offload their own generated tasks to the satellite. DRO introduces a robust optimization baseline with a box uncertainty set [44], adjusting the key model parameter, channel gain H_m^n and H_m^l, to fluctuate up and down by ±10%.

Figure 2a illustrates the relationship between the normalized system cost Q and the weighting factor $\bar{\omega}$ under different weights and various user tasks. It can be observed that as the delay weighting factor increases, the Q value also increases. Since the optimization objectives of delay and energy consumption conflict with each other, a normalization method is used for the solution. Regardless of how the weighting factor changes, the optimized value Q remains within a certain range and does not fluctuate significantly.

Figure 2b analyzes the convergence and sensitivity to initial conditions of the AOTORA algorithm proposed in this paper. Simulation results show that regardless of changes in the weighting factors, the proposed algorithm consistently decreases rapidly during the early iterations and stabilizes after the fifth iteration. In addition, we exchanged the iteration order of the three subproblems in 4.1, 4.2, and 4.3 (hereafter denoted as A, B, and C, respectively), and the experimental results indicate that the final results remain stable, with fluctuations of the optimization problem P value Cost staying within 1%. In Fig. 3a, we present a sensitivity analysis of the key penalty parameter ρ on the system's AOTORA algorithm. The experiments show that, as the penalty parameter ρ increases, the convergence speed accelerates, but the overall final Cost value remains essentially unchanged. The above results demonstrate its robustness and also indicate that the proposed AOTORA algorithm has good convergence performance.

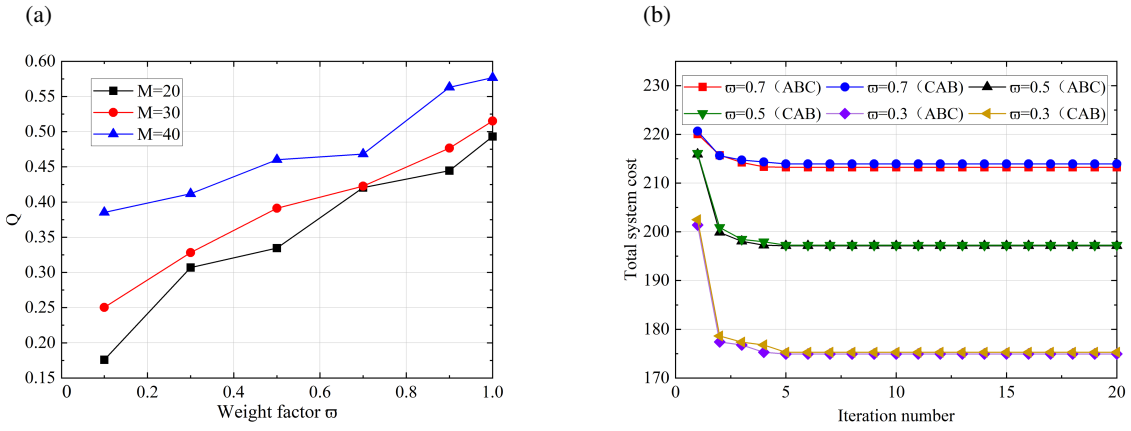

Fig. 2. Performance of AOTORA algorithm: comparison of Q values for different $\bar{\omega}$ and different device quantities (a) and sensitivity analysis of AOTORA algorithm performance to different weight factors and iteration orders (b).

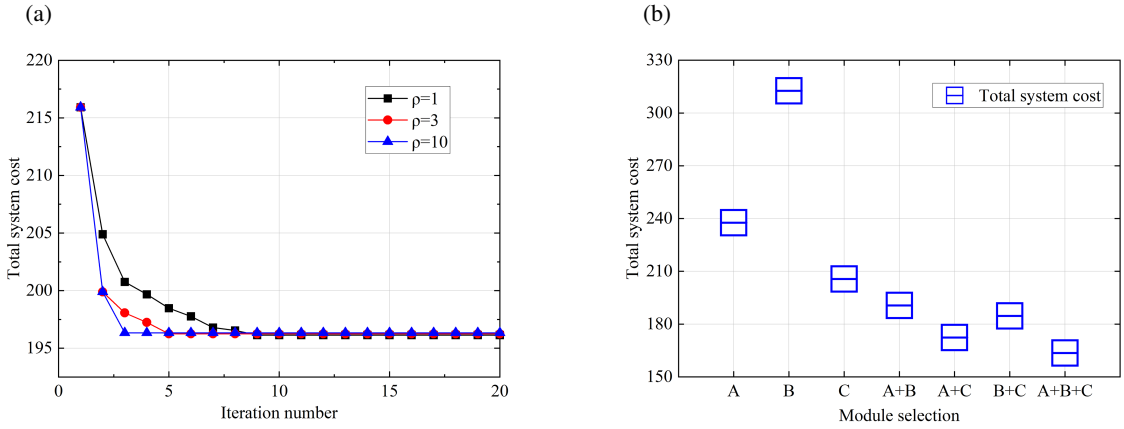

Fig. 3. Performance of AOTORA algorithm: sensitivity analysis of the system with respect to the penalty factor ρ (a) and ablation study comparison of each subproblem and its combination modules (b).

Figure 3b evaluates the optimization contributions of each subproblem and its combined modules through an ablation study. The experimental results show that when only a single module participates in the optimization, subproblem C has the largest contribution, indicating that offloading scheduling has a significant impact on the delay and energy consumption of computation offloading. Next, when two submodules participate together, their contributions are higher than that of a single module, with subproblems A and C contributing more, suggesting that bandwidth allocation has a secondary influence on the optimization objective. Finally, when all three submodules participate in the optimization, the optimization value is minimized, and the contribution is maximized, indicating that computing resources are the third influencing factor.

Figure 4a describes the relationship between the number of UDs in different algorithms and the total system cost. It is easy to see that as the number of UDs increases, the total system computation cost also becomes higher. First, the RO algorithm has a larger total computation cost because the system's allocation for bandwidth or offloading scheduling is probabilistic and random. Second, although the EBA algorithm uses ADMM to seek an optimal offloading schedule, communication between users and UAVs uses equal bandwidth, which, to some extent, increases the total system cost. In contrast, for the OLS algorithm, the calculation offloading cost for satellites is higher than that for UAVs due to distance factors. For the DRO algorithm, channel fluctuations degrade link quality, reducing computation task transmission, and the system needs to invoke more computational resources to compensate, ultimately leading to a higher total system cost. Therefore, based on the above analysis and simulation results, the proposed AOTORA scheme reduces the average cost by 25.8% compared with the RO algorithm, by 12.48% compared with the OLS algorithm, by 11.63% compared with the EBA algorithm, and by 6.48% compared with the DRO algorithm. Compared with other methods, the AOTORA scheme shows slower growth in system computation cost and can effectively reduce the total cost of computation tasks.

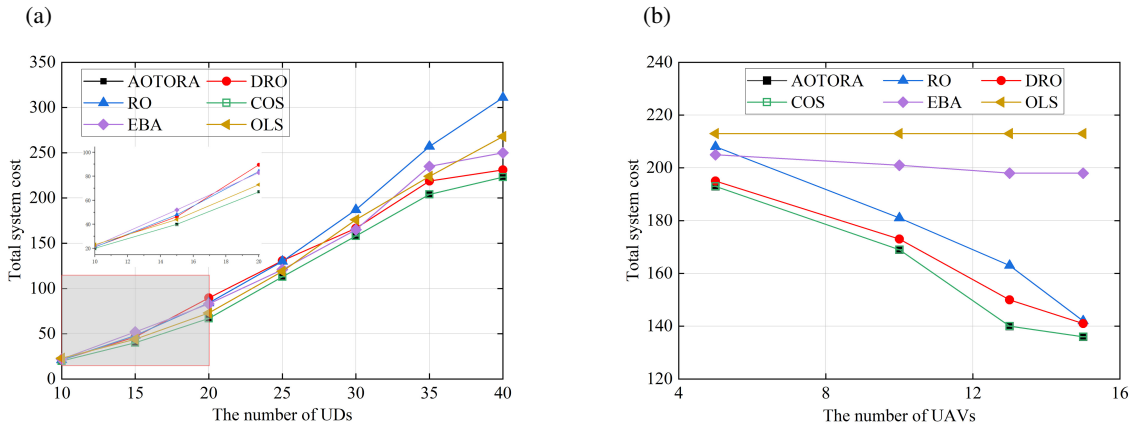

Fig. 4. Performance of AOTORA algorithm: relationship between number of devices and total system cost (a) and relationship between UAV quantity and total system cost (b).

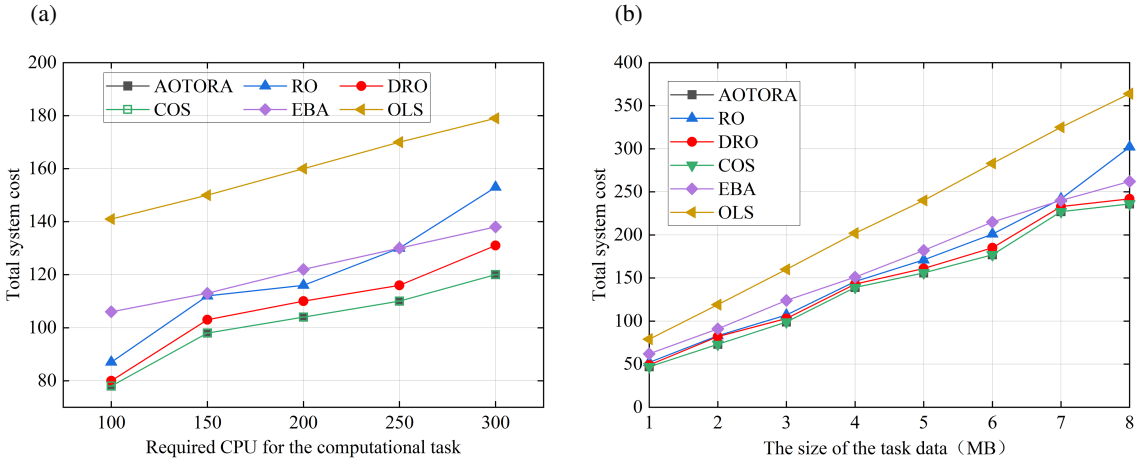

Fig. 5. Performance of AOTORA algorithm: comparison of task CPU frequency and total system cost (a) and comparison of task size and total system cost (b).

Figure 4b describes the relationship between the number of UAVs and the total system cost under different algorithms. We can observe that the AOTORA algorithm outperforms the RO, OLS, and EBA algorithms. First, as the number of UAVs increases, the total system cost decreases. This is because with more UAVs, the computational resources in the system increase, allowing more tasks to be offloaded to UAVs for processing, thereby reducing the total system cost. The channel fluctuations in the DRO algorithm can increase the overhead to some extent. However, there is a certain cost associated with devices processing tasks, so when the number of UAVs reaches 15, the total system costs of the AOTORA, COS, RO, and DRO algorithms are relatively close. Second, due to the average allocation of bandwidth in the EBA algorithm, the cost difference of processing tasks on UAVs and satellites is small, so an increase in the number of UAVs has little impact on the algorithm's performance. Finally, since tasks are not offloaded to UAVs in the OLS algorithm, increasing the number of UAVs does not affect the algorithm's performance.

Figure 5a illustrates the relationship between the number of CPU cycles required for computing tasks and the total system cost under different algorithms. We can observe that as the number of CPU cycles required by computing tasks increases, the total system computing cost for each algorithm also rises. Specifically, the OLS algorithm has higher computing costs than the other algorithms due to distance factors; the simulation results for the RO algorithm fluctuate more because of its randomness, and the DRO algorithm shows variations due to channel fluctuations, sometimes falling below or exceeding the EBA algorithm. Overall, compared with the RO, OLS, and EBA algorithms, the AOTORA algorithm proposed in this paper demonstrates better performance and can effectively reduce the total system computing cost.

Figure 5b describes the relationship between system task data size and total system cost. As shown in Fig. 5b, the proposed AOTORA algorithm is compared with other schemes. It can be observed that as the task scale increases, the total system cost increases in all five optimization algorithms. This is because, for ground users, whether offloading tasks to UAVs or satellite devices, the total system cost is related to the task scale and increases as the task scale grows. However, as the data volume increases, compared to the random allocation and scheduling in RO, the idle UAV computing resources in OLS, and the equal-bandwidth transmission in EDA, the proposed AOTORA algorithm jointly optimizes bandwidth allocation, computing resource allocation, and user scheduling, more effectively reducing the total computation cost for users. In addition, the curve of the proposed AOTORA algorithm is almost identical to that of the COS algorithm, indicating that the proposed computation offloading strategy can achieve the optimal solution of the COS algorithm.

Figure 6 illustrates the total computing costs of five optimization algorithms (AOTORA, RO, OLS, EBA, and DRO) and the distribution of total system costs for different algorithms. It can be seen from the figure that for the RO and EBA algorithms, a larger portion of users' total computing costs is distributed on LEO satellites, while the OLS algorithm offloads all user tasks to LEO satellites, which undoubtedly increases the system's total cost. In the DRO algorithm, the offloading proportion between UAVs and satellites is balanced, whereas the AOTORA algorithm offloads a

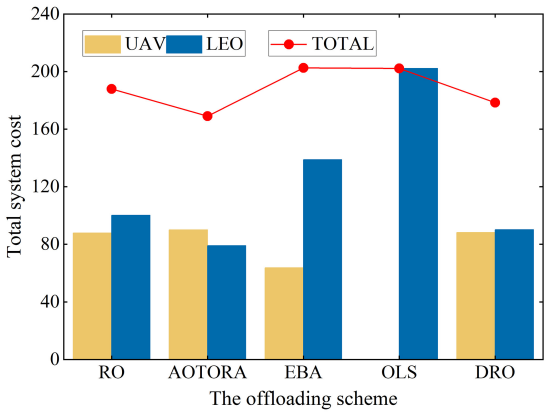

Fig. 6. Distribution of computing costs under different mechanisms.

larger proportion of tasks to UAVs, resulting in lower system overhead. Its total cost is lower than that of the other four algorithms because UAVs, compared to satellites, have certain computing resources and lower costs, playing a key role in this system.

5.3. Applicability and adaptability analysis

The AOTORA algorithm achieves effective control of computational complexity by decomposing complex problems into independent subproblems, such as resource allocation and task scheduling. Simulations show that its solution time grows approximately linearly with the number of users, rather than exponentially. This means that whether in small local networks or large-scale networks covering wide areas, the algorithm can complete optimization within an acceptable time, possessing the ability to cope with dynamic network expansion and contraction.

Although the algorithm relies on perfect, static channel conditions, it operates under periodic constraints. Before the start of a cycle in the joint optimization framework, when the quality of a link (such as a satellite link) is monitored, the algorithm selects high-quality channels, thereby adjusting task offloading decisions and resource allocation schemes to maintain overall performance. The algorithm's optimization objective – a weighted sum of delay and energy consumption – serves as a flexible regulator itself. The network can directly adjust the weights according to the priority of services in different scenarios. For example, in emergency rescue, low latency is prioritized, while in routine monitoring, low energy consumption is prioritized, meeting the diverse needs of real-world applications.

6. Conclusion and future work

This paper investigates the problem of remote IoT task offloading and resource allocation for LEO satellites under a dual-layer heterogeneous network collaborative architecture, considering their high mobility and dynamically changing channel environment, with the goal of minimizing the total computation cost for UDs. To address the complex MINLP problem, the optimization problem is decomposed into different subproblems, which are solved individually. An AOTORA algorithm based on the space-air dual-layer network architecture is proposed. Simulation results show that the proposed scheme outperforms other benchmark schemes in both small-scale and large-scale scenarios. In terms of the average total computation cost for users, it reduces costs by 12.48%, 25.8%, 11.63%, and 6.84% compared with OLS, RO, EBA, and DRO, respectively. Despite these achievements, this work is based on a static resource allocation framework within a single time slot and does not account for the dynamic randomness of tasks and the ultra-large-scale networks characteristic of IoT scenarios. Therefore, in our future work, we will study a multi-time-slot dynamic optimization framework that incorporates task data dependencies and user mobility models to enhance long-term computation adaptability.

Data availability statement

Data sharing is not applicable to this article as no new data were created or analyzed in this study.

Acknowledgments

This work was supported by the Key Project of the Henan Province Science and Technology Research and Development Program Joint Fund (grants No 235200810040 and 231111221500), the Major Science and Technology Projects of the Longmen Laboratory (grant No. 231100220500), the National Natural Science Foundation of China (grant No. 62072158), and in part by the Henan Province Science and Technology Project (grant No. 242102210192). The publication costs of this article were partially covered by the Estonian Academy of Sciences.

References

1. Bertsekas, D. *Convex Optimization Theory*. Athena Scientific, Belmont, Massachusetts, 2009.
2. Boyd, S. and Vandenberghe, L. Localization and cutting-plane methods. *Stanford EE 364b Lecture Notes*, 2007, **386**, 2.
3. Chen, B., Li, N., Li, Y., Tao, X. and Sun, G. Energy efficient hybrid offloading in space-air-ground integrated networks. In *2022 IEEE Wireless Communications and Networking Conference (WCNC), Austin, TX, USA, 10–13 April 2022*. IEEE, 2022, 1319–1324. https://doi.org/10.1109/WCNC51071.2022.9771798
4. Chen, J.-H., Kuo, W.-C. and Liao, W. SpaceEdge: optimizing service latency and sustainability for space-centric task offloading in LEO satellite networks. *IEEE Transactions on Wireless Communications*, 2024, **23**(10), 15435–15446. https://doi.org/10.1109/TWC.2024.3429510
5. Chen, X., Zhang, H., Wu, C., Mao, S., Ji, Y. and Bennis, M. Optimized computation offloading performance in virtual edge computing systems via deep reinforcement learning. *IEEE Internet of Things Journal*, 2019, **6**(3), 4005–4018. https://doi.org/10.1109/JIOT.2018.2876279
6. Chen, Y., Ai, B., Niu, Y., Zhang, H. and Han, Z. Energy-constrained computation offloading in space-air-ground integrated networks using distributionally robust optimization. *IEEE Transactions on Vehicular Technology*, 2021, **70**(11), 12113–12125. https://doi.org/10.1109/TVT.2021.3116593
7. Chen, Z., Zhou, H., Du, S., Liu, J., Zhang, L. and Liu, Q. Reinforcement learning-based resource allocation and energy efficiency optimization for a space-air-ground-integrated network. *Electronics*, 2024, **13**(9), 1792. https://doi.org/10.3390/electronics13091792
8. Cheng, N., Lyu, F., Quan, W., Zhou, C., He, H., Shi, W. et al. Space/aerial-assisted computing offloading for IoT applications: a learning-based approach. *IEEE Journal on Selected Areas in Communications*, 2019, **37**(5), 1117–1129. https://doi.org/10.1109/JSAC.2019.2906789
9. Grant, M., Boyd, S. and Ye, Y. *CVX: Matlab software for disciplined convex programming*. Stanford University, Stanford, CA, USA, 2008.
10. He, L., Li, J., Wang, Y., Zheng, J. and He, L. Balancing total energy consumption and mean makespan in data offloading for space-air-ground integrated networks. *IEEE Transactions on Mobile Computing*, 2024, **23**(1), 209–222. https://doi.org/10.1109/TMC.2022.3222848
11. Jiang, H., Lee, Y. T., Song, Z. and Wong, S. C.-w. An improved cutting plane method for convex optimization, convex-concave games, and its applications. In *Proceedings of the 52nd Annual ACM SIGACT Symposium on Theory of Computing,* 2020, 944–953. https://doi.org/10.1145/3357713.3384284
12. Kers, J., Majak, J., Goljandin, D., Gregor, A., Malmstein, M. and Vilsaar, K. Extremes of apparent and tap densities of recovered GFRP filler materials. *Composite Structures*, 2010, **92**(9), 2097–2101. https://doi.org/10.1016/j.compstruct.2009.10.003
13. Kong, L., Tan, J., Huang, J., Chen, G., Wang, S., Jin, X. et al. Edge-computing-driven Internet of Things: a survey. *ACM Computing Surveys*, 2022, **55**(8), 1–41. https://doi.org/10.1145/3555308
14. Laghari, A. A., Wu, K., Laghari, R. A., Ali, M. and Khan, A. A. Retracted article: A review and state of art of Internet of Things (IoT). *Archives of Computational Methods in Engineering*, 2022, **29**(3), 1395–1413. https://doi.org/10.1007/s11831-021-09622-6
15. Li, J., Shi, Y., Dai, C., Yi, C., Yang, Y., Zhai, X. et al. A learning-based stochastic game for energy efficient optimization of UAV trajectory and task offloading in space/aerial edge computing. *IEEE Transactions on Vehicular Technology*, 2025, **74**(6), 9717–9733. https://doi.org/10.1109/TVT.2025.3540964
16. Li, S., Li, W., Zheng, W., Xia, Y., Guo, K., Peng, Q. et al. Multi-user joint task offloading and resource allocation based on mobile edge computing in mining scenarios. *Scientific Reports*, 2025, **15**, 16170. https://doi.org/10.1038/s41598-025-00730-y
17. Li, W., Li, S., Hao, J., Wu, Q. and Wang, R. Efficient task offloading and resource allocation in space-air-ground-sea networks: a MAPPO-based approach. In *Wireless Artificial Intelligent Computing Systems and Applications. WASA 2025. Lecture Notes in Computer Science* (Cai, Z., Zhu, Y., Wang, Y. and Qiu, M., eds). Springer, Singapore, 2025, **15688**, 117–126. https://doi.org/10.1007/978-981-96-8731-2_12
18. Liao, Z., Ma, Y., Huang, J., Wang, J. and Wang, J. HOTSPOT: a UAV-assisted dynamic mobility-aware offloading for mobile-edge computing in 3-D space. *IEEE Internet of Things Journal*, 2021, **8**(13), 10940–10952. https://doi.org/10.1109/JIOT.2021.3051214
19. Liu, J., Shi, Y., Fadlullah, Z. M. and Kato, N. Space-air-ground integrated network: a survey. *IEEE Communications Surveys & Tutorials*, 2018, **20**(4), 2714–2741. https://doi.org/10.1109/COMST.2018.2841996
20. Liu, J., Hou, Z., Liu, B. and Zhou, X. Mathematical and machine learning innovations for power systems: predicting transformer oil temperature with beluga whale optimization-based hybrid neural networks. *Mathematics*, 2025, **13**(11), 1785. https://doi.org/10.3390/math13111785
21. Liu, J., Hou, Z., Wang, B. and Yin, T. Optimizing microgrid energy management via DE-HHO hybrid metaheuristics. *Computers, Materials & Continua*, 2025, **84**(3). https://doi.org/10.32604/cmc.2025.066138
22. Liu, Y., Jiang, L., Qi, Q. and Xie, S. Energy-efficient space–air–ground integrated edge computing for Internet of Remote Things: a federated DRL approach. *IEEE Internet of Things Journal*, 2023, **10**(6), 4845–4856. https://doi.org/10.1109/JIOT.2022.3220677
23. Mach, P. and Becvar, Z. Mobile edge computing: a survey on architecture and computation offloading. *IEEE Communications Surveys & Tutorials*, 2017, **19**(3), 1628–1656. https://doi.org/10.1109/COMST.2017.2682318
24. Mao, S., He, S. and Wu, J. Joint UAV position optimization and resource scheduling in space-air-ground integrated networks with mixed cloud-edge computing. *IEEE Systems Journal*, 2021, **15**(3), 3992–4002. https://doi.org/10.1109/JSYST.2020.3041706
25. Maray, M. and Shuja, J. [Retracted] Computation offloading in mobile cloud computing and mobile edge computing: survey, taxonomy, and open issues. *Mobile Information Systems*, 2022, **2022**(1), 1121822. https://doi.org/10.1155/2022/1121822
26. Mei, C., Gao, C., Wang, H., Xing, Y., Ju, N. and Hu, B. Joint task offloading and resource allocation for space–air–ground col-

laborative network. *Drones*, 2023, **7**(7), 482. https://doi.org/10.3390/drones7070482
27. Qi, X., Chong, J., Zhang, Q. and Yang, Z. Collaborative computation offloading in the multi-UAV fleeted mobile edge computing network via connected dominating set. *IEEE Transactions on Vehicular Technology*, 2022, **71**(10), 10832–10848. https://doi.org/10.1109/TVT.2022.3188554
28. Ren, C., Zhang, G., Gu, X. and Li, Y. Computing offloading in vehicular edge computing networks: full or partial offloading?. In *2022 IEEE 6th Information Technology and Mechatronics Engineering Conference (ITOEC), Chongqing, China, 4–6 March 2022*. IEEE, 2022, 693–698. https://doi.org/10.1109/ITOEC53115.2022.9734360
29. Sadeeq, M. M., Abdulkareem, N. M., Zeebaree, S. R., Ahmed, D. M., Sami, A. S. and Zebari, R. R. IoT and cloud computing issues, challenges and opportunities: a review. *Qubahan Academic Journal*, 2021, **1**(2), 1–7. https://doi.org/10.48161/qaj.v1n2a36
30. Satyanarayanan, M., Bahl, P., Caceres, R. and Davies, N. The case for VM-based cloudlets in mobile computing. *IEEE Pervasive Computing*, 2009, **8**(4), 14–23. https://doi.org/10.1109/MPRV.2009.82
31. Shang, B., Yi, Y. and Liu, L. Computing over space-air-ground integrated networks: challenges and opportunities. *IEEE Network*, 2021, **35**(4), 302–309. https://doi.org/10.1109/MNET.011.2000567
32. Shen, S., Shen, G., Dai, Z., Zhang, K., Kong, X. and Li, J. Asynchronous federated deep-reinforcement-learning-based dependency task offloading for UAV-assisted vehicular networks. *IEEE Internet of Things Journal*, 2024, **11**(19), 31561–31574.
33. Sriharsha, C. and Murthy, C. S. R. Energy-efficient computation offloading in 6G space-air-ground integrated networks. In *2022 IEEE International Conference on Advanced Networks and Telecommunications Systems (ANTS), Gandhinagar, Gujarat, India, 18–21 December 2022*. IEEE, 2023, 1–6. https://doi.org/10.1109/ANTS56424.2022.10227801
34. Su, J., Yu, S., Li, B. and Ye, Y. Distributed and collective intelligence for computation offloading in aerial edge networks. *IEEE Transactions on Intelligent Transportation Systems*, 2023, **24**(7), 7516–7526. https://doi.org/10.1109/TITS.2022.3160594
35. Sun, J., Chen, X., Jiang, C. and Guo, S. Distributionally robust optimization of on-orbit resource scheduling for remote sensing in space-air-ground integrated 6G networks. *IEEE Journal on Selected Areas in Communications*, 2025, **43**(1), 382–395. https://doi.org/10.1109/JSAC.2024.3460057
36. Tang, Q., Fei, Z., Li, B. and Han, Z. Computation offloading in LEO satellite networks with hybrid cloud and edge computing. *IEEE Internet of Things Journal*, 2021, **8**(11), 9164–9176. https://doi.org/10.1109/JIOT.2021.3056569
37. Wang, N., Li, F., Chen, D., Liu, L. and Bao, Z. NOMA-based energy-efficiency optimization for UAV enabled space-air-ground integrated relay networks. *IEEE Transactions on Vehicular Technology*, 2022, **71**(4), 4129–4141. https://doi.org/10.1109/TVT.2022.3151369
38. Wang, X., Chen, H. and Tan, F. Hybrid OMA/NOMA mode selection and resource allocation in space-air-ground integrated networks. *IEEE Transactions on Vehicular Technology*, 2024. https://doi.org/10.1109/TVT.2024.3452477
39. Xie, J., He, J., Gao, Z., Wang, S., Liu, J. and Fan, H. An enhanced snow ablation optimizer for UAV swarm path planning and engineering design problems. *Heliyon*, 2024, **10**(18, e37819). https://doi.org/10.1016/j.heliyon.2024.e37819
40. Xu, S., Li, X., Zhang, J., Li, F., Liang, Y. and Hao, S. Bilateral collaborative computing offloading via LEO satellites for remote network applications. *Computer Networks*, 2025, **261**, 111124. https://doi.org/10.1016/j.comnet.2025.111124
41. Zhang, J., Zhang, J., Shen, F., Yan, F. and Bu, Z. DOGS: dynamic task offloading in space-air-ground integrated networks with game-theoretic stochastic learning. *IEEE Internet of Things Journal*, 2025, **12**(2), 1655–1672. https://doi.org/10.1109/JIOT.2024.3457855
42. Zhang, L., Xie, Y., Chen, J., Feng, L., Chen, C. and Liu, K. A study on multiform multi-objective evolutionary optimization. *Memetic Computing*, 2021, **13**(3), 307–318. https://doi.org/10.1007/s12293-021-00331-y
43. Zhang, Y., Na, Z., Wen, Z., Nallanathan, A. and Lu, W. Joint service caching, computation offloading and resource allocation for dual-layer aerial Internet of Things. *Computer Networks*, 2025, **257**, 110974. https://doi.org/10.1016/j.comnet.2024.110974
44. Zhong, L., Liu, Y., Deng, X., Wu, C., Liu, S. and Yang, L. T. Distributed optimization of multi-role UAV functionality switching and trajectory for security task offloading in UAV-assisted MEC. *IEEE Transactions on Vehicular Technology*, 2024, **73**(12), 19432–19447. https://doi.org/10.1109/TVT.2024.3434354

Ühiste tööülesannete allalaadimine ja ressursijaotus kaug-IoT jaoks kosmos-õhk-maa võrkude arhitektuuris

Zhenhua Li, Guoqiang Zheng, Zhe Han, Pingjie Xia, Huahong Ma ja Baofeng Ji

Piirkondades, kus maismaataristu on ebapiisav, on kasutajaseadmetel piiratud arvutusressursid, mistõttu lühikese viivituse ja energiatõhusa andmetöötluse tagamine osutub keeruliseks. Selle probleemi lahendamiseks pakub käesolev töö välja kahekihilise heterogeense võrguarhitektuuri, mis kasutab mehitamata õhusõidukite ja Maa-lähedase orbiidi (LEO) satelliitide arvutusressursse. Arvestades LEO-satelliitide suurt liikuvust, kanali muutlikkuse parameetreid ja tööülesannete allalaadimise järjekorra viivitust, formuleeritakse optimeerimisülesanne mittelineaarse segatüüpi täisarvulise programmeerimise probleemina. Eesmärk on minimeerida viivituse ja energiatarbimise kaalutud summat (st kogu süsteemi kulu). Töös pakutakse välja arvutuslikult lihtne alternatiivne algoritm. Algne probleem jaotatakse kolmeks alamprobleemiks: ribalaiuse jaotus, protsessori taktsageduse jaotus ja ülesannete ajastamise optimeerimine. Need alamülesanded lahendatakse vastavalt kumeroptimeerimise, Lagrange'i kordajate meetodi ja vahelduvate suundadega Lagrange'i kordajate meetodi abil. Lõpuks rakendatakse Pareto optimaalset jaotust parima tasakaalu leidmiseks erinevate optimeerimiskriteeriumide vahel. Arvutustulemused näitavad, et väljatöötatud AOTORA süsteemi keskmine kogukulu väheneb vastavalt 25,8%, 11,63%, 12,48% ja 6,84% võrreldes stohhastilise optimeerimise, võrdse ribalaiuse jaotuse, LEO-allalaadimisalgoritmi ja jaotuslikult robustse optimeerimisega.

Proceedings of the Estonian Academy of Sciences
2026, **75**, 1, 75–86

https://doi.org/10.3176/proc.2026.1.07

www.eap.ee/proceedings
Estonian Academy Publishers

FOOD MICROBIOLOGY, CELL BIOLOGY

RESEARCH ARTICLE

Received 19 October 2025
Accepted 6 January 2026
Available online 16 February 2026

Keywords:
food safety and quality, *Avena sativa*, maceration assay, membrane filtration, seed germination potential

Corresponding author:
Idriz Vehapi
idrizz.vehapi@gmail.com

Citation:
Millaku, L., Kutleshi, M., Orllati, J. and Vehapi, I. 2026. Microbiological assessment of dry oat (*Avena sativa* L.) seeds before and after maceration. *Proceedings of the Estonian Academy of Sciences*, **75**(1), 75–86. https://doi.org/10.3176/proc.2026.1.07

Microbiological assessment of dry oat (*Avena sativa* L.) seeds before and after maceration

Lulzim Millaku, Mirvete Kutleshi, Jeton Orllati and Idriz Vehapi

Department of Biology, University of Prishtina, George Bush Street, 10 000 Pristina, Republic of Kosovo

ABSTRACT

The aim of this study was to differentiate surface-associated microflora and microorganisms resistant to washing in dry oat (*Avena sativa* L.) seeds and to evaluate the effect of 24 h maceration in sterile distilled water on microbial release. Commercial seed samples were processed aseptically in the microbiology laboratory. Two experimental phases were applied: (i) pre-maceration, where seeds were briefly rinsed in sterile distilled water and the suspension was analyzed for surface-associated microorganisms, and (ii) post-maceration, where seeds were soaked for 24 h, allowing the release of microorganisms resistant to washing and associated with protected seed-coat niches. Suspensions were filtered through 0.45 µm membranes and cultured on selective and differential media: nutrient agar for heterotrophs, m-Endo agar for total coliforms, m-FC agar for fecal coliforms, Salmonella–Shigella agar for enteric pathogens, and potato dextrose agar (PDA) for yeasts and molds. Results showed that before maceration, the highest microbial load was fecal coliforms (244 CFU/100 mL), followed by heterotrophs and total coliforms (39 CFU/100 mL), while no yeasts or molds were detected. After maceration, microbial counts decreased by 41% for fecal coliforms, 90% for *Salmonella*/*Shigella*, and more than 90% for heterotrophs. These findings indicate that dry oat seeds may harbor potentially harmful microorganisms not only on the surface but also tightly associated with protected structures of the seed coat. The internal presence of microorganisms has important implications for agriculture, as it may adversely affect seed germination and early plant development in the field, thereby reducing growth quality and productivity. Maceration combined with membrane filtration represents a simple and effective approach to detect these risks, with direct relevance for seed quality control and food safety.

Introduction

Cereals represent one of the most important groups of agricultural crops, as they are the main source of energy and food for more than half of the world's population. Their consumption is closely related to food security, economic development, and public health. Among them, oats (*Avena sativa* L.) have gained particular importance over the past decades, not only as a staple food but also for their functional and bioactive values. Oats differ from other cereals due to their rich chemical composition in soluble fibers, especially β-glucans, which contribute to lowering cholesterol and regulating blood glucose levels (Whitehead et al. 2014). In addition, they contain proteins of high biological value, unsaturated lipids, and a wide spectrum of bioactive compounds, including avenanthramides, which show strong antioxidant and anti-inflammatory activity (Peterson 2001). From an agricultural point of view, oats are a crop resistant to cold and humid conditions, making them suitable for regions where wheat or maize provide lower yields. They are widely used as food for humans and animals, as well as in the pharmaceutical and cosmetic industries due to their bioactive composition (Butt et al. 2008). From the perspective of public health, the World Health Organization (WHO 2023a) and the European Food Safety Authority (EFSA 2011) have emphasized the importance of regular consumption of oat β-glucans for the prevention of cardiovascular diseases and type 2 diabetes. Consequently, the global demand for oat-based products has increased significantly, turning oats from a crop once considered modest into a "superfood", highly valued in modern markets (EFSA 2011). The importance of oats is not limited to the nutritional aspect. They also play an essential role in the economy, public health, and industrial

innovation. Furthermore, their agricultural sustainability due to lower requirements for chemical inputs makes them a favorable crop for biodiversity conservation and more ecological production systems. In this research, oat seeds represent not only carriers of genetic information and productive potential of plants but also a small microscopic ecosystem rich in microorganisms. These microorganisms, including bacteria, fungi, and yeasts, are known as the seed microflora and play an important role in the plant life cycle and in the final quality of agricultural production. Many of them perform beneficial functions: some bacteria of the genera *Pseudomonas* and *Bacillus* act as plant probiotic agents by colonizing the seed surface and later the root system, creating a biological shield against soil pathogens (Nelson 2018). However, seed microflora are not always favorable. Seeds often carry pathogenic microorganisms that remain latent during storage and become active after germination, one of the main routes for the spread of diseases in agricultural crops. Among them, fungi of the genera *Fusarium*, *Alternaria*, and *Aspergillus* are the most problematic, as they can produce phytotoxic secondary metabolites that negatively affect the initial metabolism of seeds, impair germination, and reduce seedling vigor. These fungi are known to produce toxins such as trichothecenes, fumonisins, aflatoxins, and alternariol, which interfere with key metabolic processes during early seed development (Desjardins 2006; Logrieco et al. 2009; Munkvold 2009).

Such seed-borne infections affect yield, quality, and food safety. Contaminated products from infected seeds may enter the food chain, causing severe health consequences. For this reason, international organizations such as the Food and Agriculture Organization of the United Nations (FAO) and WHO have set strict limits for the presence of mycotoxins in food products, emphasizing the importance of control starting from the seed stage (FAO n.d.; WHO 2023b). The process of seed colonization by microorganisms is among the most fascinating mechanisms in plant ecology, as it represents the first point of contact between microflora and a biological system that will later develop into a complete plant. This colonization occurs in two main ways: superficial and endophytic. In superficial colonization, microorganisms reside on the seed coat or its outer layers and are able to survive in dry and nutrient-poor conditions due to protective mechanisms against oxidative stress. Some of them become active immediately after seed soaking, releasing hydrolytic enzymes or substances that stimulate germination (Shade et al. 2017). Endophytic colonization is more complex, as microorganisms penetrate the inner tissues of the seed through the micropyle or microscopic injuries during seed formation. Once inside, they may settle in the endosperm or embryo, forming a close association with the future root system. This symbiosis is often beneficial: endophytes may produce hormones such as auxins and cytokinins that stimulate root development or secondary metabolites that increase resistance to biotic and abiotic stress (Truyens et al. 2015). However, confirmation of true endophytic colonization requires rigorous surface sterilization protocols prior to seed grinding, which were not applied in the present study. Infection of seeds by pathogenic microorganisms is one of the most serious challenges in agriculture, as it affects the most critical phase of the plant life cycle, the germination process. Infected seeds often show low germination rates, delayed seedling emergence, and weakness in root and hypocotyl structures. This reduces field uniformity and makes the plant more sensitive to biotic and abiotic stress (Gebeyaw 2020). A direct consequence is the loss of seed vitality. Pathogens such as *Fusarium* spp. or *Alternaria* spp. degrade the nutrient reserves of the endosperm and damage the embryo, causing early seedling death or symptoms such as root rot and necrosis (Munkvold 2009). Some fungi generate phytotoxic toxins that negatively affect the initial metabolism of the seed. These infections can significantly reduce yield, since plants developed from infected seeds often have weaker root systems and limited growth, remaining a continuous source of infection in the field (Dell'Olmo et al. 2023; Uwineza et al. 2024). From the food safety point of view, infected seeds present a great risk because the pathogens frequently produce mycotoxins such as aflatoxins, trichothecenes, and fumonisins – substances with carcinogenic and immunosuppressive effects that pose a serious threat to public health (Desjardins et al. 2007). Despite the legal limits set by international authorities, their practical monitoring remains challenging, especially in developing countries. Recent studies have demonstrated that microbial growth, inhibition, and community stability are strongly influenced by equilibrium processes governed by environmental conditions and substrate availability. Such equilibrium-driven interactions determine the balance between microbial persistence and suppression under different treatment conditions, providing an important conceptual framework for understanding changes in seed-associated microflora (Tenno et al. 2018).

The control of seed infections and the assurance of seed quality require the use of modern methods that enable early detection and effective reduction of microbial load. One of the earliest and still widely used methods is the maceration of seeds under sterile conditions, followed by cultivation on nutrient media. This method allows the identification of microorganisms through the formation of colonies and their morphological characteristics. Although simple and low-cost, the method is time-consuming and has limitations in distinguishing morphologically similar pathogens (Agarwal and Sinclair 1997). Another approach is the use of membrane filters, where the seed extract is filtered and the trapped microorganisms are then cultured on selective media. This method increases the efficiency of detecting pathogens present in low numbers and is particularly useful for microorganisms that are not uniformly distributed within the seed (ISTA 2018). The counting of colony-forming units (CFU) remains the classical quantitative method, which provides a clear idea of the microbial load of seeds and serves as an indicator of potential risks. However, it does not distinguish between pathogenic, harmless, or beneficial microorganisms, limiting its use in precise diagnostics (Nelson 2018). Modern techniques include molecular analyses such as polymerase chain reaction (PCR) and quantitative PCR (qPCR), which enable specific and rapid detection of certain pathogens, even at very low levels, providing results within a few hours (Selcuk et al. 2008; Pecchia et al. 2019). In recent years, high-throughput sequencing approaches, such as Illumina-based analyses, have been increasingly applied to investigate microbial community structure, growth dynamics, and inhibition mechanisms under different environmental and processing conditions, providing a deeper understanding of microbial interactions beyond culture-based methods (Kallistova et al. 2021). Based on the literature and the importance of seed microflora for plant health and food safety, the objective of this research is to analyze the presence and diversity of microorganisms in oat (*Avena sativa*) seeds. Our study focuses on identifying the main microbial groups associated with seed quality and safety, including total heterotrophic bacteria, total coliform bacteria, fecal coliforms, as well as dangerous pathogenic microorganisms such as *Salmonella* and *Shigella*. Particular attention has also been given to analyzing the presence of fungi, including yeasts and molds, which are often associated with reduced seed vitality and the production of mycotoxins. The final goal of this study is to evaluate the level of microbial load in oat seeds and the potential impact of these microorganisms on food safety. The results obtained aim to contribute to a deeper understanding of the role of seed microflora, the identification of possible sources of contamination, and the creation of a foundation for safer practices of seed storage and utilization in agriculture and the food industry. This study provides a clear overview of the hygienic-microbiological condition of *Avena sativa* seeds, aiming to strengthen preventive measures for consumer protection.

Materials and methods

Selection of plant material

For this study, oat seeds (*Avena sativa*) were used, obtained from a cereal storage facility importing grain from abroad. The selected samples were packaged and analyzed at the Microbiology Laboratory of the Department of Biology, Faculty of Mathematical and Natural Sciences, University of Prishtina, where standard microbiological analyses were performed, including the enumeration of total coliforms, fecal coliforms, *Salmonella*/*Shigella*, heterotrophic bacteria, and fungi, using selective culture media. After sampling, seed samples were stored in their original packaging at room temperature (20–22 °C), and microbiological analyses were performed within 24–48 h after sampling.

Preparation of nutrient media

For the isolation and identification of microorganisms, selective media were prepared according to international standards (ISO 4833-1:2013; Salfinger and Tortorello 2015). All media were prepared following standard formulations and sterilization procedures when required.

Heterotrophic bacteria: standard peptone–agar medium (pH 7.4 ± 0.2), sterilized in an autoclave at 121 °C for 15 minutes.

Fecal coliforms: a selective medium containing proteose peptone, tryptose, lactose, and bile salts, with methylene blue as an indicator, prepared according to standard formulations. All components were of analytical grade and used at concentrations recommended by the manufacturer.

Total coliforms: lauryl sulfate agar with basic fuchsin as an indicator.

Salmonella/Shigella: deoxycholate citrate agar, prepared without autoclaving to avoid denaturation of selective salts.

Fungi (yeasts and molds): malt extract agar, sterilized in an autoclave at 121 °C for 15 minutes, which represents a standard and sufficient sterilization procedure for fungal culture media. After preparation, all media were poured into sterile Petri dishes (Ø 6 cm and Ø 10 cm) and allowed to solidify under aseptic conditions.

Preparation of samples and isolation of microorganisms

From each sample, 10 g of dry oat seeds were weighed and transferred into a sterile Erlenmeyer flask containing 100 mL of sterilized water. After shaking for 2 h using a Startech apparatus, 10 mL of the resulting suspension was taken and serially diluted (1:9) with sterile water to a final concentration of 10^{-3}.

Alternative procedure (for microorganisms resistant to washing)

10 g of seeds were ground in a sterile porcelain mortar with 50 mL of sterilized water to obtain a homogeneous mixture (milk-like emulsion). From this extract, 10 mL was taken and diluted in the same way to 10^{-3}. No chemical surface sterilization (e.g., ethanol or sodium hypochlorite) was applied prior to maceration or grinding; therefore, this procedure does not allow discrimination between true endophytic microorganisms and tightly attached or protected surface-associated microflora.

Membrane filtration method

For colony enumeration, the membrane filtration (MF) method was applied according to Salfinger and Tortorello (2015) and EPA (2023).

Advantec filters (Ø 47 mm; pore size 0.45 μm) were used.

- From each dilution, 10 mL of suspension was filtered using a Sartorius apparatus.
- Filters were then transferred to the appropriate media and incubated under the following conditions: heterotrophic bacteria, total coliforms, fecal coliforms, *Salmonella*/*Shigella*: 37 °C for 48 h.
- Fungi (yeasts and molds): room temperature for 7 days.

After incubation, the developed colonies were counted on Petri plates, and results were expressed as colony forming units (CFU/mL or CFU/g). Counts were based on the average number of colonies from two parallel plates for each dilution.

Calculation of colony numbers

The total number of colonies was calculated according to the following equation:

$$\mathrm{TCN} = \left(\frac{\mathrm{NC} \times \mathrm{DF} \times 100}{V}\right), \quad (1)$$

where:

- NC = number of counted colonies per plate,
- DF = dilution factor,
- V = volume of the filtered sample (mL).

Results were reported as CFU per 100 mL of suspension or per 1 g of dry seed.

Microbial contamination index

To evaluate the overall contamination level of the seeds, the microbial contamination index (MCI) was calculated as the ratio of total heterotrophic colonies to the sum of all other identified microbial groups:

$$\mathrm{MCI} = \left(\frac{\mathrm{CFU\ of\ heterotrophic\ bacteria}}{\mathrm{CFU\ of\ total\ coliforms} + \mathrm{CFU\ of\ fecal\ coliforms} + \mathrm{CFU}\frac{Salmonella}{Shigella} + \mathrm{CFU\ fungi}}\right). \quad (2)$$

This index provides a comparative indicator of the dominance of non-pathogenic microflora over potentially pathogenic microorganisms and can be used as an additional parameter to assess the microbiological quality of oat seeds.

Statistical analysis

All experimental data were analyzed using GraphPad Prism version 10. Microbiological results were expressed as colony-forming units per gram (CFU/g) and tested for normality prior to statistical comparisons. Differences in microbial counts between samples analyzed before and after maceration were evaluated using a paired *t*-test ($n = 3$), as the same samples were measured under both conditions. Percentage and logarithmic ($\log_{10}$) reductions were calculated to describe the efficiency of the maceration treatment for each microbial group, including total coliforms, fecal coliforms, *Salmonella*/*Shigella*, heterotrophic bacteria, and fungi.

Results were expressed as mean ± standard deviation (SD), and differences were considered statistically significant at $p < 0.05$. The MCI was calculated to assess changes in the relative proportion of non-pathogenic to potentially pathogenic microorganisms before and after maceration.

To explore potential relationships among microbial indicators, Pearson correlation coefficients (r) were calculated between the bacterial groups: total coliforms (TC), fecal coliforms (FC), *Salmonella*/*Shigella* (SS), heterotrophic bacteria (HB) and fungal counts (F). Correlation strength was interpreted as weak ($r < 0.3$), moderate ($0.3 \leq r < 0.7$), or strong ($r \geq 0.7$).

Graphical representations, including bar plots, radar charts, and comparative log-scale plots, were generated using GraphPad Prism to visualize relative changes in microbial counts, percentage reductions, and compliance with international microbiological standards (CXC 75-2015; ISO 6579-1:2017; ISO 21528-1:2017; EFSA 2022).

Results and discussion

In this study, microbiological analyses of *Avena sativa* seeds were carried out with two main objectives: first, to determine the initial microbial load before treatment, and second, to assess the effect of maceration on its reduction. Several key indicators were selected for this purpose: TC, FC (*Escherichia coli*), pathogens of the SS group, HB, and F. These indicators are recognized as the most commonly used parameters for evaluating the safety and hygiene of cereal grains according to international standards. Codex Alimentarius (hereafter Codex) and ISO specify that some microorganisms, such as *Salmonella* and *E. coli*, must be completely absent, while others, such as HB or F, are acceptable only within defined limits. Data for these indicators before and after maceration are presented in Table 1.

The results showed that the microbial load of the oat (*Avena sativa*) seeds before treatment was relatively high, particularly for FC (244 CFU/g) and SS (29 CFU/g). Both of these groups are considered critical indicators of food safety. According to international standards (Codex/ISO), *E. coli* should be completely absent in 1 g of a sample, while *Salmonella* must be absent in 25 g. This indicates that the analyzed samples may have undergone fecal contamination or exposure to pathogens during cultivation or storage.

After maceration treatment, a noticeable decrease in microbial load was observed, especially for TC, approximately 94.9% reduction, and HB, approximately 92.3% reduction. However, for FC and SS, although a decrease occurred, their levels remained above acceptable limits: FC decreased to 144 CFU/g, but the standard requires complete absence, while SS decreased to 6 CFU/g, although the standard requires complete absence in 25 g. This finding suggests that maceration alone is not sufficient to eliminate these pathogens, and additional decontamination methods are necessary.

A positive finding was the absence of fungi, both before and after maceration. This is important because cereals are often susceptible to fungal contamination and the potential production of mycotoxins. The absence of fungi suggests that the samples were stored under relatively good conditions, with limited humidity and minimal exposure time. Overall, the data clearly indicate that maceration effectively reduced the general bacterial load (TC and HB), but it was not adequate for the complete removal of critical pathogens such as FC and SS. Therefore, additional technological measures are required to meet microbiological safety standards. Alternative decontamination

Table 1. Microbiological profile of oat (*Avena sativa*) seeds before and after maceration

Code	Before (CFU/g)	After (CFU/g)	Absolute reduction	Relative reduction (%)	Ratio before/after	$\log_{10}$ reduction ($\log_{10}$ before/after)	Standard	Risk level
TC	39	2	37	94.87	19.50	1.29	$\leq 10^2$ CFU/g (according to ISO 4833-1:2013)	Low
FC	244	144	100	40.98	1.69	0.23	0/1 g (according to ISO 21528-1:2017, Codex)	Elevated
SS	29	6	23	79.31	4.83	0.68	0/25 g (according to ISO 6579-1:2017, Codex)	Very high
HB	39	3	36	92.31	13.00	1.11	$\leq 10^4$–10^5 CFU/g (according to ISO 4833-1:2013)	Non-pathogenic
F	0	0	0	0.00	1.00	–	$\leq 10^2$–10^3 CFU/g (according to EFSA 2022)	None

TC – total coliforms, FC – fecal coliforms (*Escherichia coli*), SS – *Salmonella/Shigella*, HB – heterotrophic bacteria, F – fungi. Standards: ISO 21528-1:2017 (*Enterobacteriaceae/E. coli*), ISO 6579-1:2017 (*Salmonella* spp.), CXC 75-2015 (Codex Alimentarius), EFSA (2022). The values for TC, HB, and F are based on indicative hygienic limits for cereals and plant-based products. Differences between before and after maceration were statistically significant (paired *t*-test, $p < 0.05$–0.01). Statistical significance is indicated in Figs 1 and 2. Risk categories are used as descriptive indicators based on relative microbial load and presence of safety-relevant microorganisms and do not represent absolute or regulatory risk classifications.

approaches, such as UV irradiation, ozonation, or mild oxidative washing, have been proposed for dry cereals and could be evaluated in future studies as complementary steps to maceration for improved pathogen control. To visualize the changes before and after treatment, a two-panel figure was used: microbial counts (Fig. 1a) and the MCI (Fig. 1b).

Figure 1 illustrates the effect of maceration on the microbial profile of *Avena sativa* seeds. Figure 1a presents the absolute counts (CFU/g) for each indicator: TC, FC (*E. coli*), SS, HB, and F, while Fig. 1b summarizes the same data as the MCI, as described in the *Materials and methods* section. The corresponding numerical data are provided in Table 1. In Fig. 1a, a clear decrease is observed in TC and HB after maceration. This pattern is typical of a treatment that acts primarily on the surface: weakly attached microorganisms are removed through washing and agitation,

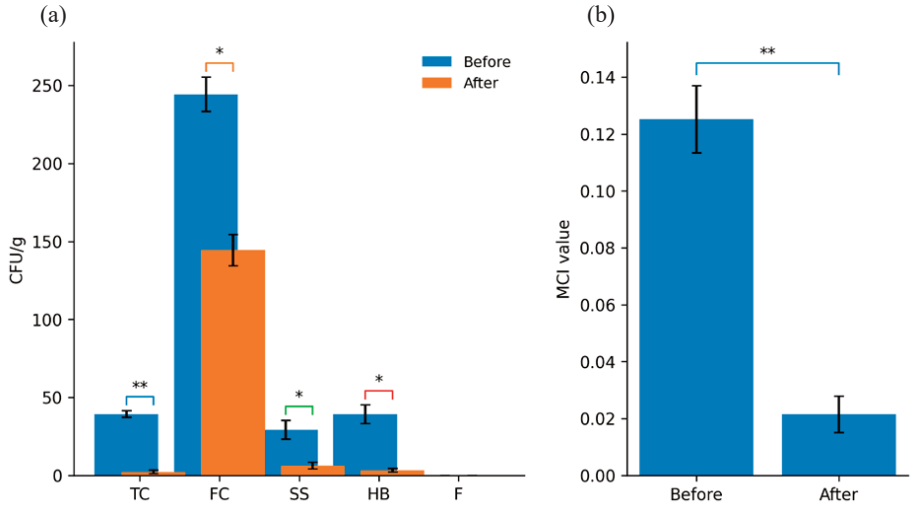

Fig. 1. Microbiological counts (CFU/g) of *Avena sativa* seeds before and after maceration (a) and the corresponding values of the microbial contamination index (MCI) before and after treatment (b). Values are expressed as mean ± SD ($n = 3$). Statistical significance between before and after maceration was assessed using a paired *t*-test (*$p < 0.05$, **$p < 0.01$). Pearson correlation analysis was applied in an exploratory manner to examine linear relationships between selected microbial indicators. The resulting correlation coefficients (r) did not materially affect the interpretation of the overall microbial profile, which is primarily driven by before/after comparisons, $\log_{10}$ reductions, and presence/absence criteria. Therefore, Pearson correlation is not emphasized as a central analytical outcome in this study.

resulting in a reduction of approximately 1 $\log_{10}$. This indicates a marked improvement in hygienic background, where environmental and saprophytic microflora are largely reduced without achieving sterilization.

For FC and SS, a more resistant behavior is observed. Although these indicators also decreased after treatment, they remained detectable. This suggests their localization within micro-niches on the seed coat, stronger surface adhesion, or the presence of biofilm-like structures that make them less sensitive to a single washing step. It should be emphasized that the persistence of microorganisms after maceration reflects resistance to washing and possible association with protected seed-coat micro-niches or biofilm-like structures, rather than confirmed endophytic colonization, as no chemical surface sterilization was applied prior to maceration or grinding. Since Codex and ISO regulatory criteria require complete absence of *E. coli* in 1 g and *Salmonella* in 25 g of a sample, their persistence after maceration indicates that maceration alone is insufficient to meet food safety standards. The fungal indicator F remained unchanged: no growth was detected either before or after maceration. This aligns with storage under dry and controlled humidity conditions. It should be emphasized that only colony counts were reported; mycotoxins were not analyzed, so no conclusions can be drawn regarding their potential risks.

Figure 1b (MCI) summarizes the overall picture. The index drops sharply after maceration, reflecting a general reduction in microbial load dominated by TC and HB. However, a lower MCI represents hygienic improvement, not necessarily regulatory compliance for enteric pathogens such as FC and SS. When considered together with Fig. 1a, both panels show a clear contrast: the general microbial background decreases significantly, while critical safety components remain present. Overall, Fig. 1 demonstrates that maceration functions as a preliminary step for reducing total bacterial load. To achieve the "zero tolerance" requirements for *E. coli* and *Salmonella*, an additional bactericidal or bacteriostatic step (e.g., mild heat treatment, controlled acidification, or low-dose oxidative washing) would be necessary, evaluated using the same microbiological indicators as in this study. This two-step approach background reduction through maceration followed by pathogen inactivation aligns with best practices in cereal processing and food safety standards. MCI was selected to provide a single, integrative measure of treatment effect across all the indicators (TC, FC, SS, HB, F). Equation (1) normalizes each indicator before calculation to prevent groups with higher absolute counts (e.g., TC or HB) from dominating the result. This makes before/after and between-batch comparisons more consistent and interpretable. In our data, MCI decreased markedly after maceration (Fig. 1b), consistent with reductions in TC and HB shown in Fig. 1a; however, the index did not reach zero because FC and SS remained detectable. Thus, MCI reflects hygienic improvement but not full compliance with "zero" standards for *E. coli* and *Salmonella*. Practically, this indicates that maceration can serve as a first step, while MCI helps compare and optimize subsequent decontamination processes (e.g., time/temperature, seed-to-water ratio, or alternative treatments) in future experiments.

Through Fig. 2, these dynamics are further visualized, showing both the before/after counts (bars) and the relative reduction (%) for each indicator, based on the same data as Table 1. This combined representation facilitates interpretation of treatment effects even when initial microbial loads differ across groups. The trend is consistent with Fig. 1: TC and HB exhibit the strongest reductions (~95% and ~92%), typical of surface-associated or loosely bound microflora, which are removed efficiently by washing and agitation. SS also shows a notable reduction (~79%), while FC (*E. coli*) shows a smaller decrease (~41%), indicating higher resistance to a single water-based treatment. For F, the reduction line reaches 0% because no colonies were detected either before or after treatment, thus reflecting absence, not lack of effect. The percentage line highlights a practical insight: relative reduction in TC and HB is high even when absolute counts differ between indicators. Conversely, the FC profile clearly shows the limitation of maceration as a standalone process – it lowers microbial load but does not render samples "undetectable." This distinction is crucial for safety interpretation: improvement in background hygiene (TC/HB) does not automatically equate to compliance with *E. coli/Salmonella* safety standards. In this context, Fig. 2 reveals the heterogeneous response among microbial groups: the background indicators (TC, HB) are efficiently reduced by maceration, whereas the critical safety indicators (FC, SS) persist and require an additional step (e.g., extended maceration time, mild heat treatment, acidification, or low-dose oxidative rinse). Together, Figs 1 and 2 provide a practical framework for process optimization,

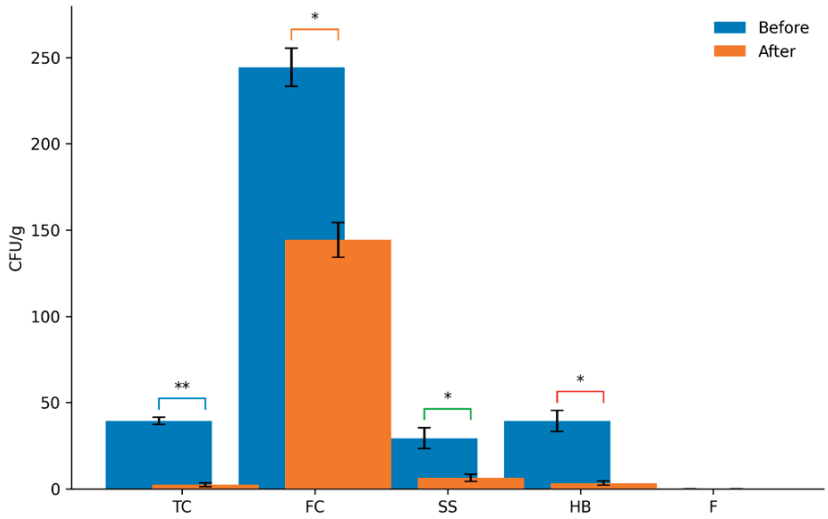

Fig. 2. Microbiological counts (CFU/g) of *Avena sativa* seeds before and after maceration. Values are expressed as mean ± SD (n = 3). Statistical significance between before and after maceration was assessed using a paired t-test (*p < 0.05, **p < 0.01).

showing that maceration serves as a preparatory step to reduce general microbial load, while the second phase should directly target FC and SS to achieve full "zero" compliance.

In Fig. 3, it is evident that for HB and F, our values are consistent with or below the global standards, whereas for FC and SS, there remains a significant discrepancy compared to food safety requirements. This clear contrast indicates that improvements can only be achieved through the application of additional treatment methods and by enhancing storage and transport conditions.

In this study, the microbiological results were expressed as CFU per 100 mL of *Avena sativa* seed suspension, reflecting a methodological approach based on maceration. This form of expression is important for transparency, as unlike the direct analysis of 1 g of dry material, the microbial load here was evaluated in the liquid extract obtained during treatment.

Regarding the applied standards for FC and SS, the mandatory criteria defined by Codex and ISO were applied, which require complete absence in 25 g of a sample, making the "zero tolerance" standard non-negotiable for cereal products. For HB, it should be noted that there is no universal binding international limit; therefore, a reference threshold of $\leq 10^3$ CFU/g was adopted based on scientific literature describing average microbial loads in stored cereals, thus providing a reasonable framework for data interpretation.

The absence of fungi, although not regulated by a specific CFU standard, represents a positive indicator of proper seed storage conditions, minimizing the risk of mycotoxin production.

Overall, this comparison highlights that despite the substantial reductions achieved after maceration, most microbial indicators remain above the permissible limits for cereals. This implies

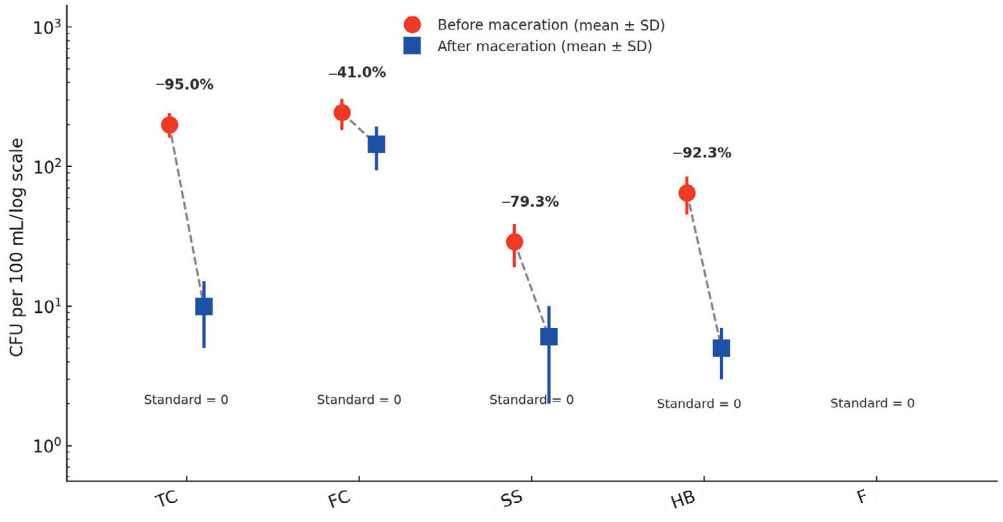

Fig. 3. Comparison of microbiological indicators before and after maceration in relation to international standards.

that the maceration process alone is insufficient to ensure food safety compliance according to international standards.

In this study, a marked reduction was observed in TC (39 → 2 CFU/g, ≈1.29 $\log_{10}$) and HB (39 → 3 CFU/g, ≈1.11 $\log_{10}$) after maceration. It should be noted that the relatively high microbial counts observed before maceration reflect the actual microbiological status of the analyzed market samples and indicate that the starting material may have been grossly contaminated. This profile agrees with the findings of Liu et al. (2022) and Acuff et al. (2023) for low-moisture foods, where water-based or wetting treatments mainly remove loosely attached surface microflora and typically yield approximately one log-unit reduction, without a complete bactericidal effect.

Comparable treatment-dependent patterns of microbial inhibition and selective survival have been reported in recent studies, indicating that processing steps may act as selective pressures shaping microbial communities rather than exerting a uniform inactivation effect. Nikitina et al. (2023) demonstrated that different microbial groups exhibit variable resistance and adaptive responses depending on environmental stressors and substrate interactions, which is consistent with the selective reductions observed in the present study following maceration.

Similar background reductions in microbial load have also been reported in other dry cereals. Rose et al. (2012) described that physical cleaning steps before milling in the wheat chain result in approximately a one-log reduction of the bacterial load, which is consistent with the magnitude observed here for TC and HB. Likewise, the review by Podolak et al. (2010) emphasized that, in low-moisture matrices, physical interventions lead to limited reductions on the order of 1 log CFU/g, consistent with our observations for non-pathogenic indicators. For *Avena sativa*, Anthero et al. (2019) modeled maceration as a two-phase process: a rapid capillary uptake in the outer layers followed by a slower diffusion phase toward the core. The data fit well with Peleg's model and Fick's second law, supporting the expectation that surface microflora (TC and HB) would be greatly reduced while the process would not act as a full-scale inactivation treatment. In simple terms, maceration "washes" the outer layer but does not eliminate microorganisms that are resistant to washing or associated with protected seed-coat niches.

In our data, *E. coli* decreased from 244 to 144 CFU/g (≈0.23 $\log_{10}$) and *Salmonella/ Shigella* from 29 to 6 CFU/g (≈0.68 $\log_{10}$); both remained detectable. This same pattern is widely described for dry matrices: Liu et al. (2022) and Acuff et al. (2023) note that enteric pathogens in low-moisture foods (LMF) (e.g., *Salmonella* spp., *E. coli*) can persist for long periods and are not eliminated by mild water-based interventions. In wheat flour, Forghani et al. (2019) demonstrated long-term survival of *Salmonella enterica* and enterohemorrhagic *E. coli* (EHEC), with thermal-death curves indicating enhanced resistance under dry conditions. Hence, the persistence observed in our samples is typical for cereals and other LMF.

International standards require the complete absence of these pathogens: ISO 6579-1:2017 mandates absence of *Salmonella* spp. in 25 g, ISO 21528-1:2017 describes detection of *Enterobacteriaceae* (with *E. coli* as fecal indicator) in enriched test portions, and CXC 75-2015 for LMF clearly frames pathogen criteria as "presence/absence" in the final product. Within this framework, the post-maceration presence of *E. coli* and/or *Salmonella/Shigella* fails to meet the "absence" requirement, consistent with previous LMF reviews. Beyond *Avena sativa*, studies on wheat flour confirm similar persistence of *Salmonella* spp. and *E. coli* after mild processing steps, for example, the studies by Forghani et al. (2019) on survival and thermal inactivation in flour and by Podolak et al. (2010) on sources and risk factors in LMF. These works reinforce the idea that approximately 1 log reductions in overall counts do not equate to pathogen absence. In practical terms, reviews of the wheat-processing chain (Rose et al. 2012) note that pre-milling physical cleaning produces visible microbial reductions but not guaranteed eliminations. In the present study, fungi were not detected in either stage (before or after maceration), indicating storage under adequately dry and non-favorable conditions. Nevertheless, EFSA (2011, 2017) reports frequent detection of T-2/HT-2 toxins (trichothecene mycotoxins) and deoxynivalenol (DON) in European oat surveys; thus, the absence of fungal colonies in culture does not automatically imply absence of mycotoxins along the production chain. The most recent EFSA (2022) update continues to discuss exposure to T-2/HT-2 in cereals, maintaining oats among matrices of ongoing concern. Most cereal-related literature reports data as CFU/g (dry matter) or as presence/absence according to ISO standards. Similarly, the interpretation in this study focuses on the before/after trend showing strong decreases

in total coliforms and heterotrophic bacteria but residual presence of *E. coli* and *Salmonella*/*Shigella*. This approach is consistent with LMF reviews, which emphasize evaluating trends and presence/absence for pathogens rather than direct numerical equivalence among analytical protocols. In our data, MCI decreased sharply after maceration because total coliforms and heterotrophic bacteria were substantially reduced; however, the index did not reach its minimum value because *E. coli* and *Salmonella*/*Shigella* remained detectable. This reflects the overall condition: a clear improvement in the microbial profile but not complete compliance with key safety indicators – an interpretation fully aligned with the ISO 6579-1, ISO 21528-1, and CXC 75-2015 frameworks. While culture-based CFU analysis provides a robust initial hygiene and safety assessment, it does not capture the full complexity of seed-associated microbiota. Therefore, the present results should be interpreted within the limits of culture-dependent methods. Higher-resolution approaches, such as high-throughput sequencing (e.g., Illumina-based analyses), could complement future studies by providing deeper insight into microbial community structure, selective survival, and community dynamics under maceration and related treatments.

Conclusion

In our study, we aimed to emphasize the importance of safety during the storage and preservation of cereal seeds. As a case study, we took oat (*Avena sativa*) seeds. Through a simple "before/after" maceration protocol, we assessed the microbiological status of the packaged oat seeds on the market. The analysis before maceration showed a broad bacterial presence. Maceration was used to evaluate whether contamination was limited to surface-associated microflora or involved microorganisms resistant to washing and associated with protected seed structures. As a physical process, maceration washed the outer layers and substantially reduced the overall bacterial load but did not eliminate the enteric risk. Numerically, maceration reduced total coliforms from 39 to 2 CFU/g (≈95%, 1.29 $\log_{10}$ reduction) and heterotrophic bacteria from 39 to 3 CFU/g (≈92%, 1.11 $\log_{10}$ reduction), while fecal coliforms decreased from 244 to 144 CFU/g (≈41%) and *Salmonella*/*Shigella* from 29 to 6 CFU/g (≈79%), remaining detectable. Fecal markers and enteric pathogens remained detectable, which indicates that a single wetting displaces the "free" microorganisms from the surface, whereas the micro-niches of the seed coat and stronger adhesions remain unaffected. These remaining microorganisms should not be interpreted as confirmed endophytic microflora, as no chemical surface sterilization was applied prior to maceration or grinding. The use of seeds with this profile, without further evaluation, carries a real risk of transferring contamination to the sowing environment or to the stages of food processing. The absence of fungal growth in both phases is consistent with dry storage but does not allow a judgment on mycotoxins (they were not measured). The microbial contamination index (MCI) reflected this analysis; it decreased with the reduction of background indicators, but remained sensitive to the presence of safety indicators and does not replace presence/absence criteria. Since our study is based on the maceration protocol, comparisons with the literature should be read as profiles and trends, not as a numerical equivalence across different matrices. Essentially, maceration improves seed cleanliness by reducing surface-associated microflora but does not guarantee microbiological safety or confirm endophytic colonization. This paper reflects the real status of the samples on the market and sets the basis for further assessments of compliance with the standard criteria of pathogen presence/absence.

Data availability statement

The data sets used and/or analyzed during the current study are available from the corresponding author at reasonable request.

Acknowledgments

The authors thank the Institute of Microbiology at the University Clinical Center of Kosovo for their valuable support during the microbiological analyses. The publication costs of this article were partially covered by the Estonian Academy of Sciences.

References

Acuff, J. C., Dickson, J. S., Farber, J. M., Grasso-Kelley, E. M., Hedberg, C., Lee, A. et al. 2023. Practice and progress: updates on outbreaks, advances in research, and processing technologies for low-moisture food safety. *Journal of Food Protection*, **86**(1), 100018. https://doi.org/10.1016/j.jfp.2022.11.010

Agarwal, V. K. and Sinclair, J. B. 1997. *Principles of Seed Pathology*. 2nd ed. CRC Press, Boca Raton. https://doi.org/10.1201/9781482275650

Anthero, A. G. S., Lima, J. M., Cleto, P. B., Jorge, L. M. M. and Jorge, R. M. M. 2019. Modeling of maceration step of the oat (*Avena sativa*) malting process. *Journal of Food Process Engineering*, **42**(7), e13266. https://doi.org/10.1111/jfpe.13266

Butt, M. S., Tahir-Nadeem, M., Khan, M. K. I., Shabir, R. and Butt, M. S. 2008. Oat: unique among the cereals. *European Journal of Nutrition*, **47**(2), 68–79. https://doi.org/10.1007/s00394-008-0698-7

CXC 75-2015. *Code of hygienic practice for low-moisture foods*. Codex Alimentarius.

Dell'Olmo, E., Tiberini, A. and Sigillo, L. 2023. Leguminous seed-borne pathogens: seed health and sustainable crop management. *Plants*, **12**(10), 2040. https://doi.org/10.3390/plants12102040

Desjardins, A. E. 2006. *Fusarium Mycotoxins: Chemistry, Genetics, and Biology*. APS Press.

Desjardins, A. E. and Proctor, R. H. 2007. Molecular biology of *Fusarium* mycotoxins. *International Journal of Food Microbiology*, **119**(1–2), 47–50. https://doi.org/10.1016/j.ijfoodmicro.2007.07.024

EFSA (European Food Safety Authority). 2011. Scientific opinion on the risks for animal and public health related to the presence of T-2 and HT-2 toxin in food and feed. *EFSA Journal*, **9**(12), 2481. https://doi.org/10.2903/j.efsa.2011.2481

EFSA. 2017. Risks to human and animal health related to the presence of deoxynivalenol and its acetylated and modified forms in food and feed. *EFSA Journal*, **15**(9), e04718. https://doi.org/10.2903/j.efsa.2017.4718

EFSA. 2022. Assessment of information as regards the toxicity of T-2 and HT-2 toxin for ruminants. *EFSA Journal*, **20**(9), e07564. https://doi.org/10.2903/j.efsa.2022.7564

EPA (United States Environmental Protection Agency). 2023. Method 1103.2: *Escherichia coli* (*E. coli*) in water by membrane filtration using membrane-thermotolerant *Escherichia coli* agar (mTEC). https://www.epa.gov/system/files/documents/2024-06/method-1103.2-10022023_508.pdf

FAO (Food and Agriculture Organization of the United Nations). *Food safety and quality: mycotoxins*. https://www.fao.org/food/food-safety-quality/a-z-index/mycotoxins/en/?utm_source=chatgpt.com (accessed 2025-10-18).

Forghani, F., den Bakker, M., Liao, J.-Y., Payton, A. S., Futral, A. N. and Diez-Gonzalez, F. 2019. *Salmonella* and enterohemorrhagic *Escherichia coli* serogroups O45, O121, O145 in wheat flour: effects of long-term storage and thermal treatments. *Frontiers in Microbiology*, **10**, 323. https://doi.org/10.3389/fmicb.2019.00323

Gebeyaw, M. 2020. Review on: Impact of seed-borne pathogens on seed quality. *American Journal of Plant Biology* , **5**(4), 77–81. https://doi.org/10.11648/j.ajpb.20200504.11

ISO 4833-1:2013. *Microbiology of the food chain – Horizontal method for the enumeration of microorganisms – Part 1: Colony count at 30 °C by the pour plate technique*.

ISO 6579-1:2017. *Microbiology of the food chain – Horizontal method for the detection, enumeration and serotyping of Salmonella – Part 1: Detection of Salmonella spp.*

ISO 21528-1:2017. *Microbiology of the food chain – Horizontal method for the detection and enumeration of Enterobacteriaceae – Part 1: Detection of Enterobacteriaceae*.

ISTA (International Seed Testing Association). 2018. *International rules for seed testing*. https://www.seedtest.org/en/publications/international-rules-seed-testing.html

Kallistova, A., Nikolaev, Y., Grachev, V., Beletsky, A., Gruzdev, E., Kadnikov, V. et al. 2021. New insight into the interspecies shift of anammox bacteria *Ca*. "Brocadia" and *Ca*. "Jettenia" in reactors fed with formate and folate. *Frontiers in Microbiology*, 2022, **12**, 802201. https://doi.org/10.3389/fmicb.2021.802201

Liu, S., Roopesh, M. S., Tang, J., Wu, Q. and Qin, W. 2022. Recent development in low-moisture foods: microbial safety and thermal process. *Food Research International*, **155**, 111072. https://doi.org/10.1016/j.foodres.2022.111072

Logrieco, A., Moretti, A. and Solfrizzo, M. 2009. *Alternaria* toxins and plant diseases: an overview of origin, occurrence and risks. *World Mycotoxin Journal*, **2**(2), 129–140. https://doi.org/10.3920/WMJ2009.1145

Munkvold, G. P. 2009. Seed pathology progress in academia and industry. *Annual Review of Phytopathology*, 47, 285–311. https://doi.org/10.1146/annurev-phyto-080508-081916

Nelson, E. B. 2018. The seed microbiome: origins, interactions, and impacts. *Plant and Soil*, **422**(1), 7–34. https://doi.org/10.1007/s11104-017-3289-7

Nikitina, A. A., Kallistova, A. Y., Grouzdev, D. S., Kolganova, T. V., Kovalev, A. A., Kovalev, D. A. et al. 2022. Syntrophic butyrate-oxidizing consortium mitigates acetate inhibition through a shift from acetoclastic to hydrogenotrophic methanogenesis and alleviates VFA stress in thermophilic anaerobic digestion. *Applied Sciences*, **13**(1), 173. https://doi.org/10.3390/app13010173

Pecchia, S., Caggiano, B., Da Lio, D., Cafà, G., Le Floch, G. and Baroncelli, R. 2019. Molecular detection of the seed-borne pathogen *Colletotrichum lupini* targeting the hyper-variable IGS region of the ribosomal cluster. *Plants*, **8**(7), 222. https://doi.org/10.3390/plants8070222

Peterson, D. M. 2001. Oat antioxidants. *Journal of Cereal Science*, **33**(2), 115–129. https://doi.org/10.1006/jcrs.2000.0349

Podolak, R., Enache, E., Stone, W., Black, D. G. and Elliott, P. H. 2010. Sources and risk factors for contamination, survival, persistence, and heat resistance of *Salmonella* in low-moisture foods. *Journal of Food Protection*, **73**(10), 1919–1936. https://doi.org/10.4315/0362-028X-73.10.1919

Rose, D. J., Bianchini, A., Martinez, B. and Flores, R. A. 2012. Methods for reducing microbial contamination of wheat flour and effects on functionality. *Cereal Foods World*, **57**(3), 104–109.

Salfinger, Y. and Tortorello, M. L. (eds) 2015. *Compendium of Methods for the Microbiological Examination of Foods*. 5th ed. APHA Press, Washington DC. https://doi.org/10.2105/MBEF.0222

Selcuk, M., Oksuz, L. and Basaran, P. 2008. Decontamination of grains and legumes infected with *Aspergillus* spp. and *Penicillium* spp. by cold plasma treatment. *Bioresource Technology*, **99**(11), 5104–5109. https://doi.org/10.1016/j.biortech.2007.09.076

Shade, A., Jacques, M.-A. and Barret, M. 2017. Ecological patterns of seed microbiome diversity, transmission, and assembly. *Current Opinion in Microbiology*, **37**, 15–22. https://doi.org/10.1016/j.mib.2017.03.010

Tenno, T., Rikmann, E., Zekker, I. and Tenno, T. 2018. Modelling the solubility of sparingly soluble compounds depending on their particles size. *Proceedings of the Estonian Academy of Sciences*, **67**(3), 300–302. https://doi.org/10.3176/proc.2018.3.10

Truyens, S., Weyens, N., Cuypers, A. and Vangronsveld, J. 2015. Bacterial seed endophytes: genera, vertical transmission and interaction with plants. *Environmental Microbiology Reports*, **7**(1), 40–50. https://doi.org/10.1111/1758-2229.12181

Uwineza, P. A., Urbaniak, M., Stępień, Ł., Gramza-Michałowska, A. and Waśkiewicz, A. 2024. Efficacy of *Lamium album* as a natural fungicide: impact on seed germination, ergosterol, and mycotoxins in *Fusarium culmorum*-infected wheat seedlings. *Frontiers in Microbiology*, **15**, 1363204. https://doi.org/10.3389/fmicb.2024.1363204

Whitehead, A., Beck, E. J., Tosh, S. and Wolever, T. M. S. 2014. Cholesterol-lowering effects of oat *β*-glucan: a meta-analysis of randomized controlled trials. *The American Journal of Clinical Nutrition*, **100**(6), 1413–1421. https://doi.org/10.3945/ajcn.114.086108

WHO (World Health Organization). 2023a. *Carbohydrate intake for adults and children: WHO guideline*. https://www.who.int/publications/i/item/9789240073593 (accessed 2023-07-17).

WHO. *Mycotoxins*. 2023b. https://www.who.int/news-room/fact-sheets/detail/mycotoxins (accessed 2025-10-18).

Kaeraseemnete mikrobioloogiline ohutus ja leotamisprotokolli mõju

Lulzim Millaku, Mirvete Kutleshi, Jeton Orllati ja Idriz Vehapi

Uuringus hinnati turul müüdavate kaeraseemnete (*Avena sativa* L.) mikrobioloogilist seisundit, et rõhutada nende ohutu käitlemise tähtsust. Kasutati enne ja pärast leotamist tehtud katsetel põhinevat tooteohutuse hindamise protokolli, et eristada viljaseemnete pinnasaastet sisemisest saastest.

Tulemused näitasid, et teraviljaseemnete leotamine vähendas märgatavalt seemnete üldist bakteriaalset saastet, kuid ei taganud täielikku tooteohutust.

Üldindikaatorid: kolilaadsete bakterite arv vähenes leotamisel u 95% ja heterotroofsete bakterite arv u 92%.

Ohutusriskid: patogeenid ja fekaalsed saasteindikaatorid jäid seemnetes endiselt tuvastatavaks – fekaalsete kolilaadsete bakterite arv vähenes 41% ja *Salmonella/Shigella* suhteline arvukus 79%.

Uuring tõestab, et teraviljaseemnete ühekordne leotamine eemaldab neilt vaid pinnal asetsevad mikroobid, kuid seemnekesta kihid kaitsevad enteraalseid patogeene teraviljas endiselt. Kuna keemilist pinnasteriliseerimist uuringus ei kasutatud, ei saa teraviljale jäänud mikroorganisme pidada kinnitunud endofüütideks ega teha sellekohaseid järeldusi mikrobioloogilise saaste kohta.

Seemnete leotamine parandab nende mikrobioloogilist puhtust, kuid ei taga mikrobioloogilise saaste suhtes täielikku ohutust. Sellise saasteprofiiliga seemnete kasutamine on riskantne nii külvikeskkonnale kui ka toiduainetööstusele. Uuring näitab jaemüügis olevate teraviljade tegelikku seisundit ja on aluseks edasistele vastavushindamistele.

Proceedings of the Estonian Academy of Sciences
2026, **75**, 1, 87–95

https://doi.org/10.3176/proc.2026.1.08

www.eap.ee/proceedings
Estonian Academy Publishers

QUATERNARY WASTEWATER TREATMENT

RESEARCH ARTICLE

Received 29 August 2025
Accepted 29 December 2025
Available online 18 February 2026

Keywords:
micropollutants, quaternary treatment, bromide, bromate, EU Wastewater Directive

Corresponding author:
Deniss Klauson
deniss.klauson@tktk.ee

Citation:
Klauson, D., Lember, E. and Jaaku, J. 2026. Bromides in treated wastewater: limiting the choice of quaternary wastewater treatment technologies for residual micropollutant removal. An Estonian case study. *Proceedings of the Estonian Academy of Sciences*, **75**(1), 87–95. https://doi.org/10.3176/proc.2026.1.08

Bromides in treated wastewater: limiting the choice of quaternary wastewater treatment technologies for residual micropollutant removal. An Estonian case study

Deniss Klauson[a], Erki Lember[a] and Jaak Jaaku[b]

[a] Institute of Engineering and Circular Economy, TTK University of Applied Sciences, Pärnu mnt. 62, 10135 Tallinn, Estonia

[b] Department of Civil Engineering and Architecture, Tallinn University of Technology, Ehitajate tee 5, 19086 Tallinn, Estonia

ABSTRACT

The recent changes in the European Union Wastewater Directive require micropollutant elimination from the effluents of wastewater treatment plants serving at least 150 000 population equivalents, and in some cases even starting from 10 000. While ozonation can degrade micropollutants without secondary wastes, the treated effluent composition must be considered, specifically the concentration of bromide (Br^-). Depending on its amount and oxidant dose, bromide can potentially be oxidised to carcinogenic bromate (BrO_3^-). This research investigates bromide amounts in the effluents of Estonian wastewater treatment plants serving at least 10 000 population equivalents as preliminary work for quaternary wastewater treatment aimed at micropollutant removal.

Introduction

Quaternary treatment for micropollutant removal: legislation

The latest amendments to the EU Wastewater Directive (European Union 2024), which are currently being adopted by legislations, demand that all the wastewater treatment plants (WWTPs) that serve at least 150 000 population equivalents (p.e.) are to adopt quaternary treatment for the elimination of micropollutants. In the EU, there are currently 24 971 operating WWTPs, among which 933 serve at least 150 000 p.e. (Water News Europe 2024). Additionally, WWTPs serving 10 000 p.e. and above may also have to introduce quaternary treatment if their discharge area is considered sensitive to micropollutants, e.g. locations where the dilution rate of the WWTP discharge is low, the discharge goes to water bodies used as drinking water sources, for the growth and production of shellfish, or for bathing purposes. Quaternary treatment is to be fully operational from 2045, with intermediate results expected by 2033.

According to the amendments to the Wastewater Directive, WWTPs must monitor and remove at least 80% of the following micropollutants:

- first category (relatively easily removable compounds): amisulpride, carbamazepine, citalopram, clarithromycin, diclofenac, hydrochlorothiazide, metoprolol, and venlafaxine;
- second category (relatively easy to handle compounds): benstriasol, candesartan, irbesartan, and a mixture of 4-methylbensotriasol and 6-bensotriasol.

Micropollutant removal methods

In the literature, numerous technologies, notably Advanced Oxidation Processes (AOPs), are proposed for the elimination of micropollutants, including ozonation (assisted or catalysed), Fenton and Fenton-like systems, adsorption, photocatalytic oxidation, plasma-based treatment methods, and more. While they can degrade literally any kind of pollutants until total mineralisation, that is too costly; combining moderate AOP treatment with biological treatment was shown to efficiently eliminate even the most recalcitrant pollution in a far more sustainable way (Klauson et al. 2015; Klein et al. 2017; Trapido et al. 2017). However, not all of these AOPs are readily

scalable and applicable. Real-life practical applications use technologies that are already operational and have shown multiple proofs of efficiency, narrowing the choice mainly to ozonation and activated carbon adsorption.

Ozonation, both through molecular ozone and radicals, can degrade micropollutants up to complete mineralisation. Due to the relatively high cost of ozone production, partial degradation of the micropollutants into non-toxic and biodegradable by-products is more cost-efficient than outright mineralisation. The ozone dosage choice for the real-life micropollutant removal is more complicated, as the biggest consumer of oxidants is the wastewater matrix. This requires an empirical approach coupled with the measurements of required micropollutants. There are some indications from the authors' previous experience that small doses of ozone, in the range of several mg/L, may degrade micropollutants selectively, without being affected by the general wastewater matrix and without affecting it significantly (Klauson et al. 2019).

Adsorption is an equilibrium mass-transfer process: a higher concentration of a substance dissolved in the aqueous phase results in a higher amount of it adsorbed on the surface of activated carbon. Consequently, micropollutants are a minority of the substances adsorbed by the activated carbon before its surface is filled, and it needs replacement. Spent activated carbon, with its surface laden with concentrated micropollutants and other compounds, becomes a hazardous waste or produces such upon regeneration.

Bromides in wastewater: a possible threat

Bromide (Br^-) in municipal wastewater may originate from several sources, including groundwater with seawater intrusion, relict seawater, surface water bodies fed by groundwater sources, groundwater infiltration into wastewater, and discharges of bromine-disinfected swimming pools or cooling water. These are gaining popularity, as bromine is a more efficient oxidant than chlorine, being simultaneously less irritating (WHO 2018). In the presence of strong oxidants, the bromide ion is prone to stepwise oxidation, terminating in the formation of the carcinogenic bromate anion. In the case of bromide-containing water ozonation, the following reactions take place, both with molecular ozone and OH-radicals (Morrison et al. 2023):

$$Br^- + O_3 \rightarrow BrO^- + O_2, \quad (1)$$

$$BrO^- + H^+ \rightleftarrows HOBr, \quad (2)$$

$$BrO^- + O_3 \rightarrow BrO_2^- + O_2, \quad (3)$$

$$HOBr + O_3 \rightarrow BrO_2^- + O_2 + H^+, \quad (4)$$

$$BrO_2^- + O_3 \rightarrow BrO_3^- + O_2, \quad (5)$$

$$BrO_2^- + O_3 \rightarrow \bullet BrO_2 + \bullet O_3^-, \quad (6)$$

$$2 \bullet BrO_2 \rightleftarrows Br_2O_4, \quad (7)$$

$$Br_2O_4 + H_2O \rightarrow BrO_2^- + BrO_3^- + 2\,H^+, \quad (8)$$

$$Br^- + \bullet OH \rightarrow \bullet Br + OH^-, \quad (9)$$

$$\bullet Br + O_3 \rightarrow \bullet BrO + O_2, \quad (10)$$

$$\bullet BrO + O_3 \rightarrow \bullet BrO_2 + O_2, \quad (11)$$

$$\bullet BrO_2 + \bullet OH \rightarrow BrO_3^- + H^+. \quad (12)$$

Radical reactions (see Eqs (9)–(12)) are known to have a significant role in ozonation only at alkaline pH (e.g. Asgari et al. 2017). At conditions closer to neutral, as expected in the WWTP effluents, their role is marginal, leaving the reactions of molecular ozone as the main pathway. At near-neutral pH, ca 96% of the hypobromite ion formed in reaction (1) exists in water as hypobromous acid (HOBr), as its pK_a is 8.65 (Perrin 1982). This is a potent disinfectant and brominating agent. Its oxidation to bromite (Eq. (3)) is a slow process compared to that of the hypobromite ion, with the second-order rate constants being 0.01 L/(mol × s) for Eq. (4) and 100 L/(mol × s) for Eq. (2), respectively (Morrison et al 2023). While reaction (5) was originally proposed to describe the oxidation of bromite to bromate (Haag and Hoigne 1983), more recent research (Odeh et al. 2004) suggests that the mechanism is somewhat more complex, as described by Eqs (6)–(8). Additionally, the hypobromite anion formed in reaction (1) can undergo reduction by ozone, partially reverting to bromide (Morrison et al. 2023):

$$BrO^- + O_3 \rightarrow Br^- + 2O_2. \quad (13)$$

Moreover, in many places around the world, WWTP effluents are disinfected by chlorine-based chemicals before the discharge. That can be described by the following reaction equations (Mestri et al. 2023):

$$Br^- + HOCl \rightarrow Cl^- + HOBr, \quad (14)$$

$$HOBr + HOCl \rightarrow HBrO_2 + Cl^- + H^+, \quad (15)$$

$$HBrO_2 + HOCl \rightarrow BrO_3^- + Cl^- + 2\,H^+. \quad (16)$$

The maximum level of bromate allowed in drinking water is 10 mg/L (European Union 2020); due to the absence of straightforward guidelines for treated discharged wastewater, this figure could be used as a benchmark in this situation. It has been previously suggested (CWPharma 2020) that potentially unsafe bromide concentrations could be 0.15 mg/L when applying ozone doses above 0.7 mg O_3/mg DOC.

This way, bromides in wastewater impose constraints on the method choices for micropollutant abatement. While ozonation is generally considered to be almost free from side

effects, the presence of bromide requires preliminary studies and process fine-tuning before actual applications. Adsorption, inevitably producing large amounts of concentrated wastes, can be applied in cases where ozonation would seem too risky.

So far, no meaningful bromide removal from water has been shown in the literature. While there have been studies addressing biological, physical, and physico-chemical processes, they largely fail: only reverse osmosis and, to a smaller extent, nanofiltration have provided efficient results (Chowdhury et al. 2022). However, these are not the methods to be applied to the average WWTP effluent. While some studies provided decent to good results for selective ion exchange, these worked well in low-ionic-strength waters, while adding other ionic admixtures present in real-life WWTP effluents lowered bromide removal efficiency drastically (Chowdhury et al. 2022). Consequently, any real-life WWTP treatment aimed at micropollutant removal must face the challenges and restrictions posed by bromides in water.

Estonian groundwater: hydrogeological context

The Republic of Estonia is a country in Northern Europe, situated on the eastern coast of the Baltic Sea. With a population of roughly 1.34 million, Estonia has only two WWTPs serving over 150 000 p.e., namely, in Tallinn, the capital city, and Tartu, the second-largest city. However, some of the municipalities with WWTPs serving at least 10 000 p.e. may also be affected by the micropollutant-connected changes in the EU Wastewater Directive, based on the discharge area risk assessment. Around 2/3 of Estonian drinking water consumption originates from groundwater, the composition of which is strongly affected by the history of the Baltic Sea formation in the geological past. Figure 1 shows the hydrogeological map of Estonia.

Geologically, Estonia is situated on the southern slope of the Baltic Shield, with sedimentary beds inclined southwards by 2–4 m/km, underlain by a porphyritic granite crystalline basement (Karro et al. 2009). The upper part of the basement is partially fractured and contains saline water. The basement is overlain, in turn, by clay minerals from basement granite weathering, Vendian and Cambrian siltstone and sandstone, Silurian and Ordovician limestone, middle-Lower and Middle Devonian siltstone and sandstone, and is finally covered by Quaternary deposits made up mostly of glacial till, glaciolacustrine deposits, and glaciofluvial sand (Karro et al. 2004; Karro et al. 2009). The water-bearing sedimentary rock beds are separated by clay-based aquitards.

In the northernmost part of Estonia, including ca 10% of Tallinn, groundwater from the Cambrian–Vendian aquifers (0.3–2 g/L of the total dissolved solids, TDS) is used; the water-bearing layers are composed of sandstone and are separated by limestone and clay. They are connected to the sea at the bottom of the Gulf of Finland, some 20 km from the shoreline (Karro et al. 2004), making bromide-containing saltwater intrusion a naturally occurring phenomenon. In general, the Cambrian–Vendian aquifer is recharged in Southern Estonia and flows northward at a velocity of 0.0005–0.005 m/d (Karro et al. 2004). This way, the mineral composition of the Cambrian–Vendian groundwater is mainly affected by the water–rock interaction geochemistry (Karro et al. 2004). Additionally, local recharges with modern water take place in buried erosional valleys, formed in the pre-Quaternary interglacial, glacial, and postglacial times. At least 10 larger and around 20 smaller buried valleys have been detected along the Northern Estonian coast (Karro et al. 2004).

At the same time, the Cambrian–Vendian groundwater layer is underlain by more saline water in the fractured crystalline basement, with up to 51–61 mg/L Br^- and up to 5 g/L TDS (Karro et al. 2004). This way, the coastline-related Cambrian–Vendian groundwater wells in the Northern Estonian plain can experience increased salinity due to both seawater intrusion and saline groundwater intrusion, giving bromide levels of up to 4 mg/L. As the Cambrian–Vendian water pumped close to the seashore has a higher Br^-/Cl^- ratio than the seawater from the Gulf of Finland, underlying saltwater levels with an increased bromide content seem to be the main source of elevated bromide concentrations in the northernmost Estonian groundwater (Karro et al. 2004).

The largest city in Northern Estonia, Tallinn, gets around 90% of its water from Lake Ülemiste, situated within the city borders and mainly fed by surface waters from Central Estonia. On the contrary, in other areas of Northern Estonia, around 3/4 of water supply comes from the Cambrian–Vendian aquifer (Karro et al. 2004). In North-Eastern Estonia, due to mining activities, saltwater intrusion into the Cambrian–Vendian aquifers is the most pronounced, resulting in the increased content of salts, including those of barium (up to 6.4 mg/L) (Karro et al. 2009).

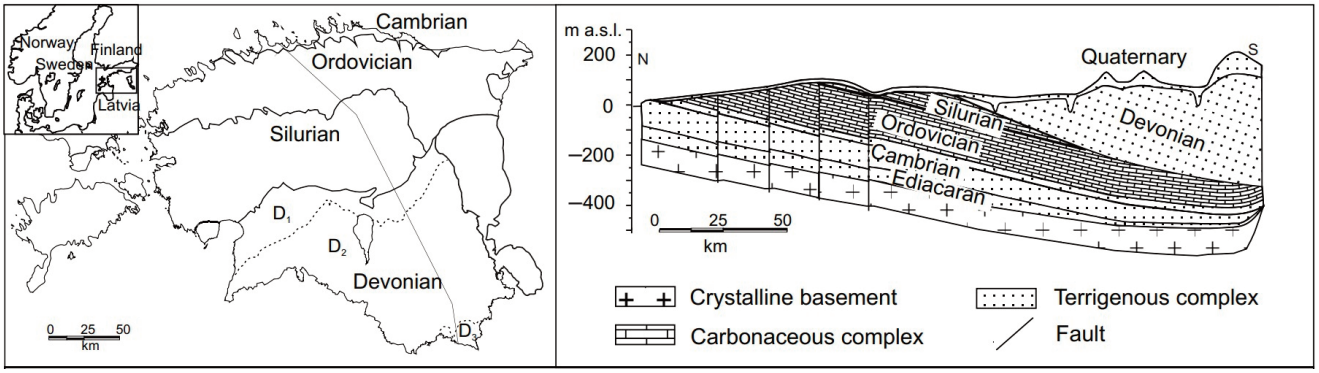

Fig 1. Groundwater map of Estonia (adapted from Karro et al. 2020).

Northern, Western and Central Estonia get their groundwater from the Silurian–Ordovician aquifers, where the water-bearing rock is composed of layers of limestone and dolomite. It consists of interbedded 1–2 m thick carbonaceous zones with lateral water flow, separated by 5–10 m thick fissured zones where water flows vertically (Karro et al. 2009). With the carbonaceous rocks karstified, especially in the upper 30 m (Karro et al. 2009), the aquifer allows rapid refilling of the layer, along with fast contaminant transport. Therefore, Central Estonia with its agricultural lands is a nitrate-sensitive area, where the mainly agricultural pollution, including nitrates and pesticides, ends up in deeper water layers, used as drinking water sources. Groundwater in Western Estonia is known to have pockets of relict seawater: it has elevated concentrations of salts, including above 6 mg/L of F^- and above 2 mg/L of B, together with elevated concentrations of Cl^- and Br^-. The Silurian–Ordovician groundwater has TDS of 0.2–1.5 g/L (Karro et al. 2009).

Southern Estonia uses groundwater from the Devonian aquifers, where the water-bearing rock is again siltstone and sandstone. South-Eastern Estonia is characterised by the availability of relict seawater; in the easternmost part of Southern Estonia, some relict seawater layers have a relatively high mineral content (up to 22 g/L TDS), and brackish mineral water is produced there in Värska. The Middle Devonian water is the most widely used groundwater in Southern Estonia; the water has low salt content (0.2–0.6 g/L TDS), with its characteristic mineral additive being iron, reaching up to 26 mg/L (Karro et al. 2020). The second-largest Estonian city, Tartu, uses both the shallower Devonian and the deeper Silurian–Ordovician wells.

Materials and methods

Sampling was carried out during 2022–2023 in 10 Estonian WWTPs serving 10 000 p.e. or more, with each site sampled twice. Bromide concentrations were measured by a modification of the standard N,N-diethyl-p-phenylenediamine (DPD) method: one droplet of 0.1 N $Na_2S_2O_3$ was added to 50 mL of sample to remove any possible interference from oxidants, with two minutes taken as reduction time. This was followed by 1 mL of 3% H_2O_2. After five-minute oxidation, 10 mL of the obtained solution was taken and measured according to the HACH DPD Method 8016: a sachet of DPD was added to the solution, and the measurement was carried out after one minute of colour development at the wavelength of 530 nm. The calibration made by the authors allowed measurements in the range of 0.01–2.25 mg/L Br^-, with the determination coefficient of $R^2 = 0.907$. The measurement results were double-checked using a bromide-sensitive electrode HI716 by Hanna Instruments (minimal detection practically 0.1 mg/L Br^-). The difference between the two methods was within the limits of analytical precision, while the photocolorimetric method, having greater sensitivity, was employed as the main measurement approach. Additionally, the following parameters were measured: pH, dissolved oxygen, redox potential, electrical conductivity, total phosphorus and nitrogen, ammonium (bromate formation suppressor), nitrites (ozone consumers) and nitrates, suspended solids (ozone consumers, hydraulic load), chemical oxygen demand, total organic carbon, and dissolved organic carbon (main ozone consumer). The measurement parameters were selected to cover the key factors in planning quaternary wastewater treatment.

Results and discussion

Bromides in the analysed WWTP effluent

For the sake of discretion of the companies involved, Fig. 2 shows the results as the average composition of the analysed WWTP effluents. As the analysed WWTPs have different discharge requirements (above 10 000 p.e. and above 100 000 p.e.), the variability in values is noticeable.

The results show an average of 0.12 mg Br^-/L, with a minimum concentration of 0.07 mg Br^-/L and an observed maximum of 0.24 mg Br^-/L. Figure 3 shows the geographic distribution of the results and the concentration ranges. What is interesting to note is that the proximity to the sea, often regarded by default as a source of seawater intrusion and a source of bromides, is not a direct pre-requisite to high bromide content in the WWTP discharge.

Role of nitrogen species

Nitrites present in the WWTP plant effluents show that the nitrification is incomplete. While the detected amounts (average 0.2 mg/L) are not significant in terms of WWTP effluent discharge, they affect quaternary treatment by consuming part of the ozone for the oxidation to nitrates, which at the average effluent pH proceeds via molecular reactions:

$$NO_2^- + O_3 \rightarrow NO_3^- + O_2. \quad (17)$$

As shown earlier (CWPharma 2020), the amount of ozone for micropollutant degradation in the presence of nitrites can be calculated as follows:

$$D(O_3) = D_{DOC} \times DOC + 3.43 \times C(NO_2^-), \quad (18)$$

where $D(O_3)$ is the calculated ozone dosage (mg O_3/L), D_{DOC} is the DOC-specific ozone dosage (0.3 to 0.9 mg O_3/(mg DOC)) (CWPharma 2020), DOC is the dissolved organic carbon content in mg/L, and $C(NO_2^-)$ is the concentration of nitrite in the wastewater (mg/L).

Accordingly, for an average Estonian WWTP effluent with a DOC of ca 30 mg/L, the determined amount of nitrite (0.2 mg/L) increases the ozone dosage by 3% to 10%. With an average ozonation energy consumption of 10 kWh/kg O_3 (Sarron et al. 2021) and an average electric energy price of 0.25 EUR/kWh, this may result in additional costs of ca 1500 to 70 000 EUR, depending on the WWTP and the required ozone dosage when using liquefied oxygen (LOX) as the ozone source. When using treated outdoor air to produce oxygen, this additional cost can be in the range of 1700 to 81 000 EUR annually. This highlights the importance of efficient nitrification before micropollutant removal using ozonation.

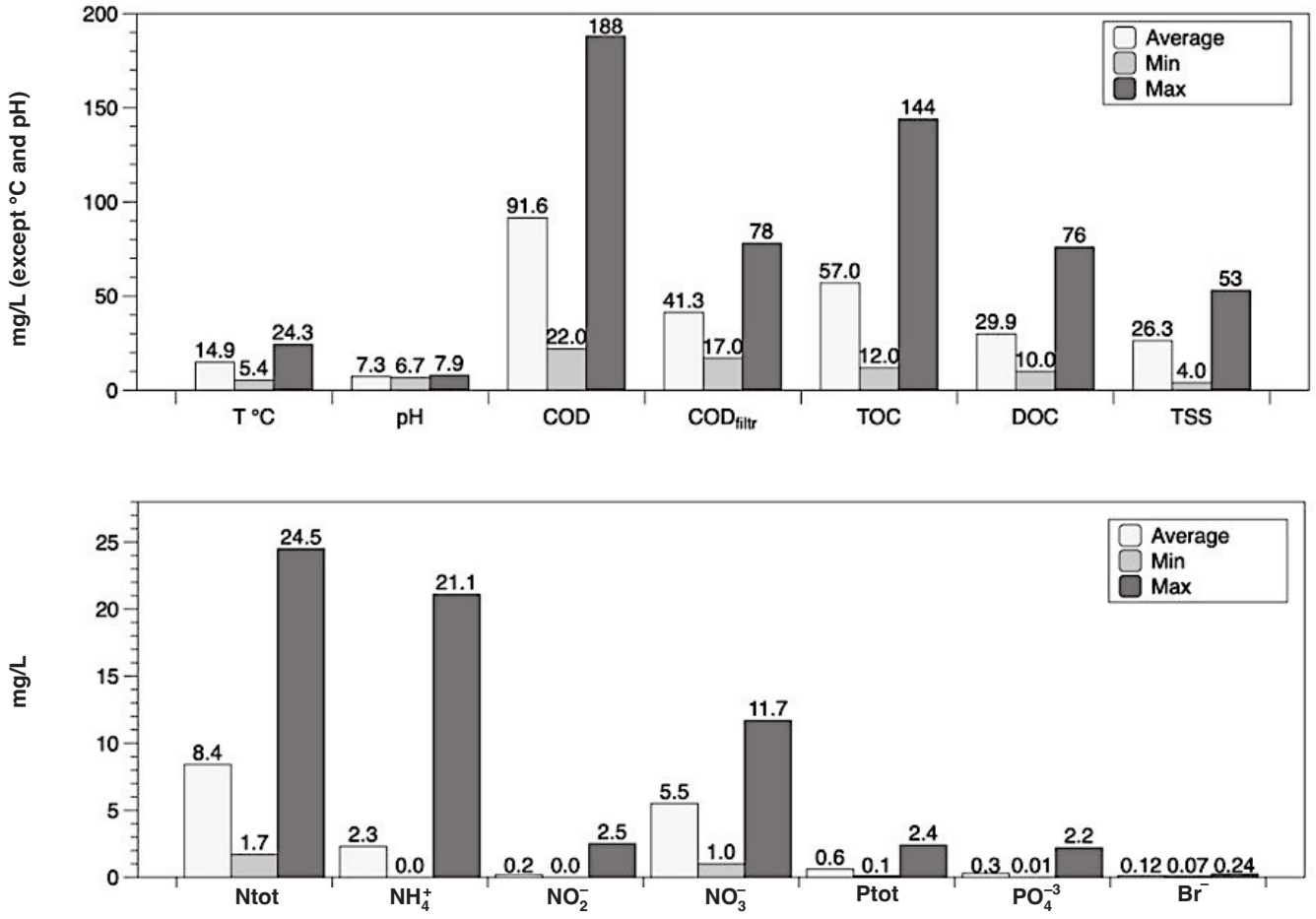

Fig. 2. The average composition of wastewater treatment plant effluents analysed in this study.

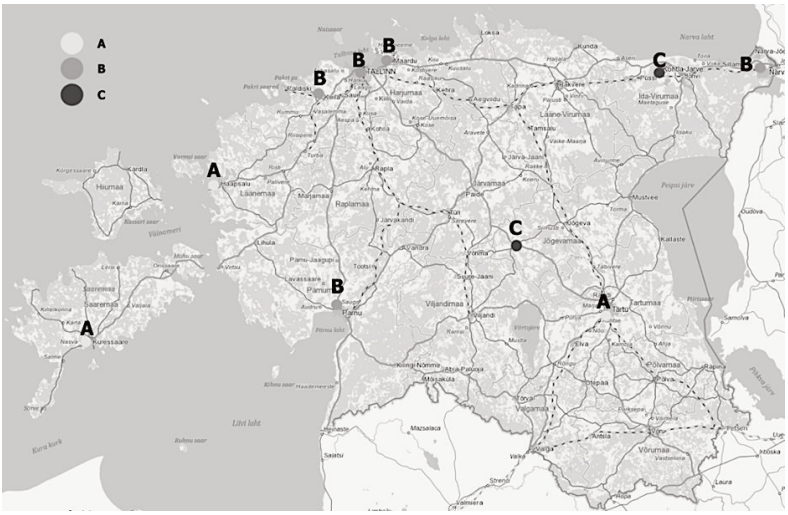

Fig. 3. Geographic distribution and concentrations of Br^- in wastewater plant effluents: <0.1 mg/L Br^- (A), 0.1–0.14 mg/L Br^- (B), and ≥0.15 mg/L Br^- (C). Map source: Land and Spatial Development Board of Estonia.

The presence of ammonium (average detected 2.3 mg/L) in WWTP effluents has more far-reaching effects. During ozonation at the near-neutral WWTP effluent pH = 7.3, reactions of molecular ozone prevail; unlike radicals, molecular ozone cannot oxidise the ammonium ion to a noticeable degree (Hoigne and Bader 1978). When subjecting bromide-containing water to ozonation, excess amounts of NH_4^+ were shown (e.g. Morrison et al. 2023) to supress bromate formation. Hypobromous acid, formed from hypobromite at pH values lower than 8.65, readily reacts with hypobromite to form monobromamine (NH_2Br), as shown in the following equation:

$$HOBr + NH_4^+ \rightarrow NH_2Br + H_2O + H^+. \quad (19)$$

Reaction (19) effectively removes hypobromites and hypobromous acid, considerably hindering their possible oxidation to bromates. It also undergoes ozonation, with

bromide and nitrate ions being the major products, as suggested in the following equation:

$$NH_2Br + 3\,O_3 \rightarrow Br^- + NO_3^- + 3\,O_2 + 2\,H^+. \quad (20)$$

While hypobromous acid reacts with ammonium (Eq. (19)) quickly, then the degradation of monobromamine by ozone (Eq. (20)) is slow. For example, for reaction (19), Morrison et al. (2023) provide a reaction rate constant of 5.5–7.5 × 10^7 L/(mol × s) for ideal conditions, suggesting that it may decrease by up to two orders of magnitude in practice. To compare, the rate constant for reaction (18) is 40 L/(mol × s). Thus, monobromamine forms ca 10 000 times faster than it degrades.

While bromide oxidation reactions are reported as second-order, both ozone and ammonia are present in large excess relative to bromide (with ozone constantly replenished). Consequently, to estimate the ozonation products' concentration, the pseudo-first-order kinetics can be used. Additionally, a continuous stirred-tank reactor (CSTR) model should be applied to continuous-flow ozonation, thus giving the following equation to operate with:

$$C_t = \frac{C_0}{1 + k't}, \quad (21)$$

where k' is the pseudo-first-order reaction rate constant (1/s), t is the reaction time (s), and C_0 is the initial concentration of the respective compound (mol/L).

The pseudo-first-order reaction constant can be obtained by multiplying the second-order rate constant k_2 by the initial concentration of the reagent in excess (ozone or ammonium), e.g.:

$$k' = k_2 \times C_0(O_3). \quad (22)$$

Additionally, the amounts of ozone available for the oxidation reactions, which have moderate reaction rate constants at earlier stages, can be deduced as the difference between the supplied ozone (20 mg O_3/L for the average WWTP effluent) and the ozone consumed by the DOC and the nitrate present in water (see Eq. (17)). For an average ozone dose of 0.6 mg O_3/mg DOC, with DOC = 30 mg/L and 0.2 mg/L NO_2^-, this would result in 18.7 mg O_3/L, making 1.3 mg O_3/L available for bromide oxidation.

The initial oxidation of bromide to hypobromite (Eq. (1)) is reported to have a reaction rate constant of 160 L/(mol × s). Thus, a 30-minute ozonation of 0.15 mg/L of bromide results in the nearly 90% conversion and the formation of ca 0.16 mg/L BrO^-. The hypobromite ion is conjugated with hypobromous acid, having a pK_a = 8.65 (Perrin 1982). The amount of dissociated hypobromous acid at any given pH can be determined as follows:

$$\omega(BrO^-) = 10^{pH - pK_a(HOBr)}. \quad (23)$$

The calculation according to Eq. (23) suggests that, at pH = 7.3, only 4.5% of the formed hypobromite remains in ionic form, while all the rest transforms into hypobromous acid on formation. While this remaining hypobromite can be reduced to bromide, according to Eq. (13), hypobromous acid undergoes fast conversion to monobromamine. Up to 2/3 of the formed monobromamine degrades according to reaction (20), producing nitrates and bromides, while around 0.05 mg/L NH_2Br could be expected to remain in the treated WWTP effluent after a 30-minute ozonation under such conditions. These calculations suggest that, for the average effluent of an Estonian WWTP serving at least 10 000 p.e., ozonation should lead to the formation of monobromamine as opposed to bromate due to the large excess of ammonium.

To compare, the kinetics of stepwise bromide-to-bromate oxidation within 30 minutes of ozonation reaction can be calculated, starting likewise with 0.15 mg/L bromide but without ammonium. There, the formation of bromate can be calculated to ca 0.06 mg/L using the more refined electron-transfer approach (Eqs (6)–(8)). Longer contact times and higher concentrations of both bromide and ozone would allow reaching the dangerous 10 mg BrO_3^-/L threshold, but a 30-minute contact time with average ozone doses seems to rule out that possibility at least in theory. Also, up to 0.15 mg/L hypobromous acid is expected to accumulate. Figure 4 sums up the major reactions taking place in bromide ozonation, both in the absence and in the presence of dissolved ammonium.

It must be noted that with the concentrations of this magnitude, mass transfer will impose additional limitations on the formation of the products; the undertaken analysis results in higher concentrations than could be achieved in reality. This kinetic study was envisioned not to provide

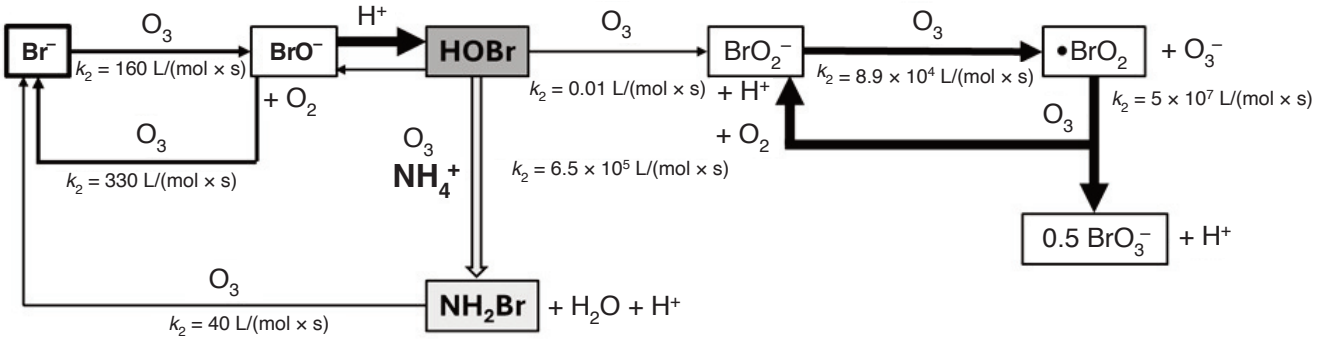

Fig. 4. Major reactions during bromide-containing water ozonation. Arrows reflect the relative reaction rate; major transformation products are in bold. Dark grey background: products obtainable without ammonium, light grey background: products obtainable in the presence of ammonium.

absolute values but as a comparison to provide an insight into the probability of obtaining different bromine-containing products. Mass transfer-induced restrictions would not, however, change the principle qualitative outcomes in terms of obtained products.

Consequently, the average effluent of an Estonian WWTP serving at least 10 000 p.e. is not expected to produce enough bromates on ozonation, with the ammonium present suppressing bromate formation. Instead, monobromamine formation takes place. If the ozonation step is followed by a biofilter, the expected amounts of monobromamine may affect the biofilter performance. The degradation of monobromamine by ozonation alone is time-consuming. In the absence of ammonium, significant formation of bromate would also not be expected according to the kinetic calculations, resulting in the formation and accumulation of hypobromous acid.

To estimate the outcomes of bromide-containing water ozonation in terms of bromide oxidation, one must compare the three distinct products formed: bromate, hypobromous acid, and monobromamine. The direct comparison of the three compounds' aquatic toxicity is not possible, as hypobromous acid and monobromamine are not stable enough to conduct the toxicity tests. Their instability is manifested through reactions forming brominated organics that can be more hazardous than bromate. Consequently, it is highly imperative to consider their reactions with polyaromatic natural organic matter (NOM), which, for the sake of simplicity, we can model here with phenol. Phenol has a pKa value of ca 10 (PubChem 2025), meaning that, at pH = 7.3, it is almost exclusively in molecular form, with only around 0.2% dissociated to the phenolate anion. However, the phenolate anion has a very high reactivity compared to the undissociated molecule, with the $-O^-$ group activating the aromatic cycle through resonance better than the undissociated -OH group: the respective reaction rate can vary by several orders of magnitude in favour of phenolate (Gallard et al. 2003). Once phenolate is reacted, a portion of phenol dissociates to maintain the equilibrium.

In terms of compound toxicity and direct hazards, bromate certainly poses the greatest threat. While bromate is a strong oxidant in theory, the kinetics of organics oxidation by it are very slow, and its bromination ability is the weakest among these three compounds. This is due to high stability of the bromate anion, arising from its tetrahedral shape, resonance stabilisation, and a relatively high number of electrons needed to reduce it. Bromate can react at reasonable rates only with strong reducing agents; these are typically not found in natural waters, including WWTP discharges, but are abundant inside cells (sulfide groups and disulfide bridges in proteins, Fe^{2+}, amino groups in proteins and nucleic acids, etc.), resulting in bromate toxicity and carcinogenicity, as we know it. Consequently, neither NOM in general nor phenol (neither molecule nor the phenolate ion) are affected by bromate as an oxidant or a brominating agent to any noticeable degree.

Hypobromous acid, on the contratry, presents a real danger through the electrophilic substitution reactions it initiates with NOM. HOBr is a strong brominating agent with the respective reaction rates being high, e.g. bromination of phenol proceeds with the apparent reaction rate constant of up to 3.5×10^5 L/(mol × s) (Gallard et al. 2003), taking into account the individual reactions of molecular HOBr and phenol, HOBr and the phenolate ion, hypobromite and the phenolate ions, and the degree of dissociation of HOBr and phenol at pH = 7.3. As an outcome of these reactions, C–Br bonds are created, which easily break and form in different places in photochemical reactions in the environment, leading to the formation of various brominated compounds. During ozonation, the bromination of organic compounds by HOBr creates specific sites for ozone to attack – the carbon atom which had its adjacent hydrogen replaced by bromine, leading to the rupture of aromatic cycles and the production of numerous trihalomethanes (THMs) and other compounds generally referred to as disinfection by-products or DBPs. Many brominated organic compounds, including DBPs, can be considered more dangerous than bromate (Wu et al. 2019).

Finally, in the case of monobromamine, we need to take into consideration its pH-related equilibrium before proceeding with the discussion. An experimentally determined monobromamine pK_a has been reported, due to the compound's relative instability over a wider range, with 6.5 (Johannesson 1960) being perhaps the most cited figure. Taking that into account would mean that, at pH = 7.3, ca 84% of monobromamine is present in the neutral molecular form (see Eq. (23) describing the hypobromite/hypobromous acid pH equilibrium), while the remaining 16% is present as the monobromammonium ion NH_3Br^+, which is a stronger electrophile and therefore more reactive, primarily attacking phenolate anions. Consequently, bromination of phenol at neutral media by monobromamine has the reaction rate of ca 1.3×10^2 L/(mol × s) (Heeb et al. 2017). The rate of phenol bromination by monobromamine is thus three orders of magnitude slower than in the case of HOBr, resulting in the lower formation of brominated organics and bromine-containing DBPs. At the same time, monobromamine degrades by ozone (see Eq. (40)), in addition to undergoing several self-decomposition pathways, producing bromide, gaseous nitrogen, nitrate, nitrogen oxides, etc. (Hu et al. 2021). Consequently, monobromamine reacts relatively slowly and degrades by various mechanisms at a comparable rate, liberating the bromide ion back to the solution. Based on this, the availability of ammonium in the solution appears to summarily shield the bromide anion from any meaningful oxidation that could result in the formation of either directly hazardous bromate or hypobromous acid, which is a precursor to even more hazardous brominated organic compounds, in any meaningful amounts.

These findings allow the authors to suggest that ozonation can in principle be applied to remove micropollutants in the quaternary treatment of WWTP effluents aimed at the abatement of micropollutants, even if the bromide anions are present. However, the amounts of the bromide anions must be firmly estimated, and the availability of ammonium – either deliberately added or remaining from incomplete nitrification – must be assured in order to obtain monobromamine instead of hypobromous acid, the precursor to various brominated

organic compounds. To assure that no bromate is produced in significant amounts, the pH of the treated effluents must be kept below 8, where the role of radical reactions in ozonation is negligible. Any additives that can be used to enhance OH-radical production (H_2O_2, Mn^{2+}, MnO_2, etc.) must likewise be avoided, and no chlorination of the effluent is advised. Additionally, at pH above 8, the alkalinity of water, i.e. carbonates and bicarbonates produced by both organic matter degradation and carbonaceous materials dissolution (Tenno et al. 2018), scavenges hydroxyl radicals, producing enough carbonate radicals. These radicals can oxidise the hypobromite ions at a reaction rate constant of 4.3×10^7 L/(mol × s) (Morrison et al. 2023), enabling the formation of bromates. A further detailed experimental investigation into these matters in the context of Estonian WWTP effluents is currently underway.

Conclusions

The goal of the current research was to map the concentration of bromide (Br^-) in Estonian wastewater treatment plant (WWTP) effluents, identifying areas where the potential use of ozonation for the micropollutant removal in WWTP effluents requires special attention. The results show that among the 10 studied WWTPs throughout Estonia, two measuring sites are clearly above the 0.15 mg/L Br^- threshold suggested by the earlier studies, with another five staying close to it (0.11–0.14 mg/L Br^-). Consequently, for most of the analysed WWTP effluents, the possibility of safely implementing ozonation as the means to remove micropollutants, while backed by kinetic analysis presented in this paper, must still be proven experimentally before undertaken in practice. Moreover, the possible disinfection by chlorination of these effluents would not be advised. An experimental study into this is currently conducted by the authors and is a basis for future publications.

Taking into consideration the composition of an average effluent of Estonian WWTPs serving 10 000 population equivalents or more, the preliminary ozonation conditions (ozone dose 20 mg O_3/L, contact time 30 minutes) suggest that the formation of bromates (BrO_3^-) in significant amounts is not to be expected, based on the available knowledge of reaction kinetics. Instead, monobromamine (NH_2Br) is expected as the main bromine-containing by-product, due to the presence of significant amounts of ammonium in the effluents. In the absence of ammonium, hypobromous acid (HOBr) is the dominant bromine-containing product. This substance is a fast and strong brominating agent, leading to the formation of brominated organics, which is more dangerous than bromate. In comparison, monobromamine seems to be a far more harmless compound, brominating organics ca 1000 times slower than hypobromous acid and degrading simultaneously, with the release of bromide.

The research also results in the general awareness of potential challenges caused by bromide in wastewater, including those arising from the implementation of the latest version of the EU Wastewater Directive. The continuation of this research, which is currently in progress, aims to evaluate the experimental applicability of ozonation as a quaternary treatment technology and to elaborate the working conditions under which ozonation may be considered safe.

Data availability statement

All research data are contained within the article and can be shared upon request from the authors.

Acknowledgements

The authors would like to express their gratitude to Ms Diana Lagoida and Mr Karl-Jochen Komp for the help with sample collection and preparation. Financial support of the Estonian Environmental Investment Centre (projects RE.4.10.22-0049 and RES.4.10.24-0024) is greatly appreciated. The publication costs of this article were covered by the Estonian Academy of Sciences.

References

Asgari, G., Samiee, F., Ahmadian, M., Poormohammadi, A. and Solimanzadeh, B. 2017. Catalytic ozonation of pentachlorophenol in aqueous solutions using granular activated carbon. *Applied Water Science*, **7**, 393–400. https://doi.org/10.1007/s13201-014-0254-y

Chowdhury, S., Koyappathody, T. M. F. and Karanfil, T. 2022. Removal of halides from drinking water: technological achievements in the past ten years and research needs. *Environmental Science and Pollution Research*, **29**, 55514–55527. https://doi.org/10.1007/s11356-022-21346-z

CWPharma. 2020. *Guideline for advanced API removal: optimisation and control of advanced treatment*. https://evel.ee/wp-content/uploads/2021/01/CWP_Guideline_GOA3_4_Final.pdf (accessed 2025-06-11).

European Union. 2020. *Directive (EU) 2020/2184 of the European Parliament and of the Council of 16 December 2020 on the quality of water intended for human consumption (recast)*. https://eur-lex.europa.eu/legal-content/EN/TXT/?uri=celex%3A32020L2184 (accessed 2025-05-26).

European Union. 2024. *Directive of the European Parliament and of the Council concerning urban wastewater treatment (recast)*. https://data.consilium.europa.eu/doc/document/PE-85-2024-INIT/en/pdf (accessed 2024-11-08).

Gallard, H., Pellizarri, F., Croué, J. P. and Legube, B. 2003. Rate constants of reactions of bromine with phenols in aqueous solution. *Water Research*, **37**(12), 2883–2892. https://doi.org/10.1016/S0043-1354(03)00132-5

Haag, W. R. and Hoigne, J. 1983. Ozonation of bromide-containing waters: kinetics of formation of hypobromous acid and bromate. *Environmental Science & Technology*, **17**(5), 261–267. https://doi.org/10.1021/es00111a004

Heeb, M. B., Kristiana, I., Trogolo, D., Arey, J. S. and von Gunten, U. 2017. Formation and reactivity of inorganic and organic chloramines and bromamines during oxidative water treatment. *Water Research*, **110**, 91–101. https://doi.org/10.1016/j.watres.2016.11.065

Hoigne, J. and Bader, H. 1978. Ozonation of water: kinetics of oxidation of ammonia by ozone and hydroxyl radicals. *Environmental Science & Technology*, **12**(1), 79–84. https://doi.org/10.1021/es60137a005

Hu, W., Lee, Y. and Allard, S. 2021. Kinetics and mechanistic investigations of the decomposition of bromamines in the presence of Cu(II). *Water Research*, **207**, 117791. https://doi.org/10.1016/j.watres.2021.117791

Johannesson, J. K. 1960. The bromination of swimming pools. *American Journal of Public Health*, **50**, 1731–1736. https://doi.org/10.2105/AJPH.50.11.1731

Karro, E., Marandi, A. and Vaikmäe, R. 2004. The origin of increased salinity in the Cambrian–Vendian aquifer system on the Kopli Peninsula, northern Estonia. *Hydrogeology Journal*, **12**, 424–435. https://doi.org/10.1007/s10040-004-0339-z

Karro, E., Marandi, A., Vaikmäe, R. and Uppin, M. 2009. Chemical peculiarities of the Silurian–Ordovician and Cambrian–Vendian aquifer systems in Estonia: an overview of hydrochemical studies. *Estonian Journal of Earth Sciences*, **58**(4), 342–352. https://doi.org/10.3176/earth.2009.4.12

Karro, E., Veeperv, K., Hiiob, M. and Uppin, M. 2020. The occurrence and geological sources of naturally high iron in the Middle Devonian aquifer system, Estonia. *Estonian Journal of Earth Sciences*, **69**(4), 281–294. https://doi.org/10.3176/earth.2020.17

Klauson, D., Kivi, A., Kattel, E., Klein, K., Viisimaa, M., Bolobajev, J. et al. 2015. Combined processes for wasterwater purification: treatment of a typical landfill leachate with a combination of chemical and biological oxidation processes. *Journal of Chemical Technology and Biotechnology*, **90**, 1527−1536. https://doi.org/10.1002/jctb.4484

Klauson, D., Romero Sarcos, N., Krichevskaya, M., Kattel, E., Dulova, N., Dedova, T. et al. 2019. Advanced oxidation processes for sulfonamide antibiotic sulfamethizole degradation: process applicability study at ppm level and scale-down to ppb level. *Journal of Environmental Chemical Engineering*, **7**(5), 103287. https://doi.org/10.1016/j.jece.2019.103287

Klein, K., Kattel, E., Goi, A., Kivi, A., Dulova, N., Saluste, A. et al. 2017. Combined treatment of pyrogenic wastewater from oil shale retorting. *Oil Shale*, **34**(1), 82–96. https://doi.org/10.3176/oil.2017.1.06

Mestri, S., Dogan, S. and Tizaoui, C. 2023. Bromate removal from water using ion exchange resin: batch and fixed bed column performance. *Ozone: Science & Engineering*, **45**(3), 291–304. https://doi.org/10.1080/01919512.2022.2114420

Morrison, C. M., Hogard, S., Pearce, R., Mohan, A., Pisarenko, A. N., Dickenson, E. R. V. et al. 2023. Critical review on bromate formation during ozonation and control options for its minimization. *Environmental Science & Technology*, **57**(47), 18393−18409. https://doi.org/10.1021/acs.est.3c00538

Odeh, I. N., Nicoson, J. S., Huff Hartz, K. E. and Margerum, D. W. 2004. Kinetics and mechanisms of bromine chloride reactions with bromite and chlorite ions. *Inorganic Chemistry*, **43**(23), 7412−7420. https://doi.org/10.1021/ic048982m

Perrin, D. D. (ed.) 1982. *Ionisation Constants of Inorganic Acids and Bases in Aqueous Solution. IUPAC Chemical Data*. 2nd ed. Pergamon Press, Oxford.

PubChem. *Phenol (compound)*. https://pubchem.ncbi.nlm.nih.gov/compound/Phenol#section=Refractive-Index (accessed 2025-12-02).

Sarron, E., Gadonna-Widehem, P. and Aussenac, T. 2021. Ozone treatments for preserving fresh vegetables quality: a critical review. *Foods*, **10**(3), 605. https://doi.org/10.3390/foods10030605

Tenno, T., Rikmann, E., Zekker, I. and Tenno, T. 2018. Modelling the solubility of sparingly soluble compounds depending on their particles size. *Proceedings of the Estonian Academy of Sciences*, **67**(3), 300–302. https://doi.org/10.3176/proc.2018.3.10

Trapido, M., Tenno, T., Goi, A., Dulova, N., Kattel, E., Klauson, D. et al. 2017. Bio-recalcitrant pollutants removal from wastewater with combination of the Fenton treatment and biological oxidation. *Journal of Water Process Engineering*, **16**, 277−282. https://doi.org/10.1016/j.jwpe.2017.02.007

Water News Europe. *Global database of WWTPs and their effluents*. https://www.waternewseurope.com/global-database-wwtps/ (accessed 2024-11-11).

WHO (World Health Organization). 2018. *Bromine as a drinking-water disinfectant.* https://cdn.who.int/media/docs/default-source/wash-documents/wash-chemicals/bromine-02032018.pdf?sfvrsn=8890aff_3 (accessed 2026-02-12).

Wu, Q.-Y., Zhou, Y.-T., Li, W., Zhang, X., Du, Y. and Hu, H.-Y. 2019. Underestimated risk from ozonation of wastewater containing bromide: both organic byproducts and bromate contributed to toxicity increase. *Water Research*, **162**, 43–52. https://doi.org/10.1016/j.watres.2019.06.054

Bromiidid puhastatud reovees: kvaternaarsete reoveepuhastusmeetodite valiku piirangud jääk-mikrosaasteainete eemaldamisel. Eesti juhtumiuuring

Deniss Klauson, Erki Lember ja Jaak Jaaku

Töös uuritakse bromiidide sisaldust vähemalt 10 000 inimekvivalenti teenindavate Eesti reoveepuhastusjaamade heitvees. Bromiididel (Br^-) võib olla oluline roll kvaternaarsete puhastusmeetodite valikul mikrosaasteainete eemaldamiseks heitveest, mida hakkab nõudma peatselt jõustuv uuenenud Euroopa reoveedirektiiv. Nimelt võib bromiide sisaldava vee osoonimisel tekkida kõrvalproduktina ohtlike omadustega bromaate (BrO_3^-); autorite varasemad uuringud on näidanud, et ohtlikuks piiriks võib olla 0,15 mg/L Br^-. Töö käigus tehtud analüüsid näitavad, et ainult 20% reoveepuhastusjaamadest on bromiidide sisaldus heitvees selgelt alla ohtliku piiri, 60% jaamades on see piiripealne ja 20% jaamades märgatavalt suurem. Samas näitab keskmise heitvee koostise põhjal tehtud kineetiline analüüs, et põhilised broomi sisaldavad kõrvalsaadused on pigem monobroomamiin (NH_2Br) ja hüpobroomishape (HOBr). See vajab praktilist kinnitust katselisel viisil, mis kajastub autorite järgnevates publikatsioonides.

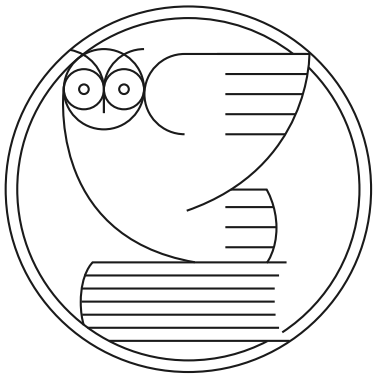

Estonian Academy Publishers
Kohtu 6, 10130 Tallinn, Estonia
Email: info@eap.ee
Subscription information available at
www.eap.ee/subscription
subscription@eap.ee

Proceedings of the Estonian Academy of Sciences 2026, 75/1

Contents

9 771736 604015